Universität Hamburg
DER FORSCHUNG | DER LEHRE | DER BILDUNG

mpsd
Max-Planck-Institut für
Struktur und Dynamik der Materie

Strong electron phonon correlation in quasi one-dimensional crystals and the excitonic insulator candidate Ta_2NiSe_5

Dissertation
zur Erlangung des Doktorgrades
an der Fakultät für Mathematik, Informatik und Naturwissenschaften
Fachbereich Physik
der Universität Hamburg

vorgelegt von

Lukas Windgätter

Hamburg
14.09.2022

Gutachter/innen der Dissertation:	Prof. Dr. Angel Rubio Prof. Dr. Ludwig Mathey
Zusammensetzung der Prüfungskomission:	Prof. Dr. Angel Rubio Prof. Dr. Ludwig Mathey Prof. Dr. Henning Moritz Prof. Dr. Michael Potthoff Dr. Simone Latini
Vorsitzender der Prüfungskomission:	Prof. Dr. Michael Potthoff
Datum der Disputation:	18.11.2022
Vorsitzender des Fach-Promotionsausschusses:	Professor Dr. Wolfgang J. Parak
Leiter des Fachbereichs Physik:	Prof. Dr. Günther H. W. Sigl
Dekan der Fakultät MIN:	Prof. Dr.-Ing. Norbert Ritter

Contents

1 Introduction **1**

2 Methods **4**
2.1 Density Functional Theory 4
2.1.1 Density Functional Theory Basics 4
2.1.2 Exchange-Correlation functional 6
2.2 One-Particle Greens Function and the GW approximation 9
2.2.1 Hedin's equations and the GW approximation 11
2.2.2 GW and DFT 12
2.3 Bethe-Salpether Equation 14

3 Controlling structural phases of quantum materials through the electron phonon coupling **16**
3.1 Effects of electron phonon coupling 17
3.2 Exciton phonon coupling 20
3.3 Publication I: Unconventional excitonic states with phonon sidebands in layered silicon diphosphide 23
3.4 Publication II: Fresnel-Floquet theory of light-induced terahertz reflectivity amplification in Ta_2NiSe_5 32

4 Excitonic Insulator **57**
4.1 Basic excitonic properties 58
4.2 A one dimensional Excitonic Insulator model 60
4.3 Candidate Materials 67
4.4 Publication III: Nature of Symmetry Breaking at the Excitonic Insulator Transition: Ta_2NiSe_5 69
4.5 Publication IV: Common microscopic origin of the phase transitions in Ta_2NiS_5 and the excitonic insulator candidate Ta_2NiSe_5 76
4.6 Publication V: The spontaneous symmetry breaking in Ta_2NiSe_5 is structural in nature 92

5 Discussion **104**

Bibliography **109**

Eidesstattliche Versicherung **120**

Preface

The following work, presented in this cumulative thesis, has been conducted from June 2018 until November 2022 at the Max Planck Institute for Structure and Dynamics. It is based on the publications I-V presented in the chapters 3 and 4. My work in the theory department of Angel Rubio has been funded by the Max Planck Society, the Deutsche Forschungsgemeinschaft (SFB-925 project 170630586) and the European Research Council (ERC-2015-AdG694097). The work was supervised by Prof. Angel Rubio, Dr. Simone Latini and as secondary supervisor by Prof. Ludwig Mathey.

Acknowledgements

First and foremost I have to thank Angel Rubio for his guidance and support. I am very happy to have been granted the opportunity to join his theory department and work under his supervision.
My deepest gratitude belongs to Simone Latini. As my PostDoc supervisor he guided me in countless meetings through my whole PhD project and was involved in every detail of my work. I really appreciated his support in stressful times, his patience when being confronted with my ignorance and the time he spent to make this work possible.
I would like to thank my three office mates Kevin Lively, Damian Hofmann and Mona Kalthoff with whom I shared many private conversations and laughs and who ultimately became my friends.
And lastly I would like to thank everyone in my life outside the institute, my family for supporting me and making studying physics possible, my friends for keeping me attached to the world outside of academia and of course my girlfriend Frederike Schwick who has supported me in countless ways during the last four years.

Abstract

Understanding and controlling the interaction between quasiparticles in quantum materials is still an ongoing endeavour in condensed matter physics. In this thesis the interaction between phononic, electronic and excitonic degrees of freedom is investigated using first principles and model calculations for prototype candidates of a family of correlated materials.

In the first part of this thesis I am going to present two different cases, where the strong coupling between electrons and phonons can be used to control the material properties in a solid. The first example, which I am going to discuss, is SiP_2. I will show that its quasi one-dimensional structure gives rise to peculiar hybrid dimensional excitons. These are shown to be detectable through their strong coupling to the ionic degrees of freedom, which leads to the emergence of exciton phonon sidebands. These have been detected by our experimental collaborators, which marks the first measurement of such low dimensional exciton phonon sidebands in a bulk system and show a prime example of symmetry engineering of the electronic degrees of freedom. For a second example I will show, how the ionic system can be dynamically controlled via an electronic excitation which allows to manipulate the reflectivity in the THz regime. I will identify the microscopical coupling mechanism of this phenomenon, which arises through the strong coupling between the involved electronic and phononic states, and explain how this manifests in an enhancement of the reflectivity of the system.

In the second part of the thesis I will present how one can understand the nature of competing phase transitions using a combined ab-initio and model calculation approach. I will discuss Ta_2NiSe_5, which is currently the most discussed candidate to host a phase transition to an excitonic insulating state. The difficulty in understanding this transition is that it is intrinsically coupled to a structural phase transition which makes the unique signature of the conjectured excitonic insulating groundstate elusive. Therefore, it is necessary to understand the nature of both transitions separately and disentangle the contribution of the two. I will discuss how an excitonic instability in this system could arise and identify its order parameter, but then show that the actual material does not realize it. Instead Ta_2NiSe_5 displays a structural instability, which leads to changes in the electronic system that is in agreement with the experiments for this material. Thus, we conclude that the phase transition is stemming from a structural instability rather than an excitonic instability.

Zusammenfassung

Das Verständnis und die Kontrolle von Quasiteilchen in Quantenmaterialien ist bis heute eine Herausforderung für die aktuelle Forschung. In dieser Dissertation werde ich die Wechselwirkung zwischen eletronischen, exzitonischen und phononischen Freiheitsgraden mittels ab-initio und Modellrechnungen untersuchen.

In dem ersten Teil dieser Arbeit werde ich zwei verschiedene Beispiele von Systemen präsentieren, deren Eigenschaften sich durch ihre starke Wechselwirkung zwischen Ionen und Elektronen manipulieren lassen. In dem ersten Projekt diskutiere ich SiP_2. Dies ist ein Kristall mit quasi-eindimensionaler Struktur, welcher Exzitonen mit einer besonderen hybrid-dimensionalen Struktur beheimatet. Es wird gezeigt, dass diese Struktur erlaubt die starke Wechselwirkung dieser Teilchen mit Phononen zu messen, da dieser stark korrelierte Exziton-Phonon Zustand als Nebenpeak zu den exzitonischen Hauptpeaks sichtbar wird. Diese wurden von unseren experimentellen Kollegen gemessen, was die erste Messung dieser niedrigdimensionalen Exziton-Phonon Nebenmaxima in einem dreidimensionalen Kristall darstellt. In einem zweiten Projekt werde ich zeigen wie das ionische System durch seine starke Kopplung zu dem elektronischen System gezielt durch die Anregung des letzteren manipuliert werden kann. So ist es möglich die Reflektivität des Systems mittels eines gezielten Laserpulses signifikant zu erhöhen. Ich werde in dieser Arbeit den mikroskopische Mechanismus dieses Phänomens identifizieren, zeigen welche elektronischen und ionischen Zustände dazu stark miteinander koppeln und erklären wie dies zu der Vergrößerung der Reflektivität des Kristalls führt.

In dem zweiten Teil dieser Arbeit werde ich zeigen wie mittels eines kombinierten Ansatzes aus ab-initio-Rechnungen, Modellrechnungen und experimentellen Daten ein kompetitiver Phasenübergang verstanden werden kann. Ich werde den Ta_2NiSe_5 Kristall diskutieren, welcher gegenwärtig der meistdiskutierte Kandidat ist um den exzitonischen Isolator Zustand zu realisieren. Die Schwierigkeit bei der Suche nach diesem Zustand ist, dass dieser in Ta_2NiSe_5 intrinsisch mit einem strukturellen Phasenübergang gekoppelt ist. Dies macht es schwer den vermuteten exzitonisch isolierenden Zustand eindeutig zu identifizieren. Deshalb ist es nötig beide Phasenübergänge einzelnd genau zu verstehen, um ihre Signatur in dem kompetitiven Phasenübergang unterscheiden zu können. Ich werde dies anhand dieses exzitonischen Isolator Kandidaten aufzeigen und diskutieren wie solch eine exzitonische Instabilität aussehen könnte und ihren Ordnungsparameter identifizieren. Anschließend werde ich jedoch zeigen, dass diese exzitonische Instabilität im realen Material nicht realisiert ist und stattdessen eine strukturelle Instabilität den Phasenübergang dominiert. Diese führt zu einer Signatur, welche im Einklang mit den experimentellen Messungen ist. Deshalb ist das Fazit, dass der exzitonische Isolator in dem Phasenübergang in Ta_2NiSe_5 keine Rolle spielt.

List of Publications

This cumulative dissertation is based on the publications I-V, which are listed below in the order in which they appear in this dissertation.
The first two publications, publication I and II, discuss two different systems which exhibit strong electron- and exciton phonon coupling, which leads the emergence of phonon sidebands stemming from hybrid dimensionality excitons in one case and an enhanced THz reflectivity in the other case.
The following publications, publication III-V, discuss the excitonic insulator candidate Ta_2NiSe_5 using ab-initio methods and theory models as well as time resolved ARPES spectra from our experimental collaborators.

- **Publication I**: Ling Zhou, Junwei Huang, **Lukas Windgaetter**, Chin Shen Ong, Xiaoxu Zhao, Cao-rong Zhang, Ming Tang, Zeya Li, Caiyu Qiu, Simone Latini, Yangfan Lu, Di Wu, Huiyang Gou, Andrew T. S. Wee, Hideo Hosono, Steven G. Louie, Peizhe Tang, Angel Rubio, and Hongtao Yuan. Unconventional excitonic states with phonon side-bands in layered silicon diphosphide. *Nature Materials*, 21(7):773–778, Jul 2022

- **Publication II**:Marios Michael, Sheikh Rubaiat Ul Haque, **Lukas Windgaetter**, Simone Latini, Yuan Zhang, Angel Rubio, Richard D. Averitt, and Eugene Demler. Fresnel-floquet theory of light-induced terahertz reflectivity amplification in Ta_2NiSe_5. 2022. Preprint published at `https://arxiv.org/abs/2207.08851`

- **Publication III**: Giacomo Mazza, Malte Rösner, **Lukas Windgätter**, Simone Latini, Hannes Hübener, Andrew J. Millis, Angel Rubio, and Antoine Georges. Nature of symmetry breaking at the excitonic insulator transition: Ta_2NiSe_5 . *Phys. Rev. Lett.*, 124:197601, May 2020

- **Publication IV**: **Lukas Windgätter**, Malte Rösner, Giacomo Mazza, Hannes Hübener, Antoine Georges, Andrew J. Millis, Simone Latini, and Angel Rubio. Common microscopic origin of the phase transitions in Ta_2NiS_5 and the excitonic insulator candidate Ta_2NiSe_5. *npj Computational Materials*, 7(1):210, Dec 2021.

- **Publication V**: Edoardo Baldini, Alfred Zong, Dongsung Choi, Changmin Lee, Marios H. Michael, **Lukas Windgaetter**, Igor I. Mazin, Simone Latini, Doron Azoury, Baiqing Lv, Anshul Kogar, Yao Wang, Yangfan Lu, Tomohiro Takayama, Hidenori

Takagi, Andrew J. Millis, Angel Rubio, Eugene Demler, and Nuh Gedik. The spontaneous symmetry breaking in Ta_2NiSe_5 is structural in nature. 2020. Preprint published at `https://arxiv.org/abs/2007.02909`.

Declaration of Contribution

In the following I will list my contribution to all of the presented publications.

- **Publication I**: I performed the ab-initio calculations (Computation of bandstructure and geometry optimization) and contributed to the development of the models used in this publication. All authors have contributed to the analysis of the data and the creation of the manuscript.
- **Publication II**: I performed all Density Functional Theory, GW and BSE simulations and created the corresponding figures. All authors have contributed to the analysis of the data and the writing of the manuscript.
- **Publication III**: I performed the ab-initio calculations (Computation of bandstructure and geometry optimization). All authors have contributed to the analysis of the data and the creation of the manuscript.
- **Publication IV**: I performed all simulations and created all figures in this publication. All authors have contributed to the analysis of the data and the writing of the manuscript.
- **Publication V**: I performed all ab-initio calculations (Density Functional Theory and GW) and created the corresponding figures. All authors have contributed to the analysis of the data and the writing of the manuscript.

1 Introduction

The overarching goal of condensed matter physics is to understand and control complex physical systems such as solids and molecules. With this we would like to be able to create materials with tailored electronic and ionic properties on demand, which can be used for new technological applications. Possibly the most famous example for such a breakthrough is the invention of the transistor [1], which triggered the revolution of information technology and is now part of almost any information technology device such as computers and smartphones. Up to date silicon is, due to its abundance in nature and easy controllability, still the base element for most of these devices. However, the growing demand for even more specialized devices has sparked the search for new materials. Therefore, the goal to find novel materials with highly controllable properties is still an ongoing challenge in condensed matter physics. Some of the most interesting candidate materials to realize such potential new breakthrough applications are for instance cuprates which exhibit superconductivity at unusually high temperatures [2–4] or perovskite crystals which can be used to produce very high efficiency solar cell modules [5,6]. In recent years, the possibility to create layered materials such as van-der Walls single- or hetero-layers [7–11] and being able to control them via symmetry engineering, i.e. by introducing a twist [12], have opened even more pathways to tailor the properties of a crystal.

Often new emergent physical phenomena are described in terms of so called quasiparticles. These are collective excitations which can be reframed as a single particle, but only exist in their specific system. The most common examples for such quasiparticles in condensed matter systems are phonons, which are collective vibrations of the ions, or holes, which are electron vacancies that behave similar to positrons. An example of a two component quasiparticle is the so called exciton. It is a bound pair of an electron and a hole and has properties comparable to an hydrogen atom. While a lot of research has been focused on understanding how these quasiparticles emerge and what their spectroscopic signature is, understanding and controlling the complex interaction between them still poses an immense challenge.
From a theoretical point of view the main difficulty is the numerical complexity of the physical problem at hand. For real systems this complexity does not allow to compute an exact solution and many methods have been proposed to solve it approximately. These are generally divided into two subcategories. One are so called ab-initio methods. These are methods designed to work for any physical condensed matter system, requiring only

the atomic species and lattice as minimal input. Arguably its most famous representant is Density Functional Theory (DFT), which has shown immense success in describing the properties of crystals. However, besides its generality, ab-initio methods often struggle to describe the complex interactions between multiple (quasi-)particles and strong correlation phenomena. The second common approach to overcome this issue is to build physical models and to solve these numerically. Because these are usually tailored to capture the physics of very specific interactions between particles in great detail while neglecting all other interactions, they often fail to translate between systems and need external parameters as input.
The goal of this thesis is to show how a combined approach using ab-initio simulations and ab-initio inspired model calculations together with experimental data can be used to understand the complex microscopic dynamics between quasiparticles and their influence on phase transitions. I will focus on the interplay between electrons, phonons and excitons and show how such an interdisciplinary approach can be used to understand and control these complex physical objects.

In the first part of this dissertation I will investigate how engineering crystal structures can influence the properties and interaction between the quasiparticles and how this interaction can be tuned to manipulate the material properties. I will introduce two materials, that exhibit a very strong interaction between the electronic and phononic system, due to their highly anisotropic quasi one-dimensional character. I will show that this coupling can be used in one of these crystals to control reflectivity of the system through optical laser pumping. By selective excitation of the electronic system via such a pump, we can tune the reflectivity of the crystal and significantly enhance it on demand. For a second material I will show, that the coupling between excitons and phonons can be used to detect unconventional hybrid dimensionality excitonic states, whose exotic nature has been imprinted by the underlying lattice symmetry. This allows for the first detection of low dimensional exciton phonon sidebands in a bulk material. These two projects are prime examples of controlling the electronic or ionic properties of a solid, by exploiting the strong coupling between these two channels and selectively manipulating the corresponding other degree of freedom.

In the second part of this thesis I will discuss an exotic new state of matter which is called the Excitonic Insulator (EI). In its groundstate it consists of a condensate of excitonic particles. This state has been envisioned over half a decade ago as the electron-hole analogue of the superconducting state [13–19], but never been measured. In recent years it has gained a lot of new interest, because of the ability to create new layered or low dimensional candidate materials [20–25]. Out of these candidate materials none has been confirmed to host an EI, because the phase transition into the EI groundstate is usually accompanied by another transition. These can be the formation of a charge density wave

(CDW) [21, 26, 27] or in the case of Ta_2NiSe_5, which is discussed in this thesis, a structural phase transition [28–31]. Therefore, it is incredibly challenging to experimentally disentangle these two transitions and unambigously confirm the EI. I will show in this project how one can understand these competing phase transitions using a combination of model calculations and ab-initio methods and show for the case of Ta_2NiSe_5 that this material exhibits a predominantly lattice driven transition rather than an EI transition. With this finding I will provide an important contribution in the controversial discussion surrounding this material.

The dissertation is structured as follows:

- **Chapter 2:** In this chapter I will introduce the ab-initio methods which are used for a majority of the calculation. I will highlight very briefly the ideas of Density Functional Theory, the differences between some of the functionals used in this work and introduce Many Body Theory methods, that go beyond DFT.
- **Chapter 3:** Here I will introduce the basic concept of electron phonon coupling and derive the main spectroscopic feature of strongly coupled exciton-phonon states which appear as sidebands. The following two publications I and II will highlight examples for such strong electron and exciton phonon coupling effects: We will show how exciton-phonon sidebands arise from hybrid dimensionality excitons in SiP_2 and how the THz reflectivity in Ta_2NiSe_5 can be controlled via a peculiar nonlinear electron phonon coupling process.
- **Chapter 4:** I will introduce the basic idea of an exciton and the concept of an excitonic insulating groundstate. I will highlight its similarity to Bardeen-Cooper-Schrieffer (BCS) theory and its spectroscopic features. Then I will discuss in the publications III-V the controversially debated EI candidate Ta_2NiSe_5 and show that its phase transition is predominantly of structural nature rather than exitonic.
- **Chapter 5:** The final chapter will be a comprehensive discussion of the obtained results in light of the recent developments in the field.

2 Methods

2.1 Density Functional Theory

Among the electronic structure theory methods Density Functional Theory (DFT) has become one of the most successful and widespread methods. Being proposed in the 1960s with key works from Hohenberg, Kohn and Sham [32, 33], its overwhelming success started in the 1990s with the introduction of new accurate functionals, such as the PW91 and PBE functional [34, 35], and growing computational resources (see Fig. 2.1). Walter Kohn has been awarded the nobel prize in chemistry in 1998 "for his development of the density-functional theory" [36].
In the following section I am going to explain very briefly the basic concepts of Density Functional Theory and discuss the different classes of exchange correlation functionals which will be used in this work.

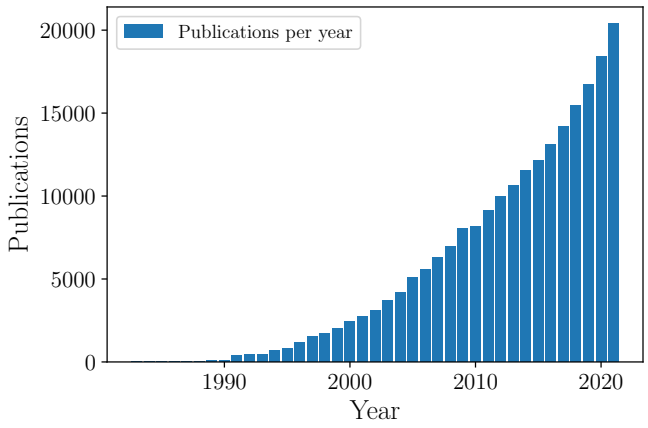

Fig. 2.1 Number of Density Functional Theory related publications obtained using a WebOf-Science search with the keywords: Density Functional Theory, Density-Functional Theory and Density-Functional-Theory (1.3.2022, 16:08). Adapted from [37]

2.1.1 Density Functional Theory Basics

We start from the standard Many-Body electronic Hamiltonian within the Born-Oppenheimer approximation for N particles in atomic units

$$H = \underbrace{\sum_{i=1}^{N}(-\frac{\nabla_i^2}{2m_i})}_{\text{kin. Energy}} + \underbrace{\sum_{i=1}^{N} V(\mathbf{r_i})}_{\text{ext. potential}} + \underbrace{\sum_{i<j=1}^{N} V_e(\mathbf{r_i}, \mathbf{r_j})}_{\text{el.-el. interaction}} \quad , \tag{2.1}$$

where $V(\mathbf{r})$ is the so called external potential given by the ions. $V_e(\mathbf{r_1}, \mathbf{r_2})$ is the electron-electron interaction potential which is commonly chosen as the Coulomb potential. Directly solving the Schrödinger equation associated with the above Hamiltonian is impossible for realistic systems, because of its overwhelming numerical complexity. The main idea of Density Functional Theory is to recast the many-body problem into a minimization problem with respect to a single-particle density $n(\mathbf{r}) = \int (\prod_{i=2}^{N} d^3\mathbf{r}_i) \;\; |\Psi(\mathbf{r}, \mathbf{r}_2, ..., \mathbf{r}_N)|^2$, which in turn uniquely determines the groundstate wavefunction. This is proven using the so called Hohenberg Kohn theorems which are the formal foundation of DFT [32]. They read:

Hohenberg-Kohn theorem 1

The external potential V_{ext} (and hence the total energy), is a unique functional of the electron density.

Hohenberg-Kohn theorem 2

A universal functional $E(n)$ in terms of the density n can be defined for any external potential V_{ext}. For any given V_{ext} the global minimum is the exact ground state energy of that system and the groundstate density n_0, that minimizes it is unique

$$\min \{E[n]\} = E[n_0].$$

The Hohenberg-Kohn theorem 1 proves that there exists a one-to-one correspondence between the groundstate density n_0 and the external potential which in turn uniquely defines the Hamiltonian and its groundstate wavefunction. Thus, all the information given by the full Many Body wavefunction is already encoded in the much simpler object of the one particle density. The Hohenberg-Kohn theorem 2 proves, that this groundstate density can be found via minimization of the Energy functional $E[n]$:

$$\begin{aligned} E[n] &= T[n] + V[n] + U[n] \qquad \text{with} \\ T[n] &= \text{kinetic energy} \\ V[n] &= \text{e-i interaction} \\ U[n] &= \text{e-e interaction} \end{aligned} \tag{2.2}$$

However, it is unknown how to explicitly construct this exact energy functional. Therefore, Kohn and Sham have proposed to simplify this problem: Instead of trying to find the exact energy functional, one should consider the energy functional of a system of non-interacting particles in an effective potential which has the same groundstate density as

the interacting system [33]:

$$\begin{aligned}
E[n_{KS}] &= T_{KS}[n_{KS}] + V[n_{KS}] + U_H[n_{KS}] + U_{XC}[n_{KS}] \quad \text{with} \\
n_{KS}(\mathbf{r}) &= \text{Kohn-Sham density} \equiv \rho = \sum_{i=1}^{N} |\phi_i|^2(\mathbf{r}) \\
T_{KS}[\rho] &= \text{kinetic Energy} = -\sum_{i=1}^{n} \phi_i^*(\mathbf{r}) \frac{\nabla_{r_i}^2}{2m} \phi_i(\mathbf{r}) \\
V[\rho] &= \text{e-i interaction} = \int d^3r V(\mathbf{r})\rho(\mathbf{r}) \\
U_H[\rho] &= \text{Hartree interaction} = e^2 \int d^3r\, d^3r' \frac{\rho(\mathbf{r})\rho(\mathbf{r}')}{|\mathbf{r}-\mathbf{r}'|} \\
U_{XC}[\rho] &= \text{exchange correlation functional}
\end{aligned} \tag{2.3}$$

The effective potential is called the exchange correlation potential and formally includes all exchange and correlation effects of the interacting system. In practice it is unknown and has to be approximated. The Kohn-Sham energy functional is then minimized using the variational principle which gives the Kohn-Sham equations that are the basic of any DFT algorithm [33]

$$\epsilon_i \phi_i(\mathbf{r}) = -\frac{\nabla^2}{2m}\phi_i(\mathbf{r}) + V(\mathbf{r})\phi_i(\mathbf{r}) + e^2 \int d^3r' \frac{\rho(\mathbf{r})}{|\mathbf{r}-\mathbf{r}'|}\phi_i(\mathbf{r}) + \underbrace{V_{XC}[\rho]\phi_i(\mathbf{r})}_{\frac{\delta U_{XC}}{\delta \phi_i^*}}. \tag{2.4}$$

2.1.2 Exchange-Correlation functional

Since the foundation of Density Functional Theory in the 60s [32, 33] there has been a plethora of different exchange correlation functionals. These can be classified by their degree of approximations and differ in both chemical accuracy and computational workload. The simplest approximation to the exchange correlation functional is setting it to zero and considering only the Hartree interaction in the Kohn-Sham equations. Of course this is a very crude approximation and can be improved by considering corrections in the density only (LDA), the density and its gradient correction of different orders (GGA and metaGGA) or by including exact exchange (EXX) which requires the calculation of the non-local Coulomb integrals entering the Fock-term. An overview of these different classes of functionals is given by the Jacobs ladder of exchange correlation functionals (see Fig.2.2), which shows the different classes of functionals ranked by their chemical accuracy but also computational hardness. For each of these sub-classes there exists a zoo of different functionals which take slightly different approaches to approximate the exact exchange correlation functional. Over the years some of these functionals have proven to perform very well for a variety of systems. In the following I will briefly discuss the most relevant functionals for this work.

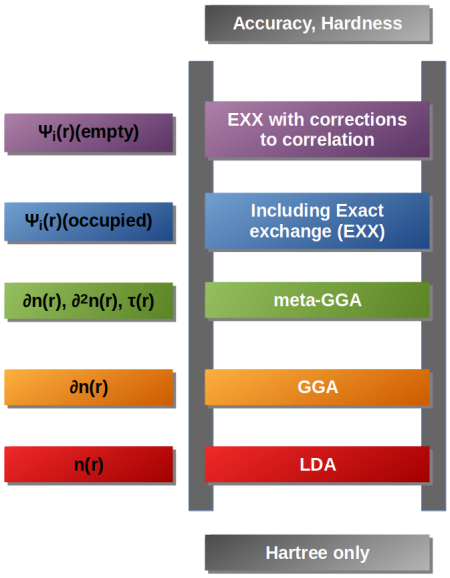

Fig. 2.2 Jacobs ladder of exchange correlation functionals. The chemical accuracy increases together with the computational hardness for the different functionals along this ladder. Adapted from [38].

The LDA and PBE Functional

The local density approximation, or often called LDA functional, is the simplest functional, that is still being used. It depends only on the density ρ and approximates the exchange and correlation contributions with those of the homogeneous electron gas [33,39]

$$\begin{aligned} E_{XC}^{\mathrm{LDA}}[\rho] &= E_{X}^{\mathrm{LDA}}[\rho] + E_{C}^{\mathrm{LDA}}[\rho] \\ &= \overbrace{\frac{3}{4}\left(\frac{3}{\pi}\right)^{\frac{1}{3}} \int \rho(\mathbf{r})^{\frac{3}{4}} d\mathbf{r}} + E_{C}^{\mathrm{LDA}}[\rho]. \end{aligned} \tag{2.5}$$

For the correlation energy no analytical expression is known and it is parameterized using high precision Monte-Carlo data from Ceperly and Alder [39]. Many modern functionals that go beyond LDA use different approaches approximating the exchange term while still relying on the Ceperly and Alder data for the correlation part.

The simplest extension of the LDA functional is the so called generalized gradient approximation (GGA) which parameterizes the functional not only using the density ρ but also its gradient

$$E_{XC}^{\mathrm{GGA}} = E_{XC}^{\mathrm{GGA}}[\rho, \nabla\rho]. \tag{2.6}$$

There exists a variety of different GGA functionals with the Perdew-Burke-Enzerhoff (PBE) functional [34] being the most commonly used one up to date. It is a non-empiric functional which offers high performance while retaining a reasonable numerical accuracy for almost any system.

Modified-Becke-Johnson functional

The modified-Becke-Johnson functional (mBJ) [40] is a popular meta-GGA functional, which is an extension to the standard Becke-Johnson functional [41]. The idea of the standard Becke-Johnson functional is to include the exact exchange contribution from Hartree-Fock theory using a local effective potential which removes the orbital dependence of the exchange interaction. This allows an approximate treatment of the exchange in terms of the electron density [41,42]. This exchange contribution is then used together with the LDA correlation term.
Becke and Johnson have built such a functional under the constraints of reproducing certain limits (e.g. it has to reproduce the exact uniform electron gas potential in the limit of the density being the density of the electron gas). This functional has been the starting point for Tran and Blaha, who modified it using a semi-empirical approach. The modified functional is [40]

$$V_{\mathrm{mBJ},x,\sigma} = c\, V_{BR}(\mathbf{r}) + (3c-2)\frac{1}{\pi}\sqrt{\frac{5}{12}}\sqrt{\frac{2\,\tau_\sigma(\mathbf{r})}{\rho_\sigma(\mathbf{r})}}, \tag{2.7}$$

where $V_{BR}(\mathbf{r})$ is the Becke-Roussel potential [42], an effective potential describing the local exchange effect. It is completely determined by $\rho, \nabla\rho_\sigma, \nabla^2\rho_\sigma$ and the kinetic energy density $\tau_\sigma = \sum_{i=1}^{N} \nabla\phi^*_{\sigma,i}\nabla\phi_{\sigma,i}$. The second term is a correction term to the Becke-Roussel potential proposed by Becke and Johnson [41]. The mBJ functional contains a free parameter c, that controls the strength of the effective exchange interaction of the potential. It can either be optimized manually to fit experimental results or computed self-consistently using the charge density and a semi-empirical formula, which has been chosen such that it reproduces bandgaps of a range of solids well

$$c = \alpha + \beta\left(\frac{1}{V_{\mathrm{cell}}}\int_{\mathrm{cell}}\frac{|\nabla\rho(\mathbf{r})|}{\rho(\mathbf{r})}d^3r\right). \tag{2.8}$$

These empirical parameters are $\alpha = -0.012$ and $\beta = 1.023\,\mathrm{bohr}^{-1}$. For c=1 the original Becke-Johnson functional is recovered [41]. Note that in their formulation the Slater potential has been used instead of the Becke-Roussel potential, but these two have been shown to be quasi-identical for atoms [40,41].

Hybrid Functionals

Hybrid functionals are considered to be among the most accurate exchange correlation functionals for DFT calculations. They exist in different flavors but their underlying idea, which all have in common, is that they replace part of the exchange contribution of the standard gradient corrected functionals with the exact Hartree-Fock exchange [43–45]

$$E_{\mathrm{HF},x} = -\frac{e^2}{2}\sum_{n\mathbf{k}n'\mathbf{k}'} f_{n\mathbf{k}} f_{n'\mathbf{k}'}\int\frac{\phi^*_{n\mathbf{k}}(\mathbf{r})\,\phi^*_{n'\mathbf{k}'}(\mathbf{r}')\,\phi_{n\mathbf{k}}(\mathbf{r}')\,\phi_{n'\mathbf{k}'}(\mathbf{r})}{|\mathbf{r}-\mathbf{r}'|}d^3r d^3r' \quad . \tag{2.9}$$

As such hybrid functionals are non-local objects that explicitly depend on the wavefunctions and go beyond the standard formulation of DFT. The formal foundation for such functionals has been set by Levy [46] who has generalized the Hohenberg Kohn theorems for one particle density matrix and wavefunction based functional approaches.
In this work we will be using the range-separated hybrid functionals HSE03 and HSE06 introduced by Heyd, Scuseria and Enzerhof [47,48], which differentiate between a short range contribution and a long range contribution to the exchange energy. The decomposition of the Coulomb interaction into these two contributions is done using the error function

$$\frac{1}{|\mathbf{r}-\mathbf{r}'|} = \frac{\mathrm{erfc}(\mu|\mathbf{r}-\mathbf{r}'|)}{|\mathbf{r}-\mathbf{r}'|} + \frac{\mathrm{erf}(\mu|\mathbf{r}-\mathbf{r}'|)}{|\mathbf{r}-\mathbf{r}'|}, \tag{2.10}$$

with μ being the so called range separation parameter. Using this range separation the exchange correlation energy can be written

$$E_{XC}^{\mathrm{HSE}} = \frac{1}{4}E_x^{\mathrm{HF,SR}}(\mu) + \frac{3}{4}E_x^{\mathrm{PBE,SR}}(\mu) + E_x^{\mathrm{HF,LR}}(\mu) + E_c^{\mathrm{PBE}} \quad . \tag{2.11}$$

Therefore, only $\frac{1}{4}$ of the short range (SR) contribution of the PBE exchange is replaced with the exact Hartree-Fock exchange, while both the long range (LR) exchange and correlation contributions of the PBE functional are kept. It has been shown, that the optimal choice for the range separation parameter μ is between 0.2 and 0.3. Usually one chooses it to either 0.2 or 0.3 which corresponds to the so called HSE06 and HSE03 functionals [47,48], that I will be using in this work.

2.2 One-Particle Greens Function and the GW approximation

A systematic approach to improve on the results of DFT calculations is to employ Many Body Perturbation Theory methods [49,50]. The basis for almost all standard Many Body Perturbation Theory (MBPT) methods is the one-particle Greens function. For zero temperature it is defined as the expectation value of the time-ordered product of creation and annihilation operators [51]

$$G(1;2) = -i\langle\psi_0^N|\mathcal{T}\left\{\psi_H(1)\psi_H^\dagger(2)\right\}|\psi_0^N\rangle \tag{2.12}$$

with

- $|\psi_0^N\rangle$ being the N-particle groundstate at $t = t_0$ and temperature $T = 0$K
- $\psi_H(1)$, $\psi_H^\dagger(2)$ being the (fermionic) field operators in the Heisenberg picture
- Notation $i = (\boldsymbol{x_i}, t_i)$ with $\boldsymbol{x_i}$ being a collective space-spin variable
- T being the time ordering operator.

In principle this definition can also be extended to include finite temperatures. This is done by extending the definition of the time variable to complex values and defining time ordering on the Keldysh contour [51, 52]. This is the so called Keldysh formalism, which has been proposed to describe also non-equilibrium processes. For our purpose, however, the zero temperature Greens function is sufficient and introducing the Keldysh formalism would go beyond the scope of this thesis.
Physically, the Greens function describes the probability amplitude for a particle being created at $(\mathbf{x_1}, t_1)$ to propagate to $(\mathbf{x_2}, t_2)$. The Greens function is a very powerful mathematical tool as it allows to compute the expectation value of any one-particle operator $\hat{O}(t)$ via

$$O(t) = \int d\boldsymbol{x_1} d\boldsymbol{x_2} O(\boldsymbol{x_1}, \boldsymbol{x_2}, t) \rho(\boldsymbol{x_1}, \boldsymbol{x_2}, t). \tag{2.13}$$

where $\rho(\boldsymbol{x_1}, \boldsymbol{x_2}, t)$ is the one-particle density, which can be obtained from the Greens function

$$\rho(\boldsymbol{x_1}, \boldsymbol{x_2}, t_1) = -iG(\boldsymbol{x_1}, t_1; \boldsymbol{x_2}, t_1^+) \quad . \tag{2.14}$$

Here, t_1^+ is a time infinitesimally later than t. Full knowledge of the one-particle Greens function even allows to compute the exact groundstate energy of the Many Body system using the Galitski-Migdal formula [53]. However, the definition of the Greens function (2.12) is often not convenient for actual calculations as it incorporates the N-particle groundstate, which is not known. Thus, one usually defines the Greens function via its equations of motion

$$i\frac{d}{dt_1}G(1;2) - \int d3h(1;3)G(3;2) + i\int d3v_c(1;3)G_2(1,3;2,3^+) = \delta(1;2) \tag{2.15}$$

$$-i\frac{d}{dt_2}G(1;2) - \int d3G(1;3)h(3;2) + i\int d3G_2(1,3^-;2,3)v_c(3;2) = \delta(1;2). \tag{2.16}$$

Here

- $h(1;2)$ is the one-particle part of the Hamiltonian
- $v_c(1,2)$ is the Coulomb interaction term
- $G_2(1,2;1',2')$ is the 2-particle Greens-function.

These equation of motion can be easily obtained by substituting the equation of motion for the creation and annihilation operators. However, because of the two-particle Coulomb operator, the two-particle Greens function appears in the equation of motion of G. It is defined as [51]

$$G_2(1,2;1',2') = -\langle\psi_0^N|\mathcal{T}\left\{\psi_H(1)\psi_H(2)\psi_H^\dagger(2')\psi_H^\dagger(1')\right\}|\psi_0^N\rangle \tag{2.17}$$

and describes the two particle scattering processes such as the propagation of two electrons, two holes or an electron hole pair.

Having the two-particle Greens function in the defining equation of the one-particle Greens function is problematic for practical calculations, because the equation of motion for the two-particle Greens function again contains the next higher order Greens function due to the interaction term. This is a general property and the infinite hierarchy of equations which arises is called Martin-Schwinger-Hierarchy [51, 54].
To truncate this hierarchy one introduces a quantity called self-energy, Σ, which is defined as [51]

$$\int d3\Sigma(1;3)G(3;2) = -i\int d3v_c(1:3)G_2(1,3:2,3^+). \tag{2.18}$$

Substituting it into the equations of motion for $G(1;2)$ one obtains

$$i\frac{d}{dt_1}G(1;2) - \int d3h(1;3)G(3;2) - i\int d3\Sigma(1;3)G(3;2) = \delta(1;2)$$

$$-i\frac{d}{dt_2}G(1;2) - \int d3G(1;3)h(3;2) - i\int d3G(1;3)\Sigma(3:2) = \delta(1;2).$$

We obtain an effective single particle equation in which the self-energy plays the role of an effective non-local potential in both space and time, which arises due to the Coulomb interaction term. The equations of motion for the one-particle Greens function can also be cast into an integral form and one obtains the so called Dyson equation [51, 55]

$$G(1;2) = G_0(1;2) + \int d3d4G_0(1;3)\Sigma(3;4)G(4;2), \tag{2.19}$$

where $G_0(1;2)$ denotes the one-particle Greens function of the non-interacting system. $G_0(1;2)$ satisfies the same equations of motions as the interacting one-particle Greens function (2.15, 2.16), only with vanishing self-energy.

2.2.1 Hedin's equations and the GW approximation

Calculating the self-energy in order to obtain the one-particle Greens function is a formidable task and generally not possible. Usually one relies on a perturbative expansion of the self-energy operator in terms of Feynman diagrams or using a functional approach, which has to be truncated after a certain order. Hedin's equations recast the problem of calculating the self-energy into a closed set of equations which allows for a very convenient way to

apply approximations. They read [56]

$$\begin{aligned} G(1;2) &= \int d3\, d4\, G_0(1;3)\left[v_H(3)\delta(3;4) + \Sigma_{XC}(3;4)\right] G(4;2) \\ \Sigma_{XC}(1;2) &= i\int d3\, d4\, G(1;4)W(1^+;3)\Gamma(4,2;3) \\ W(1;2) &= v(1;2) + \int d3\, d4\, v_c(1;3)P(3;4)W(4;2) \\ P(1;2) &= -i\int d3\, d4\, G(1;3)G(4;1)\Gamma(3,4;2) \\ \Gamma(1,2;3) &= \delta(1;3)\delta(2;3) + \int d4\, d5\, d6\, d7\, \frac{\delta\Sigma_{XC}(1;2)}{\delta G(4;5)} G(4;6)G(7;5)\Gamma(6,7;3) \end{aligned} \tag{2.20}$$

where $G(1;2)$ is the one-particle Greens function discussed above, $\Sigma_{XC}(1;2)$ the self-energy from which we have stripped the Hartree contribution v_H, $W(1;2)$ the screened interaction, $P(1;2)$ the polarizability , $\Gamma(1,2;3)$ the so called vertex function and $v_c(1;2)$ the Coulomb interaction. This set of equations is still exact and solving them iteratively allows for the exact computation of the one particle Greens function and its self-energy. This is, however, not possible in practice. Therefore, one usually truncates these equations by approximating the vertex function to

$$\Gamma(1,2;3) = \delta(1;3)\delta(2;3) \quad . \tag{2.21}$$

This is the so called GW approximation which effectively neglects all higher order terms in the screened interaction. Hedin's equations reduce to

$$\begin{aligned} G(1;2) &= \int d3\, d4\, G_0(1;3)\left[v_H(3)\delta(3;4) + \Sigma_{XC}(3;4)\right] G(4;2) \\ \Sigma_{XC}(1;2) &= i\, G(1;2)W(2;1) \\ W(1;2) &= v(1;2) + \int d3\, d4\, v_c(1;3)P(3;4)W(4;2) \\ P(1;2) &= -iG(1;2)G(2;1). \end{aligned} \tag{2.22}$$

This also explains the name of the GW approximation as the self-energy can now be computed as the product between one-particle Greens function G and the screened interaction W. In principle Hedin's equations are now solvable using the Hartree Fock wavefunctions for G and solving the equations (2.22) iteratively. This approach is known as scGW-method. Unfortunately this task is still numerically very demanding. Therefore, one usually uses a different scheme which combines density functional theory and the GW approximation.

2.2.2 GW and DFT

The idea is to perform the GW approximation starting from the DFT groundstate which already gives a good approximation of the one-particle Greens function. The GW calcu-

lation is then performed to correct the DFT results and should converge only after a few iterations.
To correct the Kohn-Sham energies using the GW approximation one usually employs the quasiparticle equation which is an equivalent formulation of the equations of motion for the one-particle Greens function (2.15) using Lehmanns representation

$$h(\boldsymbol{x})\Phi_k^{QP}(\boldsymbol{x}) + \int d\boldsymbol{x'}\Sigma(\boldsymbol{x},\boldsymbol{x'},E_k^{QP})\Phi_k^{QP}(\boldsymbol{x'}) = E_k^{QP}\Phi_k^{QP}(\boldsymbol{x}) \quad . \tag{2.23}$$

This equation allows to recast the above equation using the Kohn-Sham Hamiltonian as one-particle Hamiltonian by adding and subtracting the Kohn-Sham potential [50]

$$\begin{aligned}\underbrace{[h(x)+v_{XC}(x)]}_{h_{KS}(x)}\Phi_i^{QP} + \int dx'\left(\Sigma_{XC}(x,x',E_i^{QP}) - v_{XC}(x')\delta(x,x')\right)\Phi_i^{QP}(x') \\ = E_i^{QP}\Phi_i^{QP}(x).\end{aligned} \tag{2.24}$$

To solve this equation one can expand the self-energy in terms of the Kohn-Sham energies using a first order expansion

$$\Sigma(E_i^{QP}) = \Sigma(E_i^{KS}) + \left.\frac{\partial E(\omega)}{\partial\omega}\right|_{E_i^{KS}}(E_i^{QP} - E_i^{KS}). \tag{2.25}$$

Then one can compute the quasiparticle energy from equation (2.24) as using a first order perturbation theory expansion [50]

$$\begin{aligned}E_i^{QP} &\approx E_i^{KS} + \langle\Phi_i^{KS}|\Sigma(E_i^{QP}) - v_{KS}|\Phi_i^{KS}\rangle \\ &= E_i^{KS} + Z_i\langle\Phi_i^{KS}|\Sigma_{XC}(E_i^{KS}) - v_{XC}|\Phi_i^{KS}\rangle\end{aligned} \tag{2.26}$$

with

$$Z_i = \left(\langle\Phi_i^{KS}|1 - \left.\frac{\partial E(\omega)}{\partial\omega}\right|_{E_i^{KS}}|\Phi_i^{KS}\rangle\right)^{-1}. \tag{2.27}$$

There exist several different flavors of the GW approximation using the DFT wavefunctions as input. One can either update both the electronic wavefunctions and quasiparticle energies at every cycle of Hedin's equations (scGW) or keep the Kohn-Sham wavefunctions as input fixed and correct only the eigen-energies using the GW approach. The latter method has proven to be very successful at correcting the single particle spectrum from DFT and the obtained bandgaps agree remarkably well with the experimentally measured values [49] even for very few iterations. Even for one iteration the results are often very good and one refers to it as the G_0W_0 method. However, as the Kohn-Sham wavefunctions are kept fixed in this approach, it is important that these already give a good approximation of the exact wavefunctions of the system under consideration.

2.3 Bethe-Salpether Equation

In order to capture excitonic effects we need to go beyond the one particle picture. Starting from the GW approximation this is commonly done using the Bethe Salpether equation (BSE) which explicitly includes excitonic two-particle propagations. The BSE is commonly introduced using the four point reducible polarizability ${}^4L$, which is defined as [51]

$$ {}^4L(1,2;3,4) = G_2(1,2;3,4) - iG(1;3)G(4;2) \quad . \tag{2.28}$$

Here, $G_2(1,2;3,4)$ is the two-particle Greens function introduced in equation (2.17). ${}^4L$ is the generalization of the standard two point reducible polarizability, which can be computed as the contraction of the four point reducible polarizability via [51]

$$ \chi(1;2) = {}^4L(1,1^+;2,2^+). \tag{2.29}$$

The four point reducible polarizability satisfies the Dyson-like equation [57–59]

$$ L(1,2;3,4) = L_0(1,2;3,4) + \int d5d6d7d8\, L_0(1,2;5,6)K(5,6,7,8)L(7,8;3,4), \tag{2.30}$$

where L_0 is the non-interacting reducible polarizability defined as

$$ L_0(1,2;3,4) = -iG(1;3)G(4;2). \tag{2.31}$$

L_0 describes the propagation of two non-interacting electron-hole particles. K(1,2;3,4) is the so called interaction kernel between these two particles

$$ K(1,2;3,4) = v_c(1,3)\delta(1,2)\delta(3,4) + i\frac{\delta\Sigma_{XC}}{\delta G(3;4)}. \tag{2.32}$$

As the two particle equivalent of the self-energy, it contains the information of all Many Body effects and has to be approximated. The standard approach is again to employ for Σ_{XC} the GW approximation (2.22) and disregard variation of the screened interaction with the one-particle Greens function [58, 59]

$$ \frac{\delta W(1;2)}{\delta G(3;4)} = 0. \tag{2.33}$$

With this and equation (2.22) the interaction kernel simplifies to [58, 59]

$$ K(1,2;3,4) = v_c(1,3)\delta(1,2)\delta(3,4) + W(1,2)\delta(1,3)\delta(2,4). \tag{2.34}$$

The two terms appearing in the interaction kernel are the so called exchange interaction term, which involves the bare Coulomb interaction v_c, and the direct screened interaction term, which involves W. Even in this approximation solving the Bethe-Salpether equation is a computationally extremely intensive task and computationally not feasible for

real materials. So one has to further reduce the computational workload by replacing the frequency dependent screened interaction with its static component [59]

$$W(1;2) = \frac{1}{2\pi} W(x_1, x_2, \omega = 0)\delta(t_1, t_2). \tag{2.35}$$

This is called the static kernel approximation. This is a very drastic approximation. Nevertheless, it has been shown that it works very well for semiconducting systems, but fails for metallic systems [60]. With the static kernel approximation the frequency integration in the Bethe-Salpether equation reduces to a simple product and the BSE reads

$$\begin{aligned} L(x_1, x_2; x_3, x_4, \omega) =& L_0(x_1, x_2; x_3, x_4, \omega) + \int dx_5 dx_6 dx_7 dx_8 \, L_0(x_1, x_2; x_5, x_6, \omega) \\ & K(x_5, x_6, x_7, x_8) L(x_7, x_8; x_3, x_4, \omega). \end{aligned} \tag{2.36}$$

In principle the Bethe-Salpether equation could now be solved using the standard formula for Dyson-like equations

$$L(w) = \frac{L_0(\omega)}{1 - L_0(\omega)K} \quad , \tag{2.37}$$

where I have introduced a schematic notation suppressing all spacial coordinates. In practice, however, this equation is mapped onto the two particle eigenvalue problem [59]

$$\left(E_{c,\mathbf{k}} - E_{v,\mathbf{k}}\right) A^S_{vc\mathbf{k}} + \sum_{v'c'\mathbf{k}'} \langle vc\mathbf{k}|K|v'c'\mathbf{k}'\rangle = E^S A^S_{vc\mathbf{k}}, \tag{2.38}$$

with E^S being the eigenenergy of the excitonic state S and $A^S_{v,c,\mathbf{k}}$ being the eigenfunction of the excitonic state S in reciprocal space. This eigenvalue problem can now be solved by diagonalization and the excitonic real space wavefunction reads

$$\Psi_S(\mathbf{r}_e, \mathbf{r}_h) = \sum_{vc\mathbf{k}} A^S_{vc\mathbf{k}} \psi_{\mathbf{k}c}(\mathbf{r}_e) \psi^*_{\mathbf{k}v}(\mathbf{r}_h). \tag{2.39}$$

3 Controlling structural phases of quantum materials through the electron phonon coupling

A strong coupling between electronic and ionic degrees of freedom can have a dramatic effect on the ionic and electronic subsystems. Arguably the most famous example is the BCS theory of superconductivity, which shows how the electron phonon coupling renormalizes the electron electron interaction such that it becomes attractive. This allows for the formation of Cooper pairs, which are at the heart of the superconductive state [61,62].

Synthesizing crystals that exhibit such strong electron phonon coupling and understanding how their properties can be tuned via this coupling is still a research field itself in material science. In this section, I will show that quasi one-dimensional crystals provide an optimal platform for this endeavour. These quasi one-dimensional crystals can be realized as layered bulk materials which have an in-plane ionic structure that exhibits the formation of one dimensional ionic chains. These one-dimensional ionic chains govern the electronic structure of the material near the band edge as the electronic states tend to localize strongly along them, leading to a strong anisotropy. It is conceivable that phononic displacements of the ions in these chains are expected to strongly couple to the localized electronic states. The goal of this section is to show how this strong electron phonon coupling can be exploited to control either the ionic or electronic properties of the material.

I will introduce two quasi one-dimensional materials in the publications I and II. In publication I, I will discuss SiP_2, which is a layered material that has one dimensional Phosphorus chains along which the electronic states near the bandedge localise strongly. I will show that this leads to the formation of excitons with a peculiar hybrid dimensionality, i.e. the hole wavefunction being localized along the layered two dimensional planes and the electronic wavefunction localized along the one-dimensional Phosphorus chains. As such these excitonic particles are highly sensitive to phonon modes that displace the Phosphorus atoms and give rise to a strong exciton phonon coupling. This mechanism allows to detect these peculiar excitonic states in the photoluminescence and reflectivity experiments of our collaborators at the Beihang university. In these measurements the coupled exciton-phonon states emerge as sidepeaks to the standard excitonic spectrum.

In Publication II, I will discuss Ta_2NiSe_5 (TNSe). It is a layered material that consists of parallel Tantalum and Nickel chains that govern the electronic properties near the bandedge. I will show that exciting these electronic states near the bandedge via a pump laser pulse allows to selectively control the phononic states via a strong electron phonon coupling mechanism and ultimately leads to a strong amplification of the THz reflectivity of the material. The strong coupling of electronic and ionic degrees of freedom in this material will also be important in the next section, when discussing the conjectured excitonic insulating phase transition in TNSe which is accompanied by a structural phase transition at the critical temperature.

Before presenting the results in these two publications, I will now introduce the theoretical basics of the electron phonon coupling mechanism and discuss its most important effects. As there are many great textbooks and review articles on this theory I will give only a brief overview of the topic and orientate the discussion along the textbook by Czycholl [63] and a review by Giustino [64]. I highly recommend reading these sources for a more complete discussion of electron phonon coupling effects, that go beyond the scope of this thesis.

3.1 Effects of electron phonon coupling

In electronic structure theory calculations one commonly employs the Born-Oppenheimer approximation and separates the ionic and electronic subsystems. In this case the ionic coordinates appear in the electronic Hamiltonian as external one particle potential V and are considered to be frozen. This way one obtains a periodic Hamiltonian, that allows the application of the Bloch theorem and can be solved [63]

$$H = \sum_{i=1}^{N_e} \frac{\mathbf{p}_i}{2m} + \sum_{i=1}^{N_e} V(\mathbf{r}_i) + \sum_{i>j} U(\mathbf{r}_i - \mathbf{r}_j). \tag{3.1}$$

However, to assume that the nuclei are frozen is not correct, because they are vibrating around their equilibrium position along their phononic coordinates. This movement from the equilibrium positions effectively disturbs the periodicity of the one particle potential of the electrons and should be included in the Hamiltonian.
This is commonly done by considering the displacements $\mathbf{u}$ of the ions from their equilibrium position $\mathbf{R}_0$. For a single ion per unitcell the ionic potential can then be written using a sum over all unit cells as [63]

$$V(\mathbf{r}) = \sum_{n=1}^{N} v(\mathbf{r} - (\mathbf{R}_{n0} + \mathbf{u}_n)\,). \tag{3.2}$$

Expanding this potential of the electronic Hamiltonian in these displacements $\mathbf{u}$ gives

rise to electron phonon coupling. In its most simple case this expansion is done up to first order which leads to the electron phonon interaction potential

$$V(\mathbf{r}) = V(\mathbf{r} - \mathbf{R}_{n0}) - \underbrace{\nabla V(\mathbf{r} - \mathbf{R}_{n0})\ \mathbf{u}_n}_{V_{\text{el-ph}}}. \tag{3.3}$$

For the simplest case of one electronic state with the dispersion $E(\mathbf{k})$ and only one atom per unitcell (only acoustic phonons are possible) the Hamiltonian can then be rewritten in second quantization as [63]

$$H = \sum_{\mathbf{k}\sigma} E(\mathbf{k}) c_{\mathbf{k}\sigma} c^\dagger_{\mathbf{k}\sigma} + \frac{1}{\sqrt{N}} \sum_{\mathbf{k}\mathbf{q}\lambda\sigma} g^{(1)}_\lambda(\mathbf{k}, \mathbf{q}) \left(b_{\mathbf{q}\lambda} + b^\dagger_{-\mathbf{q}\lambda} \right) c^\dagger_{\mathbf{k}+\mathbf{q}\,\sigma} c_{\mathbf{k}\sigma} \tag{3.4}$$

with $c_{\mathbf{k},\sigma}$ and $c^\dagger_{\mathbf{k},\sigma}$ being the creation and annihilation operators of an electron with spin σ and $b_{\mathbf{q},\lambda}$ and $b^\dagger_{\mathbf{q},\lambda}$ being the creation and annihilation operators of a phononic mode λ with momentum $\mathbf{q}$. $g_\lambda(\mathbf{k}, \mathbf{q})$ is the first order electron phonon coupling matrix element. The Hamiltonian (3.4) describes the coupling of the electronic state to the acoustic phonons of the system which leads to the scattering of electrons from a state $\mathbf{k}$ to a state $\mathbf{k} + \mathbf{q}$ under the emission (absorption) of a phonon with momentum $\mathbf{q}$ $(-\mathbf{q})$. Such a scattering is called intraband scattering. This model can easily be generalized to include both more electronic states and more atoms per unit cell. If one includes more electronic bands, the electron phonon interaction also allows for interband scattering between the electronic states and if one includes more atoms per unitcell it allows to couple the electronic states to optical phonons as well.
In many cases this Hamiltonian is also extended to include second order corrections in the atomic displacements and the phononic part of the Hamiltonian. In this case we arrive at the most general form of the electron phonon coupling Hamiltonian which reads, including multiple electronic bands and N unitcells in the Born-van-Karman supercell, [64]

$$\begin{aligned} H = &\sum_{\mathbf{k}\sigma n} E(\mathbf{k}) c_{\mathbf{k}\sigma,n} c^\dagger_{\mathbf{k}\sigma n} + \sum_{\mathbf{q}\lambda} \hbar\omega_{\mathbf{q}\lambda} (b^\dagger_{\mathbf{q}\lambda} b^\dagger_{\mathbf{q}\lambda} + \frac{1}{2}) \\ &+ \frac{1}{\sqrt{N}} \sum_{\mathbf{k}\mathbf{q}\lambda\sigma mn} g^{(1)}_{\lambda mn}(\mathbf{k}, \mathbf{q}) \left(b_{\mathbf{q}\lambda} + b^\dagger_{-\mathbf{q}\lambda} \right) c^\dagger_{m\mathbf{k}+\mathbf{q}\sigma} c_{n\mathbf{k}\sigma} \\ &+ \frac{1}{N} \sum_{\mathbf{k}\mathbf{q}\mathbf{q}' mn\lambda\lambda'} g^{(2)}_{\lambda\lambda' mn}(\mathbf{k}, \mathbf{q}, \mathbf{q}') \left(b_{\mathbf{q}\lambda} + b^\dagger_{-\mathbf{q}\lambda} \right) \left(b_{\mathbf{q}'\lambda\prime} + b^\dagger_{-\mathbf{q}'\lambda'} \right) \\ &\qquad c^\dagger_{m\mathbf{k}+\mathbf{q}+\mathbf{q}'\sigma} c_{n\mathbf{k}\sigma}. \end{aligned} \tag{3.5}$$

Here, the first two terms describe the non-interacting electronic and phononic subsystems. The next term is the standard first order electron phonon coupling term and the last term is the second order electron phonon coupling term, which is also called Debye-Waller term. It couples two phononic excitations to the electrons with corresponding

Matrix element $g^{(2)}_{mn\lambda,\lambda'}(\mathbf{k},\mathbf{q},\mathbf{q}')$ [64]. Solving this Hamiltonian is numerically not feasible for realistic systems. Therefore, many simplified versions of this model have been proposed over the years, with the Holstein Hamiltonian being the most simple. The Holstein model considers only one electronic band coupled to one Einstein phonon, i.e. an optical phonon mode, coupled via the first order coupling term [65, 66]

$$H_H = \sum_{\mathbf{k}} E(\mathbf{k}) c_{\mathbf{k}} c^{\dagger}_{\mathbf{k}} + \sum_{\mathbf{q}} \hbar\omega (b^{\dagger}_{\mathbf{q}} b^{\dagger}_{\mathbf{q}} + \frac{1}{2}) + \sum_{\mathbf{kq}} g^{(1)}(\mathbf{k},\mathbf{q}) \left(b_{\mathbf{q}} + b^{\dagger}_{-\mathbf{q}} \right) c^{\dagger}_{\mathbf{k}+\mathbf{q}} c_{\mathbf{k}}. \tag{3.6}$$

We will use this model when discussing the exciton phonon coupling in Publication I. Let us now list some of the physical implications of including the electron phonon interaction for the properties of the electronic system:

- The momentum $\mathbf{k}$ is not a good quantum number anymore, because electrons with momentum $\mathbf{k}$ can be scattered via phonons into a state with momentum $\mathbf{k}+\mathbf{q}$. Therefore the electronic states with momentum $\mathbf{k}$ have a finite lifetime. This effect is for instance important to correctly describe the electronic conductivity at finite temperature [63].

- The electron phonon interaction also modifies the single particle electron states. Using perturbation theory and assuming a quadratic dispersion of the electrons $E_0 = \frac{\mathbf{k}^2}{2m}$ with effective mass m, which is valid at the band edge, one can show that the first order correction to the electronic energies at vanishing temperature is $E(\mathbf{k}) = E_0(\mathbf{k}) - E_P - \frac{\hbar\mathbf{k}^2}{2m}\lambda$, where both E_P and λ are proportional to the electron phonon coupling $g(\mathbf{q})$. Thus, the electron-phonon coupling renormalizes both the electronic energy and effective mass at the band edge. Sometimes this energy shift is called a polaronic shift [63].

- Similarly the phonon spectrum is modified if we include electron phonon coupling terms. This energy renormalization is proportional to the electron phonon coupling matrix elements between the electronic states and the phonon modes under investigation [64]. Such an effect can be used to selectively drive specific phononic modes with a pulse far out of resonance through the excitation of strongly coupled electronic states. This effect will be used in Publication II to control the reflectivity of the TNSe crystal [67].

- Allowing for mobile ions we also expect a modification of the electron-electron interaction, because displacing an electron will now lead to displacements of the ions which will add to the electronic screening. This additional screening term leads to a new effective interaction between the electrons [64], i.e. in the case of superconductivity it is essential for the description of Cooper pairs which are bound by an attractive interaction mediated by the electron phonon coupling [61,62,64,68]. Such a phononic dressing of the electronic interaction plays an important role also for

other bound particles such as excitons. For strongly coupled exciton phonon systems this leads to a shift of the excitonic binding energy as well as the emergence of exciton-phonon sidebands. I will explain this effect briefly in the following section. An example for this effect is shown in publication I, where we have presented the first case of such sidebands arising from low dimensional excitons embedded in a bulk system [69].

3.2 Exciton phonon coupling

The effect of exciton phonon coupling can be easily understood from Many Body perturbation theory. Starting from the solution of the Bethe-Salpether equation and the bare exciton particles one can compute the exciton propagator including electron phonon coupling by treating the exciton phonon coupling as perturbation and expanding the corresponding self-energy up to the first orders in this interaction. To this end it makes sense to express the exciton-phonon interaction terms using the excitonic creation operators. If we suppress the momentum indices $\mathbf{q}$ and $\mathbf{k}$, the exciton annihilation operator for an excitonic state S is defined as [68]

$$c_S = \sum_{v,c} A_{vc}^{S*} c_v^\dagger c_c \tag{3.7}$$

and the two particle Hamiltonian without coupling to phonons reads

$$H = \sum_S E_S c_S^\dagger c_S, \tag{3.8}$$

where E_S are the excitonic eigenenergies. The perturbation term to this Hamiltonian can be computed using the matrix elements of the Hamiltonian (3.5) with respect to the excitonic states

$$\begin{aligned}\langle \Psi_S | H_{ep}^{(1)} | \Psi_{S'} \rangle &= \sum_{\lambda mn} \langle \Psi_S | g_{\lambda mn} \left(b_\lambda + b_\lambda^\dagger \right) c_m^\dagger c_n | \Psi_{S'} \rangle \\ &= \sum_\lambda \underbrace{\sum_{mn} \langle \Psi_S | g_{\lambda mn} c_m^\dagger c_n | \Psi_{S'} \rangle}_{g_{\lambda SS'}^{(1)}} \left(b_\lambda + b_\lambda^\dagger \right)\end{aligned} \tag{3.9}$$

and can be written as [68]

$$V_{ep}^{(1)} = \sum_{SS'\lambda} g_{\lambda SS'}^{(1)} (b_\lambda + b_\lambda^\dagger) c_S^\dagger c_{S'}. \tag{3.10}$$

Similarly, we can compute for the Debye-Waller term

$$V_{ep}^{(2)} = \sum_{SS'\lambda\lambda'} g_{\lambda\lambda' SS'}^{(2)} (b_\lambda + b_\lambda^\dagger)(b_{\lambda'} + b_{\lambda'}^\dagger) c_S^\dagger c_{S'}. \tag{3.11}$$

The exciton phonon coupling elements describe the probability of one excitonic state being scattered into another excitonic state via a phonon and are defined as [68]

$$g^{(1)}_{\lambda SS'} = \langle \Psi_S | \left(\sum_{mn} g_{\lambda mn} c_i^\dagger c_j \right) | \Psi_{S'} \rangle \tag{3.12}$$

and

$$g^{(2)}_{\lambda\lambda' SS'} = \langle \Psi_S | \left(\sum_{m,n} g^{(2)}_{\lambda\lambda' mn} c_i^\dagger c_j \right) | \Psi_{S'} \rangle, \tag{3.13}$$

where g_{mn} are the standard electron phonon coupling matrix elements introduced in the previous section. Computing these coupling elements and neglecting terms like $g_{\lambda nn}\delta_{SS'}$ that do not couple different excitonic states we obtain [68]

$$\begin{aligned} g^{(1)}_{SS'\lambda} &= \sum_{vcv'c'} (A^S_{vc})^* A^{S'}_{v'c'} \left[g^{(1)}_{\lambda cc'} \delta_{vv'} - g^{(1)}_{\lambda vv'} \delta_{cc'} \right] \\ g^{(2)}_{SS'\lambda\lambda'} &= \sum_{vcv'c'} (A^S_{vc})^* A^{S'}_{v'c'} \left[g^{(2)}_{\lambda\lambda' cc'} \delta_{vv'} - g^{(2)}_{\lambda\lambda' vv'} \delta_{cc'} \right]. \end{aligned} \tag{3.14}$$

Computing the self-energy with these terms as perturbation is complicated and lengthy. Thus, I will refer the interested reader to a publication by Antonius and Louis [68] where this derivation is discussed in detail.

Experimentally the main feature of an exciton, which is strongly coupled to phonons, is the emergence of a side peak feature in its spectrum [70–76]. To understand the origin of this feature one can look at the simplest case of one exciton with vanishing momentum interacting with one Γ-phonon with energy $w_p(\mathbf{0}) = w_0$. To compute the energy correction due to this phonon we need to compute the diagonal part of the exciton self-energy $\Pi_S(w, T)$. It reads [68]

$$\Pi_S(w, T) = \frac{|g_{SS}(\mathbf{0}, \Gamma)|^2 P_\pm(T)}{\omega - E_S \pm w_0 + i\eta}, \tag{3.15}$$

where $P_+ = N_B(w_0, T)$ together $+w_0$ and $P_- = 1 + N_B(w_0, T)$ with $-w_0$ correspond to the absorption and emission of a phonon. $N_B(w, T)$ is the Bose-Einstein distribution. With this self-energy we can compute the excitation energy as the poles of the exciton propagator L_S, which is given by the Dyson identity

$$L_S^{-1} = L_{0,S}^{-1} - \Pi_S = \omega - E_S - \Pi_S, \tag{3.16}$$

and find

$$w = E_S \mp \frac{w_0}{2} \pm \sqrt{(\frac{w_0}{2})^2 + |g_{SS}|^2 P_\pm(T)}. \tag{3.17}$$

Thus, we find the appearance of sidepeaks to the main excitonic peak when the exciton is coupled to phonons. For the case of small exciton phonon coupling we can neglect the $|g_{SS}|^2$ term in the root and find the exciton phonon side peaks separated from the bare

excitonic peak by the phonon energy. For strong exciton phonon coupling the $|g_{SS}|^2$ term becomes relevant and the side peaks are shifted even stronger.

3.3 Publication I: Unconventional excitonic states with phonon sidebands in layered silicon diphosphide

State of the Art

So far the emergence of excitonic sidebands arising from strongly coupled one or two dimensional exciton-phonon states have only been measured for low dimensional systems such as Graphene nanotubes [73–76] and Transition Metal Dichalchogenide Monolayers [70–72]. In this collaborative experimental effort we are investigating the emergence of such sidebands in a novel quasi one-dimensional bulk SiP_2 crystal, which has been synthesized by our experimental collaborators at the Beihang university.

Main Findings

Using Photoluminescence and Reflectivity measurements our experimental collaborators have investigated the excitonic spectrum of the SiP_2 crystal and have been able to show the emergence of hybrid dimensional exciton-phonon sidepeaks for the first time in a bulk material. The phononic nature of the excitonic sidepeak is then confirmed by our theory calculations using ab-initio methods and a generalized Holstein model which can account for the interaction of both excitons and phonons. We were able to identify the corresponding excitonic states and ionic modes forming this correlated state and to reproduce the experimental signature remarkably well. Our theory calculations also suggest that the excitonic state has a novel hybrid dimensionality: while its electronic wavefunction is strongly localized along the one dimensional Phosphorus chains, the hole wavefunction is delocalized along the whole two-dimensional planes of the layered material. This opens potential pathways to control composite quasiparticles via symmetry engineering of the underlying crystal.

Status and Publication Details

This paper is published in Nature Materials [69]. It has a Supplementary Information that is being published at `https://static-content.springer.com/esm/art%3A10.1038%2Fs41563-022-01285-3/MediaObjects/41563_2022_1285_MOESM1_ESM.pdf` and not contained in this thesis.

Contribution

I performed all Density Functional Theory, GW and BSE simulations and created the corresponding figures. All authors have contributed to the analysis of the data and the writing of the manuscript. A detailed list of the contribution of the other authors as well can be found at the end of the publication.

nature materials

ARTICLES

https://doi.org/10.1038/s41563-022-01285-3

Check for updates

OPEN

Unconventional excitonic states with phonon sidebands in layered silicon diphosphide

Ling Zhou[1,12], Junwei Huang[1,12], Lukas Windgaetter[2,12], Chin Shen Ong[3,4], Xiaoxu Zhao[5], Caorong Zhang[1], Ming Tang[1], Zeya Li[1], Caiyu Qiu[1], Simone Latini[2], Yangfan Lu[6,7], Di Wu[1], Huiyang Gou[8], Andrew T. S. Wee[9], Hideo Hosono[6], Steven G. Louie[3,4], Peizhe Tang[2,10] ✉, Angel Rubio[2,11] ✉ and Hongtao Yuan[1] ✉

Complex correlated states emerging from many-body interactions between quasiparticles (electrons, excitons and phonons) are at the core of condensed matter physics and material science. In low-dimensional materials, quantum confinement affects the electronic, and subsequently, optical properties for these correlated states. Here, by combining photoluminescence, optical reflection measurements and ab initio theoretical calculations, we demonstrate an unconventional excitonic state and its bound phonon sideband in layered silicon diphosphide (SiP_2), where the bound electron–hole pair is composed of electrons confined within one-dimensional phosphorus–phosphorus chains and holes extended in two-dimensional SiP_2 layers. The excitonic state and emergent phonon sideband show linear dichroism and large energy redshifts with increasing temperature. Our ab initio many-body calculations confirm that the observed phonon sideband results from the correlated interaction between excitons and optical phonons. With these results, we propose layered SiP_2 as a platform for the study of excitonic physics and many-particle effects.

An exciton, the electron–hole pair formed via Coulomb interaction, is an ideal platform for understanding many-body effects[1–8]. The properties of excitons strongly depend on the crystal structure and dimensionality of host materials[9,10]. Due to quantum confinement, the electronic properties of quasiparticles (electrons, holes and excitons) in low-dimensional materials can be remarkably different from those in three-dimensional (3D) bulk materials. The Coulomb screening in low-dimensional quantum-confined structures, particularly in one-dimensional (1D) electronic systems, is known to be weaker than that in bulk systems and consequently leads to larger exciton binding energy[11–14] and other emergent excitonic phenomena[10]. Experimental observations of anisotropic excitons have been demonstrated in two-dimensional (2D) van der Waals (vdWs) materials in which electrons and holes taking part in the formation of 2D excitons are confined in the same monolayer[15–19]. Meanwhile, in 1D materials such as carbon nanotubes (CNTs)[12,20], 1D excitonic states have also been observed in which constituent electrons and holes are known to be confined within 1D nanostructures. A unique excitonic state with hybrid dimensionality, which is yet elusive, such as a bound electron–hole pair with an electron confined along one dimension (1D-confined electron) and a hole confined along two dimensions (2D-confined hole), or vice versa, would be of great interest and highly desired in terms of its optical properties and interactions with other emergent quasiparticles.

In this work, we demonstrate the observation of an unconventional bright exciton in a layered silicon diphosphide (SiP_2) crystal, accompanied by a correlated phonon sideband in the optical spectrum. Based on our ab initio many-body *GW* and *GW* plus Bethe–Salpeter equation (*GW*–BSE) calculations, as well as non-perturbative model calculations, we find that the electrons constituting the excitons are confined within the 1D phosphorus–phosphorus chains of SiP_2, while the correlated holes extend over the 2D SiP_2 atomic plane. Therefore, excitonic states in layered SiP_2 are expected to exhibit hybrid dimensionality properties. Photoluminescence (PL) spectroscopy and reflectance contrast (RC) spectroscopy show that, regardless of the polarization of the excitation laser, the optical response of the excitonic state is always linearly polarized along the x direction of the SiP_2 lattice and is accompanied by a unique sideband feature. Both the excitonic emission and the sideband feature undergo dramatic redshifts as the temperature increases, in contrast to a slight temperature-dependent redshift of the band edge that is mainly influenced by electron–phonon coupling[21,22]. This reveals that in SiP_2 the interaction of the electronic degrees of freedom with the phononic degrees of freedom is strongly enhanced by excitonic effects. The phonon sideband feature can be theoretically modelled using a non-perturbative approach to describe the interaction between the unconventional excitons and optical phonon modes. Note that reduced dimensionality normally leads to excitonic features that are strongly affected by extrinsic

[1]National Laboratory of Solid State Microstructures, Jiangsu Key Laboratory of Artificial Functional Materials, College of Engineering and Applied Sciences, and Collaborative Innovation Center of Advanced Microstructures, Nanjing University, Nanjing, China. [2]Max Planck Institute for the Structure and Dynamics of Matter, Center for Free Electron Laser Science, Hamburg, Germany. [3]Department of Physics, University of California, Berkeley, CA, USA. [4]Materials Sciences Division, Lawrence Berkeley National Laboratory, Berkeley, CA, USA. [5]School of Materials Science and Engineering, Peking University, Beijing, China. [6]Materials Research Center for Element Strategy, Tokyo Institute of Technology, Yokohama, Japan. [7]College of Materials Science and Engineering, National Engineering Research Center for Magnesium Alloys, Chongqing University, Chongqing, China. [8]Center for High Pressure Science and Technology Advanced Research, Beijing, China. [9]Department of Physics, National University of Singapore, Singapore, Singapore. [10]School of Materials Science and Engineering, Beihang University, Beijing, China. [11]Center for Computational Quantum Physics, Simons Foundation, Flatiron Institute, New York, NY, USA. [12]These authors contributed equally: Ling Zhou, Junwei Huang, Lukas Windgaetter. ✉e-mail: peizhet@buaa.edu.cn; angel.rubio@mpsd.mpg.de; htyuan@nju.edu.cn

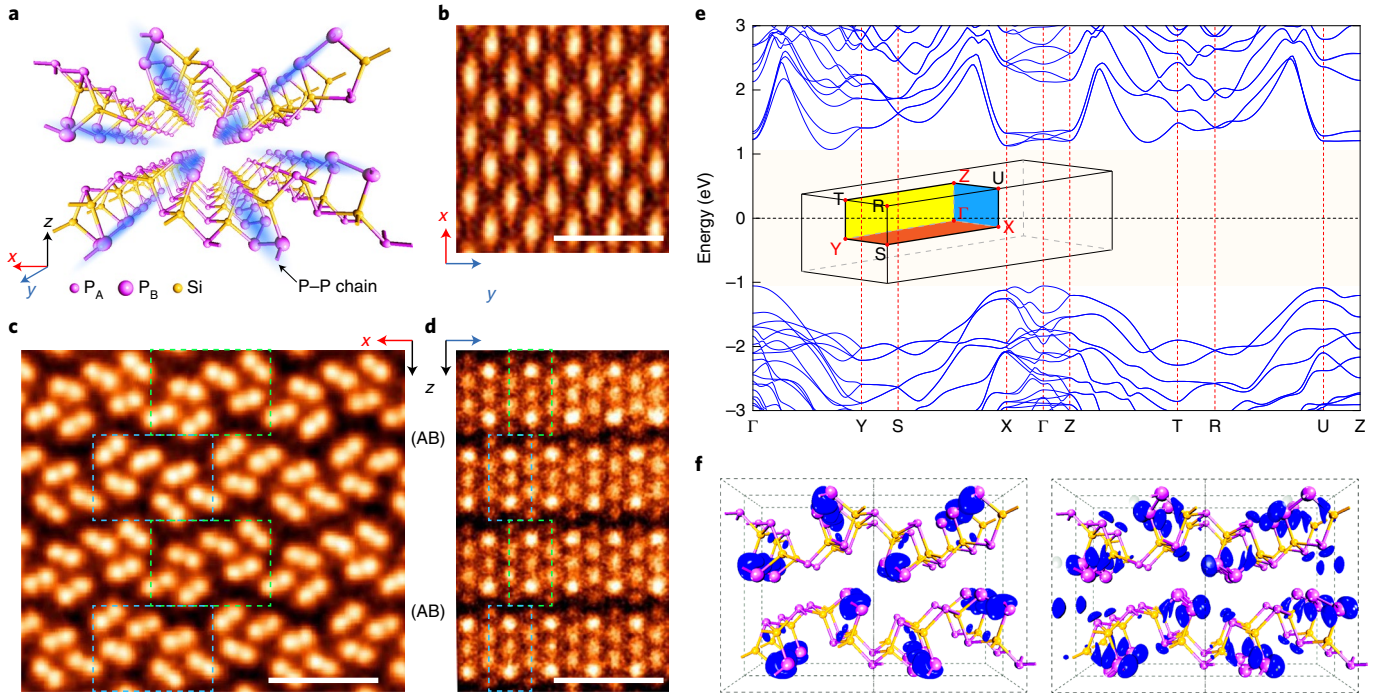

Fig. 1 | Crystal structure and band structure of layered SiP_2. **a**, Schematic layered structure of SiP_2 (*Pnma*, group number 62). The *x*,*y*,*z* coordinate system is defined according to the crystal structure, as shown in the bottom-left corner. The blue shading highlights the P_B–P_B chains formed by the P_B atoms along the *y* direction of the crystal lattice, which play a critical role in generating quasi-1D electronic and excitonic states. **b**–**d**, Top view (**b**) and cross-sectional (**c**,**d**) STEM–ADF images of SiP_2 viewed along the *y* axis (**c**) and *x* axis (**d**). Green and cyan dashed rectangles represent the periodic lattice with ABAB stacking order of SiP_2 layers. Scale bars, 1 nm. **e**, Electronic band structure of bulk SiP_2 calculated from the *GW* method. The inset shows the first BZ of bulk SiP_2. SiP_2 is a semiconductor with an indirect band gap of 2.14 eV. The valence band maximum is at the Γ point, and the conduction band minimum is located along the Γ–Y direction. The conduction band minimum state does not contribute to the formation of the A exciton due to the large direct interband transition energies at this location. **f**, Charge density distribution of the conduction band edge (left) and valence band edge (right) in real space. The isosurface of the plot is 0.02 e Å^{-3}.

environmental effects, such as disorder from the substrate and surface additives[10]. Here we provide an investigation on the intrinsic excitonic behaviour in thicker, bulk-like SiP_2 flakes. Such a tightly bound unconventional exciton in SiP_2 not only can be envisioned as a platform for the exploration of exciton–phonon (ex–ph) coupling[23–28] and other many-body physics but also may lend itself to potential applications for anisotropic optoelectronic devices.

Crystal structure and electronic property of SiP_2

Layered SiP_2 is chosen as our target material because of its following unique characteristics. Compared with hexagonal layered materials such as graphene and MoS_2, the cleavable SiP_2 crystal (space group *Pnma*) possesses an orthorhombic layered structure with a huge in-plane lattice anisotropy, as schematically shown in Fig. 1a and experimentally confirmed by scanning transmission electron microscopy–annular dark-field (STEM–ADF) imaging in Fig. 1b–d and Supplementary Figs. 1 and 2. Remarkably, based on their atomic surroundings, two types of inequivalent phosphorus atoms P_A and P_B can be distinguished in the SiP_2 lattice. As shown in Fig. 1a, P_A binds to three silicon atoms, while P_B binds to one silicon atom and the other two equivalent P_B atoms. Note that the P_B atoms along the *y* direction of the crystal lattice can naturally form phosphorus–phosphorus chains (denoted as P_B–P_B chains) embedded in the bulk SiP_2 (blue shades in Fig. 1a), which play a critical role in realizing the quasi-1D electronic states involved in exciton formation. To identify the variation in the chemical bonding environment around P_A and P_B atoms and the resulting unique properties of P_B–P_B chains in layered SiP_2, we performed arsenic doping experiments (Supplementary Information, section 2.4) and used STEM characterization (Supplementary Fig. 5). One can see that the doped arsenic atoms only selectively substitute the P_B atoms inside the P_B–P_B chains (more details in Supplementary Fig. 5), indicating that the atomic structure containing P_B–P_B chains in SiP_2 is distinct from the buckled structure in black phosphorus.

More importantly, the anisotropy induced by quasi-1D P_B–P_B chains in layered SiP_2 directly results in unique electronic properties. Figure 1e shows the band structure of semiconducting bulk SiP_2 obtained from *GW* calculations. We found that the conduction band edge states in the X–Γ–Z plane of the first Brillouin zone (BZ) are relatively flat with a large effective mass (Supplementary Table 1), and the corresponding charge densities are localized on the P_B–P_B chains (Fig. 1f), behaving like 1D-confined electrons. Importantly, in the direction along the P_B–P_B chains (the *y* direction of the crystal lattice), the electron hopping on P_B atoms is significantly larger (bandwidth, ~1.63 eV) than that across the P_B–P_B chains (bandwidth, ~0.08 eV) (see details in Supplementary Fig. 22), confirming the 1D nature of this electronic state on the conduction band edge. On the other hand, the hole states at the valence band edge do not show the same level of anisotropy (Supplementary Information, section 2.2), which, compared with 1D electrons, are relatively extended over the whole atomic plane in a quasi-2D fashion. The hybrid dimensionality of these band edge states in SiP_2 is remarkably different from those of the anisotropic 2D states in black phosphorus[15,29,30]. By analysing the calculated phonon bands given in Supplementary Information, section 13, we identify that the optical phonons localized on P_B atoms and neighbouring silicon atoms could have a large coupling with quasi-1D electronic states in layered SiP_2.

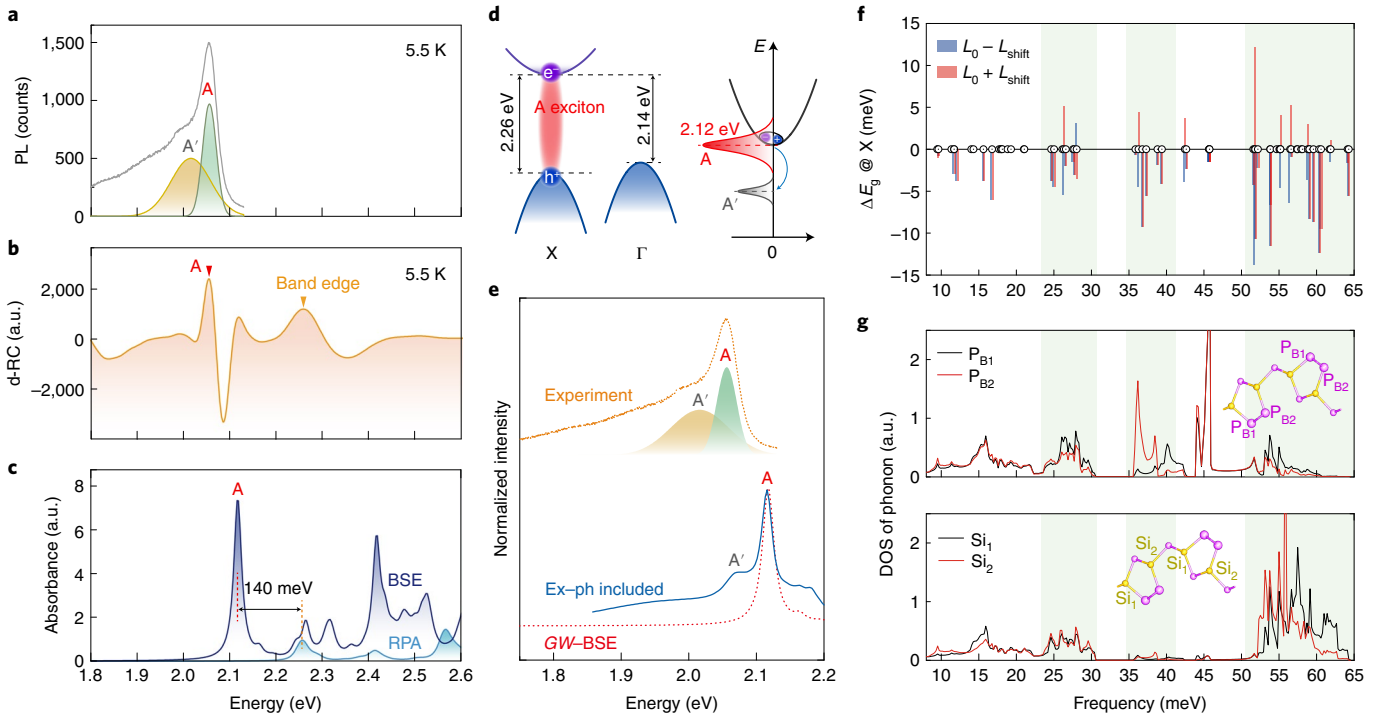

Fig. 2 | PL, absorption and ab initio calculations of the A exciton and its sideband. a, PL spectrum (grey solid line) measured at 5.5 K and its fitted results using two Gaussian peaks plus a background. The fitted peaks are assigned as A (green solid line) and A′ (yellow solid line). **b**, The second derivative of the reflectance contrast (d-RC) spectrum (orange solid line) measured at 5.5 K. The arrows indicate the absorption peaks associated with the band edge (yellow) and the A exciton (red). **c**, Calculated absorption spectra of SiP_2 by using the *GW*-BSE (dark blue) and *GW*-RPA (cyan) methods. The yellow dashed line represents the band-edge transition, the red dashed line represents the A exciton, and the binding energy is 140 meV. **d**, Left: schematic diagram for excitons bound by the Coulomb interaction and electronic band structures for bulk SiP_2. Right: schematic diagram of the quasiparticle band for excitonic states, which includes the exciton peak A (2.12 eV) and the sideband A′. **e**, Calculated absorption spectrum of SiP_2 with (blue solid line) and without (red dotted line) ex-ph interactions and the experimental PL spectrum (orange dashed line). The main A exciton peak of the blue line is obtained from *GW*-BSE calculations. The green and yellow shaded Gaussian peaks are A and A′, respectively, as defined in **a**. **f**, Energy shifts of the band gap at the X point E_g^X individually induced by each optical phonon mode with momentum $\mathbf{q}=0$ at a temperature of zero. L_0 represents the lattice structure without displacement of phonon modes. $\pm L_{shift}$ stands for atomic displacements of phonon modes. The change in the band gap is estimated by averaging the energy shifts of the band gap E_g^X with positive (red bar) and negative (dark blue bar) atomic displacements. Black circles denote energies of the corresponding phonon modes. **g**, The phonon density of states (DOS) for optical phonon modes, which is projected to the P_B atoms in the embedded P_B–P_B chains (top) and their neighbouring silicon atoms (bottom). Insets: the P_B atoms and their neighbouring silicon atoms.

Exciton with 1D-confined electron and 2D-confined hole

Figure 2a,b presents the PL spectrum and the second derivative of the RC (d-RC; see Supplementary Information, section 6) of an SiP_2 flake (228 nm) at 5.5 K, which reflects the light emission and absorption properties, respectively. The PL spectrum shows a main peak A at 2.06 eV (the lowest bright excitonic bound state denoted as the A exciton) and a broadened sideband feature A′ at 2.01 eV. The main peak A, obtained from all SiP_2 flakes measured at 5.5 K, is consistently located at an emission energy of 2.06 ± 0.01 eV (here, 0.01 eV is the energy uncertainty obtained from the standard deviation of the emission energies of several measured SiP_2 flakes; see Supplementary Information, section 7). Such a peak A in the PL spectrum matches the peak at 2.05 eV in the d-RC spectrum, as indicated by the red arrow (Fig. 2b). Due to the interference of the RC signals from the different interfaces in the SiP_2 thin films supported by substrates (Supplementary Information, section 6), the phonon sideband feature is difficult to identify from the d-RC spectrum.

Figure 2c shows the absorbance spectra obtained from the *GW*–BSE calculation and *GW* calculation with the random phase approximation (*GW*–RPA). Compared with the calculated absorption spectra based on *GW*–BSE and *GW*–RPA, we confirm that the emission peak A at 2.12 eV originates from the recombination of an excitonic state, in which the electronic states for electrons are quasi-1D and related electronic states for holes are quasi-2D (Fig. 1f). As shown in Fig. 2c,d, the calculated binding energy of such an unconventional exciton is approximately 140 meV (for more details about *GW*–BSE calculations, see Methods and Supplementary Information, section 12). From the modulus squared of the exciton wavefunction in real space shown in Fig. 3c, the observed exciton behaves like a Wannier-type exciton with twofold rotational symmetry, in sharp contrast to 2D excitons in monolayer transition-metal dichalcogenides[13]. More importantly, this exciton is embedded in a bulk layered material with an unusual atomic structure in contrast to those of reported pure 1D excitons in semiconductor nanowires[31] and CNTs[11,12], leading to strongly anisotropic Coulomb screening for 1D-confined electrons and 2D-confined holes.

Anisotropic exciton and exciton–phonon coupling

Since the unconventional A exciton is mainly contributed by electrons and holes localized along the X–Γ–Z direction in the first BZ (Supplementary Information, section 12.2), we use the band edge states at the X point as the representative **k**-point to explore the influence of electron–phonon interactions on its electronic structures and optical response. Figure 2f shows the zero-point energy

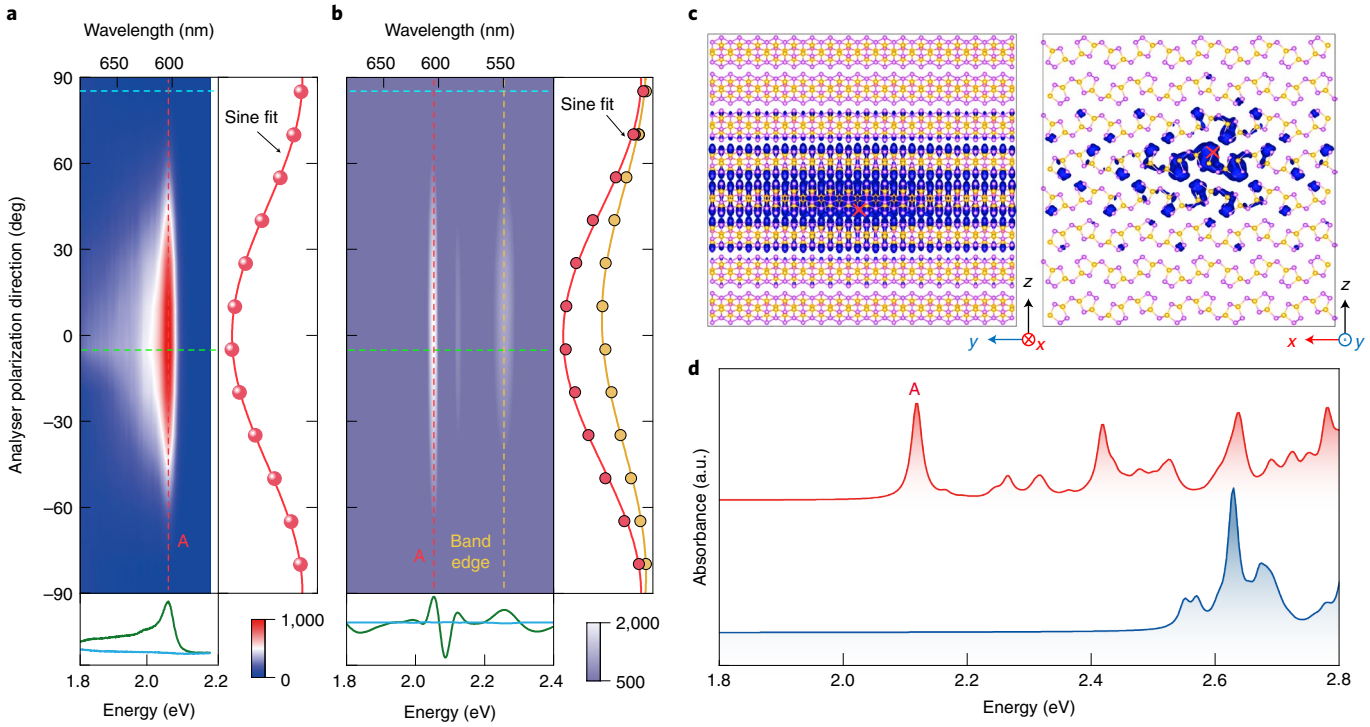

Fig. 3 | Linear polarized nature of A exciton. a, Contour plot of the PL intensity as a function of emission photon energy at different detection polarization angles θ, which denotes the angle between the analyser polarization direction and the x (defined in Fig. 1a) axis. Right: PL intensity (horizontal axis) and its sine fit versus detection angle (vertical axis) along the red dashed vertical line at 2.06 eV. 'A' indicates the position of the A exciton. Bottom: PL spectra with detection polarizations near 90° (cyan line) and 0° (green line) along the corresponding coloured horizontal dashed lines. Colour bar indicates the PL intensity. **b**, Contour plot of the d-RC as a function of photon energy and detection polarization angle. Right: d-RC intensities (horizontal axis; coloured circles) and their sine fits (coloured solid lines) versus the detection angle (vertical axis) along the yellow dashed vertical line at 2.26 eV and red dashed vertical line at 2.05 eV. 'A' and 'Band edge' indicate the positions of the A exciton and band edge, respectively. Bottom: d-RC spectra with detection polarizations near 90° (cyan line) and 0° (green line) along the corresponding coloured horizontal dashed lines. Colour bar indicates the d-RC intensity. The intensities in the right and bottom panels of (**a**) and (**b**) can be obtained from the contour plots. **c**, The modulus squared of the A exciton's wavefunction in real space distribution calculated from *GW*-BSE calculations. The red cross marks the position of the hole state. **d**, Simulated absorption spectra from the *GW*-BSE calculation along the x (red) and y (blue) directions. The absorption peak of the A exciton appears only when the polarization is along the x direction with the excitation laser incident along the z axis.

shifts of the band gap at the X point induced by all optical phonon modes with momentum $\mathbf{q}=0$ at zero temperature. Here, we use the frozen-phonon approximation[32] to estimate the influence of optical phonon vibrations on the electronic states at the X point (see Supplementary Information, section 13.2 for more details). Since the electron wavefunctions of the A exciton are localized on the P_B–P_B chains, this unconventional exciton couples most strongly to optical phonons, whose vibrational modes are in the X–Γ–Z plane and involve P_B atoms and neighbouring silicon atoms (Fig. 2g). These optical phonon modes dramatically modify the electronic structures of the quasi-1D states (Supplementary Information, section 13.4), indicating significant electron–phonon coupling within the P_B–P_B chains. Comparing the results in Fig. 2f,g, one can see that the prominent energy shifts are from the optical phonon modes with eigenenergies of ~50–60 meV. More details are given in Supplementary Information, sections 13.2 and 13.4.

The experimental observation of the sideband feature A′ also indicates that ex–ph interaction on the quasi-1D P_B–P_B chains is at least moderately strong (Supplementary Information, section 8). Therefore, we use a non-perturbative model to simulate the emergence of the sideband feature A′, where a 'generalized Holstein Hamiltonian' is used with inputs from first-principles calculations, and the self-energy effects are included beyond the first-order Fan–Migdal diagram (Methods). In this model, we found that the fitted ex–ph coupling constant M of 30 meV is comparable to the relatively small bandwidth (or hopping, $t_{ex}=-20$ meV) of the unconventional A exciton (for the estimate of t_{ex}, see Methods and Supplementary Information, section 13.3). Our approach is similar to the cumulant method considering the ex–ph coupling within the perturbative limit and makes use of the exponential assumption to include the self-energy effects from higher-order diagrammatic terms[33–35]. As shown in Fig. 2e, the appearance of the phonon sideband peak in the simulated spectrum agrees with the experimental results, indicating that sideband A′ originates from the ex–ph coupling between the unconventional exciton and the abovementioned optical phonon modes.

Figure 3a,b shows the contour plots of the PL and d-RC intensity of bulk SiP_2 as a function of emission energy at different detection polarization angles θ ($\theta=0°$ is set along the x direction), suggesting that the linear dichroic absorption and PL emission have similar twofold symmetry characteristics (see Supplementary Information, sections 4 and 12 for more details). Note that the observed linearly polarized PL emission remains along the x direction regardless of the incident laser polarization direction or the sample temperature, as shown in Supplementary Figs. 10 and 11. Our *GW*–BSE calculations (Fig. 3d and Supplementary Fig. 21b) show that the absorption peak of the quasi-1D A exciton appears only when the polarization is along the x direction. The absorption signal inside the band gap

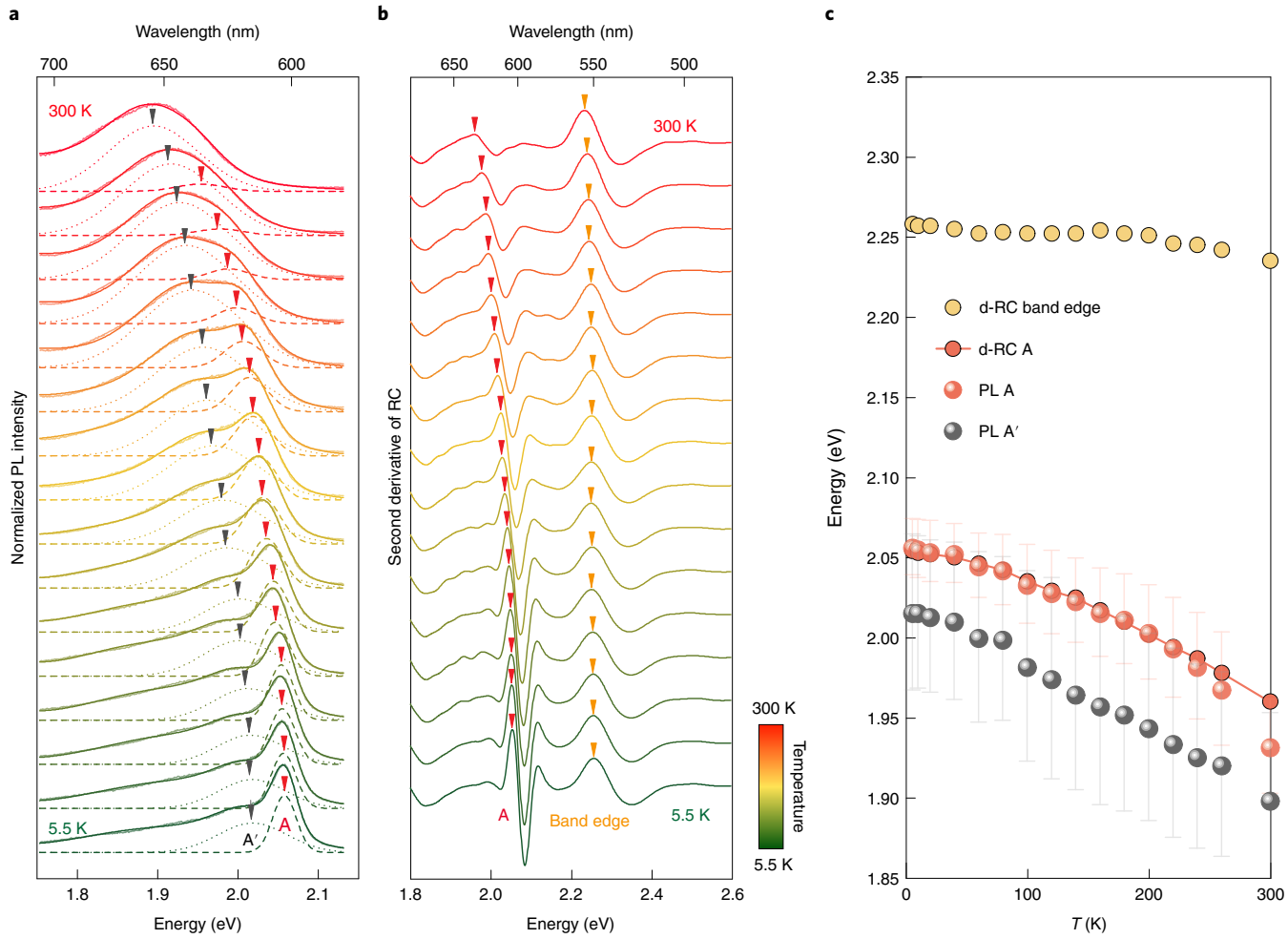

Fig. 4 | Temperature-dependent spectra and energy evolution for exciton peak A and side peak A′ in SiP_2. a,**b**, Temperature-dependent PL (**a**) and d-RC (**b**) spectra (second derivative of RC) from 5.5 K up to 300 K. The thick solid lines represent the spectra results, while the thin dashed and dotted lines represent fitting results of the PL A and A′ peaks. The solid triangle arrows highlight the redshifts of peak A (red), A′ (black) and the band edge (yellow) with increasing temperature. **c**, Temperature-dependent band edge (yellow circles) and A exciton (red circles) energies extracted from d-RC spectra, and A exciton (red spheres) and A′ (grey spheres) energies extracted by multipeak fitting of PL spectra. The error bars indicates the full width at half maximum.

along the *y* direction is forbidden by the SiP_2 crystal symmetry, which results in relevant optical excitonic matrix elements being zero (Supplementary Information, section 12.3). We also performed pump-probe transient optical measurements to characterize the dynamics of the observed bright exciton in bulk SiP_2 (see Supplementary Information, section 9 for more details). The lifetime for the exciton in SiP_2 is as short as 250 fs, which is probably related to an ultrafast process that dissociates these linearly polarized bound excitonic states into unbound and unpolarized states.

We further compare the energy shift of the A exciton peak with the energy shift of the quasiparticle band edge as the temperature changes. Figure 4a,b shows the temperature-dependent PL and d-RC spectra for bulk SiP_2. As shown in Fig. 4c, the optical absorption of the band edges and the exciton peak A, and the sideband feature A′, all exhibit clear redshifts with increasing temperature. The redshifts of the band edge can be fitted with the Bose–Einstein model (see Supplementary Information, section 7 for more details), suggesting that the interaction between electrons and phonons plays an important role in the energy shifts. The redshift of the band edge absorption resulting from the electron–phonon coupling[21,22,36] is approximately 20 meV at 300 K. On the other hand, the redshift of both peaks A and A′ is approximately 90 meV at 300 K, much larger than the energy shift of the direct band edge, indicating an additional contribution from the large coupling between the bound exciton and optical phonons. Such a result is consistent with the analysis of temperature-dependent linewidth broadening of the peak for unconventional A exciton (see Supplementary Information, section 5 for more details).

Outlook

Using optical spectroscopic measurements with the support of ab initio many-body calculations, we demonstrated the observation of an unconventional bright exciton in layered SiP_2. In contrast to those reported 1D and 2D excitons truly confined in CNTs and monolayer transition-metal dichalcogenides, the bound excitonic states in layered SiP_2 exhibit hybrid low dimensionality due to the intrinsic 1D and 2D nature of the constituent electrons and holes, respectively. Interestingly, we envision that SiP_2 can host peculiar trion states, including a negatively charged trion (composed of two 1D-confined electrons and one 2D-confined hole) and a positively charged trion (composed of one 1D-confined electron and two 2D-confined holes). Once we couple layered SiP_2 to other vdWs semiconductors, such as monolayer MoS_2, to form heterostructures, the interfacial layer coupling can change the rotational symmetry

of the semiconducting layers and could bring optical and optoelectronic functionalities via symmetry engineering at the heterointerfaces. Through the doping modulation of carrier polarity in SiP_2 or its heterostructures, rich excitonic physics with exotic dynamic behaviour can be realized in this material platform, such as interlayer excitons and Moiré excitons with tunable dimensionality. Furthermore, the interaction between this unconventional bound exciton and the optical phonon leads to an accompanying phonon sideband. Since a phonon and an exciton fall within the same energy range from zero to several hundred meV, we speculate that such many-body interactions may even lead to the emergence of elementary excitations beyond the Born–Oppenheimer limit in atomic 2D thin films or nanostructures of SiP_2. Our work will provide a platform to further understand ex–ph coupling and other essential many-body physics and inspire follow-up studies and calculation method developments therein.

Online content

Any methods, additional references, Nature Research reporting summaries, source data, extended data, supplementary information, acknowledgements, peer review information; details of author contributions and competing interests; and statements of data and code availability are available at https://doi.org/10.1038/s41563-022-01285-3.

Received: 2 June 2021; Accepted: 10 May 2022;
Published online: 16 June 2022

References

1. Mahan, G. D. *Many-Particle Physics* (Springer, 2013).
2. Singh, J. *Excitation Energy Transfer Processes in Condensed Matter: Theory And Applications* (Springer, 2013).
3. Su, J.-J. & MacDonald, A. H. How to make a bilayer exciton condensate flow. *Nat. Phys.* **4**, 799–802 (2008).
4. High, A. A. et al. Spontaneous coherence in a cold exciton gas. *Nature* **483**, 584–588 (2012).
5. Mak, K. F. et al. Tightly bound trions in monolayer MoS_2. *Nat. Mater.* **12**, 207–211 (2013).
6. You, Y. et al. Observation of biexcitons in monolayer WSe_2. *Nat. Phys.* **11**, 477–481 (2015).
7. Wang, Z. et al. Evidence of high-temperature exciton condensation in two-dimensional atomic double layers. *Nature* **574**, 76–80 (2019).
8. Madéo, J. et al. Directly visualizing the momentum-forbidden dark excitons and their dynamics in atomically thin semiconductors. *Science* **370**, 1199 (2020).
9. Haug, H. & Koch, S. W. *Quantum Theory of the Optical and Electronic Properties of Semiconductors* (World Scientific, 2009).
10. Wang, G. et al. Colloquium: Excitons in atomically thin transition metal dichalcogenides. *Rev. Mod. Phys.* **90**, 021001 (2018).
11. Spataru, C. D., Ismail-Beigi, S., Benedict, L. X. & Louie, S. G. Excitonic effects and optical spectra of single-walled carbon nanotubes. *Phys. Rev. Lett.* **92**, 077402 (2004).
12. Wang, F., Dukovic, G., Brus, L. E. & Heinz, T. F. The optical resonances in carbon nanotubes arise from excitons. *Science* **308**, 838–841 (2005).
13. Qiu, D. Y., da Jornada, F. H. & Louie, S. G. Optical spectrum of MoS_2: many-body effects and diversity of exciton states. *Phys. Rev. Lett.* **111**, 216805 (2013).
14. Chernikov, A. et al. Exciton binding energy and nonhydrogenic Rydberg series in monolayer WS_2. *Phys. Rev. Lett.* **113**, 076802 (2014).
15. Wang, X. et al. Highly anisotropic and robust excitons in monolayer black phosphorus. *Nat. Nanotechnol.* **10**, 517–521 (2015).
16. Aslan, O. B., Chenet, D. A., van der Zande, A. M., Hone, J. C. & Heinz, T. F. Linearly polarized excitons in single- and few-layer ReS_2 crystals. *ACS Photonics* **3**, 96–101 (2016).
17. Arora, A. et al. Highly anisotropic in-plane excitons in atomically thin and bulk-like 1T'-$ReSe_2$. *Nano Lett.* **17**, 3202–3207 (2017).
18. Kang, S. et al. Coherent many-body exciton in van der Waals antiferromagnet $NiPS_3$. *Nature* **583**, 785–789 (2020).
19. Hwangbo, K. et al. Highly anisotropic excitons and multiple phonon bound states in a van der Waals antiferromagnetic insulator. *Nat. Nanotechnol.* **16**, 655–660 (2021).
20. Lefebvre, J., Fraser, J. M., Finnie, P. & Homma, Y. Photoluminescence from an individual single-walled carbon nanotube. *Phys. Rev. B* **69**, 075403 (2004).
21. Dey, P. et al. Optical coherence in atomic-monolayer transition-metal dichalcogenides limited by electron-phonon interactions. *Phys. Rev. Lett.* **116**, 127402 (2016).
22. Giustino, F. Electron–phonon interactions from first principles. *Rev. Mod. Phys.* **89**, 015003 (2017).
23. Perebeinos, V., Tersoff, J. & Avouris, P. Effect of exciton–phonon coupling in the calculated optical absorption of carbon nanotubes. *Phys. Rev. Lett.* **94**, 027402 (2005).
24. Zeng, H., Zhao, H., Zhang, F.-C. & Cui, X. Observation of exciton–phonon sideband in individual metallic single-walled carbon nanotubes. *Phys. Rev. Lett.* **102**, 136406 (2009).
25. Christiansen, D. et al. Phonon sidebands in monolayer transition metal dichalcogenides. *Phys. Rev. Lett.* **119**, 187402 (2017).
26. Chen, H.-Y., Sangalli, D. & Bernardi, M. Exciton–phonon interaction and relaxation times from first principles. *Phys. Rev. Lett.* **125**, 107401 (2020).
27. Lin, K.-Q. et al. Narrow-band high-lying excitons with negative-mass electrons in monolayer WSe_2. *Nat. Commun.* **12**, 5500 (2021).
28. Funk, V. et al. Spectral asymmetry of phonon sideband luminescence in monolayer and bilayer WSe_2. *Phys. Rev. Res.* **3**, L042019 (2021).
29. Qiao, J., Kong, X., Hu, Z.-X., Yang, F. & Ji, W. High-mobility transport anisotropy and linear dichroism in few-layer black phosphorus. *Nat. Commun.* **5**, 4475 (2014).
30. Li, L. et al. Direct observation of the layer-dependent electronic structure in phosphorene. *Nat. Nanotechnol.* **12**, 21–25 (2017).
31. Wang, J., Gudiksen, M. S., Duan, X., Cui, Y. & Lieber, C. M. Highly polarized photoluminescence and photodetection from single indium phosphide nanowires. *Science* **293**, 1455–1457 (2001).
32. Capaz, R. B., Spataru, C. D., Tangney, P., Cohen, M. L. & Louie, S. G. Temperature dependence of the band gap of semiconducting carbon nanotubes. *Phys. Rev. Lett.* **94**, 036801 (2005).
33. Wingreen, N. S., Jacobsen, K. W. & Wilkins, J. W. Resonant tunneling with electron-phonon interaction: an exactly solvable model. *Phys. Rev. Lett.* **61**, 1396–1399 (1988).
34. Wingreen, N. S., Jacobsen, K. W. & Wilkins, J. W. Inelastic scattering in resonant tunneling. *Phys. Rev. B* **40**, 11834–11850 (1989).
35. Riss, A. et al. Imaging and tuning molecular levels at the surface of a gated graphene device. *ACS Nano* **8**, 5395–5401 (2014).
36. Shree, S. et al. Observation of exciton–phonon coupling in $MoSe_2$ monolayers. *Phys. Rev. B* **98**, 035302 (2018).

Methods

SiP_2 crystal growth with flux method. Single-crystalline samples were synthesized by using the tin flux method[37]. Silicon, phosphorus, gadolinium and tin were mixed at a Si:P:Gd:Sn ratio of 1:6:0.03:5 and sealed into evacuated quartz tubes. The mixture was slowly heated to 1,100 °C to avoid bumping phosphorous and kept for 48 h. Subsequently, the sample was cooled to 400 °C in 140 h and then cooled to room temperature by switching off the electric furnace. The tin flux was removed by using diluted HCl (aq). The obtained black crystals were then ultrasonicated in distilled water and ethanol to remove the residuals (such as phosphorous, adhered) on the crystal surface. This procedure was repeated until the water (or ethanol) became transparent enough after ultrasonication.

Sample preparation for optical measurements and STEM–ADF measurements. SiP_2 flakes with thicknesses of 5–200 nm were prepared by mechanical exfoliation onto SiO_2/Si wafers (300-nm-thick SiO_2 layer) or fused silica substrate. The thickness was identified by atomic force microscopy (integrated with a WITec Alpha 300 Raman system) after all optical measurements were finished. SiP_2 is stable in a nitrogen atmosphere and in vacuum and can gradually degrade when exposed to air within several hours. To avoid sample degradation, the whole sample preparation was processed in a glovebox. Atomic-resolution STEM–ADF imaging was performed on an aberration-corrected ARM200F equipped with a cold field-emission gun operating at 80 kV. The STEM–ADF images were collected using a half-angle range from ~81 to 280 mrad. The convergence semi-angle of the probe was ~30 mrad.

Optical measurements. Optical measurements, including the PL spectra and RC and Raman spectra, were performed using a confocal Raman system (WITec Alpha 300). Thickness-dependent PL measurements (Supplementary Information, section 3) were carried out at room temperature using a ×100 objective lens with an incident laser (laser power, 0.2 mW) focused to an ~1 μm spot. Nitrogen conditions were accomplished by protecting samples using continuous nitrogen gas flow. Low-temperature PL and Raman measurements were performed under vacuum conditions with samples installed in a cryostat (Cryo Instrument of America RC102–CFM microscopy cryostat) using a long working distance ×50 objective lens (laser power, 3 mW). For RC measurement, we recorded the subtracted reflectance of the sample normalized by the reflectance of the substrate, that is, RC $= 1 - \frac{R_{sample}}{R_{sub}}$, where R_{sample} represents the reflectance of the SiP_2 sample on the silicon dioxide or quartz substrate and R_{sub} represents the reflectance of the bare substrate.

First-principles calculations. First-principles density functional theory (DFT) calculations were performed by using the projector-augmented wave (PAW)[38,39] method implemented in the Vienna Ab initio Simulation Package (VASP)[40]. The energy cut-off for the plane wave basis is set to 500 eV. To test the lattice constants to compare with the experimental value, we used the exchange-correlation functionals of generalized gradient approximation (GGA) with Perdew–Burke–Ernzerhof (PBE) type, local density approximation (LDA), and the PBE functional with vdWs corrections to fully relax the lattice structures. The vdWs interactions were included by using the methods proposed by Dion et al.[41] with the optB88-vdW functional. We found that lattice constants obtained from the method including the vdWs corrections are closest to the experimental values (Supplementary Information, sections 10 and 11), which are used in the following phonon bands, *GW* and *GW*–BSE calculations. During the lattice relaxations, the force convergence criterion was 10^{-3} eV Å^{-1}, and a 9×21×7 **k**-point mesh was sampled over the BZ. For the self-consistent electronic structure calculations, we set the energy convergence criterion to 10^{-6} eV and the **k**-point mesh to 11×25×9 over the whole BZ. The phonon spectrum was calculated by the PHONOPY package[42] in the framework of density functional perturbation theory with the finite-displacement approach, in which a 2×4×1 supercell was employed.

Using VASP[43], *GW* calculations[44] were performed using Kohn–Sham DFT wavefunctions (GGA–PBE) calculated on a 4×16×4 **k**-point mesh as the initial mean field. The dielectric response function used for the fully frequency-dependent eigenvalue-self-consistent *GW* calculation is summed over 1,240 Kohn–Sham states (corresponding to a 100 eV cut-off). The frequency grid is divided into a dense part ranging from 0 to 13.75 eV and a coarse grid tail ranging from 13.75 to 178.78 eV. The grid sampling is non-uniform with 80 frequency grid points, resulting in step sizes ranging from 0.31 eV in the dense grid up to 46.35 eV in the tail[45]. We use multiple iterations in the *GW* calculation to update the eigenvalues of the Kohn–Sham states when calculating both Green's function *G* and the screened interaction *W* while keeping the initial Kohn–Sham wavefunctions unchanged. Full convergence was reached after five iterations. This procedure results in better agreement with the experimental results because the standard G_0W_0 approach underestimates the band gap by approximately 220 meV. The maximally localized Wannier functions obtained from the Wannier90 packages[46,47] were used to plot the *GW* quasiparticle band structure (Fig. 1e). In the construction of the Wannier functions, the *s* and *p* orbitals of both the silicon and phosphorus atoms were used as initial trial wavefunctions. The *GW* quasiparticle energies and Kohn–Sham wavefunctions are used to construct the kernel of the BSE[48,49]. We employed the standard Tamm–Dancoff approximation and included ten conduction bands and ten valence bands during the calculation of the *GW*–BSE Hamiltonian.

Calculation of the spectral function of the phonon sidebands. To model the spectral function of the phonon sidebands, we solved for the dressed polaron Green's function of the generalized Holstein Hamiltonian[50,51], $H = H_0 + V$, where $H_0 = \sum_{\mathbf{q}} \omega_{\mathbf{q}} b^{\dagger}_{\mathbf{q}} b_{\mathbf{q}} + \sum_{\mathbf{k}} \epsilon_{\mathbf{k}} c^{\dagger}_{\mathbf{k}} c_{\mathbf{k}}$ is the unperturbed single-particle Hamiltonian and $V = \sum_{\mathbf{k},\mathbf{q}} M_{\mathbf{k},\mathbf{q}} c^{\dagger}_{\mathbf{k}+\mathbf{q}} c_{\mathbf{k}} (b_{\mathbf{q}} + b^{\dagger}_{-\mathbf{q}})$ is the interaction Hamiltonian. For the first term constituting H_0, **q** is the crystal momentum of the phonon, $b^{\dagger}_{\mathbf{q}}$ and $b_{\mathbf{q}}$ are the phonon creation and annihilation operators, and $\omega_{\mathbf{q}}$ (which shall be taken as a constant independent of **q**) is the average phonon energy of the dominant optical branch responsible for ex–ph coupling. For the second term constituting H_0, **k** is the centre-of-mass momentum of the exciton, $c^{\dagger}_{\mathbf{k}}$ and $c_{\mathbf{k}}$ are the exciton creation and annihilation operators, and $\epsilon_{\mathbf{k}}$ is its energy dispersion. We obtain these values from our *GW* calculations. The interaction Hamiltonian, *V*, represents the ex–ph interaction, with $M_{\mathbf{k},\mathbf{q}}$ being the ex–ph coupling matrix element. Since there is only one exciton in the model Hamiltonian, its solution is independent of the statistics of particle[1]. The same solution would be obtained for any fermion or boson, such as electrons (which is more common), as long as the particles are free to move. To construct the generalized Holstein Hamiltonian, we first calculate most of its parameters from first-principles calculations and finally fit the ex–ph coupling matrix elements, $M_{\mathbf{k},\mathbf{q}}$ (also to be taken as a constant), to the experimental results.

First, we note that although more than one phonon mode contributes to the renormalization of the band gap, the dominant contributing phonon modes fall within the energy range of 50–60 meV (Fig. 2f and Supplementary Fig. 24). Since the phonon bands that project strongly onto the P_B–P_B chain are relatively flat within the X–Γ–Z plane in reciprocal space (Supplementary Fig. 23b), we assume the representative phonon band to have negligible phonon bandwidth, as in the Einstein model. Hence, we use the energy of a representative longitudinal optical (LO) phonon mode, $\omega_{\mathbf{q}} \equiv \omega_{LO} = 55$ meV, to model the ex–ph interaction, as obtained from the ab initio phonon calculations. We also assumed that the exciton has a free-particle dispersion of a periodic 1D chain, namely, $\epsilon_{\mathbf{k}} = -2t_{ex}\cos(ka)$, where $4t_{ex} = -80$ meV is the exciton bandwidth. The exciton hopping term, t_{ex}, was estimated using the hole bandwidth ($4t_h \approx -80$ meV) and the electron bandwidth ($4t_h \approx 640$ meV), which are calculated along the X–Γ–Z direction of the Brillouin zone from our *GW* calculations (Supplementary Fig. 22), with the formula $t_{ex}^{-1} = t_h^{-1} + t_e^{-1}$. Finally, using the above parameters obtained from the first-principles calculations, we only fit the ex–ph parameter, $M_{\mathbf{k},\mathbf{q}} \equiv M = 30$ meV, so that the spectral function of the calculated dressed Green's function reproduces the PL spectrum shown in the optical experiments (Fig. 2e).

In the calculation of the dressed interacting polaron Green's function, $G(\mathbf{k},\omega)$, Dyson's identity, $[G(\mathbf{k},\omega)]^{-1} = [G_0(\mathbf{k},\omega)]^{-1} - \Sigma(\mathbf{k},\omega)$ is used, where $G_0(\mathbf{k},\omega)$ is the free-particle Green's function, given by $G_0(\mathbf{k},\omega) = (\omega - \epsilon_{\mathbf{k}} + i\eta)^{-1}$ and $\Sigma(\mathbf{k},\omega)$ is the ex–ph self-energy, which consists of an infinite sum of all proper self-energy diagrams. Written more explicitly, $G(\mathbf{k},\omega)$ can be written as a continued fraction,

$$G(\mathbf{k},\omega) = \cfrac{1}{G_0^{-1}(\mathbf{k},\omega) - \cfrac{M^2}{G_0^{-1}(\mathbf{k},\omega-\omega_0) - \cfrac{2M^2}{G_0^{-1}(\mathbf{k},\omega-2\omega_0) - \cfrac{3M^2}{G_0^{-1}(\mathbf{k},\omega-3\omega_0) - \ldots}}}} = \frac{1}{G_0^{-1}(\mathbf{k},\omega) - \Sigma(\mathbf{k},\omega)},$$

such that $\Sigma(\mathbf{k},\omega)$ is the second term in the denominator given by

$$\Sigma(\mathbf{k},\omega) = \cfrac{M^2}{G_0^{-1}(\mathbf{k},\omega-\omega_0) - \cfrac{2M^2}{G_0^{-1}(\mathbf{k},\omega-2\omega_0) - \cfrac{3M^2}{G_0^{-1}(\mathbf{k},\omega-3\omega_0) - \ldots}}},$$

that when expanded in powers of M^2 reproduces the Feynman diagrams of each order[52–54]. In the calculation of the self-energy, we used the momentum-averaged non-interacting Green's function, as introduced by Berciu[53] and extended by Goodvin, Berciu and Sawatzky[54]. In this approximation, the momentum-dependent non-interacting Green's function, $G_0(\mathbf{k},\omega)$, in the expression of the self-energy, was replaced by its momentum average, $\bar{G}_0(\omega)$, given by $\bar{G}_0(\omega) = \frac{1}{N_{\mathbf{k}}}\sum_{\mathbf{k}} G_0(\mathbf{k},\omega) = \int_{-\infty}^{\infty} d\epsilon \rho_0(\epsilon) G_0(\epsilon,\omega) = \frac{\mathrm{sgn}(\omega)}{\sqrt{(\omega+i\eta)^2 - 4t_{xct}^2}}$, where $N_{\mathbf{k}}$ is the number of **k**-points and $\rho_0(\epsilon)$ is the density of states. The momentum-averaged self-energy, $\Sigma_{MA}(\omega)$, is now momentum independent, and the interacting Green's function is now $G(\mathbf{k},\omega) = \frac{1}{G_0^{-1}(\mathbf{k},\omega) - \Sigma_{MA}(\omega)}$. Finally, the spectral function was given by the imaginary part of the interacting Green's function, the main peak of which is fitted to the excitation energy of excitonic state A as obtained from *GW*–BSE calculations.

Data availability

Source data are provided with this paper. The authors declare that data generated or analysed during this study are provided as source data or included in the

Supplementary Information. Further data are available from the corresponding authors upon request. Source data are provided with this paper.

References

37. Zhang, X., Wang, S., Ruan, H., Zhang, G. & Tao, X. Structure and growth of single crystal SiP_2 using flux method. *Solid State Sci.* **37**, 1–5 (2014).
38. Blöchl, P. E. Projector augmented-wave method. *Phys. Rev. B* **50**, 17953–17979 (1994).
39. Kresse, G. & Joubert, D. From ultrasoft pseudopotentials to the projector augmented-wave method. *Phys. Rev. B* **59**, 1758–1775 (1999).
40. Kresse, G. & Hafner, J. Ab initio molecular dynamics for liquid metals. *Phys. Rev. B* **47**, 558–561 (1993).
41. Dion, M., Rydberg, H., Schröder, E., Langreth, D. C. & Lundqvist, B. I. Van der Waals density functional for general geometries. *Phys. Rev. Lett.* **92**, 246401 (2004).
42. Togo, A. & Tanaka, I. First principles phonon calculations in materials science. *Scr. Mater.* **108**, 1–5 (2015).
43. Shishkin, M. & Kresse, G. Implementation and performance of the frequency-dependent *GW* method within the PAW framework. *Phys. Rev. B* **74**, 035101 (2006).
44. Hybertsen, M. S. & Louie, S. G. First-principles theory of quasiparticles: calculation of band gaps in semiconductors and insulators. *Phys. Rev. Lett.* **55**, 1418–1421 (1985).
45. Shishkin, M. & Kresse, G. Self-consistent *GW* calculations for semiconductors and insulators. *Phys. Rev. B* **75**, 235102 (2007).
46. Mostofi, A. A. et al. wannier90: a tool for obtaining maximally-localised Wannier functions. *Comput. Phys. Commun.* **178**, 685–699 (2008).
47. Mostofi, A. A. et al. An updated version of wannier90: a tool for obtaining maximally-localised Wannier functions. *Comput. Phys. Commun.* **185**, 2309–2310 (2014).
48. Albrecht, S., Reining, L., Del Sole, R. & Onida, G. Ab initio calculation of excitonic effects in the optical spectra of semiconductors. *Phys. Rev. Lett.* **80**, 4510–4513 (1998).
49. Rohlfing, M. & Louie, S. G. Electron–hole excitations in semiconductors and insulators. *Phys. Rev. Lett.* **81**, 2312–2315 (1998).
50. Holstein, T. Studies of polaron motion: Part I. The molecular-crystal model. *Ann. Phy.* **8**, 325–342 (1959).
51. Holstein, T. Studies of polaron motion: Part II. The "small" polaron. *Ann. Phy.* **8**, 343–389 (1959).
52. Ciuchi, S., de Pasquale, F., Fratini, S. & Feinberg, D. Dynamical mean-field theory of the small polaron. *Phys. Rev. B* **56**, 4494–4512 (1997).
53. Berciu, M. Green's function of a dressed particle. *Phys. Rev. Lett.* **97**, 036402 (2006).
54. Goodvin, G. L., Berciu, M. & Sawatzky, G. A. Green's function of the Holstein polaron. *Phys. Rev. B* **74**, 245104 (2006).

Acknowledgements

This research was supported by the National Key Basic Research Program of the Ministry of Science and Technology of China (2018YFA0306200, 2021YFA1202901), the National Natural Science Foundation of China (52072168, 51861145201, 91750101, 21733001), the Fundamental Research Funds for the Central Universities (021314380078, 021314380104, 021314380147) and Jiangsu Key Laboratory of Artificial Functional Materials. A.R. acknowledges support from the European Research Council (ERC-2015-AdG-694097), Grupos Consolidados (IT1249-19) and the Max Planck-New York City Center for Non-Equilibrium Quantum Phenomena. The Flatiron Institute is a division of the Simons Foundation. P.T. acknowledges support from the Fundamental Research Funds for the Central Universities (ZG216S20A1) and the 111 Project (B17002). Part of the calculations were supported by the high-performance computing resources at Beihang University. L.W. acknowledges funding by the Deutsche Forschungsgemeinschaft (DFG, German Research Foundation) under Germany's Excellence Strategy–Cluster of Excellence Advanced Imaging of Matter (AIM) EXC 2056-390715994 and by the DFG–SFB-925–project 170620586. S.G.L. and C.S.O. acknowledge support by National Science Foundation grant number DMR-1926004 and National Science Foundation grant number OAC-2103991. X.Z. and A.T.S.W acknowledge support from MOE Tier 2 grant MOE2017-T2-2-139. X.Z. acknowleges support from a Presidential Postdoctoral Fellowship, NTU, Singapore via grant 03INS000973C150. Y.L. acknowledges the support by Grant-in-Aid for Young Scientists (Japan Society for the Promotion of Science, JSPS) number 21K14494. We thank C. Zhang and R. Wang for their support with pump-probe transient optical measurements and related data analysis.

Author contributions

L.Z., J.H. and L.W. contributed equally to this work. H.T.Y., P.T. and A.R. conceived and designed the experiments and theoretical calculations. Y.F.L., H.G. and H.H. synthesized the bulk SiP_2 crystals. L.Z., C.Z. and M.T. performed sample fabrication. L.Z., J.H., C.Q. and Z.L. performed optical measurements and analysed the optical results. L.Z., C.Q. and D.W. performed atomic force microscopy measurements. L.Z. performed reflectance contrast simulations. X.Z. and A.T.S.W. performed STEM measurement. L.W., P.T. and C.S.O. performed ab initio calculations and model simulations. L.W., P.T., C.S.O., S.L., S.G.L. and A.R. analysed theoretical calculated results. L.Z., P.T., H.T.Y., C.S.O. and A.R. wrote the manuscript with input from all authors. All authors contributed to the general discussion and revision of the manuscript.

Funding

Open access funding provided by Max Planck Society

Competing interests

The authors declare no competing interests.

Additional information

Supplementary information The online version contains supplementary material available at https://doi.org/10.1038/s41563-022-01285-3.

Correspondence and requests for materials should be addressed to Peizhe Tang, Angel Rubio or Hongtao Yuan.

Peer review information *Nature Materials* thanks the anonymous reviewers for their contribution to the peer review of this work.

3.4 Publication II: Fresnel-Floquet theory of light-induced terahertz reflectivity amplification in Ta_2NiSe_5

State of the Art

Pump probe measurements provide a powerful platform to investigate collective excitations. Several experiments have shown the possibility to induce changes in the THz reflectivity of a material following a photo excitation [77–79]. These changes stem from collective excitations that act as a Floquet drive to the system [79, 80]. Here, we investigated Ta_2NiSe_5 as a quasi one-dimensional system, which shows a strong amplification of up to 30% in the THz reflectivity after prior photoexcitation in the measurements of our experimental collaborators (to be published soon). The goal of this paper is to understand the microscopic mechanism leading to this dramatic reflectivity enhancement.

Main Findings

In this paper we show that the THz reflectivity enhancement through a 0.5 eV pump can be understood via the strong coupling of the lowest electronic valence band states to the phonon modes. We show, using ab-initio and model calculations, that once the electrons are excited from the valence to the conduction bands, they couple strongly to a 4.7 THz phonon mode which leads to a time dependent renormalization of the phonon dispersion of that mode. This squeezed phonon is then shown to act as a Floquet drive to the system which in turn leads to the observed reflectivity enhancement. Using this mechanism allows to dynamically control the properties of a solid through the electron-phonon coupling. It also highlights that the electronic properties of this material might be coupled strongly to any ionic perturbation, which will be important when discussing the origin of the conjectured excitonic insulating phase transition in the next section.

Status and Publication Details

This paper has been published as preprint on the arXiv server [67]. It is currently under review for Science Advances. This publication has a Supplementary Information that is being published at `https://arxiv.org/pdf/2207.08851.pdf` and not contained in this thesis.

Contribution

I performed all ab-initio Density Functional Theory calculations and created the corresponding figures. All authors have contributed to the analysis of the data and the creation of the manuscript.

Fresnel-Floquet theory of light-induced terahertz reflectivity amplification in Ta_2NiSe_5

Marios H. Michael,[1,*] Sheikh Rubaiat Ul Haque,[2] Lukas Windgaetter,[3] Simone Latini,[3] Yuan Zhang,[2] Angel Rubio,[3,4] Richard D. Averitt,[2] and Eugene Demler[1,5]

[1]*Department of Physics, Harvard University, Cambridge, Massachusetts 02138, USA.*

[2]*Department of Physics, University of California San Diego, La Jolla, California 92093, USA*

[3]*Max Planck Institute for the Structure and Dynamics of Matter, Luruper Chausse 149, 22761 Hamburg, Germany*

[4]*Center for Computational Quantum Physics, The Flatiron Institute, 162 Fifth Avenue, New York, 10010 New York, USA*

[5]*Institufor Theoretical Physics, ETH Zurich, 8093 Zurich, Switzerland.*

(Dated: July 20, 2022)

Abstract

We theoretically investigate a new pathway for terahertz parametric amplification, initiated by above-gap optical excitation in the candidate excitonic insulator Ta_2NiSe_5. We show that after electron photoexcitation, electron-phonon coupling can lead to THz parametric amplification, mediated by squeezed oscillations of the strongly coupled phonon. The developed theory is supported by experimental results on Ta_2NiSe_5 where photoexcitation with short pulses leads to enhanced terahertz reflectivity. We explain the key mechanism leading to parametric amplification in terms of a simplified Hamiltonian and demonstrate the validity of the simplified model in Ta_2NiSe_5 using DFT ab-initio calculations. We identify a unique 4.7 THz infrared active phonon that is preferentially coupled to the electronic bandstructure, providing a dominant contribution to the low frequency terahertz amplification. Moreover, we show that the electron-phonon coupling is strongly dependent on the order parameter. Our theory suggests that the pumped Ta_2NiSe_5 is a gain medium which can be used to create THz amplifiers in THz communication applications.

INTRODUCTION

Motivation

Optical pump-probe experiments provide a powerful avenue to explore collective dynamics in correlated quantum materials. Several experiments have demonstrated dramatic changes in the terahertz and mid-IR reflectivity following photo-excitation. In experiments on $YBa_2Cu_3O_{6.5}$ cuprate superconductors, parametric resonances caused by internal Josephson plasma oscillations can induce extra "edge" features in the optical reflectivity [1–3]. On the other hand, the phonon-polariton system SiC[4] and the bulk superconductor K_3C_{60}[5, 6] provide examples where oscillations inside these materials result in significant reflectivity enhancement, possibly exceeding unity. A unified interpretation of these seemingly disparate pump induced features can be formulated in terms of Floquet theory under the assumption that collective excitations create a system with time-periodic properties. Previous analysis has demonstrated the existence of four types of drive induced features in reflectivity, depending on the relative strength of parametric driving and dissipation[7]. Edge-like features

* Correspondence to: marios_michael@g.harvard.edu

occur from interference between different Floquet components of the transmission channels when dissipation is strong compared to the oscillation amplitude. In the opposite regime, strong amplification of reflectivity occurs when the parametric drive is not compensated by dissipation and the material exhibits a lasing instability. In fact, such reflectivity features can serve as reporters of a lasing instability, indicating that the effective Floquet medium can be used as a gain medium in a laser.

Here, we develop a theory to explain the experimentally observed pump-induced terahertz amplification of the reflectivity in layered quasi-1D semiconductor Ta_2NiSe_5, a potential excitonic insulator material. An excitonic insulator phase can emerge when bound electron-hole pairs form a condensate in a semi-metallic phase opening up a gap and causing a phase transition to an insulating state[8]. In Ta_2NiSe_5, alternating chains of Ta and Ni are aligned along the axis, forming a sheet in the *ac*-plane, and multiple layers are stacked along the *b*-axis (see Fig. 1A). An exchange of electron between adjacent Ta and Ni chains along the *a*-axis creates an exciton across the chain (along the *c*-axis) [9–17]. Previous studies have reported a second order monoclinic-orthorhombic phase transition at $T_c = 326$ K. This leads to an insulating gap below the critical temperature which grows to be 160 meV at low temperatures. The pump-probe experiment demonstrates that above-gap frequency optical excitation induces reflectivity amplification which is maximal at 4.7 THz, corresponding to an IR-active B_{3u} phonon mode confirmed by previous infrared measurements [14, 15]. This turns out to be a surprising result given that the high-frequency pump cannot directly excite the collective THz modes. We show phenomenologically and using ab-initio calculations that this dramatic down conversion is caused by a nontrivial interplay of electron-phonon interactions and phonon non-linearities.

The multi-step process described in this article, converting high frequency pumping to THz amplification of reflectivity, is schematically illustrated in figure 1(a) and is outlined as follows: a) The pump excites electrons from the valence bands to the conduction bands through direct dipole transitions. b) The photo-excited electrons exhibit an unusual quadratic coupling to the 4.7 THz phonons (see Results):

$$H_{el-ph} = \sum_k g_k n_{el,k} Q^2, \tag{1}$$

where Q is the IR-phonon displacement, $n_{el,k}$ the photo-excited electron occupation and g_k the effective electron-phonon coupling. The pump is non-resonant with the IR active

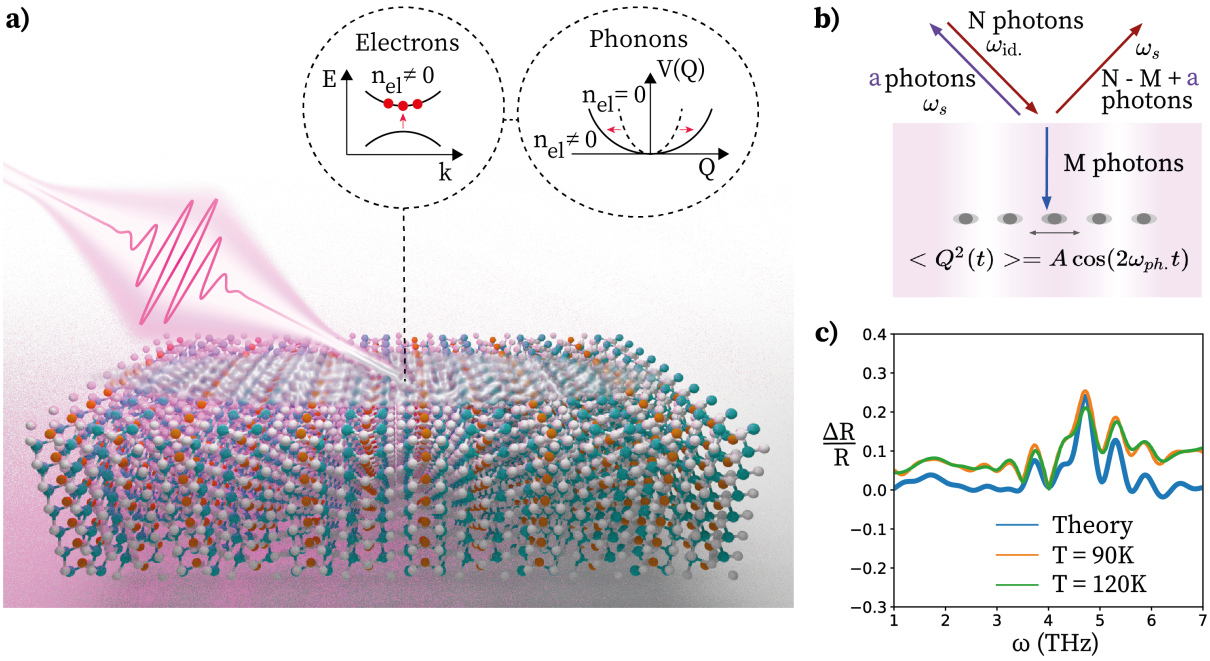

FIG. 1: Schematic mechanism that leads to amplification of THz optical reflectivity following high frequency pumping. a) An ultrafast laser pulse (0.5eV, 150 fs) photoexcites electrons through direct dipole transitions between the valence and conduction bands. The photo-excited electrons generate pairs of phonons through the electron-phonon interaction squeezing the phonon field (see equation (1)). b) Reflectivity amplification of pumped Ta_2NiSe_5. Coherent phonon field fluctuations oscillate at twice the phonon frequency, ω_{ph}, creating an effective THz Floquet medium. Parametric driving from the phonon oscillations can create pairs of photons at the signal and idler frequency once stimulated by the probe pulse. This enhances the reflectivity and also scatters counter-propagating light oscillating at the idler frequency. c) Relative change in the reflectivity as a function of frequency subsequent to photoexcitation. The experimental results are shown at two different temperatures together with the theoretical fit which considers parametric amplification by a 9.4 THz oscillating field.

terahertz phonons and thus does not directly initiate the enhanced reflectivity dynamics. Instead, IR-phonon pair generation occurs via a Raman process caused by pump induced changes in the electronic occupation. The result is that the expectation value of the phonon displacement is zero, $\langle Q \rangle = 0$, but the fluctuations are squeezed and coherently oscillate at twice the phonon frequency, $\langle Q^2(t) \rangle = \langle Q^2 \rangle_0 + A\cos(2\omega_{\rm ph}t)$. c) The squeezed phonon

oscillations and phonon nonlinearities create a Floquet material oscillating at $2\omega_{\rm ph} = 9.4$ THz. d) Parametric resonances due to the oscillating field occur primarily around $\omega_{\rm ph}$, parametrically amplifying the reflectivity as depicted in Figure 1 (b).

The theory developed in this article addresses two inter-connected questions: 1) Can a Floquet material oscillating at 9.4 THz provide parametric amplification similar to experimental observations? 2) What is the origin of the 9.4 THz oscillation?.

Summary of results

We begin our analysis by showing that the parametrically amplified reflectivity at 4.7 THz is consistent with the presence of a coherently oscillating Raman mode at twice the frequency, 9.4 THz. The theoretical fit captures the experimental amplification profile, plotted in figure 1(c). A schematic Hamiltonian describing parametric amplification of the optical reflectivity in the presence of a coherently oscillating mode at $\omega_d = 9.4$ THz is given by:

$$H_{ampl.} = X(t)a^\dagger_{1,k}a^\dagger_{2,-k} + h.c., \tag{2}$$

where $X(t)$ is a Raman mode and $\{a^\dagger_{1,k}, a^\dagger_{2,-k}\}$ are the creation operators of photons with opposite momentum which may be associated with different phonon-polariton bands $\{1, 2\}$ at frequencies parametrically resonant with the drive, $\omega_1(k) + \omega_2(-k) = \omega_d$. As shown in figure 1(b), Floquet drive can generate pairs of photons at the signal frequency of the incoming probe, ω_s, and a photon oscillating at the idler frequency, $\omega_{\rm id} = \omega_d - \omega_s$. Reflectivity amplification is then caused by stimulated emission of photon pairs by the driven material. To compute the reflection coefficient, we use degenerate Floquet perturbation theory to construct the eigenmodes and solve the Fresnel equations at the boundary.

We then proceed to investigate the origin of the 9.4 THz oscillation. We show that electron-phonon coupling between electronic bands involved in the photo-excitation and the 4.7 THz IR-phonon naturally leads to phonon squeezing. Phonon squeezing oscillations have twice the frequency of the phonon and act as a Raman mode. We find that this mechanism is generic and should apply to all IR-phonons present in the system. However, for phonon squeezing oscillations to create an effective Floquet material that can significantly enhance the reflectivity, the phonon needs to be both strongly coupled to the photo-excited bands and also have a strong coupling to the electric field.

We hence perform ab-intio calculations to determine both the magnitude of the electron phonon coupling and the IR activity of the different phonon modes. We find that, indeed, the 4.7 THz IR-phonon is special, exhibiting strong electron-phonon coupling and appreciable IR activity as compared to other IR-phonons in the same frequency range. Moreover, we confirm that phonon fluctuations are responsible for the THz amplification. The theory shows that the predicted reflectivity amplification is a reporter of a lasing instability, implying that pumped Ta_2NiSe_5 could, in principle, serve as a Floquet gain medium for THz lasing.

As a final intriguing aspect, we find that the 4.7 THz mode is strongly coupled to the elusive and hotly debated order parameter of Ta_2NiSe_5[9, 11, 12, 18–21], which is thought to have some excitonic insulating character. A number of state-of-the-art experiments have been performed to shed light on the origin of the phase transition at 326 K as well as what role the excitonic and lattice instabilities play in this phase transition process. However, the results show contradictory results [10, 13–18, 22–37] and the question whether Ta_2NiSe_5 hosts an excitonic insulator phase remains an open question. Using DFT frozen phonon calculations, we find that the electron-phonon coupling for the 4.7 THz phonon effectively vanishes in the high temperature orthorhombic phase. This indicates that the THz parametric amplification of reflectivity is mediated by the low temperature phase and is expected to be sensitive to the phase transition. This interplay between the order parameter and phase transition has been observed in pump-probe [10, 22], near infrared [26, 27], and time-resolved ARPES experiments [18, 30, 37, 38] , and has unraveled key ingredients in the physics of Ta_2NiSe_5 in addition to providing a clearer understanding of the nature of the order parameter. The link between the 4.7 THz phonon and the order parameter opens new avenues for using parametric amplification as a novel method to track order parameter dynamics.

RESULTS

Parametric amplification of reflectivity in pumped Ta_2NiSe_5

1. *Equilibrium reflectivity*

The reflectivity of a material is captured by the frequency dependent refractive index appearing in the Maxwell equations:

$$\left(\frac{n(\omega)^2\omega^2}{c^2} - k^2\right) E = 0 \tag{3}$$

where E is the electric field and all information about phonons and other IR active modes is encoded in $n(\omega)$. We assume that the probe corresponds to an electromagnetic wave reflected from the sample at normal incidence. The propagation direction is along the b-axis of the crystal, which we refer to as the y-direction, whereas the electric field points in the a-direction which we refer to as the z-axis. The refractive index can be directly extracted experimentally from the complex reflection coefficient at normal incidence in an equilibrium system[39]:

$$n(\omega) = \frac{1 - r(\omega)}{1 + r(\omega)}. \tag{4}$$

2. *Eigenstates in Floquet state*

Once we have obtained the refractive index from the equilibrium reflectivity, we model the Floquet material as experiencing a parametric drive oscillating at frequency, ω_d, which mixes signal and idler frequencies:

$$E(t) = e^{iky}\left(E_s e^{-i\omega_s t} + E_{id} e^{i\omega_{id} t}\right). \tag{5}$$

where ω_s is the frequency of the incoming probe and $\omega_{id} = \omega_d - \omega_s$. Such mixing corresponds to degenerate perturbation theory in Floquet systems and the idler component is the nearest Floquet band contribution to ω_s which is responsible for parametric instabilities [3, 40, 41]. The oscillating mode is included phenomenologically through a time-periodic contribution to the electric permittivity:

$$\delta\epsilon(t) = 2A_{\text{drive}} \cos(\omega_d t). \tag{6}$$

Using the ansatz in equation (5), the equations of motion in the Floquet state for the different oscillating components of the electric field become:

$$\left(\frac{n(\omega_s)^2\omega_s^2}{c^2} - k^2\right) E_s + A_{dr}E_{id} = 0 \tag{7a}$$

$$\left(\frac{n(\omega_{id})^2\omega_{id}^2}{c^2} - k^2\right) E_{id} + A_{dr}E_s = 0. \tag{7b}$$

To compute the reflectivity at normal incidence, we first find the allowed k values for a given ω_s. Due to the coupling of signal and idler components, two such k values exist, associated with two transmission channels, both of which oscillate at signal and idler frequencies. The transmission channels correspond to eigenvectors of the Floquet equations of motion inside the material,

$$E_i = t_i E_0 e^{ik_i y}\left(e^{-i\omega_s t} + \alpha_i e^{i\omega_{id}t}\right), \tag{8}$$

where α_i is the relative amplitude of the signal and idler component in the eigenvector of wave-vector k_i, t_i is the transmission coefficient of the i-th channel and E_0 the amplitude of the incoming field.

3. Floquet-Fresnel equations

In a reflection problem, the eigenvalue equation (7) enables computation of the transmitted wavevectors as a function of a fixed frequency set by the incoming light. However, the answer is given in terms of k_i^2 rather than k_i and the correct root is chosen such that the field vanishes at infinity, $\mathrm{Im}\{k_i\} > 0$. The reflectivity is computed by solving the Floquet-Fresnel equations, matching electric and magnetic fields parallel to the surface both at frequency ω_s and at frequency ω_{id}. Inside the material we have the electric field:

$$E_{mat} = E_0 \sum_i t_i e^{ik_i y}\left(e^{-i\omega_s t} + \alpha_i e^{i\omega_{id}t}\right), \tag{9}$$

and for vacuum we have:

$$\begin{aligned} E_{vac} =& E_0\left(e^{i\omega_s/cy - i\omega_s t} + r_s e^{-i\omega_s/cy - i\omega_s t}\right) + \\ & E_0 r_{id} e^{i\omega_{id}t. + i\omega_{id}y}. \end{aligned} \tag{10}$$

Using the homogeneous Maxwell equations, $\nabla \times E = -\partial_t B$ to compute the magnetic field and matching boundary conditions at $y = 0$, we obtain the Fresnel equations for the driven

system:

$$1 + r_s = t_1 + t_2, \tag{11a}$$

$$1 - r_s = \frac{k_1}{\omega_s} t_1 + \frac{k_2}{\omega_s} t_2, \tag{11b}$$

$$r_{id} = t_1 \alpha_1 + t_2 \alpha_2, \tag{11c}$$

$$r_{id} = \frac{k_1}{\omega_{id}} t_1 \alpha_1 + \frac{k_2}{\omega_{id}} t_2 \alpha_2. \tag{11d}$$

To fit the data, we choose a drive at 9.4 THz and allow for small changes in the static properties of the system such as a photo-induced conductivity stemming from photo-excited charge carriers. The fitted parameters are given in the Materials and Methods section.

Phonon squeezing initiated by photoexcited electrons

1. Electron phonon coupling

In this section, we develop a microscopic theory of the coupling of electronic bands to IR active phonons. In the dipolar gauge[42], the effective dipole of the phonon is linearly coupled to the electronic dipole. For two electronic bands with an allowed dipole transition, this coupling takes the form:

$$H_{\mathrm{el-ph}} = Q \sum_k \lambda_k \left(\hat{c}^\dagger_{1,k} \hat{c}_{2,k} + \hat{c}^\dagger_{2,k} \hat{c}_{1,k} \right), \tag{12}$$

where Q is the phonon coordinate, $\hat{c}_1$ and $\hat{c}_2$ the annihilation operators of the two electronic bands and λ_k the electron-phonon coupling matrix element as a function of momentum k. Using a Schrieffer-Wolff transformation, we "integrate out" the linear electron-phonon coupling, which is non-resonant due to the different energy scales between the IR-phonon and the electronic transition, to reveal the resonant non-linear coupling between the electron occupation number and the phonon squeezing operator, Q^2. In the materials and methods material, we show that this procedure leads to the effective coupling:

$$H_{\mathrm{el-ph,eff.}} = \sum_k \frac{\lambda_k^2}{\Delta_k} \left(n_{1,k} - n_{2,k} \right) Q^2, \tag{13}$$

where $\Delta_k = E_{1,k} - E_{2,k}$ is the energy difference between the electronic states and $\hat{n}_{i,k} = \hat{c}^\dagger_{i,k} \hat{c}_{i,k}$ the number operator. The above equation applies to phonons that are coupled to

independent pairs of electronic bands. If three or more bands are simultaneously coupled to a specific phonon the effective electron-phonon Hamiltonian is more complicated but with similar qualitative features, such as the coupling of electron density to the square of the phonon coordinate.

2. Phonon squeezing

Once electrons have been photo-excited, the finite number of optically excited electrons quenches the frequency of the phonon:

$$H_{\text{el-ph,eff.}} = \frac{Mf(t)Q^2}{2}, \tag{14}$$

where M is the mass of the phonon. In equation (14), the parametric driving $f(t)$ comes from the photo-excited distribution of electrons that is strongly coupled to the phonon:

$$f(t) = \sum_k \frac{2\lambda_k^2}{M\Delta_k} \left(\langle n_{1,k} \rangle (t) - \langle n_{2,k}(t) \rangle \right), \tag{15}$$

The photo-excited electron dynamics are fast and can be approximated as a delta function in time. More generally we can approximate the photo-excited distribution as having a characteristic life time, $f(t) = f_0\theta(t)e^{-t/t_{decay}}$, but this does not change our conclusions.

The above electron induced drive describes a Raman process that does not excite the phonon directly (i.e. $\langle Q \rangle = 0$). However, the squeezing operator starts oscillating at frequency equal to twice the phonon frequency, as shown in the materials and methods:

$$\left(\partial_t^2 - (2\omega_{\text{ph}})^2\right) \left\langle Q^2 \right\rangle = -4f(t) \left\langle Q^2 \right\rangle_0, \tag{16}$$

where $\langle Q^2 \rangle_0$ is the equilibrium fluctuations and ω_{ph} is phonon frequency at zero momentum which is renormalized by the coulomb force, $\omega_{\text{ph}}^2 = \omega_{\text{ph},0}^2 + \frac{Z^2}{\epsilon\epsilon_0 M}$.

To show that this phenomenon is related to squeezing, we expand Q^2 in terms of creation and annihilation operators, using $Q = \frac{a+a^\dagger}{\sqrt{2M\omega_{ph}}}$:

$$Q^2(t) = \frac{1}{2M\omega_{ph}} \left(a^\dagger(t)a^\dagger(t) + a(t)a(t) + a^\dagger(t)a(t) + a(t)a^\dagger(t) \right). \tag{17}$$

Expectation values of $a(t)a(t)^\dagger$ do not oscillate rapidly while the anomalous pairs $a^\dagger(t)a^\dagger(t)$ and $a(t)a(t)$ oscillate at twice the phonon frequency. As a result a state with phonon fluctuations, Q^2, that oscillate at twice the phonon frequency implies the existence of a condensate of phonon pairs $\left\langle a^\dagger(t)a^\dagger(t) \right\rangle \neq 0$.

3. Floquet matter

Coherent oscillations of long lived modes, such as the phonon squeezing oscillations, turn matter into Floquet matter with time-periodic properties through non-linear interactions with the rest of the material. Following the same steps as in references [40, 43], we show in the materials and methods how a lattice anharmonicity proportional to Q^4 and squeezing dynamics lead to the signal and idler coupling in equation (7). For this model, we find that the signal idler coupling is proportional to the IR activity of the mode, Z, the phonon anharmonicity, u, and the amplitude of the oscillations, B : $A_{\text{drive}} \propto Z^2 u B$.

Ab-initio calculations : the 4.7 THz IR-Phonon

The above discussion is generic and in principle applies to every IR-phonon inside a given material. In this section we use DFT calculations to determine which phonons make the dominant contribution to the parametric amplification of reflectivity in Ta_2NiSe_5. We start our discussion by identifying which valence and conduction bands are involved in photo-absorption by evaluating the optical dipole transitions matrix elements. In Fig. 2(a), we plot the momentum resolved optical contribution, for field polarization along the a-axis, of each band to dipole allowed transitions within the experimentally relevant energy window between 0.33 and 0.9 eV set by the pump parameters. For a given valence(conduction) band and k-point, the optical contribution is defined by summing the square of the dipole transition matrix elements associated with the transition. We find that it is the first three conduction bands that are predominantly excited by the pump.

Turning our attention to phonons, we use ab-initio calculations to identify all IR active phonons. In particular, we find a number of phonons in the low temperature monoclinic phase between 4 and 5 THz shown in the supplementary material. In Fig. 2 (b) we plot the IR activity of phonons as a function of frequency and identify the 4.7 THz phonon which, as shown below, turns out to be the most strongly electron coupled phonon.

We compute the electron-phonon interaction between IR active phonons and electrons. This is to identify the phonons that dominate the interaction with the photo-excited electronic bands. To accomplish this we use the method of frozen phonons. In this approach, the electronic bands are recalculated with the lattice shifted along a phonon eigendisplacement.

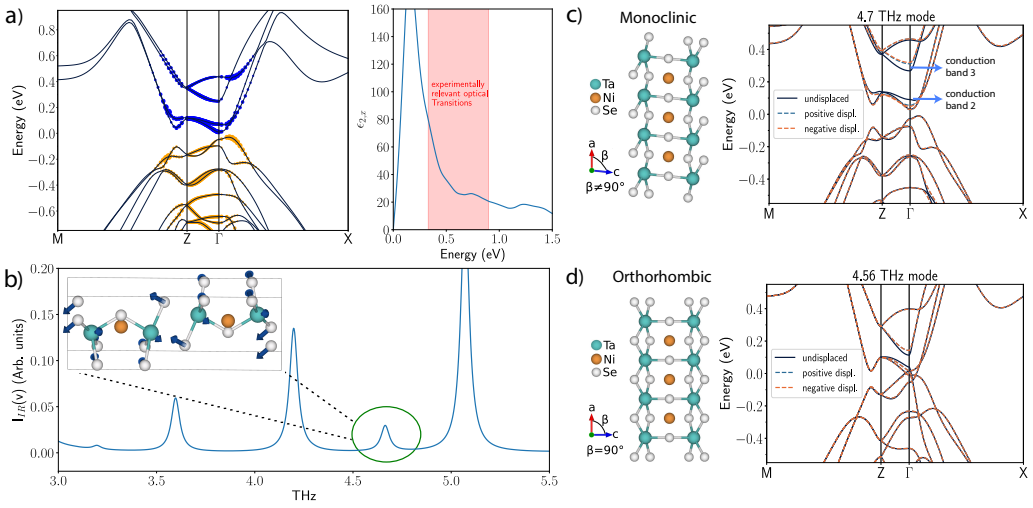

FIG. 2: Summary of ab-initio calculations. a) Optical matrix elements along the a-axis calculated for the frequency region between 0.4 to 0.9 eV. The size of the circles is proportional to the magnitude of the matrix elements and indicates which electronic valence and conduction bands are involved in photo-absorption. b) IR activity of the most IR active phonons; the phonon at 4.7 THz which dominates electron-phonon interactions in that region is highlighted with the mode character shown in the inset. A complete list of IR active phonons in this region for TNS is given in materials and methods. c) and d) show the effect of electron-phonon coupling on the band structure in the monoclinic and orthorhombic phase respectively. The electron-phonon coupling is captured by calculating the electronic band-structures using DFT in the presence of either negative or positive phonon displacement (frozen phonon approximation). The phonon 4.7 THz in the monoclinic phase is strongly coupled to the electronic bands 2 and 3 which are highlighted in the figure. In the high temperature orthorhombic phase the effective electron-phonon coupling is reduced by an order of magnitude. This indicates that the electron-phonon interaction is very sensitive to the order parameter.

To quantify the coupling strength of a specific phonon to a particular electronic band we integrate the energy changes of the band in the presence of the phonon over the Brillouin zone as outlined in the supplementary material. We find that in the vicinity of 4.5 THz, relevant to the experimental observables, the 4.7 THz mode has roughly an order of magnitude larger electron-phonon coupling strength compared to the nearby phonons. In particular, as shown in Fig. 2(c), the 2nd and 3rd conduction bands (in this paper we number the conduction

bands from lowest to highest in energy) are significantly renormalised in the presence of the 4.7 THz phonon. Since the phonon is mostly coupled to two electronic bands, the frozen phonon calculations are consistent with equation (13) leading to the two bands shifting in energy by an equal and opposite amount given by:

$$\begin{aligned} E_{k,3}|_{\langle Q\rangle\neq 0} - E_{k,3}|_{\langle Q\rangle=0} &= -\left(E_{k,2}|_{\langle Q\rangle\neq 0} - E_{k,2}|_{\langle Q\rangle=0}\right) \\ &= \langle Q\rangle^2 \frac{\lambda_k^2}{\Delta_k\left(1-\frac{\omega_{ph,0}^2}{\Delta_k^2}\right)} \end{aligned} \tag{18}$$

where $E_{k,2}$ and $E_{k,3}$ is energy of conduction band two and three at momentum k, and Δ_k is the energy difference of the two bands in equilibrium. Therefore, in this case, calculating the energy shifts as a function of momentum in the frozen phonon approximation allows for direct computation of the electron-phonon interaction.

To summarize, we use ab-initio calculations to identify the electron bands excited by pumping and to establish the IR-active phonons in Ta_2NiSe_5. Subsequently, frozen phonon calculations allowed for the identification of the phonon with the dominant electron-phonon coupling to the excited electronic bands. This leads to the identification of the 4.7 THz mode as responsible for the parametric amplification observed in experiments through the mechanism outlined in previous subsections. We note that we do not exclude the possibility of subdominant amplification in reflectivity spectra arising from other phonons at different frequencies. In the supplementary material, we provide more details of our DFT analysis of IR-phonons in Ta_2NiSe_5, the frozen phonon calculations and the calculation of optical matrix elements.

1. Connection to the order parameter

Finally, we discuss the effects of the phase transition on the phonon squeezing process. In figure 2, we compute the electron-phonon interaction of the 4.7 THz phonon in the low temperature monoclinic phase while for the high temperature orthorhombic phase we compute the electron-phonon interaction of the phonon adiabatically connected to the 4.7 THz phonon eigenstate (for details on the identification of the adiabatically connected phonon see supplementary material). The electron-phonon interaction effectively disappears in the high temperature phase providing evidence that electron-phonon coupling is mediated by the

order parameter. In particular, we suggest that close to the phase transition the electron-phonon coupling is proportional to the order parameter, $\lambda_k = \Phi B_k$, where Φ is the order parameter and B_k a constant. This, in turn, suggests that parametric amplification can be used as a nontrivial probe to investigate order parameter dynamics. The microscopic reason for the strong dependence of the electron-phonon coupling to the order parameter is a very interesting question that could reveal new insights about the nature of the order parameter in Ta_2NiSe_5 and will be addressed in a subsequent publication.

DISCUSSION

We have investigated the microscopic mechanism of amplification of THz optical reflectivity in Ta_2NiSe_5 arising from high frequency optical pumping. We showed that strong electron-phonon coupling opens new pathways towards realizing THz parametric amplification through high frequency pumping. Ab-initio calculations highlight the importance of the 4.7 THz IR-active phonon which is strongly coupled to electrons allowing for the amplification to manifest in the THz reflection spectrum.

Our theory indicates that choosing which electronic band to photoexcite selects the IR-phonon that is most strongly coupled to that electronic band. As a result, we can use different pumping frequencies in the same material to tune the frequency of the THz parametric amplification through mode-selective phonon squeezing.

Finally, we showed that the electron-phonon coupling is strongly dependent on the order parameter and becomes suppressed in the high temperature orthorhombic phase. This suggests that THz amplification of reflectivity can be used as a new probe to order parameter dynamics.

MATERIALS AND METHODS

Theoretical fit of the parametric reflectivity amplification in pumped Ta_2NiSe_5

As mentioned in the main text in equation (4), in principle the complex refractive index can be directly computed by the complex reflectivity amplitude, $r(\omega)$. However, small phase errors upon experimental extraction of $r(\omega)$ could lead to unphysical behaviour of the reflectivity. To overcome this complication, we fit the data by assuming that for an insulator

like Ta_2NiSe_5 the refractive index is real. As a result, we can instead use the absolute value of $|r| = \sqrt{R}$ and express the refractive index as:

$$n(\omega) = \frac{1+\sqrt{R}}{1-\sqrt{R}}. \tag{19}$$

Upon parametric resonance and solving equation (7) together with the Floquet-Fresnel boundary conditions in equation (11), assuming a purely real spectrum with no dissipation leads to highly divergent behavior on parametric resonance. As a result, we put back dissipation by including an imaginary component to the refractive index. In the driven case we argue that this is physical, since $n_{\text{driven}}(\omega)^2 = n^2(\omega) + i\sigma_{\text{driven}}/\omega$ and dissipation can arise through through a transient contribution to the conductivity by electrons excited across the gap of the insulator. To fit the data we choose a parametric drive at $\omega_d = 9.4$ THz, drive amplitude $A_{\text{drive}} = 7.5\frac{THz^2}{c^2}$, overall constant renormalization of the refractive, $n^2_{\text{drive}} = n^2(\omega) + \delta n^2$, with $\delta n^2 = 0.1 + 0.01i$ and an overall Gaussian broadening function with standard deviation of 0.1 THz.

Electron - phonon interaction

The Hamiltonian of two electronic bands coupled by an allowed direct dipole transition that is, in turn, coupled to a phonon is given by:

$$H_{\text{el}} = \frac{\Delta}{2}\left(\hat{c}_1^\dagger \hat{c}_1 - \hat{c}_2^\dagger \hat{c}_2\right) + \lambda\left(\hat{c}_1^\dagger \hat{c}_2 + \hat{c}_2^\dagger \hat{c}_1\right) Q, \tag{20}$$

where $\Delta = E_1 - E_2$ is the difference in energy between the two bands, λ is the coupling constant coming from the dipole-dipole interaction in the dipole gauge, Q is the phonon coordinate and $\{\hat{c}_1, \hat{c}_2\}$ are the annihilation operators of the two electron bands. The IR-phonon quadratic hamiltonian is given by:

$$H_{\text{ph}} = ZEQ + M\omega^2_{\text{ph},0}\frac{Q^2}{2} + \frac{\Pi^2}{2M},$$

where Π is the conjugate momentum of the phonon coordinate Q, Z the effective coupling to the electromagnetic field, E, and $\omega_{\text{ph},0}$ the phonon frequency. Since the transition itself is not resonant with the phonon mode, we decouple the linear electron phonon interaction perturbatively using a Schrieffer-Wolff transformation. This generates an interaction between the electron-hole pair density and the fluctuations of the phonon field which can be a

resonant process. To perform this transformation, it is convenient to note that bilinear combinations of $\{\hat{c}_1^\dagger, \hat{c}_1, \hat{c}_2^\dagger, \hat{c}_2\}$ appearing in the Hamiltonian, obey SU(2) commutation relations by making the following identification:

$$S^x = \frac{\hat{c}_1^\dagger \hat{c}_2 + \hat{c}_2^\dagger \hat{c}_1}{2}, \tag{21a}$$

$$S^y = -i\frac{\hat{c}_1^\dagger \hat{c}_2 - \hat{c}_2^\dagger \hat{c}_1}{2}, \tag{21b}$$

$$S^z = \frac{\hat{c}_1^\dagger \hat{c}_1 - \hat{c}_2^\dagger \hat{c}_2}{2}, \tag{21c}$$

where their commutators are $[S^x, S^y] = iS^z$ and its cyclic permutations. In terms of the spin operators, we separate the Hamiltonian into a non-interacting and an interacting part:

$$H_0 = \Delta S^z + M\omega_{ph,0}^2 \frac{Q^2}{2} + \frac{\Pi^2}{2M}, \tag{22}$$

$$V = 2\lambda S^x Q \tag{23}$$

To remove the interacting part V to linear order in λ, we consider a unitary transformation of the type:

$$U = \text{Exp}\{iA\}, \tag{24}$$

$$A = \alpha Q S^y + \beta \Pi S^x \tag{25}$$

The Schrieffer-Wolff expansion is given by:

$$UH_{total}U^\dagger = H_0 + V - i\left[H_0, A\right] - i\left[V, A\right] - \frac{1}{2}\left[\left[H_0, A\right], A\right]. \tag{26}$$

The parameters α and β are found such that:

$$V = i\left[H_0, A\right] \tag{27}$$

Matching linear terms in Π and Q, leads to the parameters:

$$\beta = \frac{\alpha}{M\Delta}, \tag{28a}$$

$$-\Delta\alpha + 2\lambda + M\omega_{\text{ph},0}^2\beta = 0, \tag{28b}$$

$$\Rightarrow \alpha = \frac{2\lambda}{\Delta\left(1 - \frac{\omega_{\text{ph},0}^2}{\Delta^2}\right)}, \tag{28c}$$

which confirms that this perturbation theory can be carried out as long as $\omega_{\text{ph},0}$ is off-resonant with the transition energy Δ. The effective electron-phonon interaction after the Schrieffer-Wolff transformation is given by:

$$\begin{aligned} H_{\text{eff}} =& -i\left[V,A\right]-\frac{1}{2}\left[\left[H_0,A\right],A\right]=-\frac{i}{2}\left[V,A\right], \\ =& \frac{2\lambda^2}{\Delta\left(1-\frac{\omega_{\text{ph},0}^2}{\Delta^2}\right)}Q^2S^z+\frac{2\lambda^2}{\Delta\left(1-\frac{\omega_{\text{ph},0}^2}{\Delta^2}\right)}\left(S^x\right)^2, \end{aligned} \tag{29}$$

where the second term does not depend on the phonons. The residual electron phonon interaction is thus give by:

$$H_{\text{el}-\text{ph,eff}} = \frac{\lambda^2}{\Delta\left(1-\frac{\omega_{\text{ph},0}^2}{\Delta^2}\right)}Q^2\left(n_1-n_2\right) \tag{30}$$

where $n_1=\hat{c}_1^\dagger\hat{c}_1$ is the occupation number of mode 1. This implies that if either mode 1 or mode 2 are photo-excited the phonon can be squeezed.

The linear term in the electric field, ZEQ, appearing in equation 1, is also transformed by the Schrieffer-Wolff transformation. It gives rise to a term βZES^x which provides a small renormalization of the dipole transition amplitude between the bands and does not affect our discussion.

The above result can be generalized to an arbitrary number of independent pairs of electronic states. For example, for two electronic states the above result in the limit of $\frac{\omega_{ph,0}^2}{\Delta_k^2}\to 0$ is generalized to:

$$H_{\text{el}-\text{ph,eff}} = \sum_k \frac{\lambda_k^2}{\Delta_k}Q^2\left(n_{1,k}-n_{2,k}\right), \tag{31}$$

This expression is the one used in the main text.

Phonon squeezing

Using a Hartree-Fock type approximation on the effective electron-phonon Hamiltonian in equation (31), we derive an effective Hamiltonian for the phonon system only:

$$H_{\text{ph}} = ZEQ + M\left(\omega_{\text{ph},0}^2+f(t)\right)\frac{Q^2}{2}+\frac{\Pi^2}{2M} \tag{32}$$

where Z is the IR activity of the phonon mode, $\omega_{\text{ph},0}$ the bare phonon frequency and the effective parametric drive, $f(t)$, is given by photo-excited electron density coupled to the

phonon mode:

$$f(t) = \sum_k \frac{2\lambda_k^2}{M\Delta_k} \left(\langle n_{1,k} \rangle - \langle n_{2,k} \rangle \right), \tag{33}$$

Due to the fast dynamics of electrons, $f(t)$ acts as an impulsive delta function like parametric drive. Such a drive is not periodic but it can linearly excite phonon fluctuations $\langle Q^2 \rangle$ which will oscillate in time. To show this, we compute the equations of motion for fluctuations of the phonon field:

$$\partial_t \left\langle Q^2 \right\rangle = \frac{\langle \Pi Q + Q\Pi \rangle}{M}, \tag{34a}$$

$$\begin{aligned} \partial_t \langle \Pi Q + Q\Pi \rangle = &- 2M \left(\omega_{\text{ph},0}^2 + f(t) \right) \left\langle Q^2 \right\rangle + \\ &2\frac{\langle \Pi^2 \rangle}{M} - 2Z \langle EQ \rangle, \end{aligned} \tag{34b}$$

$$\begin{aligned} \partial_t \left\langle \Pi^2 \right\rangle = &- M \left(\omega_{\text{ph},0}^2 + f(t) \right) \langle (\Pi Q + Q\Pi) \rangle - \\ &Z \langle E\Pi + \Pi E \rangle. \end{aligned} \tag{34c}$$

At $k = 0$, we can use Maxwell's equations to remove the electric field dependence, $E = \frac{Z}{\epsilon\epsilon_0} Q$. Performing this substitution simplifies the equations of motion,

$$\partial_t \left\langle Q^2 \right\rangle = \frac{\langle \Pi Q + Q\Pi \rangle}{M}, \tag{35a}$$

$$\partial_t \langle \Pi Q + Q\Pi \rangle = - 2M \left(\omega_{\text{ph}}^2 + f(t) \right) \left\langle Q^2 \right\rangle + 2\frac{\langle \Pi^2 \rangle}{M}, \tag{35b}$$

$$\partial_t \left\langle \Pi^2 \right\rangle = - M \left(\omega_{\text{ph}}^2 + f(t) \right) \langle (\Pi Q + Q\Pi) \rangle. \tag{35c}$$

where $\omega_{\text{ph}}^2 = \omega_{\text{ph},0}^2 + \omega_{\text{pl,phonon}}^2$ is the frequency of the phonon at $k = 0$ which differs from the bare frequency by the phonon plasma frequency given by $\omega_{\text{pl,phonon}}^2 = \frac{Z^2}{\epsilon\epsilon_0 M}$. Being perturbative in the drive $f(t)$, we expand the phonon fluctuations,

$$\left\langle Q^2 \right\rangle = \left\langle Q^2 \right\rangle_0 + \left\langle Q^2 \right\rangle_1, \tag{36}$$

where $\langle Q^2 \rangle_0$ is the thermal expectation value and $\langle Q^2 \rangle_1 \propto f(t)$. To linear order in $f(t)$, the equations of motion imply, $\langle \Pi^2 \rangle_1 / M = M\omega_{\text{ph}}^2 \langle Q^2 \rangle_1 + M f(t) \langle Q^2 \rangle_0 + \mathcal{O}(f^2)$. Finally, combining equations in (35) we find that:

$$\left(\partial_t^2 + 4\omega_{\text{ph}}^2 \right) \left\langle Q^2 \right\rangle_1 = -4 f(t) \left\langle Q^2 \right\rangle_0. \tag{37}$$

This result shows that phonon fluctuations are linearly driven by photo-excitation and oscillate at twice the phonon frequency, $2\omega_{\text{ph}}$. These coherent oscillations of phonon fluctuations behave as a Raman mode.

Floquet matter from squeezing dynamics of phonons

Material properties such as the electric permittivity, become time-periodic in the presence of oscillating fields through interactions. Here, we demonstrate how lattice potential anharmonicities lead to a time-periodic index of refraction:

We consider a phonon system with a Q^4 anharmonicity for the IR-phonon with a Hamiltonian:

$$H_{\rm ph} = ZEQ + M\left(\omega_{\rm ph,0}^2 + f(t)\right)\frac{Q^2}{2} + \frac{\Pi^2}{2M} + uQ^4 \tag{38}$$

The equations of motion for the phonon given by the Hamiltonian in equation (38) is

$$\left(\partial_t^2 + \gamma\partial_t + \omega_{\rm ph,0}^2 + 4uQ^2\right)Q = \frac{Z}{M}E. \tag{39}$$

Using a gaussian ansatz for the phonons, we can linearize the above equation as:

$$\left(\partial_t^2 + \gamma\partial_t + \omega_{\rm ph,0}^2 + 12u\left\langle Q^2\right\rangle(t)\right)Q = \frac{Z}{M}E, \tag{40}$$

where the fluctuations $\langle Q^2\rangle = \langle Q^2\rangle_0 + A\cos(2\omega_{ph}t)$. The phonon mode appears in the Maxwells equations as:

$$\left(\frac{1}{c^2}\partial_t^2 - k^2\right)E = -Z\partial_t^2 Q. \tag{41}$$

To find the effective signal idler mixing presented in equation (7), we expand the equations of motion in signal and idler contributions:

$$Q = Q_s e^{-i\omega_s t} + Q_{\rm id}e^{i\omega_{\rm id}t} \tag{42}$$

Equation (40) becomes:

$$\begin{pmatrix} Q_s \\ Q_{id}\end{pmatrix} = \begin{pmatrix} \frac{Z}{\omega_s^2 + i\gamma\omega_s - \omega_{\rm ph}^2} & 0 \\ 0 & \frac{Z}{\omega_{\rm id}^2 + i\gamma\omega_{\rm id} - \omega_{\rm ph}^2}\end{pmatrix}\cdot\begin{pmatrix} E_s \\ E_{\rm id}\end{pmatrix} + \frac{ZuA}{\left(\omega_s^2 + i\gamma\omega_s - \omega_{\rm ph}^2\right)\left(\omega_{\rm id}^2 + i\gamma\omega_{\rm id} - \omega_{\rm ph}^2\right)}\begin{pmatrix} E_{\rm id} \\ E_s\end{pmatrix}. \tag{43}$$

Substituting equation 43 in Maxwells equation we find the equations of motion for the signal and idler component of the electric field to be:

$$\left(\frac{n_{eq.}^2(\omega_s)}{c^2}\omega_s^2 - k^2\right)E_s + A_{\rm drive,s}(\omega_s,\omega_{\rm id})E_{\rm id} = 0, \tag{44a}$$

$$\left(\frac{n_{eq.}^2(\omega_{\rm id})}{c^2}\omega_s^2 - k^2\right)E_s + A_{\rm drive,id}(\omega_s,\omega_{\rm id})E_{\rm id} = 0 \tag{44b}$$

where the signal and idler driving amplitudes, $A_{\text{drive,s}}$ and $A_{\text{drive,id}}$ are given by:

$$A_{\text{drive,s}} = \frac{Z^2 u A \omega_s^2}{\left(\omega_s^2 + i\gamma\omega_s - \omega_{\text{ph}}^2\right)\left(\omega_{\text{id}}^2 + i\gamma\omega_{\text{id}} - \omega_{\text{ph}}^2\right)}, \tag{45a}$$

$$A_{\text{drive,id}} = \frac{Z^2 u A \omega_{\text{id}}^2}{\left(\omega_s^2 + i\gamma\omega_s - \omega_{\text{ph}}^2\right)\left(\omega_{\text{id}}^2 + i\gamma\omega_{\text{id}} - \omega_{\text{ph}}^2\right)}. \tag{45b}$$

[1] S. Kaiser, C. R. Hunt, D. Nicoletti, W. Hu, I. Gierz, H. Y. Liu, M. Le Tacon, T. Loew, D. Haug, B. Keimer, and A. Cavalleri, Optically induced coherent transport far above T_c in underdoped yba$_2$cu$_3$o$_{6+\delta}$, Phys. Rev. B **89**, 184516 (2014).

[2] A. von Hoegen, M. Fechner, M. Först, N. Taherian, E. Rowe, A. Ribak, J. Porras, B. Keimer, M. Michael, E. Demler, and A. Cavalleri, Parametrically amplified phase-incoherent superconductivity in $YBa_2Cu_3O_{6+x}$ (2020), arXiv:1911.08284 [cond-mat.supr-con].

[3] M. H. Michael, A. von Hoegen, M. Fechner, M. Först, A. Cavalleri, and E. Demler, Parametric resonance of josephson plasma waves: A theory for optically amplified interlayer superconductivity in $YBa_2Cu_3O_{6+x}$, Phys. Rev. B **102**, 174505 (2020).

[4] M. F. Limonov, M. V. Rybin, A. N. Poddubny, and Y. S. Kivshar, Fano resonances in photonics, Nature Photonics **11**, 543 (2017).

[5] M. Budden, T. Gebert, M. Buzzi, G. Jotzu, E. Wang, T. Matsuyama, G. Meier, Y. Laplace, D. Pontiroli, M. Riccó, F. Schlawin, D. Jaksch, and A. Cavalleri, Evidence for metastable photo-induced superconductivity in K_3C_{60} (2020), arXiv:2002.12835 [cond-mat.supr-con].

[6] P. E. Dolgirev, A. Zong, M. H. Michael, J. B. Curtis, D. Podolsky, A. Cavalleri, and E. Demler, Periodic dynamics in superconductors induced by an impulsive optical quench (2021), arXiv:2104.07181 [cond-mat.supr-con].

[7] M. H. Michael, M. Först, D. Nicoletti, S. R. U. Haque, A. Cavalleri, R. D. Averitt, D. Podolsky, and E. Demler, Generalized fresnel-floquet equations for driven quantum materials (2021), arXiv:2110.03704 [cond-mat.str-el].

[8] D. Jérome, T. M. Rice, and W. Kohn, Excitonic insulator, Phys. Rev. **158**, 462 (1967).

[9] T. Kaneko, T. Toriyama, T. Konishi, and Y. Ohta, Orthorhombic-to-monoclinic phase tran-

sition of ta_2nise_5 induced by the bose-einstein condensation of excitons, Phys. Rev. B **87**, 035121 (2013).

[10] D. Werdehausen, T. Takayama, M. Höppner, G. Albrecht, A. W. Rost, Y. Lu, D. Manske, H. Takagi, and S. Kaiser, Coherent order parameter oscillations in the ground state of the excitonic insulator Ta_2NiSe_5, Science Advances **4**, eaap8652 (2018).

[11] K. Sugimoto, S. Nishimoto, T. Kaneko, and Y. Ohta, Strong coupling nature of the excitonic insulator state in Ta_2NiSe_5, Phys. Rev. Lett. **120**, 247602 (2018).

[12] G. Mazza, M. Rösner, L. Windgätter, S. Latini, H. Hübener, A. J. Millis, A. Rubio, and A. Georges, Nature of symmetry breaking at the excitonic insulator transition: Ta_2NiSe_5, Phys. Rev. Lett. **124**, 197601 (2020).

[13] Y. F. Lu, H. Kono, T. I. Larkin, A. W. Rost, T. Takayama, A. V. Boris, B. Keimer, and H. Takagi, Zero-gap semiconductor to excitonic insulator transition in Ta_2NiSe_5, Nature Communications **8**, 14408 (2017).

[14] T. I. Larkin, A. N. Yaresko, D. Pröpper, K. A. Kikoin, Y. F. Lu, T. Takayama, Y.-L. Mathis, A. W. Rost, H. Takagi, B. Keimer, and A. V. Boris, Giant exciton fano resonance in quasi-one-dimensional Ta_2NiSe_5, Phys. Rev. B **95**, 195144 (2017).

[15] T. I. Larkin, R. D. Dawson, M. Höppner, T. Takayama, M. Isobe, Y.-L. Mathis, H. Takagi, B. Keimer, and A. V. Boris, Infrared phonon spectra of quasi-one-dimensional Ta_2NiSe_5 and ta_2nis_5, Phys. Rev. B **98**, 125113 (2018).

[16] S. Mor, M. Herzog, J. Noack, N. Katayama, M. Nohara, H. Takagi, A. Trunschke, T. Mizokawa, C. Monney, and J. Stähler, Inhibition of the photoinduced structural phase transition in the excitonic insulator Ta_2NiSe_5, Phys. Rev. B **97**, 115154 (2018).

[17] K. Seki, Y. Wakisaka, T. Kaneko, T. Toriyama, T. Konishi, T. Sudayama, N. L. Saini, M. Arita, H. Namatame, M. Taniguchi, N. Katayama, M. Nohara, H. Takagi, T. Mizokawa, and Y. Ohta, Excitonic bose-einstein condensation in Ta_2NiSe_5 above room temperature, Phys. Rev. B **90**, 155116 (2014).

[18] E. Baldini, A. Zong, D. Choi, C. Lee, M. H. Michael, L. Windgaetter, I. I. Mazin, S. Latini, D. Azoury, B. Lv, A. Kogar, Y. Wang, Y. Lu, T. Takayama, H. Takagi, A. J. Millis, A. Rubio, E. Demler, and N. Gedik, The spontaneous symmetry breaking in Ta_2NiSe_5 is structural in nature (2020), arXiv:2007.02909 [cond-mat.str-el].

[19] D. Golež, Z. Sun, Y. Murakami, A. Georges, and A. J. Millis, Nonlinear spectroscopy of

collective modes in an excitonic insulator, Phys. Rev. Lett. **125**, 257601 (2020).

[20] Z. Sun and A. J. Millis, Bardasis-schrieffer polaritons in excitonic insulators, Phys. Rev. B **102**, 041110 (2020).

[21] A. Subedi, Orthorhombic-to-monoclinic transition in ta_2nise_5 due to a zone-center optical phonon instability, Phys. Rev. Materials **4**, 083601 (2020).

[22] D. Werdehausen, T. Takayama, G. Albrecht, Y. Lu, H. Takagi, and S. Kaiser, Photo-excited dynamics in the excitonic insulator ta2nise5, Journal of Physics: Condensed Matter **30**, 305602 (2018).

[23] S. Mor, M. Herzog, D. Golež, P. Werner, M. Eckstein, N. Katayama, M. Nohara, H. Takagi, T. Mizokawa, C. Monney, and J. Stähler, Ultrafast electronic band gap control in an excitonic insulator, Phys. Rev. Lett. **119**, 086401 (2017).

[24] M.-J. Kim, A. Schulz, T. Takayama, M. Isobe, H. Takagi, and S. Kaiser, Phononic soft mode behavior and a strong electronic background across the structural phase transition in the excitonic insulator ta_2nise_5, Phys. Rev. Research **2**, 042039 (2020).

[25] K. Kim, H. Kim, J. Kim, C. Kwon, J. S. Kim, and B. J. Kim, Direct observation of excitonic instability in ta_2nise_5, Nature Communications **12**, 1969 (2021).

[26] H. M. Bretscher, P. Andrich, P. Telang, A. Singh, L. Harnagea, A. K. Sood, and A. Rao, Ultrafast melting and recovery of collective order in the excitonic insulator ta2nise5, Nature Communications **12**, 1699 (2021).

[27] H. M. Bretscher, P. Andrich, Y. Murakami, D. Golež, B. Remez, P. Telang, A. Singh, L. Harnagea, N. R. Cooper, A. J. Millis, P. Werner, A. K. Sood, and A. Rao, Imaging the coherent propagation of collective modes in the excitonic insulator Ta_2NiSe_5 at room temperature, Science Advances **7**, eabd6147 (2021).

[28] P. A. Volkov, M. Ye, H. Lohani, I. Feldman, A. Kanigel, and G. Blumberg, Critical charge fluctuations and emergent coherence in a strongly correlated excitonic insulator, npj Quantum Materials **6**, 52 (2021).

[29] S. Pal, S. Grover, L. Harnagea, P. Telang, A. Singh, D. V. S. Muthu, U. V. Waghmare, and A. K. Sood, Destabilizing excitonic insulator phase by pressure tuning of exciton-phonon coupling, Phys. Rev. Research **2**, 043182 (2020).

[30] T. Tang, H. Wang, S. Duan, Y. Yang, C. Huang, Y. Guo, D. Qian, and W. Zhang, Non-coulomb strong electron-hole binding in Ta_2NiSe_5 revealed by time- and angle-resolved photoemission

spectroscopy, Phys. Rev. B **101**, 235148 (2020).

[31] L. Chen, T. T. Han, C. Cai, Z. G. Wang, Y. D. Wang, Z. M. Xin, and Y. Zhang, Doping-controlled transition from excitonic insulator to semimetal in Ta_2NiSe_5, Phys. Rev. B **102**, 161116 (2020).

[32] Y.-S. Seo, M. J. Eom, J. S. Kim, C.-J. Kang, B. I. Min, and J. Hwang, Temperature-dependent excitonic superfluid plasma frequency evolution in an excitonic insulator, Ta_2NiSe_5, Scientific Reports **8**, 11961 (2018).

[33] Y. Wakisaka, T. Sudayama, K. Takubo, T. Mizokawa, M. Arita, H. Namatame, M. Taniguchi, N. Katayama, M. Nohara, and H. Takagi, Excitonic insulator state in Ta_2NiSe_5 probed by photoemission spectroscopy, Phys. Rev. Lett. **103**, 026402 (2009).

[34] A. Nakano, T. Hasegawa, S. Tamura, N. Katayama, S. Tsutsui, and H. Sawa, Antiferroelectric distortion with anomalous phonon softening in the excitonic insulator Ta_2NiSe_5, Phys. Rev. B **98**, 045139 (2018).

[35] T. Saha, D. Golež, G. De Ninno, J. Mravlje, Y. Murakami, B. Ressel, M. Stupar, and P. c. v. R. Ribič, Photoinduced phase transition and associated timescales in the excitonic insulator Ta_2NiSe_5, Phys. Rev. B **103**, 144304 (2021).

[36] J. Lee, C.-J. Kang, M. J. Eom, J. S. Kim, B. I. Min, and H. W. Yeom, Strong interband interaction in the excitonic insulator phase of Ta_2NiSe_5, Phys. Rev. B **99**, 075408 (2019).

[37] T. Suzuki, Y. Shinohara, Y. Lu, M. Watanabe, J. Xu, K. L. Ishikawa, H. Takagi, M. Nohara, N. Katayama, H. Sawa, M. Fujisawa, T. Kanai, J. Itatani, T. Mizokawa, S. Shin, and K. Okazaki, Detecting electron-phonon coupling during photoinduced phase transition, Phys. Rev. B **103**, L121105 (2021).

[38] D. Golez, S. K. Y. Dufresne, M.-J. Kim, F. Boschini, H. Chu, Y. Murakami, G. Levy, A. K. Mills, S. Zhdanovich, M. Isobe, H. Takagi, S. Kaiser, P. Werner, D. J. Jones, A. Georges, A. Damascelli, and A. J. Millis, Unveiling the underlying interactions in Ta_2NiSe_5 from photo-induced lifetime change (2021), arXiv:2112.06298 [cond-mat.str-el].

[39] F. Wooten, Chapter 2 - maxwell's equations and the dielectric function, in *Optical Properties of Solids*, edited by F. Wooten (Academic Press, 1972) pp. 15–41.

[40] S. Sugiura, E. A. Demler, M. Lukin, and D. Podolsky, Resonantly enhanced polariton wave mixing and floquet parametric instability, arXiv:1910.03582 (2019).

[41] A. Eckardt and E. Anisimovas, High - frequency approximation for periodically driven quan-

tum systems from a floquet - space perspective, New Journal of Physics **17**, 093039 (2015).

[42] J. Li, D. Golez, G. Mazza, A. J. Millis, A. Georges, and M. Eckstein, Electromagnetic coupling in tight-binding models for strongly correlated light and matter, Phys. Rev. B **101**, 205140 (2020).

[43] M. H. Michael, M. Först, D. Nicoletti, S. R. U. Haque, A. Cavalleri, R. D. Averitt, D. Podolsky, and E. Demler, Generalized fresnel-floquet equations for driven quantum materials (2021), arXiv:2110.03704 [cond-mat.str-el].

4 Excitonic Insulator

The excitonic insulator (EI) is an exotic phase of matter which has been proposed in the 1960s by Mott, Keldysh, Kohn, and Kozlov [13–19]. It is envisioned to exist in any metal or semiconductor material which satisfies the condition that the excitonic binding energy is bigger than the electronic bandoverlap or bandgap. If this condition is met the groundstate of the crystal becomes unstable against the spontaneous formation of excitons which collectively condense into the new insulating groundstate (see Fig. 4.1).
Although the idea of the EI is over half a decade old, no material has yet been confirmed to host such a groundstate. Very recently the field has gained a lot of interest with the discovery of several candidate materials [21–25, 27, 82–85]. However, confirming the existence of the EI state poses a major experimental challenge, because the conjectured excitonic phase transition is intrinsically coupled to other phase transitions such as the formation of charge density waves (CDW) [21, 26, 27, 86, 87] or structural phase transitions [20, 28, 29, 31]. As such, it is exceptionally difficult from an experimental point of view to disentangle the competing phase transitions and to unambiguously identify the signature of the EI. This is the reason why all EI candidates are still under debate and in some cases similar experimental measurements even led to seemingly contradictory interpretations [20, 30, 88–93] .
Therefore, to be able to tell the effects of both phase transitions apart, understanding the crystal from a theoretical perspective is crucial and is the only way to selectively include the relevant interaction terms.

In the following chapter I will present this discussion for the currently most debated EI candidate material, Ta_2NiSe_5 (TNSe). I have investigated the material by means of a combined approach consisting of model and ab-initio calculations as well as experimental data from our collaborators to fully understand the nature of the phase transition.
I will start this chapter by discussing the fundamental theory of the EI. First, I will introduce the basic properties of excitons and then discuss a model hosting an excitonic insulating groundstate. The goal is to understand the underlying idea of the EI and to explain its most prominent spectroscopic features.
Afterwards, I will present a series of papers which discuss TNSe by tackling the phase transition from different angles. The first publication, publication III, [94] will discuss the conjectured electronic transition and identify a possible excitonic instability and its order parameter using an extended Hubbard model. Then, the next two publications, publication IV and V [90, 95], will investigate if such an electronic instability is realized

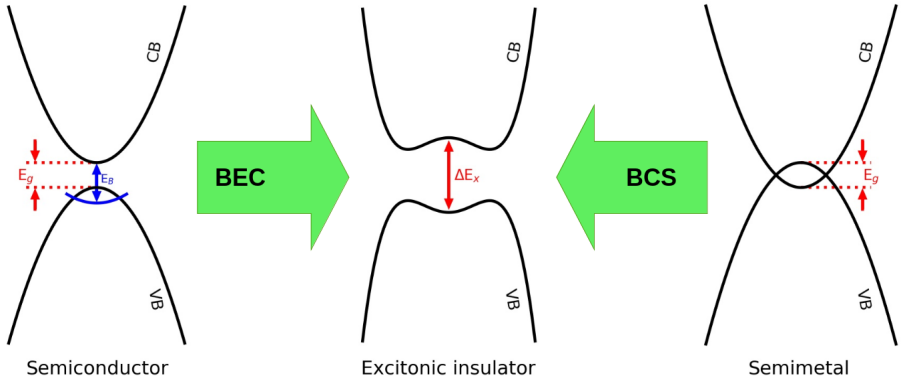

Fig. 4.1 Schematics of the EI scenario. The EI can arise from a semiconducting state, when the excitonic binding energy exceeds the electronic bandgap. Then the system becomes unstable against the formation of excitons which condense into the new groundstate via a BEC mechanism. Similarly the EI state can be reached from a semimetallic state with a small bandoverlap via a BCS like mechanism. This figure has been adapted from [81]

.

in the crystal using DFT based ab-initio calculations and time resolved ARPES (trARPES) data. We will show that the phase transition in TNSe is predominantly lattice driven and that the ab-initio results suggest that most experimental evidence hinting towards the existence of an excitonic insulating state [20,31,96–100,100,101], can also be explained by the structural instability in this material.

4.1 Basic excitonic properties

In this section I will introduce excitons and discuss their basic properties. Since there are many great textbooks on this topic, I will follow Czycholl's Solid State Theory book [63] in this section and summarize the most important results.
Excitons are quasiparticles which consist of a bound electron-hole pair. The most simplistic model which displays excitons consists of one valence band v and one conduction band c which interact via an attractive Coulomb force. Such a Hamiltonian reads [63]

$$H = \sum_{\mathbf{k}} \left(E_v(\mathbf{k}) c^\dagger_{v\mathbf{k}} c_{v\mathbf{k}} + E_c(\mathbf{k}) c^\dagger_{c\mathbf{k}} c_{c\mathbf{k}} \right) + \sum_{\mathbf{k_1},\mathbf{k_2},\mathbf{k_3},\mathbf{k_4}} V_{\mathbf{k_1}\mathbf{k_2}\mathbf{k_3}\mathbf{k_4}} c^\dagger_{v\mathbf{k_1}} c^\dagger_{c\mathbf{k_2}} c_{c\mathbf{k_3}} c_{v\mathbf{k_4}}. \tag{4.1}$$

The first sum describes the two uncoupled bands with their dispersion relations $E_v(\mathbf{k})$ and $E_c(\mathbf{k})$ and the second sum the interband coupling term. Note that we have neglected all intraband interactions and suppressed spin in our model for simplicity. We choose a parabolic band dispersion for the conduction and valence bands which are separated by a bandgap G [63]

$$E_v(\mathbf{k}) = -\frac{\mathbf{k}^2}{2m_v}, \qquad E_c(\mathbf{k}) = \frac{\mathbf{k}^2}{2m_c} + G, \tag{4.2}$$

m_c and m_v denote the effective masses of the two bands. As interaction we choose a screened Coulomb interaction with the dielectric constant ε [63]

$$V_{\mathbf{k_1}\mathbf{k_2}\mathbf{k_3}\mathbf{k_4}} = \int d\mathbf{r_1} d\mathbf{r_2}\, \phi^*_{v\mathbf{k_1}}(\mathbf{r_1}) \phi^*_{c\mathbf{k_2}}(\mathbf{r_2}) \frac{1}{\varepsilon\, |\mathbf{r_1} - \mathbf{r_2}|} \phi_{c\mathbf{k_3}}(\mathbf{r_2}) \phi_{v\mathbf{k_4}}(\mathbf{r_1}). \tag{4.3}$$

The groundstate of this model has only the valence band fully occupied

$$|\Psi_0\rangle = \prod_{\mathbf{k}} c^\dagger_{v\mathbf{k}} |0\rangle, \tag{4.4}$$

where $|0\rangle$ describes the vacuum state with no particles. The energy of this state is $E_0 = \sum_{\mathbf{k}} E_v(\mathbf{k})$. The simplest excited state within this model contains the excitation of one electron from the valence to the conduction band. The corresponding excited wavefunction has the form

$$|\Psi_I\rangle = \sum_{\mathbf{k}\mathbf{k}'} A_{\mathbf{k}\mathbf{k}'} c^\dagger_{c\mathbf{k}} c_{v\mathbf{k}'} |\Psi_0\rangle. \tag{4.5}$$

We can now compute the expansion coefficients $A_{\mathbf{k},\mathbf{k}'}$ such that $|\Psi_I\rangle$ is an eigenstate of the Hamiltonian in equation (4.1). After some manipulation one arrives at

$$\sum_{\mathbf{k}\mathbf{k}'} \left(A_{\mathbf{k}\mathbf{k}'} \left[E_0 - E + E_c(\mathbf{k}) - E_v(\mathbf{k}') \right] - \sum_{\mathbf{k}'',\mathbf{k}'''} V_{\mathbf{k}''\mathbf{k}\mathbf{k}'''\mathbf{k}'} A_{\mathbf{k}''\mathbf{k}'''} \right) c^\dagger_{c\mathbf{k}} c_{v\mathbf{k}'} |\Psi_0\rangle = 0. \tag{4.6}$$

We notice that we obtain the trivial result for this eigenvalue problem for vanishing interaction, that is the energy being increased by promoting one electron from the valence to the conduction band

$$E = E_0 + E_c(\mathbf{k}) - E_v(\mathbf{k}'). \tag{4.7}$$

Including the Coulomb interaction between the two bands gives rise to more interesting solutions. If we approximate the Coulomb matrix elements neglecting the G, G' dependence of the interaction [63]

$$V_{\mathbf{k}\mathbf{k}'\mathbf{k}''\mathbf{k}'''} = \frac{4\pi}{\varepsilon\Omega} \frac{1}{|k'' - k'|^2} \delta_{k''-k',k-k'''}, \tag{4.8}$$

with Ω being the unit cell volume, one finds the following eigenvalue equation in reciprocal space

$$(E - E_0 - G) A_{\mathbf{k},\mathbf{k}'} = (E_v(\mathbf{k}) + E_c(\mathbf{k})) A_{\mathbf{k},\mathbf{k}'} - \sum_{\mathbf{q}} \frac{4\pi}{\varepsilon V \mathbf{q}^2} A_{\mathbf{k}'+\mathbf{q},\mathbf{k}+\mathbf{q}}. \tag{4.9}$$

This equation is equivalent to the two particle Schrödinger equation of two free charged particles with an attractive screened Coulomb interaction and effective masses m_v and

m_c, which in real space reads [63]

$$\left(-\frac{\nabla^2_{\mathbf{r}}}{2m_c} - \frac{\nabla^2_{\mathbf{r}'}}{2m_v} - \frac{1}{\varepsilon|\mathbf{r}-\mathbf{r}'|}\right)\psi(\mathbf{r},\mathbf{r}') = \mathcal{E}\psi(\mathbf{r}.\mathbf{r}'). \tag{4.10}$$

Therefore, we can map this problem to the Hydrogen atom problem by introducing the relative coordinates

$$\mathbf{R} = \frac{m_c\mathbf{r} + m_v\mathbf{r}'}{m_c + m_v}, \quad \mathbf{x} = \mathbf{r} - \mathbf{r}' \tag{4.11}$$

and the effective mass $\mu = \frac{m_v m_c}{m_v + m_c}$ .We find analogously to the Hydrogen problem a Rydberg series for the eigenenergies of these excitons

$$\mathcal{E}_{\mathbf{Q},n} = \frac{\mathbf{Q}^2}{2(m_v + m_c)} - \frac{E_B}{n^2}. \tag{4.12}$$

Here E_B denotes the exciton binding energy

$$E_B = \frac{\mu}{2\varepsilon^2} \tag{4.13}$$

which is the energy one needs to dissociate the exciton into unbound electron-hole pairs. $\mathbf{Q}$ denotes the exciton center of mass momentum. Within this picture the exciton can be interpreted as a bound pair of a positively charge hole and a negatively charged electron in the valence and conduction band. Their energy is

$$\begin{aligned} E_{\text{ex}} &= E_0 + G + \mathcal{E}_{\mathbf{Q},n} \\ &= E_0 + (G + \frac{\mathbf{Q}^2}{2(m_v + m_c)} - E_B) \end{aligned} \tag{4.14}$$

and the lowest excited excitonic state has the energy $E_{\text{ex},0} = E_0 + (G - E_B)$. Therefore, excitonic states have a lower energy than free electron-hole pairs (see. Fig.4.2).

As a final remark I should highlight that the excitonic binding energy, which will play an important role in the EI groundstate, is inversely proportional to the dielectric screening constant ε. This means that the excitons are more tightly bound the more unscreened the interaction between electron and hole is. This is the reason why low dimensional systems, in which the electric field in one or more spatial directions is unscreened, exhibit very strongly bound excitons with high excitonic binding energies.

4.2 A one dimensional Excitonic Insulator model

To understand the basic concepts of the EI, I will review the most basic model that contains an excitonic insulating groundstate and highlight its most important spectroscopic features. The idea of the EI has been introduced in a series of works by Mott, Kohn, Keldysh, Kozlov and Maksimov [13–19]. As such the following paragraph will closely

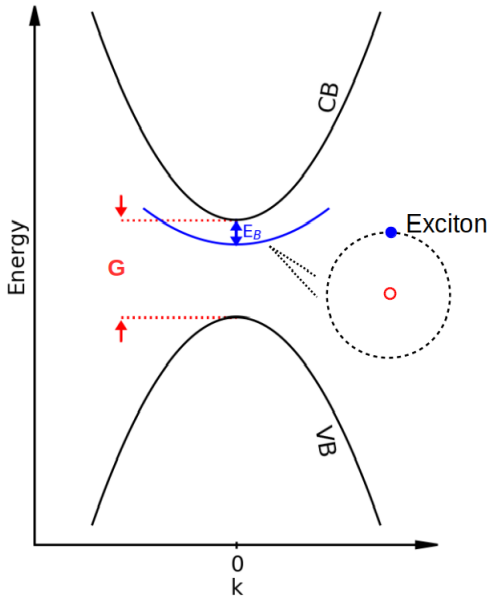

Fig. 4.2 Schematic illustration of the exciton level in a bandstructure.

follow the ideas of one of these references by Jerome et al. [18].
We consider a two level Hamiltonian with one valence band a and one conduction band b interacting via a Coulomb interaction term [18, 102]

$$H = \sum_k \epsilon_a(k) a_k^\dagger a_k + \sum_k \epsilon_b(k) b_k^\dagger b_k + \frac{1}{2} V(q)\rho(q)\rho(-q) \tag{4.15}$$

with $V(q) = \frac{4\pi}{\varepsilon q^2}$ and $\rho(q) = \sum_k a_{k+q}^\dagger a_k + b_{k+q}^\dagger b_k$. It is convenient to tranform this Hamiltonian into position space and it reads [18]

$$H = \sum_{i=a,b} \int \psi_i^\dagger(x)\epsilon_i(x)\psi_i(x) + \frac{1}{2}\int dx dx' \rho(x)\rho(x')V(x-x') \tag{4.16}$$

with

$$\begin{aligned} \rho(x) &= \psi_a^\dagger(x)\psi_a(x) + \psi_b^\dagger(x)\psi_b(x) \\ V(x-x') &= \text{ Coulomb interaction } = \frac{1}{|x-x'|} \end{aligned} \tag{4.17}$$

and $\psi_a(x)$ and $\psi_b(x)$ being the field operators of the two bands a and b with dispersion $\epsilon_a(x)$ and $\epsilon_b(x)$. For now these dispersions are arbitrary, but shall be chosen later for simplicity to describe either a semimetallic or a small bandgap semiconducting system with a parabolic dispersion and a bandgap (bandoverlap) G

$$\epsilon_b(k) = \frac{G}{2} + \frac{k^2}{2m_a} \qquad \epsilon_a(k) = -\frac{G}{2} - \frac{k^2}{2m_b}. \tag{4.18}$$

To analyze the spectroscopic features it is instructive to define, in similarity to the Bardeen-Cooper-Schrieffer (BCS) theory of superconductivity, the diagonal parts of the one-particle Greens function as [18, 103]

$$\begin{aligned} G_a(1,2) &= -i\langle 0|\mathcal{T}\left(\psi_a(1)\psi_a^\dagger(2)\right)|0\rangle \\ G_b(1,2) &= -i\langle 0|\mathcal{T}\left(\psi_b(1)\psi_b^\dagger(2)\right)|0\rangle \end{aligned} \tag{4.19}$$

and also the off-diagonal parts F as

$$\begin{aligned} F(1,2) &= -i\langle 0|\mathcal{T}\left(\psi_b(1)\psi_a^\dagger(2)\right)|0\rangle \\ F^\dagger(1,2) &= -i\langle 0|\mathcal{T}\left(\psi_a(1)\psi_b^\dagger(2)\right)|0\rangle. \end{aligned} \tag{4.20}$$

The latter are sometimes also called anomalous Greens functions and are expected to be non-zero in the excitonic insulating phase. Note that I have adopted the notation introduced in chapter 1, which means that $1 = (x_1, t_1)$ and $2 = (x_2, t_2)$ and that we are working in the Heisenberg notation of operators. The equation of motion for the two Greens functions G_a and G_b can be obtained as usual using the canonical commutation relation for the fermionic field operators $\psi_a(x)$ and $\psi_b(x)$

$$\left[\psi_i(1), \psi_j^\dagger(2)\right]_+ = \delta_{i,j}\ \delta(1,2) \quad , \qquad i,j = a,b \tag{4.21}$$

and the Heisenberg equation of motion for operators. With these ingredients we find

$$\begin{aligned} &\left[\frac{d}{dt_1} - \epsilon_a(1)\right] G_a(1,2) \\ &\quad = \delta(1,2) + i\int d3V(1,3)\langle\mathcal{T}\left([\psi_a^\dagger(3)\psi_a(3) + \psi_b^\dagger(3)\psi_b(3)]\psi_a(1)\psi_a^\dagger(2)\right)\rangle \end{aligned} \tag{4.22}$$

$$\begin{aligned} &\left[\frac{d}{dt_1} - \epsilon_b(1)\right] G_b(1,2) \\ &\quad = \delta(1,2) + i\int d3V(1,3)\langle\mathcal{T}\left([\psi_a^\dagger(3)\psi_a(3) + \psi_b^\dagger(3)\psi_b(3)]\psi_b(1)\psi_b^\dagger(2)\right)\rangle. \end{aligned} \tag{4.23}$$

Using Wick's theorem we can factorize the four operator correlation functions. Doing this, we obtain three non-vanishing terms. Two are the standard Hartree-Fock-terms which we will consider to be included in the one particle spectrum $\epsilon_a(1)$ and $\epsilon_b(1)$ already. Therefore we will neglect it here. The second non-vanishing term consists of the anomalous Green's functions F and $F^\dagger$ [18, 104]

$$\left[\frac{d}{dt_1} - \epsilon_a(1)\right] G_a(1,2) = \delta(1,2) + i\int d3V(1,3)F^\dagger(1,3)F(3,2) \tag{4.24}$$

$$\left[\frac{d}{dt_1} - \epsilon_b(1)\right] G_b(1,2) = \delta(1,2) + i\int d3V(1,3)F^\dagger(3,2)F(1,3). \tag{4.25}$$

Therefore, to compute the Green's functions G_a and G_b we have to compute also the equations of motion for F and $F^\dagger$. Performing a similar calculation as for G we obtain

$$\left[i\frac{d}{dt_1} - \epsilon_b(1)\right] F(1,2) = -i\int d3V(1,3)\langle\mathcal{T}\left(\psi_a^\dagger(3)\psi_a(3)\psi_b(1)\psi_a^\dagger(2)\right)\rangle \tag{4.26}$$

$$\left[i\frac{d}{dt_1} - \epsilon_a(1)\right] F^\dagger(1,2) = -i\int d3V(1,3)\langle\mathcal{T}\left(\psi_b^\dagger(3)\psi_b(3)\psi_a(1)\psi_b^\dagger(2)\right)\rangle \tag{4.27}$$

and after factorization with Wick's theorem

$$\left[i\frac{d}{dt_1} - \epsilon_b(1)\right] F(1,2) = i\int d3V(1,3)F(1,3)G_a(3,2) \tag{4.28}$$

$$\left[i\frac{d}{dt_1} - \epsilon_a(1)\right] F^\dagger(1,2) = i\int d3V(1,3)F^\dagger(1,3)G_b(3,2). \tag{4.29}$$

Summarizing the four equations of motion for the Green's functions, we obtain [18]

$$\left[\frac{d}{dt_1} - \epsilon_a(1)\right] G_a(1,2) = \delta(1,2) + i\int d3V(1,3)F^\dagger(1,3)F(3,2) \tag{4.30}$$

$$\left[\frac{d}{dt_1} - \epsilon_b(1)\right] G_b(1,2) = \delta(1,2) + i\int d3V(1,3)F^\dagger(3,2)F(1,3) \tag{4.31}$$

$$\left[i\frac{d}{dt_1} - \epsilon_b(1)\right] F(1,2) - i\int d3V(1,3)F(1,3)G_a(3,2) = 0 \tag{4.32}$$

$$\left[i\frac{d}{dt_1} - \epsilon_a(1)\right] F^\dagger(1,2) - i\int d3V(1,3)F^\dagger(1,3)G_b(3,2) = 0 \tag{4.33}$$

and notice, that these form a closed set of equations which can be solved. This is done by Fourier transforming

$$G(1,2) = \sum_k \int \frac{d\omega}{2\pi} G(k,\omega)e^{k(x_1-x_2)-\omega(t_1-t_2)}, \tag{4.34}$$

where we have used that G depends only on the differences of t_1 and t_2. Using equation (4.34), one obtains the algebraic equations [18]

$$[\omega - \epsilon_a(k)]\, G_a(k,\omega) - \Delta^\dagger(k)F(k,\omega) = 1 \tag{4.35}$$

$$[\omega - \epsilon_b(k)]\, G_b(k,\omega) - \Delta(k)F^\dagger(k,\omega) = 1 \tag{4.36}$$

$$[\omega - \epsilon_b(k)]\, F(k,\omega) - \Delta(k) G_a(k,\omega) = 1 \tag{4.37}$$

$$[\omega - \epsilon_a(k)]\, F_a^\dagger(k,\omega) - \Delta^\dagger(k) G_b(k,\omega) = 1, \tag{4.38}$$

where we have defined the so called Gap function in analogy to BCS theory as [18]

$$\Delta(k) = \sum_{k'} \int \frac{d\omega}{2\pi} V(k-k') F(k',\omega'). \tag{4.39}$$

Solving the algerebraic equations (4.35-4.38) we obtain [18]

$$G_a(k,\omega) = \frac{1}{\omega - \epsilon_a(k) - \frac{|\Delta(k)|^2}{\omega - \epsilon_b(k)}} \tag{4.40}$$

$$G_b(k,\omega) = \frac{1}{\omega - \epsilon_b(k) - \frac{|\Delta(k)|^2}{\omega - \epsilon_a(k)}} \tag{4.41}$$

$$F(k,\omega) = \frac{\Delta(k)}{(\omega - \epsilon_a(k))\,(\omega - \epsilon_b(k)) - |\Delta(k)|^2} \tag{4.42}$$

$$F^\dagger(k,\omega) = \frac{\Delta^\dagger(k)}{(\omega - \epsilon_a(k))\,(\omega - \epsilon_b(k)) - |\Delta(k)|^2}. \tag{4.43}$$

From these we can easily read off the self-energy contribution to the Greens functions G_a and G_b as

$$\Sigma_a(k,\omega) = \frac{|\Delta(k)|^2}{\omega - \epsilon_b(k)} \tag{4.44}$$

$$\Sigma_b(k,\omega) = \frac{|\Delta(k)|^2}{\omega - \epsilon_a(k)} \tag{4.45}$$

and notice, that we only get a change in the eigenvalues of the interacting system from the non-interacting system, if the gap function is non-zero. Similarly the anomalous Green's functions F and $F^\dagger$ are only non-trivial for finite Δ. Therefore, Δ can be considered as the order parameter of the EI transition in this model. I will discuss it in more detail later. For now let me compute how the energy spectrum of the system changes in the EI phase. To this end I compute the poles for the Green's functions, which are identical for G_a and G_b and obtain

$$\omega_\pm(k) = \frac{\epsilon_a(k) + \epsilon_b(k) \pm \sqrt{[\epsilon_a(k) - \epsilon_b(k)] + 4|\Delta(k)|^2}}{2}. \tag{4.46}$$

For a simple parabolic dispersion for the non-interacting bands a and b

$$\epsilon_b(k) = \frac{G}{2} + \frac{k^2}{2m_a} \qquad \epsilon_a(k) = -\frac{G}{2} - \frac{k^2,}{2m_b} \tag{4.47}$$

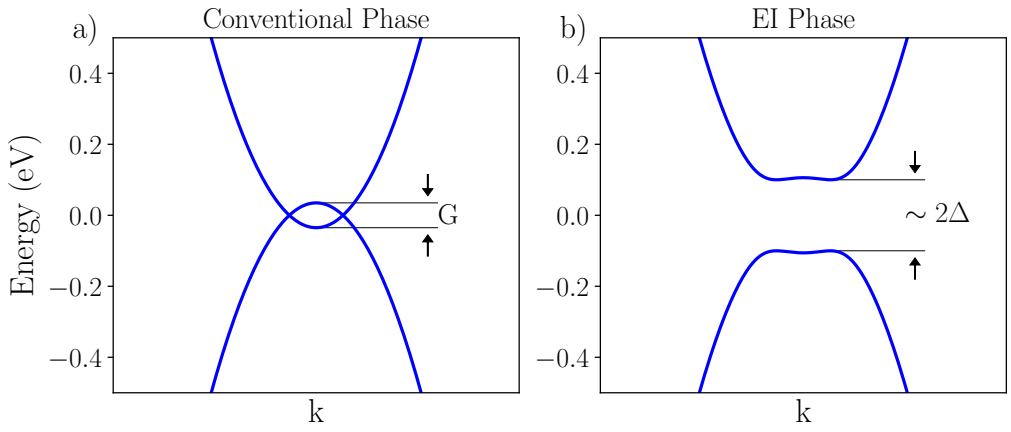

Fig. 4.3 a) Conventional semimetallic phase with $\Delta = 0$, $G = -70\,\text{meV}$ and $m_s = m_b$. b) EI phase for $G = -70\,\text{meV}$ and $\Delta = 100meV$. Due to the hybridisation between valence and conduction bands the two states display the characteristic M-shaped bands.

where G is the bandgap, the dispersion $\omega_\pm$ is displayed in figure 4.3. We notice two main features in the EI phase. First the hybridisation between conduction and valence bands can lead to the formation of flat bands, which has been considered as the characteristic spectroscopic feature in the EI phase in ARPES measurements. Second the bandgap in the EI phase is in first order proportional to $2\Delta(k)$, which explains why Δ is called the Gap function. Let us now investigate under which circumstances Δ is non-zero, which means that there exists an EI phase.

Gap Function

The gap function Δ_k has been defined in equation (4.39) as [18]

$$\Delta(k) = \sum_{k'} \int \frac{d\omega}{2\pi} V(k-k') F(k', \omega'). \tag{4.48}$$

Substituting the solution for $F(k, \omega)$ and performing the integration in ω we can simplify it to

$$\Delta(k) = \sum_{k'} V(k-k') \frac{\Delta(k')}{\sqrt{2(d^2(k') + |\Delta((k')|^2)}}, \tag{4.49}$$

where we have defined $d(k) = \frac{1}{2}(\epsilon_b(k) - \epsilon_a(k))$ as the difference between conduction and valence band energy ϵ_b and ϵ_a. To understand when the gap function becomes non-zero it is instructive to define [18]

$$\phi(k) = \frac{\Delta(k)}{2\sqrt{d^2(k) + |\Delta(k)|^2}} \tag{4.50}$$

and rewrite the gap equation (4.49) as [18]

$$2\sqrt{d^2(k) + |\Delta(k)|^2}\ \phi(k) = \sum_{k'} V(k-k')\phi(k'). \tag{4.51}$$

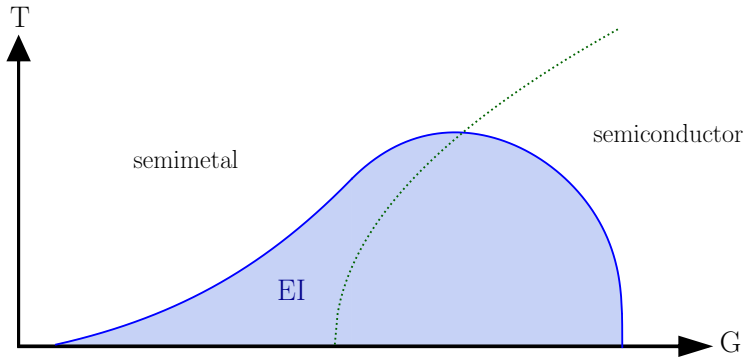

Fig. 4.4 Sketch of the phase diagram adapted from [81, 105]. It shows the characteristic dome shaped structure and falls of rapidly on the semiconducting side as G approaches the 0K bandgap. The green dotted line highlights the zero bandgap line in the trivial phase.

For our ansatz using a parabolic dispersion for both valence and conduction bands (4.47) this becomes

$$2\sqrt{(G+\frac{k^2}{\mu})^2+|\Delta(k)|^2}\;\phi(k)=\sum_{k'}V(k-k')\phi(k') \tag{4.52}$$

with $\mu=\frac{m_a m_b}{m_a+m_b}$ being the reduced mass. By comparing this with the Schrödinger equation for an exciton in its lowest energy state

$$(\frac{k^2}{2\mu}+|E_B|)\phi(k)=\sum_{k'}V(k-k')\phi(k') \tag{4.53}$$

we can see that positive solutions for $|\Delta(k)|$ exist only for excitonic binding energies E_B being greater than the Gap G [15, 18]. Therefore, this is commonly used as necessary criterium for the existence of such a phase transition in theory calculations [24,25,85]. Model calculations show that the EI phase diagram has a dome shaped structure that falls off asymmetrically in the semiconducting and the semimetallic side [81, 105]. A sketch of the phase diagram is shown in figure 4.4. As closing remark for this chapter I would like to highlight again the similarity between the EI calculation, which we have just performed and the BCS theory calculation. In a similar manner, the above results can also be obtained by diagonalizing the EI Hamiltonian (4.15) using a Bogoliubov transformation [18]

$$\begin{aligned}\alpha(k)&=u(k)a(k)-v(k)b(k)\\ \beta(k)&=v(k)^*a(k)-u^*(k)b(k).\end{aligned} \tag{4.54}$$

The groundstate in the excitonic insulator phase then becomes, in similarity to BCS theory [18],

$$\begin{aligned} |\Psi_0\rangle &= \prod_k \alpha^\dagger(k)|0\rangle \\ &= \prod_k \left(u^*(k) - v^*(k)b^\dagger(k)a(k)\right)|\Phi_0\rangle \end{aligned} \tag{4.55}$$

with $|\Phi_0\rangle = \prod_k a^\dagger(k)|0\rangle$ being the conventional groundstate of the two band Hamiltonian [18] and

$$\begin{aligned} u(k) &= \left[\frac{1}{2}(1 + \frac{d(k)}{\sqrt{d^2(k) + |\Delta(k)|^2}})\right]^{\frac{1}{2}} \\ v(k) &= \left[\frac{1}{2}(1 - \frac{d(k)}{\sqrt{d^2(k) + |\Delta(k)|^2}})\right]^{\frac{1}{2}} \frac{\Delta(k)}{|\Delta(k)|}. \end{aligned} \tag{4.56}$$

In this notation the excitonic nature of the groundstate becomes even more evident (equation (4.55)). We see that the new BCS-like groundstate of the system consists of electron-hole pairs which are created from the conventional groundstate.

4.3 Candidate Materials

In the previous section we have discussed the basic ideas of the EI using a simple two band model calculation. To realize such a system one has to identify suitable candidate materials. We have seen that the necessary condition for a material to be excitonic insulating is that its excitonic binding energy is bigger than the electronic bandgap. The excitonic binding energy for standard bulk systems is usually of the order of few tenth of meV and therefore one needs materials with a very small bandgap to realize an EI state. However, it has been shown by Keldysh that the excitonic insulating state becomes thermodynamically unstable for binding energies too close to the bandgap if one includes higher order Many Body effects. Therefore, it has been deemed desirable to search for candidate materials with high excitonic binding energies and ideally spatially separated electron and hole particles to reduce these Many Body effects.

This is the reason why the EI has become a very active field of research in the last ten years with the introduction of layered materials bound by van der Waals forces [20, 31, 106] and low dimensional materials such as TMD monolayers [24, 25]. These provide a much better platform to host an EI, because the excitonic binding energy scales inverse proportional with the dielectric screening $E_B \propto \frac{1}{\varepsilon}$. This can lead to binding energies that are a magnitude bigger than in common bulk materials, due to the reduced screening in the out of plane direction. For layered van der Waals materials excitonic binding energies around 100 meV have been measured [69,107,108] and these can even increase up to a few hundred meV for monolayer materials such as the monolayer transition metal dichalco-

genides WSe_2 and MoS_2 [109–113]. Furthermore, the possibility to arbitrarily stack different of these materials into heterostructures [7] allows for the possibility to create excitonic states with electrons and holes trapped in different layers and thus separating them spatially, while maintaining a strong Coulomb interaction between them [114,115]. Currently debated TMD candidates to host an EI are bulk MoS_2 [85], where the bandgap is controlled via pressure, or T′-MoS_2 [25] and WTe_2 [116] monolayers. Further potential hetero bilayer candidates have also been proposed in a systematic material study by Gupta et al [22].

Another very new class of candidate materials to potentially host an EI are double layer systems and Moire systems. In double layer systems two monolayers of semiconducting materials are separated by a hexagonal boron nitride layer [23,117]. This allows to separate electron in holes in each of the two layers which naturally gives rise to very stable excitons. The advantage of this system is that the bandgap of the double layer can be systematically controlled through gating and therefore, upon sufficient closing of the electronic bandgap, a phase transition to an EI insulator may be induced [23]. Additionally, the single layers can be substituted with a Moire bilayer. This allows not only to confine the electron and hole to the different layers, but also to trap the excitons in the Moire potentials which act as a potential well for the electrons [84]. This has led to a new very controlled way to investigate the EI in such systems [23,84,117].

In this thesis I will be discussing the most debated candidate material which is Ta_2NiSe_5 [28,29]. It falls into the class of layered van der Waals materials and is considered to have a quasi one-dimensional character, because the bandgap dynamics in this material are believed to be governed by in-plane parallel Tantalum and Nickel chains. The underlying idea of this candidate is that electrons and holes are localized along the different chains and give rise to an excitonic insulating transition. A detailed discussion of this EI candidate is shown in the following Publications III-V.

4.4 Publication III: Nature of Symmetry Breaking at the Excitonic Insulator Transition: Ta_2NiSe_5

State of the Art

At the time this paper has been published, TNSe had recently emerged as an excitonic insulator candidate. While it was experimentally known that the material undergoes a structural phase transition at the critical temperature of T=326K with the formation of a bandgap and flat bands [20, 30, 31, 98, 106], the exact mechanism and microscopical order parameter of the conjectured EI transition has been unknown. The goal of this publication is to investigate if this material can host an excitonic instability and to identify the microscopical order parameter of such a transition. For this investigation we have taken a combined approach using an extended Hubbard model with ab-initio input in form of Wannier-functions.

Main Findings

The main finding of this publication is that the proposed model indeed can host an excitonic instability, which we have defined as the formation of a charge density that breaks the lattice symmetries and therefore could trigger the structural transition. Such an instability arises due to a symmetry forbidden hybridisation of Tantalum and Nickel states of neighbouring one-dimensional chains, which lead to a bandgap opening similar to the one observed in prior ARPES experiments. The hybridisation has an excitonic nature and allows to define the order parameter of the transition. With this we have computed the phase diagram of the instability as a function of on-site and next nearest neighbour interaction parameters U and V. It turns out, that the phase space region of the excitonic instability is very narrow and cRPA calculations estimating U and V for the real material suggest that it indeed lies outside of the instability region. This suggests that more ab-initio calculations are needed to investigate if the transition triggered by an excitonic instability is realized in the real material.

Status and Publication Details

This paper has been published in Physical Review Letter [94]. This publication has a Supplementary Information that is being published at `https://doi.org/10.1038/s41563-022-01285-3` and not contained in this thesis.

Contribution

I performed the ab-initio calculations (computation of bandstructure and geometry optimization) and contributed to the development of the models used in this publication. All authors have contributed to the analysis of the data and the creation of the manuscript.

Nature of Symmetry Breaking at the Excitonic Insulator Transition: Ta_2NiSe_5

Giacomo Mazza,[1,2,3,*,†] Malte Rösner,[4,*,‡] Lukas Windgätter,[5] Simone Latini,[5] Hannes Hübener,[5] Andrew J. Millis,[6,7] Angel Rubio,[5,6,8] and Antoine Georges[3,6,2,1,§]

[1]*Department of Quantum Matter Physics, University of Geneva, Quai Ernest-Ansermet 24, 1211 Geneva, Switzerland*
[2]*CPHT, CNRS, Ecole Polytechnique, IP Paris, F-91128 Palaiseau, France*
[3]*Collège de France, 11 place Marcelin Berthelot, 75005 Paris, France*
[4]*Radboud University, Institute for Molecules and Materials, Heijendaalseweg 135, 6525 AJ Nijmegen, Netherlands*
[5]*Max Planck Institute for the Structure and Dynamics of Matter, Luruper Chaussee 149, 22761 Hamburg, Germany*
[6]*Center for Computational Quantum Physics, Flatiron Institute, New York, New York 10010, USA*
[7]*Department of Physics, Columbia University, New York, New York 10027, USA*
[8]*Nano-Bio Spectroscopy Group, Departamento de Física de Materiales, Universidad del País Vasco, 20018 San Sebastian, Spain*

(Received 26 November 2019; accepted 23 April 2020; published 12 May 2020)

Ta_2NiSe_5 is one of the most promising materials for hosting an excitonic insulator ground state. While a number of experimental observations have been interpreted in this way, the precise nature of the symmetry breaking occurring in Ta_2NiSe_5, the electronic order parameter, and a realistic microscopic description of the transition mechanism are, however, missing. By a symmetry analysis based on first-principles calculations, we uncover the *discrete* lattice symmetries which are broken at the transition. We identify a purely electronic order parameter of excitonic nature that breaks these discrete crystal symmetries and contributes to the experimentally observed lattice distortion from an orthorombic to a monoclinic phase. Our results provide a theoretical framework to understand and analyze the excitonic transition in Ta_2NiSe_5 and settle the fundamental questions about symmetry breaking governing the spontaneous formation of excitonic insulating phases in solid-state materials.

DOI: 10.1103/PhysRevLett.124.197601

Introduction.—Spontaneous symmetry breaking is a fundamental organizing principle for understanding the emergence of long-range order. Identifying the underlying symmetry breaking is thus a key step in the characterization of the ordered phase. This can be an elusive task when the symmetry breaking field cannot be directly tuned experimentally or when different types of ordering are coupled. The so-called *excitonic insulator* is a prominent example of such an elusive state of matter. This phase [1–4] has been identified with the spontaneous condensation of excitons (bound electron-hole pairs) stemming from the Coulomb attraction between electrons and holes in the conduction and valence bands. Excitonic condensation has been observed and intensively investigated in specially designed devices such as bilayer quantum Hall systems [5–9] or by photo stimulation of electron-hole pairs [10–12]. In contrast, spontaneous excitonic condensation in bulk materials still remains an open question and its detection a major challenge.

Ta_2NiSe_5 has been proposed as a candidate material hosting a homogeneous excitonic condensate [13–16], i.e., without charge or other nonzero momentum order [17–19]. Ta_2NiSe_5 undergoes a structural transition from a high-temperature orthorhombic to a low-temperature monoclinic phase at $T_s \simeq 328$ K [13,20,21]. Proposed evidence for excitonic condensation occurring simultaneously with the structural transition includes a characteristic flattening of the valence band close to the Γ point [14,15,22], the opening of a gap in the electronic spectrum [16,23,24], and coherent oscillations reminiscent of the excitation of an amplitude mode of the condensate [25]. Due to its characteristic chain structure Ta_2NiSe_5 has so far been interpreted as a quasi one-dimensional excitonic insulator [26,27] and Kaneko *et al.* [27] proposed a scenario in which the coupling of the excitonic condensate with phonons gives rise to a combined excitonic and structural instability.

The following symmetry considerations, however, call into question the very notion of excitonic condensation in the solid-state context. Condensation implies the breaking of a *continuous* symmetry. In the case of excitonic condensation this would be the breaking of the $U_X(1)$ symmetry related to the conservation of *relative* charge between valence and conduction states. Bulk materials, however, generally lack such a $U_X(1)$ symmetry due to the hybridization between conduction and valence bands. The only continuous symmetry being present is the one related to the *global* charge conservation $U_N(1)$. Nonetheless, internal *discrete* symmetries of the solid, such as crystal symmetries, can result in an approximate realization of the relative charge conservation with symmetry-forbidden hybridizations in particular regions of the Brillouin zone. Therefore, we propose here that the spontaneous hybridization introduced

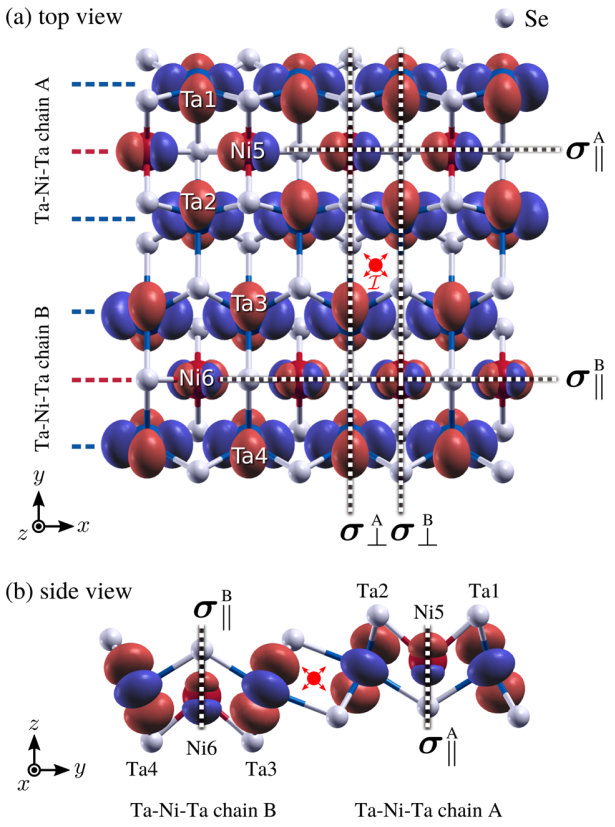

FIG. 1. Top and side view of the Ta_2NiSe_5 lattice structure including isosurfaces of Wannier wave functions localized at Ta and Ni positions (red and blue correspond to opposite MLFW-amplitude signs). Dashed lines (red dots) indicate reflection (inversion) symmetries.

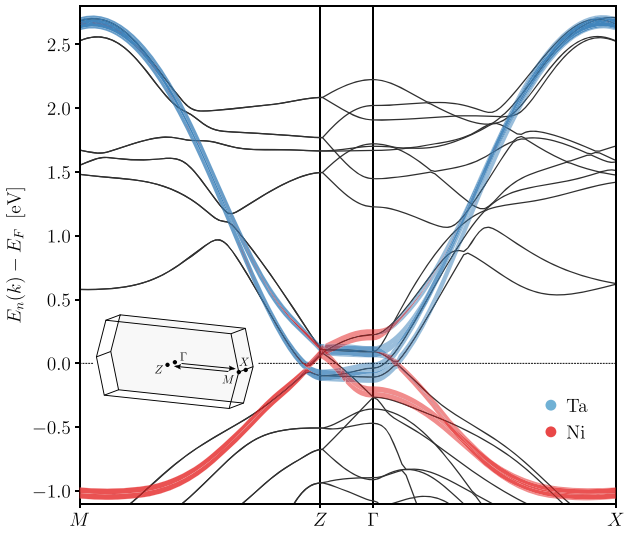

FIG. 2. *Ab initio* band structure (black lines) together with a fat-bands representation of the Wannier model. Thick blue (red) lines represent Ta (Ni) contributions as resulting from the Wannier model.

by an excitonic instability represents a general mechanism for breaking internal discrete symmetries rather than a condensation phenomenon resulting from the breaking of a continuous symmetry.

We demonstrate this concept for the case of Ta_2NiSe_5 by uncovering the symmetries that are broken by an excitonic instability. To this end, we construct a minimal yet realistic model for Ta_2NiSe_5 including its electronic band structure and electron-electron interactions from first principles. We show the existence of an electronic instability of excitonic origin leading to an electronic phase that breaks a set of discrete symmetries of the high-temperature orthorombic phase and is compatible with the low-temperature monoclinic structure. This analysis settles the fundamental question of identifying which symmetries are broken at the excitonic transition and is therefore of general relevance to the understanding and the eventual control of such transitions in Ta_2NiSe_5 and solid-state materials in general.

Crystal symmetries in Ta_2NiSe_5.—We perform DFT calculations in the high-temperature orthorhombic phase, with $a \simeq 3.51$ Å and $b \simeq 15.79$ Å being the lattice constants in x and y directions of the Bravais lattice [28]. This unit-cell is composed of two formula units with atoms arranged in two parallel Ta-Ni-Ta chains (A and B) along the x direction. The chains are shifted by half a lattice constant along x and displaced along z, which results in four reflection symmetries with planes parallel and perpendicular to the Ta-Ni-Ta chains ($\boldsymbol{\sigma}_{\parallel/\perp}^{A/B}$) and one inversion symmetry point $\mathcal{I}$, as depicted in Fig. 1. Based on these *ab initio* calculations, we construct six d_{xz}-like maximally localized Wannier functions (MLWF) centered at the Ta and Ni positions, which are shown in Fig. 1. In each Ta-Ni-Ta chain the Ta-centered d_{xz} orbitals, $\varphi_{\mathrm{Ta}}(\vec{R})$, are aligned along the chains and tilted around the x axis following the Ta-Se bonds [see Fig. 1(b)]. The Ni-centered d_{xz} MLWFs, $\varphi_{\mathrm{Ni}}(\vec{R})$, are also parallel to the Ta-Ni-Ta chains, but rotated by 45° around the y axis. The Se contributions are thus indirectly accounted for by deforming and rotating the d_{xz} orbitals.

The reflection symmetries act differently on the Ta- and Ni-centered MLWFs. While the $\varphi_{\mathrm{Ta}}(\vec{R})$ MLWFs are unaffected by all reflections, $\varphi_{\mathrm{Ni}}(\vec{R})$ change sign under $\boldsymbol{\sigma}_{\perp}$. It follows that the intrachain Ta-Ta and Ni-Ni hoppings $t_{\mathrm{TaTa/NiNi}}(\vec{R}) = \langle \varphi_{\mathrm{Ta/Ni}}^{A/B}(\vec{R})|\hat{H}|\varphi_{\mathrm{Ta/Ni}}^{A/B}(0)\rangle$ have opposite signs. We find $t(\vec{0})_{\mathrm{TaTa}} \approx -640$ meV and $t(\vec{0})_{\mathrm{NiNi}} \approx 250$ meV, which are respectively mainly responsible for the conduction and valence bands dispersions in the $\overline{MZ}$ and $\overline{\Gamma X}$ directions of the Brillouin zone. These bands are about 2.5 and 1.5 eV wide with predominant Ta (blue) and Ni (red) character as visible in the Wannier-interpolated band structure in Fig. 2. Conduction and valence bands overlap along $\overline{Z\Gamma}$ where the bands become much less dispersive and are mainly characterized by bonding and antibonding splittings of the Ta- and Ni-states between the two Ta-Ni-Ta chains.

Importantly, hopping matrix elements between Ta- and Ni-like states within the chains are *not* forbidden by any symmetry. In fact, even in the orthorhombic phase we obtain non-zero matrix elements between Ta- and Ni-MLWFs within the same chain $t_{\mathrm{TaNi}}(\vec{R})$. Specifically, $t_{\mathrm{TaNi}}(\vec{0}) \approx 36$ meV which decreases with the distance R_x along the chains. This result is universal to all tested DFT exchange-correlation functionals [28] and shows that this kind of Ta-Ni hybridization cannot spontaneously form due to exciton condensation below a critical temperature [26,27,38].

In contrast to that, we will show below that the excitonic instability can break the crystal symmetries that constrain Ta-Ni hybridization in the high-temperature phase. In particular, the reflection symmetries $\boldsymbol{\sigma}_{\perp}^{A/B}$ constrain the Ta-Ni hoppings to change sign under $\boldsymbol{\sigma}_{\perp}^{A/B}$ implying that the Wannier Hamiltonian averaged along the x direction is block diagonal with respect to the Ta and Ni states

$$\hat{H}(k_x = 0, R_y) \equiv \sum_{R_x} \hat{H}(R_x, R_y) = \begin{pmatrix} \hat{h}_{\mathrm{Ta}}(R_y) & \hat{0} \\ \hat{0} & \hat{h}_{\mathrm{Ni}}(R_y) \end{pmatrix}. \tag{1}$$

In momentum space, $t_{\mathrm{TaNi}}(k_x = 0, k_y) = 0$ so that the bands along the $\overline{Z\Gamma}$ path have purely Ta or Ni character, Fig. 2. Therefore, any excitonic instability resulting from a spontaneous Ta-Ni hybridization must break the $\boldsymbol{\sigma}_{\perp}^{A/B}$ symmetry and show up along the $\overline{Z\Gamma}$ direction. We provide evidence of such an instability by considering the effect of the electron interactions in a minimal model derived from the above symmetry analysis.

Minimal model.—We consider a two-dimensional lattice with six atoms per unit cell. The electronic Hamiltonian

$$\hat{\mathcal{H}} = \hat{H}_{\mathrm{hop}} + \hat{H}_U + \hat{H}_V \tag{2}$$

includes a hopping term $\hat{H}_{\mathrm{hop}}$, a local $\hat{H}_U$ Coulomb interaction term, and nearest-neighbor $\hat{H}_V$ one. We define $\Psi_{\vec{R}\sigma}^{\dagger} \equiv (c_{1\sigma}^{\dagger}(\vec{R}), \ldots, c_{6\sigma}^{\dagger}(\vec{R}))$, where $c_{j\sigma}^{\dagger}(\vec{R})$ creates an electron with spin σ in a localized orbital on the jth atom (labels in Fig. 1) of the unit cell $\vec{R}$.

$$\hat{H}_{\mathrm{hop}} = \sum_{\vec{R}\sigma} \sum_{\vec{\delta}} \Psi_{\vec{R}+\vec{\delta}\sigma}^{\dagger} \mathbf{T}(\vec{\delta}) \Psi_{\vec{R}\sigma} \tag{3}$$

contains intracell, $\mathbf{T}(\vec{0})$, as well as intercell, $\mathbf{T}(\pm a, \pm b)$, terms. The matrix elements are chosen consistently with the above symmetry requirement and in order to reproduce the main features of the Wannier band structure [28].

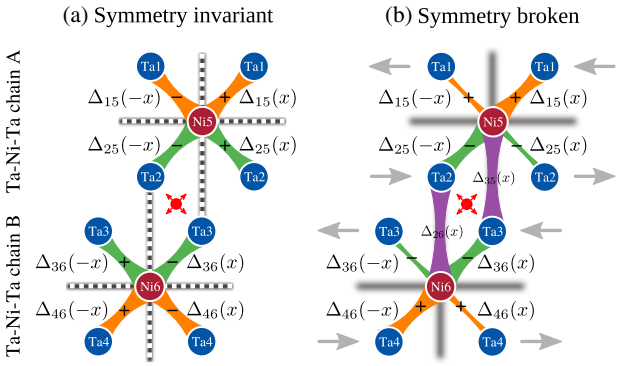

FIG. 3. Scheme of nearest neighbor Ta-Ni hybridization in the symmetry invariant (a) and symmetry-broken (b) phases. Thickness of the lines connecting the atoms indicates the absolute value of the hybridization.

The electrons interact through a local Hubbard-like term

$$\hat{H}_U = U \sum_{\vec{R}} \sum_{j} \hat{n}_{j\uparrow}(\vec{R}) \hat{n}_{j\downarrow}(\vec{R}), \tag{4}$$

where we assumed the same U for the six atoms, as supported by a constrained RPA [39] analysis of the Coulomb matrix elements ($U_{\mathrm{Ta}} \approx 2.1$ eV, $U_{\mathrm{Ni}} \approx 2.4$ eV). The next leading terms are intrachain density-density interactions between neighboring Ta and Ni atoms ($V \approx 0.9$ eV)

$$\begin{aligned} \hat{H}_V = {} & V \sum_{j=1,2} \sum_{\vec{R}\sigma\sigma'} [\hat{n}_{j\sigma}(\vec{R}) + \hat{n}_{j\sigma}(\vec{R} + \vec{\delta}_x)] \hat{n}_{5\sigma'}(\vec{R}) \\ & + V \sum_{j=3,4} \sum_{\vec{R}\sigma\sigma'} [\hat{n}_{j\sigma}(\vec{R}) + \hat{n}_{j\sigma}(\vec{R} - \vec{\delta}_x)] \hat{n}_{6\sigma'}(\vec{R}). \end{aligned} \tag{5}$$

The symmetries of the Hamiltonian are revealed by an investigation of the intrachain Ta-Ni hybridization as a function of the distance along x between the Ta and Ni atoms

$$\Delta_{ij}(x) = \langle \underbrace{c_i^{\dagger}(R_x, 0)}_{\text{Ta site}} \underbrace{c_j(0,0)}_{\text{Ni site}} \rangle, \tag{6}$$

where $i = 1, 2(3, 4)$ and $j = 5(6)$ label the Ta and Ni states, respectively, for the $A(B)$ chain. For each chain, x is defined by taking the Ni atom in that chain as origin, so that $x = R_x \mp a/2$ ($-$ for A and $+$ for B). We have dropped the spin index as we focus on the spin-singlet case. For the A chain, $\Delta_{15}(x)$ and $\Delta_{25}(x)$, i.e., the hybridizations between the lower and upper Ta with the central Ni state of the A chain, transform as

$$\boldsymbol{\sigma}_{\perp}^{A} \Delta_{15}(x) = -\Delta_{15}(-x), \qquad \boldsymbol{\sigma}_{\parallel}^{A} \Delta_{15}(x) = \Delta_{25}(x), \tag{7}$$

so that $\Delta_{15}(x) = -\Delta_{15}(-x)$ and $\Delta_{15}(x) = \Delta_{25}(x)$, as depicted in Fig. 3(a). Similarly, reflection symmetries for

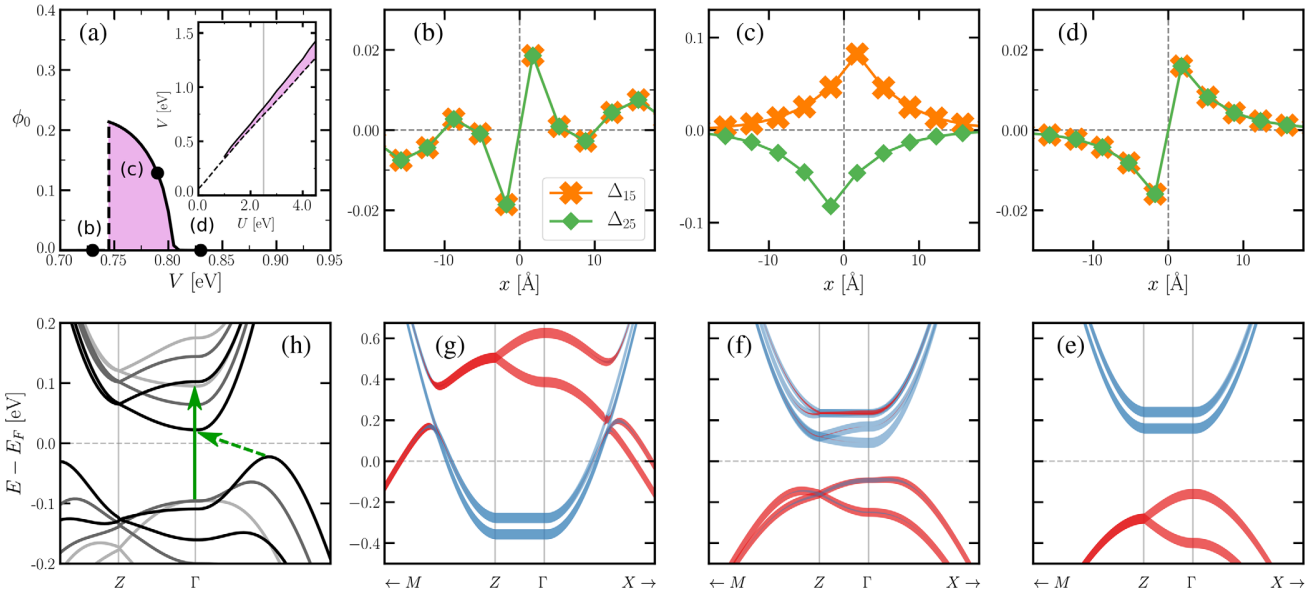

FIG. 4. (a) Order parameter at zero temperature as function of V for $U = 2.50$ eV. Dots represent $V = 0.73$, $V = 0.785$, and $V = 0.83$ corresponding to panels (b)–(d). Inset: phase diagram in U-V plane. Shaded region corresponds to the symmetry-broken phase. Dashed line indicates a metal-insulator Lifshitz transition. (b)–(d) Ta-Ni hybridization along Ta-Ni-Ta A chain in the symmetric (b) and (d) and symmetry-broken (c) phases. Crosses (diamonds) correspond to upper (lower) part of the Ta-Ni-Ta chain. (e)–(g) Bands along $M - Z - \Gamma - X$ corresponding to panels (b)–(d). Red (blue) corresponds to Ni (Ta) character. (h) Gap evolution inside the broken-symmetry phase. $U = 2.50$ eV and $V = 0.79$, 0.77, 0.75 eV from light grey to black lines. Full (dashed) green arrows highlight the direct (indirect) gap.

the B chains imply $\Delta_{36}(x) = -\Delta_{36}(-x)$ and $\Delta_{46}(x) = -\Delta_{46}(-x)$.

We investigate the possible breaking of the above symmetries due to electronic interactions, by utilizing a Hartree-Fock variational wave function allowing for a spatially homogeneous order parameter of the form:

$$\vec{\phi} = \begin{pmatrix} \phi_{15} \\ \phi_{25} \\ \phi_{36} \\ \phi_{46} \end{pmatrix}, \qquad \phi_{ij} \equiv \Delta_{ij}(a/2) + \Delta_{ij}(-a/2). \quad (8)$$

The four ϕ_{ij} are in general independent, allowing in principle for 16 different phases corresponding to the different breaking patterns of the reflections and inversion symmetries. Here, we focus on the symmetry-breaking channel consistent with the low-temperature monoclinic phase of Ta_2NiSe_5. In the monoclinic phase all reflections are broken, while their products $I^{A/B} = \sigma_\perp^{A/B}\sigma_\parallel^{A/B}$ and the inversion $\mathcal{I} = I^{A/B}\mathcal{T}$ ($\mathcal{T}$ being the translation between the two Ni atoms) are preserved. This constrains the components ϕ_{ij} as $\phi_{15} = -\phi_{25}$ and $\phi_{36} = -\phi_{46}$, due to preservation of $I^{A/B}$ and $\phi_{15} = \phi_{46}$ and $\phi_{25} = \phi_{36}$ due to $\mathcal{I}$, leading to an order parameter of the form $\vec{\phi} = \phi_0(+1, -1, -1, +1)$.

The obtained zero-temperature phase diagram in the U-V plane, Fig. 4(a), shows three distinct regions. At fixed value of U, the order parameter ϕ_0 vanishes for V smaller than a lower critical value [$V < V_l^*(U)$] and for V larger than an upper critical value [$V > V_u^*(U)$]. In these regions the Ta-Ni hybridizations transform in accordance with Eq. (7), as shown in Figs. 4(b) and 4(d). These two symmetric ground states are characterized by different electronic properties. For $V < V_l^*(U)$ [Figs. 4(b) and 4(g)] the valence and conduction bands overlap, while for $V > V_u^*(U)$ [Figs. 4(d) and 4(e)] the bands are separated by an energy gap.

In the intermediate region $V_l^*(U) < V < V_u^*(U)$ [Figs. 4(c) and 4(f)] a solution with $\phi_0 \neq 0$ is stabilized. This is the hallmark of the excitonic instability as witnessed in Fig. 4(f) by the emergence of a sizable hybridization between valence and conduction bands all along the $\overline{Z\Gamma}$ path. Valence and conduction bands acquire a strong Ta and Ni character, respectively (which is absent in the symmetric phase) and the degeneracy of the Ta-like conduction bands along $\overline{Z\Gamma}$ is lifted by hybridization with Ni-like valence bands. In real space this translates into broken $\sigma_\perp^{A/B}$ and $\sigma_\parallel^{A/B}$ symmetries yielding finite Δ_{35} and Δ_{26}, which couple the two chains, Fig. 3(b).

The upper valence band develops a mostly flat dispersion around Γ. While this has so far been interpreted as a distinctive signature of an homogeneous excitonic condensate, we show here that the interpretation is not unique. In fact this feature is a result of a direct-to-indirect gap insulator transition, driven by the splitting between the hybridized bands along $\overline{Z\Gamma}$, that can occur inside the

broken-symmetry phase [Fig. 4(h)]. By decreasing V the splitting increases, while the bottom of the conduction band moves closer to the Fermi level. At $V = V_l^*(U)$ the conduction band crosses the Fermi level and the system undergoes a Lifshitz transition accompanied by the formation of a Fermi surface in the metallic phase. We find here that this is a first-order transition which restores the symmetry for $V < V_l^*(U)$. If we allowed for a nonhomogeneous $\vec{\phi}(\vec{R})$ order parameter a finite momentum instability could occur near this point [40]. The symmetry-broken phase is found only in a small region of the phase space close to the Lifshitz transition. In this regime the symmetric phase is characterized by a very small gap, reinforcing the relevance of the above phase transition for Ta_2NiSe_5, which in the high-temperature phase has been reported to be a zero-gap semiconductor [16]. The symmetry-broken region shrinks as the Hubbard U is decreased until it disappears for $U \lesssim 1.25$ eV for which $V_l^*(U)$ and $V_u^*(U)$ merge into the Lifshitz transition line. We highlight that our constrained RPA values for U and V are in close vicinity of the symmetry-broken region.

Structural phase transition.—The electronic configuration associated with the excitonic phase is not compatible with the symmetries of the lattice. This implies that the electronic order parameter must have a linear coupling to lattice modes breaking the crystal symmetry [27,41]. Hence, the excitonic transition will coexist with a structural transition, as indeed observed experimentally. From the pattern of the Ta-Ni hybridizations in the broken-symmetry phase [Fig. 3(b)], one anticipates a distortion of the unit cell in which Ta atoms from the same Ta-Ni-Ta chain are tilted in opposite directions [arrows in Fig. 3(b)]. This corresponds to a structural transition from the orthorhombic to the monoclinic structure, which we confirm to be present by performing a full structural relaxation within DFT [28]. The interplay between the electronic and lattice instability is an interesting question for future investigations [42].

Conclusions.—We have performed a symmetry analysis backed up by first-principle calculations of Ta_2NiSe_5, with general implications for the excitonic transitions in solids. While this transition has been so far understood as a condensation phenomenon resulting from a continuous $U_X(1)$ symmetry breaking [27] we show that in realistic solids there is no such symmetry: the purely electronic transition corresponds to the breaking of discrete symmetries only. Important consequences include that all collective modes are gapped and that there is no dissipationless transport or excitonic superfluidity. We identify explicitly all discrete symmetries relevant for the structural phase transition in Ta_2NiSe_5, including the corresponding electronic order parameters and provide clear evidence for a transition into an excitonic insulator phase. This transition breaks these symmetries in a manner consistent with the experimentally observed lattice distortion into a monoclinic phase, and the order parameter couples linearly to lattice modes.

Because we find a spontaneous electronic instability for realistic values of the interactions, our results suggest an electronic contribution to the coupled transition [43–45]. However, a definitive confirmation of this point calls for experimental probes which can selectively address the electronic and lattice degrees of freedom. In the context of iron-based superconductors, where a similar question arises in relation to nematicity, it has proven possible to probe the electronic component of the susceptibility associated with the nematic instability [46,47]. Ultrafast spectroscopies offer another possible route [22,25,48,49] by exploiting the very different time scales associated with electronic and lattice degrees of freedom.

Discussions with Jennifer Cano, Denis Golež, Edoardo Baldini, Selene Mor, Tatsuya Kaneko, and Jernej Mravlje are gratefully acknowledged. We thank Merzuk Kaltak for sharing his (c)RPA implementation [50] with us. This work was supported by (A. G., G. M.) the European Research Council (ERC-319286-QMAC) and (A. M.) the US Department of Energy under Grant No. DE-SC 0019443. G. M. acknowledges support from the Swiss National Science Foundation Ambizione Grant No. PZ00P2_186146. S. L., L. W., H. H., and A. R. were supported by the European Research Council (Grant No. ERC-2015-AdG694097), the Cluster of Excellence AIM, Grupos Consolidados (Grant No. IT1249-19) and SFB925. S. L. acknowledges support from the Alexander von Humboldt foundation. The Flatiron Institute is a division of the Simons Foundation.

*These two authors equally contributed.
†giacomo.mazza@unige.ch
‡m.roesner@science.ru.nl
§ageorges@flatironinstitute.org

[1] A. N. Kozlov and L. A. Maksimov, Sov. J. Exp. Theor. Phys. **21**, 790 (1965).
[2] L. V. Keldysh and A. N. Kozlov, Sov. J. Exp. Theor. Phys. **27**, 521 (1968).
[3] D. Jérome, T. M. Rice, and W. Kohn, Phys. Rev. **158**, 462 (1967).
[4] B. I. Halperin and T. M. Rice, Rev. Mod. Phys. **40**, 755 (1968).
[5] J. Eisenstein, Annu. Rev. Condens. Matter Phys. **5**, 159 (2014).
[6] M. Kellogg, J. P. Eisenstein, L. N. Pfeiffer, and K. W. West, Phys. Rev. Lett. **93**, 036801 (2004).
[7] I. B. Spielman, J. P. Eisenstein, L. N. Pfeiffer, and K. W. West, Phys. Rev. Lett. **84**, 5808 (2000).
[8] J. I. A. Li, T. Taniguchi, K. Watanabe, J. Hone, and C. R. Dean, Nat. Phys. **13**, 751 (2017).
[9] X. Liu, K. Watanabe, T. Taniguchi, B. I. Halperin, and P. Kim, Nat. Phys. **13**, 746 (2017).
[10] D. Snoke, Science **298**, 1368 (2002).

[11] L. V. Butov, C. W. Lai, A. L. Ivanov, A. C. Gossard, and D. S. Chemla, Nature (London) **417**, 47 (2002).
[12] L. V. Butov, A. C. Gossard, and D. S. Chemla, Nature (London) **418**, 751 (2002).
[13] F. D. Salvo, C. Chen, R. Fleming, J. Waszczak, R. Dunn, S. Sunshine, and J. A. Ibers, J. Less Common Metals **116**, 51 (1986).
[14] Y. Wakisaka, T. Sudayama, K. Takubo, T. Mizokawa, M. Arita, H. Namatame, M. Taniguchi, N. Katayama, M. Nohara, and H. Takagi, Phys. Rev. Lett. **103**, 026402 (2009).
[15] K. Seki, Y. Wakisaka, T. Kaneko, T. Toriyama, T. Konishi, T. Sudayama, N. L. Saini, M. Arita, H. Namatame, M. Taniguchi, N. Katayama, M. Nohara, H. Takagi, T. Mizokawa, and Y. Ohta, Phys. Rev. B **90**, 155116 (2014).
[16] Y. F. Lu, H. Kono, T. I. Larkin, A. W. Rost, T. Takayama, A. V. Boris, B. Keimer, and H. Takagi, Nat. Commun. **8**, 14408 (2017).
[17] F. J. Di Salvo, D. E. Moncton, and J. V. Waszczak, Phys. Rev. B **14**, 4321 (1976).
[18] H. Cercellier, C. Monney, F. Clerc, C. Battaglia, L. Despont, M. G. Garnier, H. Beck, P. Aebi, L. Patthey, H. Berger, and L. Forró, Phys. Rev. Lett. **99**, 146403 (2007).
[19] A. Kogar, M. S. Rak, S. Vig, A. A. Husain, F. Flicker, Y. I. Joe, L. Venema, G. J. MacDougall, T. C. Chiang, E. Fradkin, J. van Wezel, and P. Abbamonte, Science **358**, 1314 (2017).
[20] A. Nakano, T. Hasegawa, S. Tamura, N. Katayama, S. Tsutsui, and H. Sawa, Phys. Rev. B **98**, 045139 (2018).
[21] S. Y. Kim, Y. Kim, C.-J. Kang, E.-S. An, H. K. Kim, M. J. Eom, M. Lee, C. Park, T.-H. Kim, H. C. Choi, B. I. Min, and J. S. Kim, ACS Nano **10**, 8888 (2016).
[22] S. Mor, M. Herzog, D. Golež, P. Werner, M. Eckstein, N. Katayama, M. Nohara, H. Takagi, T. Mizokawa, C. Monney, and J. Stähler, Phys. Rev. Lett. **119**, 086401 (2017).
[23] J. Lee, C.-J. Kang, M. J. Eom, J. S. Kim, B. I. Min, and H. W. Yeom, Phys. Rev. B **99**, 075408 (2019).
[24] T. I. Larkin, A. N. Yaresko, D. Pröpper, K. A. Kikoin, Y. F. Lu, T. Takayama, Y.-L. Mathis, A. W. Rost, H. Takagi, B. Keimer, and A. V. Boris, Phys. Rev. B **95**, 195144 (2017).
[25] D. Werdehausen, T. Takayama, M. Höppner, G. Albrecht, A. W. Rost, Y. Lu, D. Manske, H. Takagi, and S. Kaiser, Sci. Adv. **4**, eaap8652 (2018).
[26] K. Sugimoto, S. Nishimoto, T. Kaneko, and Y. Ohta, Phys. Rev. Lett. **120**, 247602 (2018).
[27] T. Kaneko, T. Toriyama, T. Konishi, and Y. Ohta, Phys. Rev. B **87**, 035121 (2013).
[28] See the Supplemental Material at http://link.aps.org/supplemental/10.1103/PhysRevLett.124.197601 containing details on the *ab initio* calculations and the construction of the model Hamiltonian, which includes Refs. [29–37].
[29] J. P. Perdew, K. Burke, and M. Ernzerhof, Phys. Rev. Lett. **77**, 3865 (1996).
[30] P. E. Blöchl, Phys. Rev. B **50**, 17953 (1994).
[31] G. Kresse and J. Furthmüller, Comput. Mater. Sci. **6**, 15 (1996).
[32] G. Kresse and J. Furthmüller, Phys. Rev. B **54**, 11169 (1996).
[33] S. A. Sunshine and J. A. Ibers, Inorg. Chem. **24**, 3611 (1985).
[34] A. D. Becke and E. R. Johnson, J. Chem. Phys. **124**, 221101 (2006).
[35] F. Tran and P. Blaha, Phys. Rev. Lett. **102**, 226401 (2009).
[36] A. A. Mostofi, J. R. Yates, Y.-S. Lee, I. Souza, D. Vanderbilt, and N. Marzari, Comput. Phys. Commun. **178**, 685 (2008).
[37] E. Sasioglu, C. Friedrich, and S. Blügel, Phys. Rev. B **83**, 121101(R) (2011).
[38] S. Ejima, T. Kaneko, Y. Ohta, and H. Fehske, Phys. Rev. Lett. **112**, 026401 (2014).
[39] F. Aryasetiawan, M. Imada, A. Georges, G. Kotliar, S. Biermann, and A. I. Lichtenstein, Phys. Rev. B **70**, 195104 (2004).
[40] K. Domon, T. Yamada, and Y. Ono, J. Phys. Soc. Jpn. **87**, 054701 (2018).
[41] B. Zenker, H. Fehske, and H. Beck, Phys. Rev. B **90**, 195118 (2014).
[42] L. Windgätter, M. Rösner, S. Latini, G. Mazza, H. Hübener, A. J. Millis, A. Rubio, and A. Georges (to be published).
[43] M. D. Watson, I. Marković, E. A. Morales, P. L. Fèvre, M. Merz, A. A. Haghighirad, and P. D. C. King, Phys. Rev. Research **2**, 013236 (2020).
[44] A. Subedi, arXiv:2002.08352.
[45] T. Tang, H. Wang, S. Duan, Y. Yang, C. Huang, Y. Guo, D. Qian, and W. Zhang, arXiv:2003.00514.
[46] J.-H. Chu, H.-H. Kuo, J. G. Analytis, and I. R. Fisher, Science **337**, 710 (2012).
[47] P. Massat, D. Farina, I. Paul, S. Karlsson, P. Strobel, P. Toulemonde, M.-A. Méasson, M. Cazayous, A. Sacuto, S. Kasahara, T. Shibauchi, Y. Matsuda, and Y. Gallais, Proc. Natl. Acad. Sci. U.S.A. **113**, 9177 (2016).
[48] Y. Murakami, D. Golež, M. Eckstein, and P. Werner, Phys. Rev. Lett. **119**, 247601 (2017).
[49] M. Porer, U. Leierseder, J.-M. Menard, H. Dachraoui, L. Mouchliadis, I. E. Perakis, U. Heinzmann, J. Demsar, K. Rossnagel, and R. Huber, Nat. Mater. **13**, 857 (2014).
[50] M. Kaltak, Merging GW with DMFT, Ph.D. Thesis, University of Vienna, 2015.

4.5 Publication IV: Common microscopic origin of the phase transitions in Ta_2NiS_5 and the excitonic insulator candidate Ta_2NiSe_5

State of the Art

TNSe had recently emerged as a prime candidate to host an excitonic insulating ground-state. Experimentally a phase transition had been measured at T=326K [28, 29] with the formation of characteristic flat bands [30] and a semimetal to insulator transition [20, 31, 98, 106]. While we have investigated the possibility of an excitonic instability and identified its order parameter in publication III, it was still unclear if such an instability is realized in the actual material. Also the effect of the purely structural transition onto the material was largely unknown, which is important to understand to disentangle electronic and structural contributions to the phase transition. The goal of this paper is to investigate these open questions using ab-initio methods.

Main Findings

The main finding of this work is that the transition in TNSe is predominantly structurally driven. We show that the pure structural transition, without accounting for excitonic effects, already leads to the opening of a bandgap and band flattening similar to the experimental ARPES results. We identify a soft phononic mode which is commensurate with the structural transition and show that such a mode couples strongly to the electronic degrees of freedom. We further investigate the origin of the phase transition and cannot find any sign of an excitonic instability as proposed in our previous work. This leads us to the conclusion that the phase transition is structural in nature. However, an open question that we are investigating now is, why the soft phonon mode does not appear in the Raman measurements [88, 96, 99–101] and what a possible stabilization mechanism could be. Answering this question is part of a follow up project, where we propose a phonon phonon mediated stabilization mechanism which we investigate via extensive Molecular Dynamics calculations. This confirms the conclusions in this paper and will be published soon.

Status and Publication Details

This paper has been published in the Nature Partner Journal (NPJ) computational materials. This publication has a Supplementary Information that is being published at `https://static-content.springer.com/esm/art%3A10.1038%2Fs41524-021-00675-6/MediaObjects/41524_2021_675_MOESM1_ESM.pdf` and not contained in this thesis.

Contribution

I performed all simulations and created all figures in this publication. All authors have contributed to the analysis of the data and the writing of the manuscript.A detailed list of the contribution of the other authors as well can be found at the end of the publication.

npj | Computational Materials

www.nature.com/npjcompumats

ARTICLE OPEN

Check for updates

Common microscopic origin of the phase transitions in Ta_2NiS_5 and the excitonic insulator candidate Ta_2NiSe_5

Lukas Windgätter[1]✉, Malte Rösner[2], Giacomo Mazza[3], Hannes Hübener[1], Antoine Georges[3,4,5,6], Andrew J. Millis[6,7], Simone Latini[1]✉ and Angel Rubio[1,6,8]✉

The structural phase transition in Ta_2NiSe_5 has been envisioned as driven by the formation of an excitonic insulating phase. However, the role of structural and electronic instabilities on crystal symmetry breaking has yet to be disentangled. Meanwhile, the phase transition in its complementary material Ta_2NiS_5 does not show any experimental hints of an excitonic insulating phase. We present a microscopic investigation of the electronic and phononic effects involved in the structural phase transition in Ta_2NiSe_5 and Ta_2NiS_5 using extensive first-principles calculations. In both materials the crystal symmetries are broken by phonon instabilities, which in turn lead to changes in the electronic bandstructure also observed in the experiment. A total energy landscape analysis shows no tendency towards a purely electronic instability and we find that a sizeable lattice distortion is needed to open a bandgap. We conclude that an excitonic instability is not needed to explain the phase transition in both Ta_2NiSe_5 and Ta_2NiS_5.

npj Computational Materials (2021)7:210 ; https://doi.org/10.1038/s41524-021-00675-6

INTRODUCTION

The excitonic insulator phase has been theoretically proposed in the 1960s[1–6] and is predicted to appear in semiconductors (or semimetals) with excitonic binding energies larger than the bandgap (or bandoverlap) of their conventional groundstate. Under this condition, the groundstate becomes unstable against the spontaneous formation of bound electron hole pairs, i.e. excitons. Depending on the conventional phase being semiconducting or semimetallic, the transition is described by a Bose–Einstein condensation (BEC)- or a Bardeen–Cooper–Schrieffer (BCS)-like mechanism, respectively[2,4,5].

A major challenge in the experimental detection of an excitonic insulator state in a crystal is that the excitonic transition is coupled to other degrees of freedom, such as lattice distortions, which make an unambiguous detection difficult. This is the reason why several materials such as 1T-$TiSe_2$[7,8] or $TmSe_{0.45}Te_{0.55}$[9] have not been unambiguously confirmed to host an excitonic insulating (EI) groundstate. These are indirect bandgap or semimetal materials that exhibit finite momentum ordering and in the case of 1T-$TiSe_2$, for example, the existence of a charge density wave masks the possible presence of an EI phase.

Very recently, also two-dimensional materials have shown promises to host an excitonic groundstate. Experimentally, strong evidence for the existence of EI phases has been provided both for transition metal dichalcogenide bilayers[10] and monolayers, such as WTe_2 and MoS_2[11,12]. An extensive theoretical study has identified several candidate material combinations for hetero-bilayers that could host an excitonic insulator by analysing the electronic properties of a wide range of materials[13]. Further low-dimensional excitonic insulator candidates are carbon nanotubes[14], Sb nanoflakes[15], double bilayer graphene[16,17] and topological systems[18], such as InAs/GaSb[19]. In the bulk phase, MoS_2 has recently been revealed as another candidate material since its bandgap can be tuned via pressure, yielding excitonic binding energies larger than the quasi-particle gap, which would allow for a transition into a possibly EI groundstate[20].

We investigate bulk Ta_2NiSe_5 (TNSe), which is considered to be a very promising candidate to host an excitonic condensate[21], with several experimental evidence suggesting an EI groundstate: angle-resolved photo-electron spectroscopy (ARPES) measurements have shown a characteristic band flattening near the Γ-point upon cooling below the critical temperature[22–25], a dome-shaped bandgap–temperature phase diagram, similar to the theoretically predicted one, has been found[26], and the opening of a gap has been measured in scanning tunnel spectroscopy (STS)[27], optics[26] and ARPES[24,28] experiments below the critical temperature[27]. The bandgap in the low-temperature phase is reported to be between 160 meV in optics[26] and 300 meV in STS measurements[27]. The current literature is controversially reporting the high-temperature phase of TNSe to be either a direct bandgap semiconductor[21,29] or a small bandoverlap semimetal[24]. It is, however, agreed that there exists a structural phase transition, and possibly a transition into an excitonic groundstate, at the critical temperature $T_c = 326$ K[26,30–32]. The structural transition has been reported to be from a high-temperature orthorhombic to a low-temperature monoclinic phase[30–32].

On the other hand Ta_2NiS_5 (TNS), a material of the same structure of TNSe with Sulfur replacing selenium, does not exhibit the same excitonic signatures of TNSe, such as band flattening and bandgap opening. Indeed a structural transition at 120 K[33] has been reported without the formation of flat bands or a metal to semiconductor transition[34].

Due to the uncertainty on whether TNSe has a semimetallic or gapped high-temperature phase, from a theoretical perspective it is unclear which mechanism between BEC and BCS can

[1]Max Planck Institute for the Structure and Dynamics of Matter, Luruper Chaussee 149, 22761 Hamburg, Germany. [2]Radboud University, Institute for Molecules and Materials, Heijendaalseweg 135, 6525 AJ Nijmegen, Netherlands. [3]Department of Quantum Matter Physics, University of Geneva, Quai Ernest-Ansermet 24, 1211 Geneva, Switzerland. [4]Collège de France, 11 place Marcelin Berthelot, 75005 Paris, France. [5]Center for Computational Quantum Physics, Flatiron Institute, New York, NY 10010, USA. [6]CPHT, CNRS, Ecole Polytechnique, IP Paris, 91128 Palaiseau, France. [7]Department of Physics, Columbia University, New York, NY 10027, USA. [8]Nano-Bio Spectroscopy Group, Departamento de Física de Materiales, Universidad del País Vasco, 20018 San Sebastian, Spain. ✉email: lukas.windgaetter@mpsd.mpg.de; simone.latini@mpsd.mpg.de; angel.rubio@mpsd.mpg.de

Published in partnership with the Shanghai Institute of Ceramics of the Chinese Academy of Sciences

npj nature partner journals

be applied. In fact, experimentally there is no unambiguous evidence that excitons are involved in the phase transition at all. These facts indicate that, in relation to TNSe, the concept of excitonic insulator can be source of confusion, as it has been generally employed to refer to a phase showing a characteristic gap opening and band flattening[22,23,25,27] without direct observation of excitonic features and/or excitonic condensation.

A recent symmetry analysis of the possible electronic instabilities issuing from the electron–electron interactions has shown that the electronic phase transitions in the material should not be ascribed to a condensation phenomenon but rather to the electronic lowering of the discrete lattice symmetry[35], which corresponds to the breaking of a continuous U(1) symmetry during the excitonic phase transition. This observation, together with other recent experimental and theoretical observations[24,36], suggest a prominent role of structural instabilities in the system. In this work, we abandon the concept of excitonic condensation and show that the experimental features of TNSe and TNS mentioned above can be completely explained without explicitly taking the formation of excitons into account. We demonstrate how the electronic and structural properties of the two crystals can be rationalized in terms of electronic and intrinsic lattice instabilities that drive the system from the orthorhombic to monoclinic phase. The occurrence of such a lattice-driven instability agrees with a prior report of Alaska Subedi[36].

We present a comprehensive ab initio study using density functional theory (DFT) for the transition from the orthorhombic to the monoclinic phase beyond standard generalized gradient approximation functionals. In section "Structure relaxation," we start by investigating the structural stability of the system and show that at low temperature a monoclinic groundstate is energetically favoured to the orthorhombic one, which suggests the existence of a lattice instability. A similar analysis applied to TNS highlights an equivalent structural transition mechanism from an orthorhombic to a C2/c symmetric monoclinic cell.

In section "Electronic bandstructure," we then investigate the electronic bandstructure of both the high- and low-temperature phase of TNSe and TNS using different exchange correlation functionals with increasing accuracy. For TNSe, we can establish the orthorhombic groundstate to be metallic and observe a sizeable gap opening as well as a band flattening with the phase transition. This shows that for this material the structural distortion is essential for the bandgap opening observed in optics and STS measurements and cannot be explained considering only the electronic degrees of freedom. In section "G_0W_0 calculations," we show that a similar finding results from our many-body perturbation theory-based calculations carried out at the G_0W_0 level. Performing an equivalent DFT analysis for TNS shows that both the orthorhombic and monoclinic phases are gapped systems with parabolic electronic dispersions at Γ. This explains why a metal to semiconductor transition and band flattening, which have been characterized as a signature of an excitonic insulator in TNSe, has not been observed for TNS[34]. We then show that electronic heating enhances the valence band flattening and investigate in the following section "Origin of the structural instability" the origin of the instability observed in TNSe. We find no evidence for an electronically driven spontaneous symmetry breaking in the TNSe charge density upon infinitesimal lattice distortions. In the symmetry broken lattice structure, the total energy is, however, clearly lowered, which renders the electron–phonon interaction the main driving mechanism for the structural transition. In section "Phonon dispersion," we discuss the phononic bandstructure and single out the phononic instabilities of the orthorhombic phase, the ones that could possibly drive the structural transition. A detailed discussion of the obtained phonon modes in relation with the most recent Raman measurements shows that we are able to reproduce all phonon peaks, except for the first two B_{2g} modes, which exhibit a strong broadening, which hints to a strong coupling of these modes to other degrees of freedom. Finally, in section "Electron–phonon coupling," we show that the electronic dispersion is strongly modulated by different phonon modes. In particular, it is expected that thermal occupation of the phonon mode responsible for the structural transition leads to a further bandgap opening.

RESULTS

Structure relaxation

TNSe is a layered material bound by van-der Waals forces. It consists of parallel Tantalum and Nickel chains and is thus referred to as a quasi-one-dimensional material (see Fig. 1)[32]. Experimentally, the high-temperature phase exhibits an orthorhombic structure, which is distorted to a monoclinic structure in the low-temperature phase. The distortion, however, is subtle with a change in the β angle (see Fig. 2b) of just 0.53°[32] to 0.69°[30].

We have performed a first-principles structure relaxation of atomic coordinates, cell shape and cell volume for different functionals. In all cases, the relaxation resulted in a triclinic structure. The resulting lattice parameters are shown in Supplementary Tables 1 and 5: the two functionals vdW-optB88 and vdW-optPBE[37,38], which include van der Waals corrections, result in relaxed structures that agree well with the experimentally measured values, while the Perdew–Burke–Ernzerhof (PBE) functionals overestimates the experimentally measured interlayer lattice parameter b by 10.5%[30] (see Supplementary Tables 1 and 5).

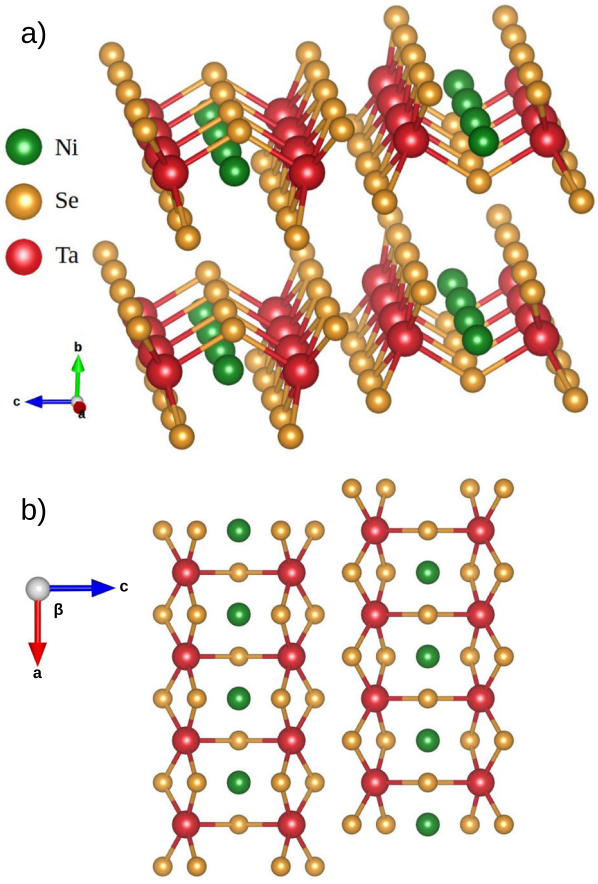

Fig. 1 Ta_2NiSe_5 structure. Layered structure of the orthorhombic phase of TNSe. The Nickel and Tantalum atoms form parallel chains along the a-axis. **a** shows a 3D view of TNSe. **b** shows the projection onto the a–c plane. For TNS, the Se atoms are simply replaced with Sulfur atoms.

As expected, this shows the importance of including van der Waals forces when describing layered structures, such as TNSe.

The angles of the relaxed triclinic structure are $\alpha = 90.005°$, $\beta = 90.644°$ and $\gamma = 89.948°$. As the two angles α and γ are almost rectangular, the triclinic cell and the corresponding monoclinic cell are almost degenerate. Furthermore, we have checked that the small triclinic distortion does not modify the electronic properties compared to the exact monoclinic structure. Thus, in the following, we refer to the fully relaxed structure as monoclinic. The monoclinic angle $\beta = 90.644°$ agrees well with the experimentally measured values 90.693°[30] and 90.53°[32].

To obtain the relaxed geometry for the high-temperature orthorhombic cell, we have performed the same relaxation using the vdw-optB88 functional enforcing the orthorhombic symmetry. The resulting lattice parameters are shown in Supplementary Tables 2 and 4. As the relaxed structure predicted by the vdW-optB88 functional has the best agreement with the experimentally measured values for both the monoclinic and orthorhombic phase, we have chosen it for all following structural calculations.

We have performed similar relaxations for the Sulfur compound: a full relaxation using the vdW-optB88 functional, again, results in a triclinic geometry that is almost degenerate with the monoclinic cell. The monoclinic angle is $\beta = 90.50°$. For the orthorhombic phase we have performed a further relaxation with fixed symmetry. The lattice parameters for both structures are shown in Supplementary Table 3 and agree very well with the experimentally measured values from X-ray diffraction. This agrees with a recent Raman study by Ye et al., which reports an orthorhombic high-temperature phase and a structural transition to a monoclinic phase at $T = 120\,\mathrm{K}$[33].

Therefore, we find that in both TNSe and TNS a monoclinic geometry is energetically favoured, which shows that a similar lattice instability occurs in both materials. In section "Phonon dispersion," we extensively discuss the phononic properties of the two materials and identify the structural instability with an unstable B_{2g} phonon. Although the structural change between monoclinic and orthorhombic phase is small, the modifications for the electronic bandstructure with the phase transition is significant (see section "Electronic bandstructure"). This hints to a strong coupling between electronic and lattice degrees of freedom (see section "Electron–phonon coupling").

Electronic bandstructure

In this section, we present a complete and systematic DFT study of both TNSe and TNS using standard and more accurate functionals. While we find that the fine electronic properties are sensitive to the details of exchange and correlation, the underlying mechanism of bandgap opening due to the structural phase transition is independent of the functional choice for both TNSe and TNS. We investigate the bandstructure of the orthorhombic and monoclinic geometries using different exchange correlation functionals, which include varying degrees of exact exchange. These are ranked in chemical accuracy with the PBE functional[39] being the most inaccurate, but computationally least demanding, followed by the modified Becke–Johnson (mBJ) functional[40–42] and finally the range separated hybrid functional HSE03[43] being the most accurate one.

The results are shown in Fig. 2. Results for the HSE06 functional are reported in Supplementary Fig. 9 and the definition of the *M*–*Z*–Γ–*X* path is given in Supplementary Note 1.

Figure 2a, b display the obtained bandstructure of TNSe: the high-temperature orthorhombic structure exhibits a metallic groundstate independently of the functional presented here, while the monoclinic structure is always semiconducting. The bandgap opening is sizeable for all the investigated functionals and its position and value changes with the amount of exchange and correlation included. With the PBE functional, we obtain an indirect bandgap value of 40 meV, with the mBJ functional a direct bandgap of 101 meV and with the HSE03 functional a direct bandgap of 183 meV. Thus, the bandgap grows with an increasing accuracy of the exchange and correlation functional. From Fig. 2b, we observe that, in the monoclinic phase, TNSe has a rather flat dispersion around Γ due to the valence band maxima being off Γ for both the PBE and mBJ functional.

By increasing the exchange contribution included in the functional, e.g. by tuning the mixing parameter in the hybrid functional or the *c* parameter in the mBJ functional, it is possible to further increase the bandgap. We observed that even in the orthorhombic phase increasing the exchange contribution can lead to a gap opening (see Supplementary Note 4 and Supplementary Figs. 5 and 6), which is consistent with prior studies[44]. The bandgap opening resulting from HSE03 agrees well with the experimentally measured bandgap of 160 meV[26]. In STS measurements, a gap of 300 meV has been reported[27]. However, we notice that the structure in ref. [27] shows a monoclinic distortion with an angle $\beta \propto 92.5°$, i.e. much larger than the angle reported in previous studies and the angle obtained in our calculation ($\beta \simeq 90.6°$). Correcting for this difference, we find that both the optics and scanning tunneling microscopic results are in good agreement with our HSE03 results (see Supplementary Note 6 for more details).

Performing similar calculations for TNS, Fig. 2c, d, we identify a major difference in the electronic behaviour of the Selenium and Sulfur compounds. We see that, using either mBJ or HSE03 hybrid functionals, the calculations predict a semiconducting groundstate even for the orthorhombic geometry. The structural transition to the monoclinic cell then leads to a further bandgap opening, with bandgap values being around twice the size of the TNSe ones. Therefore, in contrast to TNSe, no metal-to-insulator transition is observed. The bandgap is direct at the Γ-point with a parabolic dispersion towards the *X* direction. These findings agree well with the theoretical and experimental reports: ARPES as well as optical conductivity data show that TNS has a parabolic dispersion around the Γ-point[34,44] with a robust bandgap of 200 meV[34,44,45] and 250 meV in optics[46].

We stress that, while both compounds have a similar lattice instability from orthorhombic to monoclinic geometry, in the case of TNSe the structural instability is accompanied by a metal-to-insulator transition, which is absent in the case of TNS. These observations match all known experimental trends for these two systems. In the case of the Selenium compound, the metal–insulator transition accompanied by the flattening of the valence band around Γ appears to be the intrinsic outcome of the structural instability of the system and not the distinctive signature of the excitonic insulator phase, as it has been interpreted so far. We support this statement in the next sections by explicitly accounting for the role of the electronic instability and comparing the excitonic binding energy with the bandgap value.

Given that states near the band gap have significant contributions from Ta, we have checked the validity of our results by also including spin–orbit coupling effects and reported the related band structure calculations in Supplementary Figs. 2–4, Supplementary Note 3 and Supplementary Table 6. We find that, besides a band splitting in the *M*–*Z* direction and a minor renormalization of the bandgap, all our claims remain unchanged.

G_0W_0 calculations

While DFT calculations generally provide a good starting point for discussing material properties, they often lack quantitative agreement with experimental results. It is known that one needs to add many-body corrections to obtain a quantitative agreement with the experimental bandgaps. The standard approach that provides accurate bandgaps is the GW method[47–50]. The latter is a

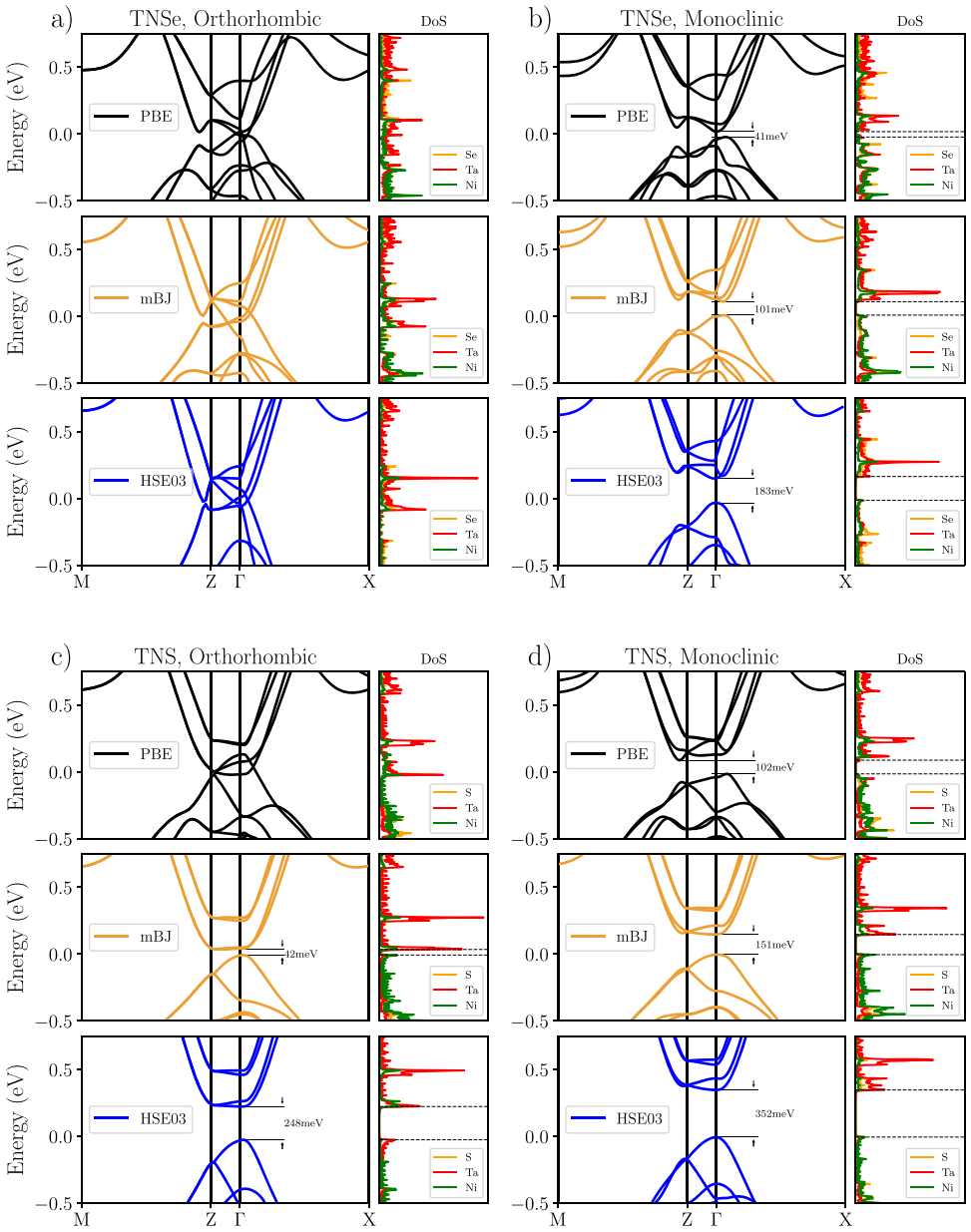

Fig. 2 Bandstructure of Ta_2NiSe_5 and Ta_2NiS_5. Band structure of TNSe and TNS for the orthorhombic and monoclinic phase. For all the investigated exchange correlation functionals, we obtain a semimetallic groundstate for the high-temperature phase of TNSe. Only after the structural transition to the monoclinic geometry, a bandgap of between 40 and 183 meV opens. In TNS, already the orthorhombic phase exhibits a positive bandgap for the modified Becke–Johnson and HSE03 functional, which increases during the structural transition to the monoclinic phase. Therefore, the metal-to-insulator transition observed in TNSe is lacking for TNS. In all plots, the Fermi energy is set to 0 eV. The self-consistently calculated *c*-value for TNSe is $c = 1.25$ and $c = 1.26$ for TNS in both geometries.

many-body theory approach that consists of solving Hedin's equations iteratively[51] while neglecting vertex corrections. There exist various flavours of the GW approximation with the G_0W_0 being the most commonly used. In G_0W_0, one approximates the starting wavefunctions to be the DFT ones and performs only one cycle of Hedin's equation to compute the self-energy and correct the electronic state energies. As such, the G_0W_0 approximation relies on the DFT wavefunctions to provide a good description of the full many-body wavefunction and it is crucial to investigate the starting point dependence of the G_0W_0 approximation. We have performed calculations using the wavefunctions and electronic dispersion resulting from PBE and HSE03 functional calculations (more hybrid functional starting points are shown Supplementary Fig. 10). The corresponding bandstructures for the monoclinic geometry of TNSe can be seen in Fig. 3. Independently of the starting point, the bandgap converges towards a similar value, increasing in the PBE case, where it is commonly underestimated, and decreasing for the HSE03 functional. In all cases, G_0W_0 predicts a bandgap between 100 and 163 meV, which is in good agreement with the experimental gap of 160 meV measured in optics[26]. The dispersion of the conduction bands shows similar features with a pronounced double well shape in *X*–Γ–*X* direction. The valence band dispersion, however, differs between the PBE and the HSE, with the PBE one being M-shaped and the HSE one being parabolic. This is inherited from the different initial DFT wavefunctions and electronic dispersion.

The comparison of the electronic dispersion with recent ARPES measurements by Baldini et al.[28] shows that the dispersion

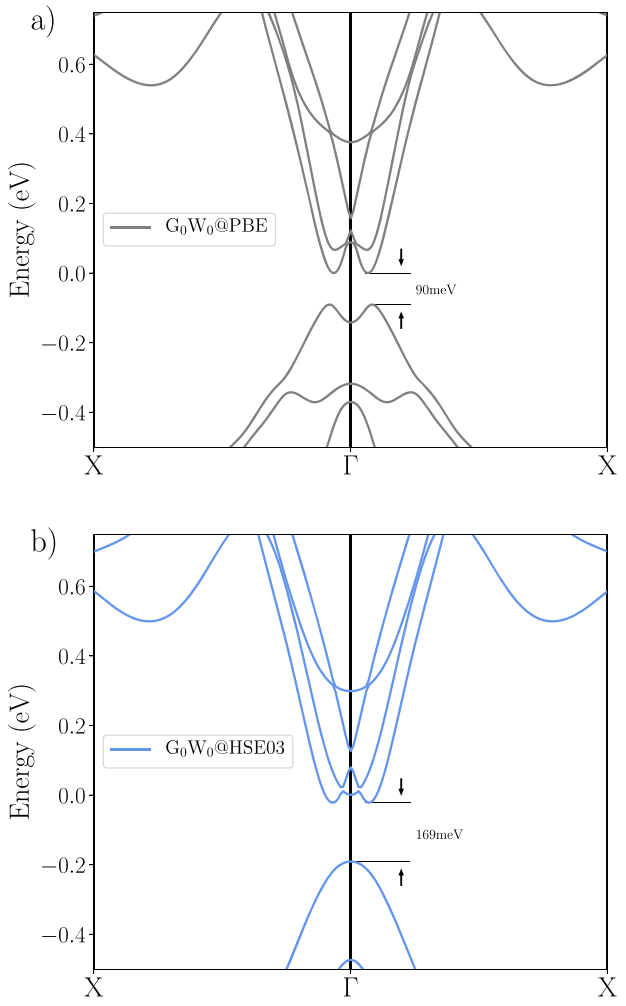

Fig. 3 G_0W_0 bandstructure of monoclinic Ta_2NiSe_5. Bandstructure of the monoclinic geometry of TNSe after performing a G_0W_0 calculation starting from the DFT groundstate of TNSe using the PBE (**a**) and the HSE03 hybrid functional (**b**). While the bandgaps are all within a small range of 100 to 163 meV, the valence band dispersions differ depending on the functional used for the initial wavefunctions. **a** has been adapted from our work in ref. [28].

obtained using the PBE functional as starting point agrees well with the experimentally measured one, reproducing both the flat valence band as well as the Mexican hat-shaped conduction band. Also Tang et al.[25] and Watson et al.[24] report an M-shaped valence band, which agrees well with the G_0W_0@PBE calculation. This reinforces the conclusion that the band structure in the monoclinic phase correctly accounts for the metal-to-insulator transition. A detailed quantitative comparison to experimental results, however, can only be achieved by including correlation beyond the PBE functional.

We also solved the Bethe–Salpether equation (BSE) starting from the G_0W_0 results[52,53] to explicitly account for exciton formation. While full convergence is not feasible with our computational resources, we can extrapolate from our *k*-point-dependent results BSE results on top of G_0W_0 and verify that the excitonic binding energy is smaller than the G_0W_0 gap in the monoclinic phase (see Supplementary Notes 7 and 8 and Supplementary Figs. 13–19). This is an indication that the condition needed for an EI phase, i.e. an exciton-binding energy larger than the gap, is not fulfilled in TNSe for the monoclinic phase.

The effect of electronic heating

The interpretation of an excitonic insulator as a phase consisting of an excitonic condensate entails that an increase of temperature above a critical value leads to the melting of the condensate and hence to a bandgap closing. Experiments aimed at demonstrating such a behaviour to prove the possibility of excitonic condensation in TNSe have indeed reported bandgap opening and band flattening for increasing pump fluence[25]. Here we mimic the photoexcitation with a thermal distribution of electrons and holes and show that the variation of the bandgap and the band flattening can be explained via a temperature increase in the same manner as in standard semiconductors. Indeed, an increase of temperature of the thermal distribution generates free carriers and it has been shown that for low carrier densities the bandgap shrinks and eventually increases again for sufficiently high densities[54,55]. The mechanism behind such a bandgap variation can be rationalized in terms of effective screening of the Coulomb interaction which modulates the effect of bandgap opening caused by the exchange contribution.

To approximately investigate the enhanced screening effects due to free carriers, we have performed a set of G_0W_0 calculations for different electronic temperatures. The electronic temperatures have been set by changing the temperature in the Fermi–Dirac function used for the occupation smearing of the Kohn–Sham states in the self-consistent DFT calculations. This effectively leads to a depletion of electrons in the valence bands and a finite electronic occupancy of the conduction bands. Specifically, we have investigated Fermi–Dirac distributions with temperatures ranging between 0 and 8000 K. G_0W_0 calculations on such thermalized groundstates can then provide bandstructures, which include the effect of the screening due to the thermally excited carriers. The resulting bandstructures and bandgap renormalizations are presented in Fig. 4a, b. One observes that introducing charged carriers to the conduction bands rapidly decreases the bandgap. It reaches its minimum around 2500 K with a bandgap 50% smaller than its equilibrium value and reopens for higher temperatures. This behaviour is consistent with the typical bandgap renormalization in standard semiconductors mentioned above. The pronounced double well feature of the valence band slightly flattens out as the Γ-point energy is shifted upwards (see Fig. 4a) and only for electronic temperature >4000 K the bandstructure changes significantly, which explains the upwards trend in the bandgap for high temperatures. To reach such high electronic temperatures with a laser, however, is experimentally unrealistic as it would damage the material.

We remark that, even though the applied computational procedure does not properly describe the experimental photo-excitation of electrons into conduction bands, we could expect a behaviour similar to the one described above upon intensive laser pumping.

Origin of the structural instability

Having established the importance of the structural instability in the determination of the insulating groundstate of TNSe, in this section we discuss possible origins of the structural instability. On general grounds, the structural instability is the result of the complex interplay between the electronic and the lattice degrees of freedom. The possibility of a purely electronic origin of the structural instability, namely a charge density that spontaneously breaks the orthorhombic symmetry at fixed ions position, has been recently discussed in the literature. Specifically, this possibility has been introduced at the model level in ref. [35] as the result of an electronic interaction-driven spontaneous hybridization between localized Wannier orbitals of different symmetry. Moreover, experimental data from symmetry-resolved Raman have been interpreted as signatures of quasi-critical charge

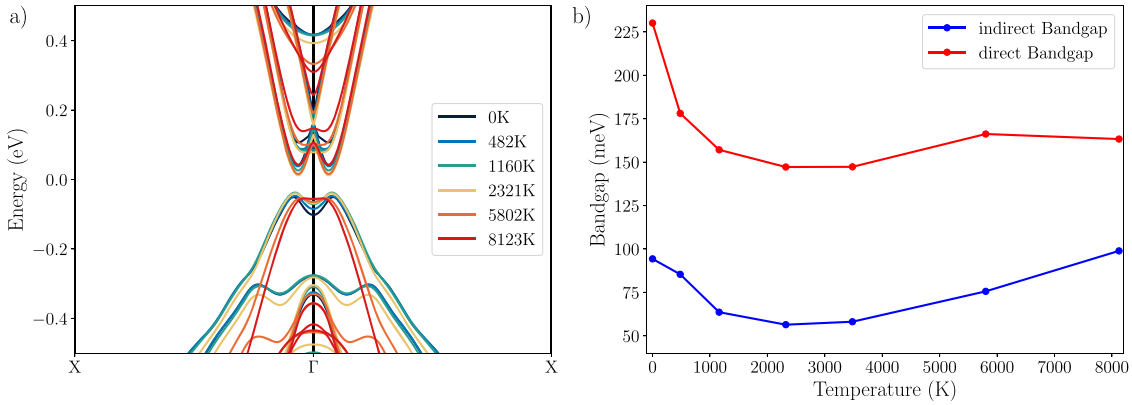

Fig. 4 Bandstructure of Ta_2NiSe_5 for different electronic temperatures. DFT+G_0W_0 calculation using different electronic smearing temperatures. **a** shows the electronic dispersion with increased temperature. The obtained bandstructures agree very well with the flat bands obtained in ARPES measurements. **b** shows the evolution of the bandgap with increasing electronic temperature. It decreases rapidly to 50% of its equilibrium value at 2000 K and increases afterwards due to an increased band flattening for very high temperatures. The direct bandgap has been measured at Γ. The figure has been adapted from our work in ref. [28].

fluctuations that are active in the corresponding symmetry channel[56].

We start by recalling the mechanism behind such an electronic instability. The mechanism can be readily understood in terms of the energetic competition between on-site (Ta-Ta and Ni-Ni) and the nearest neighbouring (Ta-Ni) density–density interaction that can render the groundstate of the system to be either metallic or insulating. In a simplified description, this energetic competition can be well understood as a problem of two electrons in two sites with on-site interaction U and inter-site interaction V. If the energy of the lowest lying orbitals in the two sites are comparable, the groundstate configuration of the problem is entirely determined by the ratio between U and V. In the limit $U \gg V$, the lowest energy configuration corresponds to the single occupation of the lowest lying orbitals on the two sites, whereas in the opposite limit $U \ll V$ the most favourable configuration is the doubly occupation of the site with the lowest energy orbital. The two configurations become quasi-degenerate for $U \sim V$ such that a coherent superposition between the two configuration due to an exchange interaction mediated by V is possible.

Assuming that in the extended system the lowest lying orbitals in the two sites contribute to the formation of two bands close to the Fermi level, the two configurations correspond respectively to a metal in which both bands are partially occupied or to an insulator in which the lowest lying band is fully occupied. The coherent superposition, instead, indicates the possibility of a spontaneous hybridization between the bands that leads to the opening of an hybridization gap. As discussed in ref. [35], this can happen only if the bands have different symmetry character and therefore an hybridization of this type would correspond to a charge density that breaks the orthorhombic lattice symmetry. Calculations based on a mean-field ansatz for a realistic model of TNSe show that the spontaneous hybridization transition can occur in a very narrow region around $U \sim 4V$ (see inset of Fig. 5), where the factor four comes from the fact that there are four neighbouring Ta atoms around each Nickel. We emphasize that the phase diagram in the inset of Fig. 5 from ref. [35] is intended to be qualitative as it is specifically calculated for a set of realistic parameters corresponding to the mBJ functional and a selection of Wannier orbitals, hence not necessarily representative for other functionals.

The smallness of this region suggests that the electronic instability relies on a delicate energetic balance between the competing metallic and insulating states, which is not guaranteed to be exactly satisfied in the real material. We therefore exploit the present full ab initio results to test this energetic balance in the

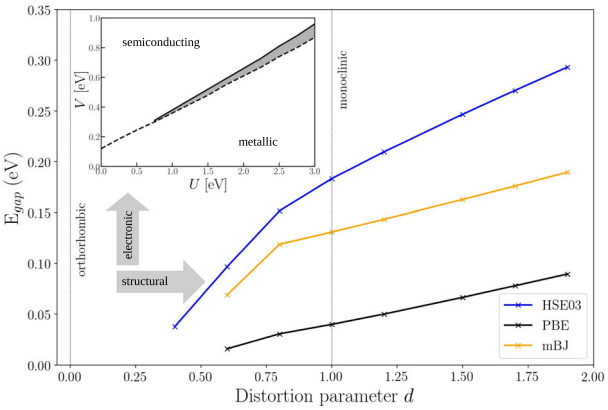

Fig. 5 Bandgap of Ta_2NiSe_5 along the phase transition. Bandgap as a function of the distortion parameter d defined in the text for different exchange correlation functionals for TNSe: for all considered exchange functionals, we obtain a positive bandgap only for finite distortions d, which then increases as a function of the distortion parameter and the functional chosen. A minimal distortion breaking all relevant lattice symmetries ($d = 0.05$) does not open a bandgap, which would be expected for an electronically driven instability (see Supplementary Note 5 and Supplementary Fig. 8). We displayed only data points that have a finite bandgap. Grey arrows indicates the bandgap opening due to structural distortion and electronic correlation using different functionals. The inset shows the phase diagram of TNSe adapted from ref. [35]. The region between dashed and solid (grey shaded) line shows the region with an electronic instability breaking the orthorhombic lattice symmetry towards the monoclinic. Above is the semiconducting region without electronic symmetry breaking and below the metallic region.

case of TNSe and, in particular, how it is affected by the lattice distortions that are neglected in the electronic instability discussion above. We do so by performing bandgap calculations, reported in Fig. 5, for different functionals on increasingly distorted structures using the distortion parameter d. To define the distortion parameter we linearly interpolate between the high-symmetric orthorhombic and low-symmetric monoclinic geometry: we parameterized this transition with a transition vector $\mathbf{v}_t$ defined as the difference between the atomic configuration of the high-symmetry and low-symmetry structure $\mathbf{v}_t = \mathbf{v}_m - \mathbf{v}_o$, with $\mathbf{v}_m$ describing the atomic configuration of the monoclinic cell and $\mathbf{v}_o$ describing the atomic configuration of the orthorhombic cell.

Using this vector, we can linearly interpolate between the orthorhombic and monoclinic structure via $\mathbf{v}_i(d) = \mathbf{v}_o + d \cdot \mathbf{v}_t$, where d is the distortion parameter. The lattice vectors are parameterized in a similar way. This means that also each of the three lattice vectors of both geometries are linearly interpolated using the difference between the monoclinic and orthorhombic lattice vectors $\mathbf{v}_{lat,t} = \mathbf{v}_{lat,m} - \mathbf{v}_{lat,o}$. Hence, the interpolated lattice vectors are $\mathbf{v}_{lat,i}(d) = \mathbf{v}_{lat,o} + d \cdot \mathbf{v}_{lat,t}$ for each of the three lattice vectors. If a gap opens as a result of the electronic instability only, we could expect that an infinitesimal distortion $d \to 0^+$ would be sufficient to stabilize an insulating groundstate with a distorted charge density. However, we observe that, independently of the functional used, a finite critical value of the distortion parameter d_c is needed in order to open a gap (see Fig. 5). This means that TNSe is indeed likely outside the region where a purely electronic instability can be expected and that a finite distortion of the lattice is critical to account for the metal–insulator transition. Nonetheless, we observe a cooperation between electronic correlations and lattice distortion in the opening of the gap. Indeed, by increasing the accuracy of the functional (from PBE to HSE), which corresponds to increasing amount of electronic exchange and correlation, the bandgap at fixed distortion is increased and the critical value of the distortion parameter d_c needed for opening a gap is significantly reduced.

We therefore conclude that, in relation to the simple mean-field phase diagram with tunable U and V interaction derived for the orthorhombic phase of TNSe, the material must be placed on the semimetallic region of the phase diagram and that the lattice distortions act in the same direction of the nearest neighbour interaction V. On the other hand, based on the previous electronic band structure results, the Sulfur compound must be placed on the semiconducting side of the phase diagram, corresponding to a larger effect of the interaction V.

As a further confirmation of the fact that the non-local interaction V is responsible for the opening of the gap in these materials, we also performed fully ab initio Hartree–Fock calculations for TNSe, which are supposed to include a larger contribution from non-local correlations: both the orthorhombic and the monoclinic phase have semiconducting groundstates with bandgaps of 436 and 836 meV, respectively (see Supplementary Fig. 11).

We finally mention that despite the fact that a purely electronic contribution is absent for TNSe we cannot exclude the system to be close enough to an electronic instability so that quasi-critical charge fluctuations can be present in the symmetry channel corresponding to the breaking of the mirror symmetries that characterizes the transition from the orthorhombic to the monoclinic phase[56]. This analysis goes beyond the scope of the present work and will be the subject of future investigations.

In the following, we focus on the possibility of having an energetically favourable electronic instability that, however, does not open a bandgap but instead stays in the metallic regime close to the orthorhombic geometry. We introduce the total energy $E \equiv E[d, \rho_-]$, as a function of two coordinates. The first one, which accounts for the lattice degrees of freedom, is the lattice distortion d. The second coordinate of the energy functional is the component ρ_- of the electronic charge density, which corresponds to a symmetry lowering from orthorhombic to monoclinic (of ref. [35]). It is defined as

$$\rho_- = \int_{x \in \text{unitcell}} |\rho(x) - \rho(R(x))| \; \mathrm{d}x, \tag{1}$$

with R being the orthorhombic symmetry operators and ρ the charge density. For the orthorhombic cmcm geometry of TNSe, four different mirror symmetries $R = \{\sigma_{A,o}, \sigma_{A,p}, \sigma_{B,o}, \sigma_{B,p}\}$ have been identified as relevant to the orthorhombic to monoclinic transition[35], where and p and o denote mirror symmetries parallel and orthogonal to the chain direction and A and B denote the corresponding one-dimensional chains in the unit cell. We will focus on these mirror symmetries in the following. In this picture, the groundstate is defined such that at d^* and ρ_-^* the total energy is minimal:

$$\frac{\partial E}{\partial d}\Big|_{d=d^*} = \frac{\partial E}{\partial \rho_-}\Big|_{\rho_- = \rho_-^*} = 0. \tag{2}$$

If the system undergoes a spontaneous electronic instability, the charge density breaks the orthorhombic lattice symmetry for infinitesimal distortions and hence:

$$\lim_{d \to 0} \rho_-(d) \neq 0. \tag{3}$$

The two possible scenarios for a lattice and an electronically driven transition are shown schematically in Fig. 6. Figure 6a shows the case of a lattice-driven phase transition. The charge density component ρ_- does not break the orthorhombic symmetries at $d = 0$ and evolves smoothly towards the groundstate of the system with increasing distortion. Figure 6b shows the case of an electronically driven phase transition where the charge density breaks the orthorhombic lattice symmetries. In this case, the charge density component ρ_- does not vanish at $d = 0$ but it is finite instead and its value increases with increasing distortion . In both cases of Fig. 6a, b, a finite d-distortion may still be needed to obtain a positive bandgap.

When we perform ab initio calculations imposing the orthorhombic symmetries, the charge density is automatically symmetrized so that $\rho_-(d = 0) = 0$ is true by construction. However, if we compute ρ_- for small lattice distortions that break the orthorhombic symmetry, we can evaluate the limit $\lim_{d \to 0} \rho_-(d)$ and verify whether an electronic instability is present. Furthermore, an electronic symmetry breaking should also result in a discontinuity in the total energy for infinitesimal lattice distortion, as a phase with a finite ρ_-^* has to lower the energy with respect to the symmetric orthorhombic phase in the electronic instability scenario. Both the computed total energy as well as ρ_- for fixed lattice distortions d are depicted in Fig. 6c, d.

Figure 6c shows that there is no discontinuity in the total energy. For the vdw-optB88 functional, the total energy decreases monotonously to its minimum for increasing d (see Supplementary Note 2 and Supplementary Fig. 1 for $q > 0.2$). For the PBE and HSE functionals, it increases first and subsequently decreases towards its minimum, which for the HSE03 functional is at around $d = 1.6$. We attribute such a non-monotonous behaviour to the fact that the distortion parameter d is defined with respect to the vdw-optB88 functional structures. This means that in the phase-space of the normal phononic mode we are not moving along the soft phonon modes but along a direction where the orthorhombic phase is a saddle point. Solving this issue would require a structure relaxation using hybrid functionals to obtain the exact soft mode coordinate, which is computationally not feasible for TNSe. Figure 6d shows the evolution of the charge density component ρ_- for different symmetry operations defined in ref. [35]. $\sigma_{A,p}$ describes the reflection symmetry parallel the Nickel chain in the xz-plane and $\sigma_{A,o}$ describes the reflection in the yz-plane orthogonal to the chain direction and along the Tantalum atoms (see inset in Fig. 6). For both reflection symmetries, ρ_- approaches 0 for $d \to 0$. This reinforces the conclusion that the transition in TNSe requires a finite lattice distortion and we do not observe a spontaneous electronic instability.

Phonon dispersion

So far, we have investigated the electronic degrees of freedom focusing on the effect of the lattice geometries. While we have introduced the concept of a structural instability in the prior

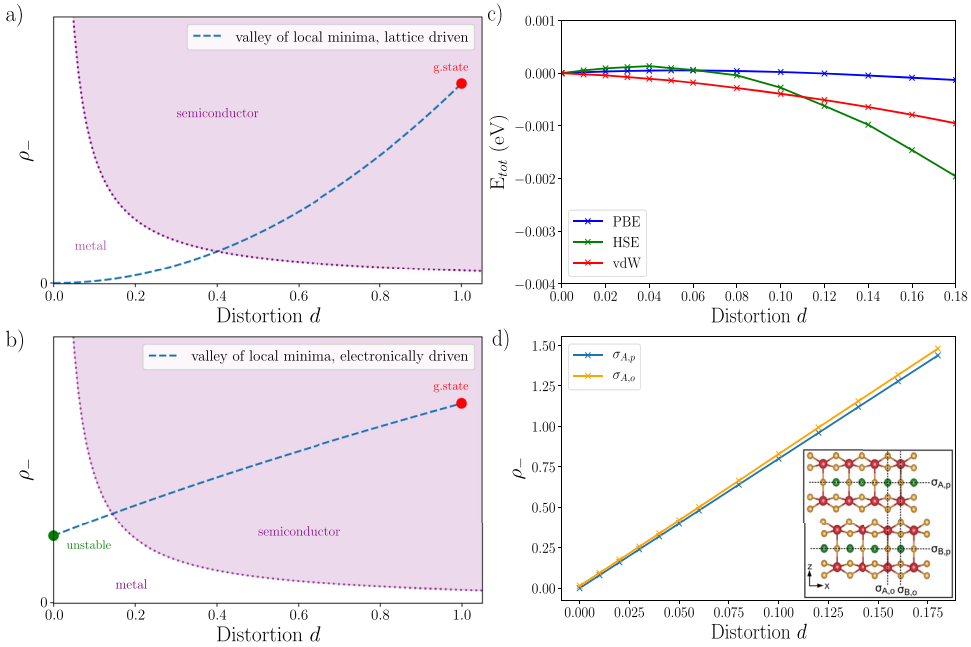

Fig. 6 Origin of the phase transition. Sketch of the energy landscape of $E[d, \rho_-]$ along the local minima valleys for **a** a lattice-driven and **b** an electronically driven phase transition. The green dot marks the groundstate defined via d^* and ρ_-^*. In the case of a lattice-driven phase transition (**a**), the charge density component ρ_- evolves smoothly from 0 to ρ_-^* as the lattice is distorted. In the case of an electronically driven phase transition, the charge density breaks the orthorhombic symmetries for infinitesimal distortions. Thus, ρ_- jumps discontinuously to a finite value (green dot marked as unstable) and evolves afterwards smoothly to the groundstate. The purple line marks that even with an electronic instability a finite d distortion may in general be needed to obtain a positive bandgap. **c** Total energy as a function of the lattice distortion for the PBE, vdw-optB88 and HSE03 functional. The total energy of the respective orthorhombic geometry was taken as reference value and set to 0. **d** Increase of the symmetry breaking parameter ρ_- with increasing lattice distortion using the HSE03 functional. If there was an electronic instability, both curves would have exhibited a discontinuity for infinitesimal lattice distortions d, with ρ_- extrapolating to a positive non-zero value. A linear fit of both curves is given by $f_{\sigma_{A,o}}(d) = 7.9964(\pm 0.0041) \cdot d + 2.2e-4(\pm 4.1e-4)$ and $f_{\sigma_{A,p}}(d) = 8.1658(\pm 0.0120) \cdot d + 2.64e-3(\pm 0.26e-3)$. The inset shows the orthorhombic symmetry planes defined by Mazza et al.[35].

sections, we show how it is related to the lattice dynamics of the crystal.

The phonon dispersion of the orthorhombic as well as the monoclinic cell of TNSe are shown in Fig. 7a: the orthorhombic cell shows two unstable optical phonon modes around the Γ-point, characterized by imaginary frequencies (indicated as negative values here), while the monoclinic cell shows no phonon instabilities.

The two unstable phonon modes belong to the B_{1g} and B_{2g} symmetry groups. Both unstable phonons lead to monoclinic distortions and become stable in the monoclinic phase. The B_{1g} leads to a $P2_1/m$ geometry and the B_{2g} mode leads to the C2/c symmetry. Just displacing the atoms within the unit cell and computing the total energy of the structure shows that the $P2_1/m$ would be favoured[36]; however, also allowing for lattice distortions, the C2/c symmetry is favoured with an energy difference of 14.4 meV per unit cell. This is in agreement with the full relaxation as well as experimental findings observing a monoclinic C2/c symmetric geometry in the low-temperature phase of TNSe[32,57]. Therefore, we can identify the B_{2g} mode as the relevant structural instability, which drives the phase transition. The eigenvector of this mode is displayed in the inset of Fig. 7a. It shows the characteristic monoclinic displacement along the chain direction, which results in a shearing of the Ta atoms around the Nickel atom (see Fig. 7c), which has been identified as the order parameter for the orthorhombic to monoclinic phase transition by Kaneko et al.[21]. Note that a similar phonon analysis using ab initio methods has been performed in ref. [36] and our calculations agree with this study.

For the sake of comparison, we have performed a calculation of the phononic spectrum at the Γ-point for both geometries of TNS. We find one phononic instability in the orthorhombic structure, which becomes stable in the monoclinic phase (see Supplementary Table 7). The instability has B_{2g} symmetry and drives, similarly to the TNSe case, the orthorhombic-to-monoclinic phase transition, which is consistent with the monoclinic groundstate being the energetically favoured one.

To investigate the evolution of the phonon instabilities when transforming the crystal from orthorhombic to monoclinic, we have performed calculations on increasingly distorted structures using the d distortion parameter introduced in the previous section. Performing phonon calculations, we obtained the phonon spectra and eigenvectors at the Γ-point for each of the distorted geometries. To follow the evolution of the phonon energies during the structural transition, we have computed the overlap between the orthorhombic eigenvectors of the two phonon instabilities with the phononic eigenvectors of all modes at a given value of the distortion parameter d. The result is displayed in Fig. 7c, d where the marker size is proportional to such overlaps. Note that the phonon eigenvectors for a given distortion d form an orthonormal system. Therefore, no overlap is visible at $d = 0$ for the two unstable modes. As the structure is transformed to the monoclinic cell, the different phonons start hybridizing that leads to non-zero overlap of the unstable orthorhombic phonons and the phonons at $d \neq 0$. We observe that the two unstable phonons are being stabilized along the phase transition and hybridize predominantly into a pair of monoclinic phonons. The unstable B_{2g} has the strongest overlap with the monoclinic 3.4 and 1.9 THz phonon modes and the unstable B_{1g} has the strongest overlap with the monoclinic 3.6 and 1.4 THz modes. In section "Electron–phonon coupling," we will show that the two monoclinic B_{2g} phonons couple strongly to the electronic degrees of freedom.

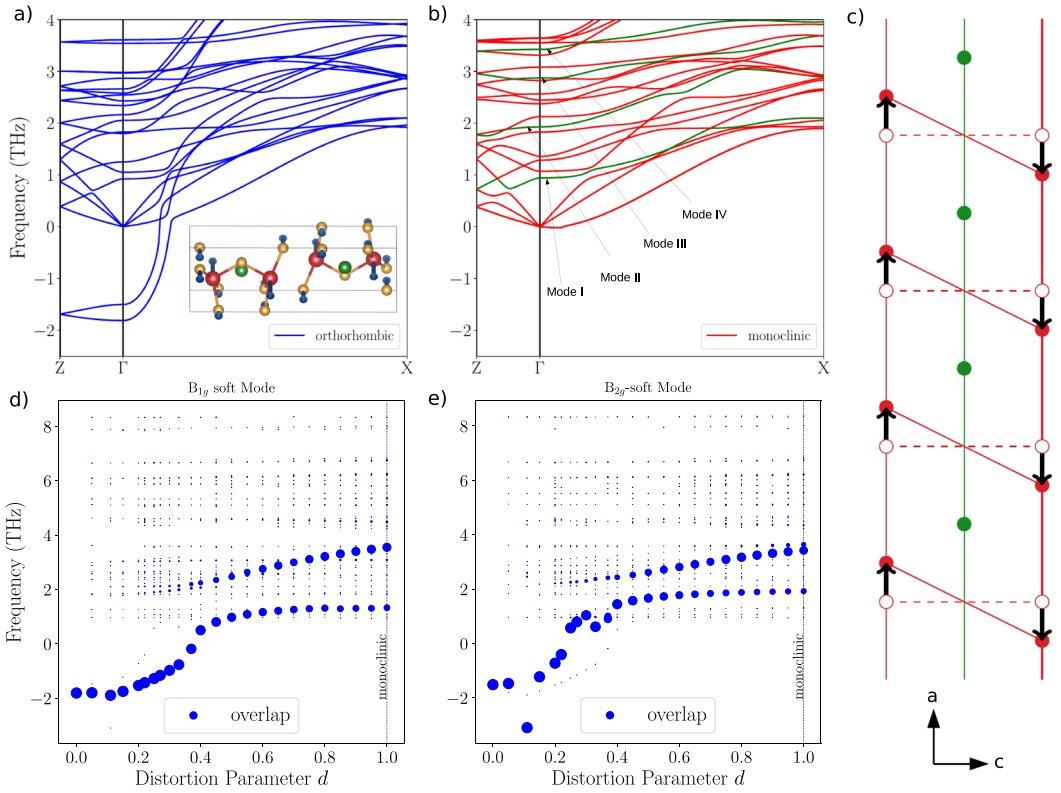

Fig. 7 Phonon properties of Ta_2NiSe_5. a TNSe phonon dispersion using the vdW-optB88 functional for the orthorhombic phase. It shows two optical instabilities, one of which is the B_{2g} soft mode. The inset shows the eigenvector of this mode. **b** Phonon dispersion of the monoclinic phase. The two unstable modes become stable. We highlighted the phonon branches of the four optical phonons I–IV for which the coupling to the electron bandstructure is discussed in the section "Electron–phonon coupling." The lowest acoustical phonon in the monoclinic phase shows an unnatural behaviour close to Γ, which is an artefact of the numerical procedure applied. **c** Schematic illustration of the shearing of the Tantalum atoms around the Nickel atoms, which has also been discussed in refs. [21,36] and is a key signature of the phase transition. **d**, **e** show the overlap of the unstable orthorhombic phonon eigenvectors with the phonon eigenvectors at different distortions d. The position of the blue dots show the phonon eigenenergy of the corresponding mode and the size the overlap between the mode eigenvector and the unstable orthorhombic mode B_{1g} mode (**d**) and B_{2g} mode (**e**) eigenvector. At $d = 0$, we have the orthorhombic geometry and at $d = 1$ the monoclinic geometry. One sees that the orthorhombic eigenvectors have maximal overlaps with the modes at 3.4 and 3.6 THz in the monoclinic phase.

Further analysis of the phonon symmetries allows us to identify all three B_{2g} and eight A_g phonon modes of the orthorhombic and all A_g phonon modes of the monoclinic geometry. Their comparison with the phononic peak positions from recent experimental Raman measurements that are sensitive to B_{2g} and A_g symmetry channel[33,56,58,59] shows a good agreement of all monoclinic A_g modes, except for one, and all orthorhombic A_g modes, even if our results are at $T = 0$. Only the first two B_{2g} modes, which are labelled 2 and 5 in the orthorhombic phase, and mode 5 in the monoclinic phase show a substantial energy difference between the calculated and the experimental results (see Figs. 8 and 9). In the most recent Raman experiments, no soft mode is reported[33,56,58–60] and the second B_{2g} mode (labelled 5) differs by roughly 0.7 THz from the theoretically calculated value at $T = 0$ K. Note that Kim et al.[56] identify mode 5 as being almost degenerate with mode 3 in the orthorhombic phase and it evolves into mode 5 of the monoclinic phase (see curve at 225 K), where we also see a small discrepancy with our calculation. The two B_{2g} modes exhibit a significant Fano-like broadening, while all other Raman active modes have a sharp lineshape. It is conceivable that the electronic structure methods used here do not properly capture all coupling channels of the phonon modes to the electronic degrees of freedom, which could be responsible for these effects. Another possible explanation are inelastic phonon–phonon contributions due to anharmonic effects that are present for the two B_{2g} modes. At the experimental temperature, phonon anharmonicity effects are expected to play a major role in renormalizing the phonon energies and stabilizing the unstable modes, as has been demonstrated in other materials exhibiting a soft mode-mediated phase transition[61]. This is especially relevant for the soft modes, which would explain why a very good agreement is observed for the other Raman modes even without including temperature effects. The anharmonic coupling of the soft mode to the continuum of other phononic modes could also be the source of the broadening of the Raman peak in the region just below 2 THz, which has been instead attributed to the coupling of the phonon to an excitonic instability. The idea of the fundamental role of phonon anharmonicity is supported by recent experimental Raman measurements on TNS by Ye et al.[33]. Indeed it is shown that, even though TNS undergoes a structural phase transition, no phonon softening is observed in the Raman data around the transition temperature at $T = 120$ K. As in the case of TNSe, the authors claim that the phase transition is the result of an acoustic mode softening, which in this case is coupled to a ferroelastic instability rather than an excitonic instability. In contrast, our calculations do not show softening of the acoustic modes for both TNSe and TNS but rather soft Raman active B_{2g} modes (see Supplementary Fig. 7). Therefore, the lack of phonon softening in the Raman measurements in TNS is likely the result of the temperature stabilization of that phonon, as explained above, and provides a further support to the structural similarities between TNS and TNSe. A detailed investigation of the temperature effects in the phonon spectrum to fully corroborate this argumentation will be

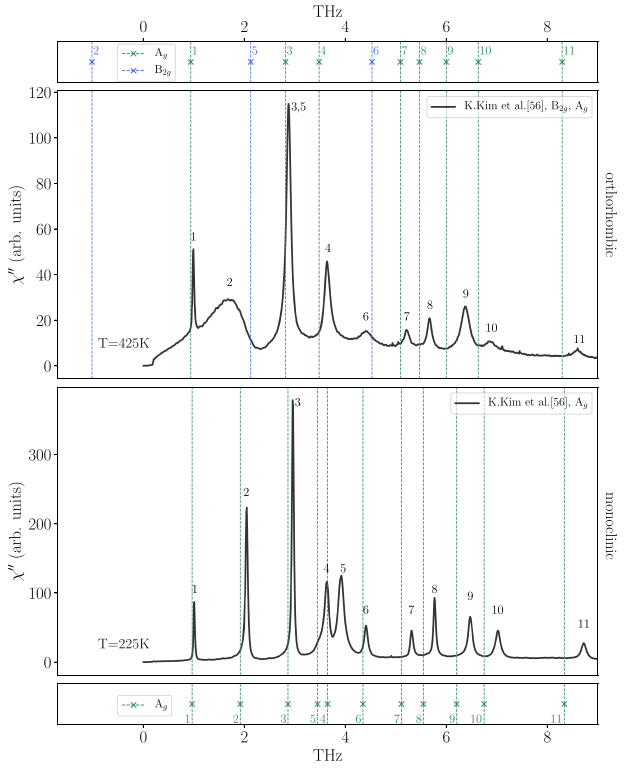

Fig. 8 Comparison of the Raman data from Kim et al.[56] with our theory results. Comparison of the theoretically calculated phonon eigenenergies at $T = 0$ K with the Raman spectra provided by Kim et al.[56]. The top panel shows the orthorhombic phonon spectrum and the bottom panel the monoclinic phonon spectrum. Note that peaks 3 and 5 are almost degenerate in energy and peak 5 only appears in the B_{2g}-channel with a much smaller amplitude than peak 3, which appears in the A_g channel. The theory spectra are obtained at $T = 0$ K and are in good agreement with Raman spectra. Only the first two B_{2g} modes of the orthorhombic geometry (peaks 2 and 5) differ substantially from their experimental values. This is consistent with these peaks having a significant broadening. The numerals in the experimental plots label the experimentally measured peaks by Kim et al.[56]. We assigned those numbers to the corresponding energies from our theory calculations by minimizing the energy differences and following the modes across the transition.

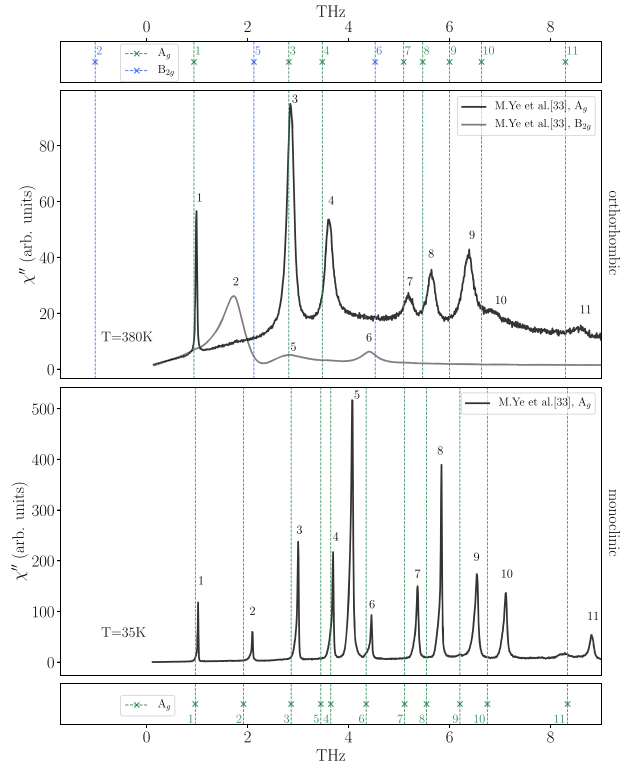

Fig. 9 Comparison of the Raman data from Ye et al.[33] with the theory results. Comparison of the theoretically calculated phonon eigenenergies at $T = 0$ K with the Raman spectra provided by Ye et al.[33]. The top panel shows the orthorhombic phonon spectrum and the bottom panel the monoclinic phonon spectrum on a linear scale. The theory spectra are obtained at $T = 0$ K and are in good agreement with the Raman spectrum. Only the first two B_{2g} modes of the orthorhombic geometry differ substantially from their experimental values. This is consistent with these peaks having a significant broadening. The numerals in the experimental plots label the experimentally measured peaks. We assigned those numbers to the corresponding energies from our theory calculations by minimizing the energy differences and following the modes across the transition.

topic of future work. In the following section, we investigate the coupling of such B_{2g} modes to the electronic bandstructure using a frozen phonon approach. We found that especially phononic modes, which displace the Tantalum and Nickel atoms along the chain direction of the crystal, such as the orthorhombic B_{2g} modes, strongly modify the electronic bandstructure and hence could in turn be renormalized.

Electron–phonon coupling

We conclude our work by demonstrating the intimate coupling between the electronic and nuclear degrees of freedom by highlighting the influence of specific phononic modes on the electronic bandstructure. Time-resolved ARPES measurements by Baldini et al. find that the gap presents oscillatory behaviour under photoexcitation[28]. The authors show that the momentum integrated photoelectron intensity is dominated by 4 frequency components: 0.98, 2.11, 3.0, and 3.67 THz. The four frequencies can be identified as the frequencies of Raman active phonons, and using our phonon dispersion calculation (Fig. 7a), we can identify the corresponding modes, with mode I at 1.1 THz, mode II at 1.9 THz, mode III at 2.9 THz and mode IV at 3.4 THz. We observe that the modes II and IV have B_{2g} symmetry and show the characteristic shearing with respect to the Tantalum atoms around the Nickel atoms, while the modes I and III that have A_g symmetry do not exhibit this shearing. They can be identified with the peaks 1, 2, 3 and 5 in the Raman measurements of Figs. 8 and 9. Mode IV mode can also be identified as the monoclinic counterpart of the B_{2g} soft mode, which is unstable in the orthorhombic geometry (see Fig. 7e).

To quantify how strongly the above discussed phonons couple to the electrons, we have calculated their effect on the electronic bandstructure by displacing the atoms along the phonon eigenmodes by an amount equal to the square root of their mean-squared displacement at zero temperature for both the positive and negative direction. The resulting bandstructures using the G_0W_0 method are shown in Fig. 10 (see Supplementary Fig. 12 for the PBE results). We see that the modes I and III show little influence, whereas both B_{2g} modes have a strong impact on the electronic structure. We stress that both of these modes exhibit the characteristic shearing of the Ta atoms around the Nickel atom in chain direction, which we also observed during the structural phase transition (see Fig. 7c) . For mode IV, the average gap between positive and negative displacement is larger than the equilibrium gap. Therefore, we expect a small increase of around 21 meV of the bandgaps predicted in the previous

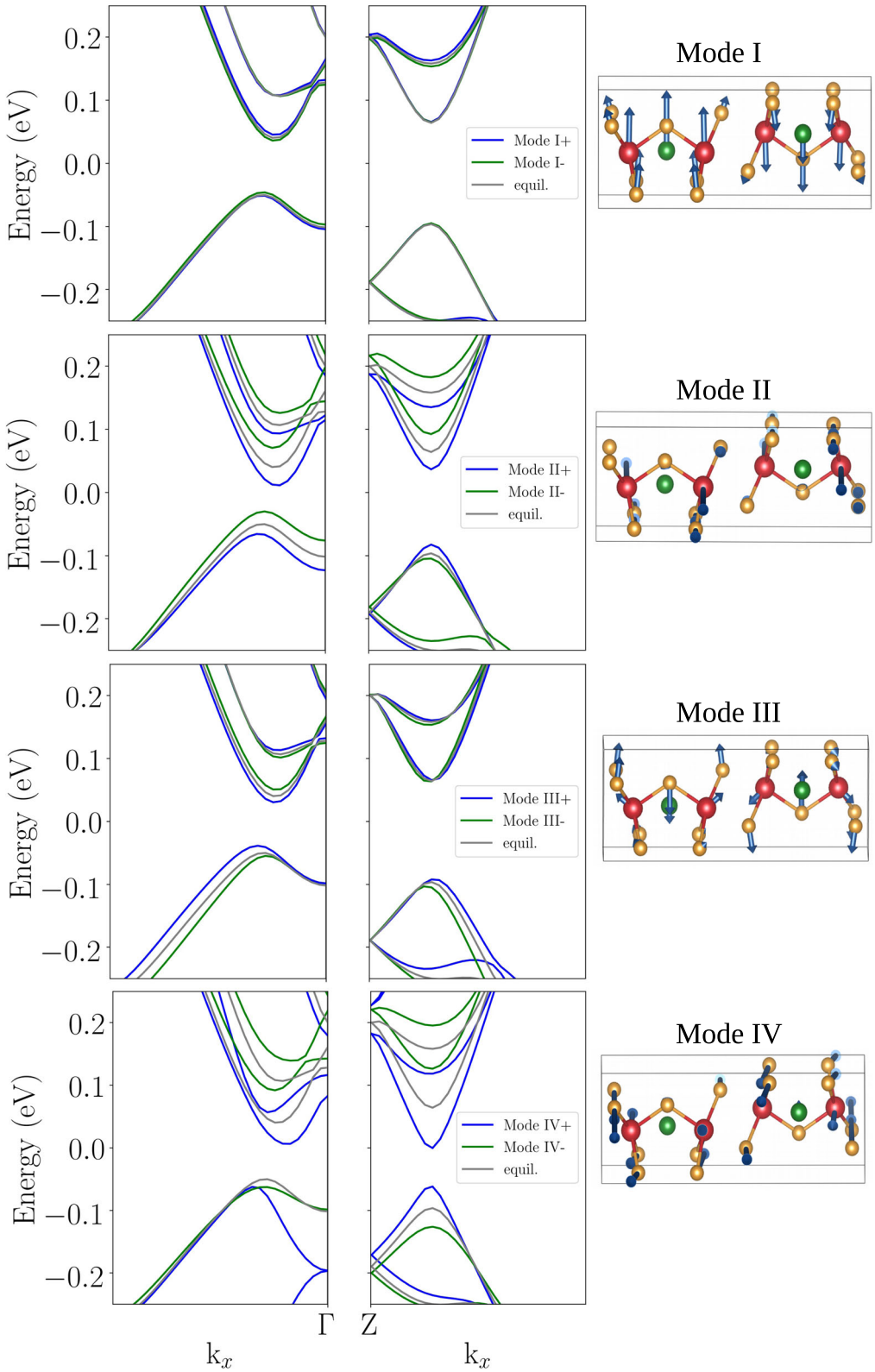

Fig. 10 Frozen phonon bandstructure. PBE+G_0W_0 calculation using the mean-squared displacement at $T = 0$ K along different phonon eigenvectors in both positive and negative direction. The bandstructure couples strongly to the B_{2g} phonon modes II and IV at 2 and 3.4 THz, which exhibit the characteristic shearing of the Ta atoms. The figure has been adapted from our work in ref. [28].

section due to the coupling of this phonon to the electronic degrees of freedom.

These results, beside confirming the strong influence of phonons on the electronic structure, hint towards the possibility of modulating the electronic bandgap through an external pumping of the above phononic modes.

DISCUSSION

We have shown that the orthorhombic phase of both TNSe and TNS is unstable at low temperatures and exhibits a soft phonon mode, which signals the structural transition to the monoclinic phase.

Performing electronic bandstructure calculations using different exchange correlation functionals, as well as calculations using the G_0W_0 approximation, we have proven that in TNSe the structural transition drives the metal-to-semiconducting phase transition, with an indirect bandgap that is comparable to the experimental results[26,27], while in TNS the semiconductive electronic nature is preserved. This demonstrates that without the structural transition the experimentally observed gap opening at the critical temperature cannot be explained. At the same time, our ab initio results show that no excitonic effects are necessary to explain the experimental evidences. Furthermore, during the structural transition a significant flattening of the valence bands is observed which is enhanced by electronic heating leading to almost flat bands, which are in agreement with recently measured (pump–probe) ARPES signatures[28].

The electronic heating shows that the bandgap never closes for increasing electronic temperatures but shows the expected renormalization effects of standard semiconductors due to the increased carrier density.

We discussed the possible origins of the structural transition in relation to the scenario of a purely electronic instability occurring at fixed ion positions and concluded that a structural distortion is required in order to observe a metal–insulator transition in TNSe. This is supported by scans of the total energy landscape and charge density as a function of the relevant distortion parameters, which show no sign of an electronic instability.

Investigating the change of the electronic bandstructure for experimentally relevant phonon modes, we found that the electrons tend to couple stronger to the phonon modes, which displace along the chain direction and induce the characteristic shearing of the Ta atoms around the Ni atom. Especially the 3.4 THz phonon mode is expected to lead to a small additional bandgap opening through the thermal occupation of this mode. We conclude that, in the low-temperature phase, TNSe and TNS behave as standard semiconductors.

METHODS

Computational details

All DFT and G_0W_0 calculations have been performed with the Vienna Ab initio Simulation Package (VASP)[62–66], and in the case of phonon calculations, we additionally used phonopy to compute phonon dispersions[67]. For the interpolation of the G_0W_0 bandstructure, we have used the wannier90 package[68]. All calculations have made use of the PBE pseudopotential set generated with VASP[69].

The structural relaxations have been performed on a $24\times4\times6$ k-mesh with an energy cutoff of 460 meV. A total free energy change of $1e{-}6$ eV has been used as cutoff criterion, which led to forces of 2.8 meV/angstrom per ion or less. The resulting input structures are shown in section 1 of the Supplementary Information. The phonon dispersion calculation has been performed using the vdw-optB88 functional and a $4\times2\times1$ supercell with a $4\times4\times3$ k-mesh. The post-processing has been performed with the phonopy package[67]. The calculation of the phonon spectra at Γ that are compared to the Raman data has been performed on a $48\times4\times6$ k-mesh using a single unit cell. The calculation of the phonon overlaps as a function of the distortion parameter d has been performed on a $16\times8\times3$ k-mesh.

The electronic bandstructure calculations have been performed on a $24\times8\times6$ k-mesh for the PBE functional and a $16\times4\times4$ k-mesh for the mBJ and HSE hybrid functionals and the Hartree–Fock calculation. The mBJ functional calculated self-consistently a c value of 1.2578 for the orthorhombic and a c-value of 1.2636 for the monoclinic phase of TNSe. For TNS, c is 1.2620 for both structural phases. The bandstructures have been computed along the path $M=(\frac{\pi}{a},0,\frac{\pi}{c})$, $Z=(0,0,\frac{\pi}{c})$, $\Gamma=(0,0,0)$ and $X=(\frac{\pi}{a},0,0)$.

The G_0W_0 calculations have been performed on a $12\times4\times2$ k-mesh with 160 frequencies ω and 1160 states with a 100 meV energy cutoff. The Wannierization has been performed with the Wannier90 package[68]. A convergence study of the relevant parameters for the presented G_0W_0 calculation can be found in the Supplementary Note 7 and Supplementary Figs. 13–15.

DATA AVAILABILITY

The authors declare that the main data supporting the findings of this study are contained within the paper and its associated Supplementary Information. All other relevant data are available from the corresponding author upon reasonable request.

CODE AVAILABILITY

The VASP software package is available at https://www.vasp.at/. The open-source software packages Wannier90 is available at http://www.wannier.org/ under the GNU General Public License (v2). The open-source phonopy package is available at https://phonopy.github.io/phonopy/ under the BSD license.

Received: 16 June 2021; Accepted: 19 November 2021;
Published online: 20 December 2021

REFERENCES

1. Kohn, W. Excitonic phases. *Phys. Rev. Lett.* **19**, 439–442 (1967).
2. Jérome, D., Rice, T. M. & Kohn, W. Excitonic insulator. *Phys. Rev.* **158**, 462–475 (1967).
3. Mott, N. F. The transition to the metallic state. *Philos. Mag.* **6**, 287–309 (1961).
4. Keldysh, L. V. & Kozlov, A. N. Collective properties of excitons in semiconductors. *Sov. Phys. JETP* **27**, 978 (1968).
5. Halperin, B. I. & Rice, T. M. Possible anomalies at a semimetal-semiconductor transistion. *Rev. Mod. Phys.* **40**, 755–766 (1968).
6. Kozlov, A. The metal-dielectric divalent crystal phase transition. *Sov. Phys. JETP* **21**, 790 (1965).
7. Cercellier, H. et al. Evidence for an excitonic insulator phase in $1T-TiSe_2$. *Phys. Rev. Lett.* **99**, 146403 (2007).
8. Kogar, A. et al. Signatures of exciton condensation in a transition metal dichalcogenide. *Science* **358**, 1314–1317 (2017).
9. Bucher, B., Steiner, P. & Wachter, P. Excitonic insulator phase in $TmSe_{0.45}Te_{0.55}$. *Phys. Rev. Lett.* **67**, 2717–2720 (1991).
10. Ma, L. et al. Strongly correlated excitonic insulator in atomic double layers. *Nature* **598**, 585–589 (2021).
11. Jia, Y. et al. Evidence for a monolayer excitonic insulator Preprint at https://arxiv.org/abs/2010.05390 (2020).
12. Varsano, D., Palummo, M., Molinari, E. & Rontani, M. A monolayer transition-metal dichalcogenide as a topological excitonic insulator. *Nat. Nanotechnol.* **15**, 367–372 (2020).
13. Gupta, S., Kutana, A. & Yakobson, B. I. Heterobilayers of 2d materials as a platform for excitonic superfluidity. *Nat. Commun.* **11**, 2989 (2020).
14. Varsano, D. et al. Carbon nanotubes as excitonic insulators. *Nat. Commun.* **8**, 1461 (2017).
15. Li, Z. et al. Possible excitonic insulating phase in quantum-confined sb nanoflakes. *Nano Lett.* **19**, 4960–4964 (2019).
16. Li, J. I. A., Taniguchi, T., Watanabe, K., Hone, J. & Dean, C. R. Excitonic superfluid phase in double bilayer graphene. *Nat. Phys.* **13**, 751–755 (2017).
17. Perali, A., Neilson, D. & Hamilton, A. R. High-temperature superfluidity in double-bilayer graphene. *Phys. Rev. Lett.* **110**, 146803 (2013).
18. Hu, Y., Venderbos, J. W. F. & Kane, C. L. Fractional excitonic insulator. *Phys. Rev. Lett.* **121**, 126601 (2018).
19. Du, L. et al. Evidence for a topological excitonic insulator in inas/gasb bilayers. *Nat. Commun.* **8**, 1971 (2017).

20. Ataei, S. S., Varsano, D., Molinari, E. & Rontani, M. Evidence of ideal excitonic insulator in bulk mos(2) under pressure. *Proc. Natl Acad. Sci. USA* **118**, e2010110118 (2021).
21. Kaneko, T., Toriyama, T., Konishi, T. & Ohta, Y. Orthorhombic-to-monoclinic phase transition of Ta_2NiSe_5 induced by the bose-einstein condensation of excitons. *Phys. Rev. B* **87**, 035121 (2013).
22. Wakisaka, Y. et al. Excitonic insulator state in Ta_2NiSe_5 probed by photoemission spectroscopy. *Phys. Rev. Lett.* **103**, 026402 (2009).
23. Seki, K. et al. Excitonic bose-einstein condensation in Ta_2NiSe_5 above room temperature. *Phys. Rev. B* **90**, 155116 (2014).
24. Watson, M. D. et al. Band hybridization at the semimetal-semiconductor transition of Ta_2NiSe_5 enabled by mirror-symmetry breaking. *Phys. Rev. Res.* **2**, 013236 (2020).
25. Tang, T. et al. Non-coulomb strong electron-hole binding in Ta_2NiSe_5 revealed by time- and angle-resolved photoemission spectroscopy. *Phys. Rev. B* **101**, 235148 (2020).
26. Lu, Y. F. et al. Zero-gap semiconductor to excitonic insulator transition in Ta_2NiSe_5. *Nat. Commun.* **8**, 14408 (2017).
27. Lee, J. et al. Strong interband interaction in the excitonic insulator phase of Ta_2NiSe_5. *Phys. Rev. B* **99**, 075408 (2019).
28. Baldini, E. et al. The spontaneous symmetry breaking in Ta_2NiSe_5 is structural in nature Preprint at https://arxiv.org/abs/2007.02909 (2020).
29. Kaneko, T., Toriyama, T., Konishi, T. & Ohta, Y. Electronic structure of Ta_2NiSe_5 as a candidate for excitonic insulators. *J. Phys. Conf. Ser.* **400**, 032035 (2012).
30. Nakano, A. et al. Antiferroelectric distortion with anomalous phonon softening in the excitonic insulator Ta_2NiSe_5. *Phys. Rev. B* **98**, 045139 (2018).
31. Di Salvo, F. et al. Physical and structural properties of the new layered compounds Ta_2NiS_5 and Ta_2NiSe_5. *J. Less Common Met.* **116**, 51–61 (1986).
32. Sunshine, S. A. & Ibers, J. A. Structure and physical properties of the new layered ternary chalcogenides tantalum nickel sulfide (Ta_2NiS_5) and tantalum nickel selenide (Ta_2NiSe_5). *Inorg. Chem.* **24**, 3611–3614 (1985).
33. Ye, M. et al. Lattice dynamics of the excitonic insulator $Ta_2Ni(Se_{1-x}S_x)_5$. *Phys. Rev. B* **104**, 045102 (2021).
34. Mu, K. et al. Electronic structures of layered Ta_2NiS_5 single crystals revealed by high-resolution angle-resolved photoemission spectroscopy. *J. Mater. Chem. C* **6**, 3976–3981 (2018).
35. Mazza, G. et al. Nature of symmetry breaking at the excitonic insulator transition: Ta_2NiSe_5. *Phys. Rev. Lett.* **124**, 197601 (2020).
36. Subedi, A. Orthorhombic-to-monoclinic transition in Ta_2NiSe_5 due to a zone-center optical phonon instability. *Phys. Rev. Mater.* **4**, 083601 (2020).
37. Klimeš, Jcv, Bowler, D. R. & Michaelides, A. Van der waals density functionals applied to solids. *Phys. Rev. B* **83**, 195131 (2011).
38. Klimeš, J., Bowler, D. R. & Michaelides, A. Chemical accuracy for the van der Waals density functional. *J. Phys. Condens. Matter* **22**, 022201 (2009).
39. Perdew, J. P., Burke, K. & Ernzerhof, M. Generalized gradient approximation made simple. *Phys. Rev. Lett.* **77**, 3865–3868 (1996).
40. Tran, F. & Blaha, P. Accurate band gaps of semiconductors and insulators with a semilocal exchange-correlation potential. *Phys. Rev. Lett.* **102**, 226401 (2009).
41. Becke, A. D. & Johnson, E. R. A simple effective potential for exchange. *J. Chem. Phys.* **124**, 221101 (2006).
42. Becke, A. D. & Roussel, M. R. Exchange holes in inhomogeneous systems: a coordinate-space model. *Phys. Rev. A* **39**, 3761–3767 (1989).
43. Heyd, J., Scuseria, G. E. & Ernzerhof, M. Hybrid functionals based on a screened coulomb potential. *J. Chem. Phys.* **118**, 8207–8215 (2003).
44. Sugimoto, K., Nishimoto, S., Kaneko, T. & Ohta, Y. Strong coupling nature of the excitonic insulator state in Ta_2NiSe_5. *Phys. Rev. Lett.* **120**, 247602 (2018).
45. Li, L. et al. Strong in-plane anisotropies of optical and electrical response in layered dimetal chalcogenide. *ACS Nano* **11**, 10264–10272 (2017).
46. Larkin, T. I. et al. Giant exciton fano resonance in quasi-one-dimensional Ta_2NiSe_5. *Phys. Rev. B* **95**, 195144 (2017).
47. van Schilfgaarde, M., Kotani, T. & Faleev, S. Quasiparticle self-consistent gw theory. *Phys. Rev. Lett.* **96**, 226402 (2006).
48. Onida, G., Reining, L. & Rubio, A. Electronic excitations: density-functional versus many-body green's-function approaches. *Rev. Mod. Phys.* **74**, 601–659 (2002).
49. Hybertsen, M. S. & Louie, S. G. First-principles theory of quasiparticles: calculation of band gaps in semiconductors and insulators. *Phys. Rev. Lett.* **55**, 1418–1421 (1985).
50. Hybertsen, M. S. & Louie, S. G. Electron correlation in semiconductors and insulators: band gaps and quasiparticle energies. *Phys. Rev. B* **34**, 5390–5413 (1986).
51. Hedin, L. New method for calculating the one-particle green's function with application to the electron-gas problem. *Phys. Rev.* **139**, A796–A823 (1965).
52. Salpeter, E. E. & Bethe, H. A. A relativistic equation for bound-state problems. *Phys. Rev.* **84**, 1232–1242 (1951).
53. Sander, T., Maggio, E. & Kresse, G. Beyond the tamm-dancoff approximation for extended systems using exact diagonalization. *Phys. Rev. B* **92**, 045209 (2015).
54. Spataru, C. D., Benedict, L. X. & Louie, S. G. Ab initio calculation of band-gap renormalization in highly excited gaas. *Phys. Rev. B* **69**, 205204 (2004).
55. Beni, G. & Rice, T. M. Theory of electron-hole liquid in semiconductors. *Phys. Rev. B* **18**, 768–785 (1978).
56. Kim, K. et al. Direct observation of excitonic instability in Ta_2NiSe_5. *Nat. Commun.* **12**, 1969 (2021).
57. Nakano, A. et al. Pressure-induced coherent sliding-layer transition in the excitonic insulator Ta_2NiSe_5. *IUCrJ* **5**, 158–165 (2018).
58. Volkov, P. A. et al. Critical charge fluctuations and emergent coherence in a strongly correlated excitonic insulator. *NPJ Quantum Mater.* **6**, 52 (2021).
59. Volkov, P. A. et al. Failed excitonic quantum phase transition in $Ta_2Ni(Se_{1-x}S_x)_5$Preprint at https://arxiv.org/abs/2104.07032 (2021).
60. Kim, M.-J. et al. Phononic soft mode and strong electronic background behavior across the structural phase transition in the excitonic insulator Ta_2NiSe_5 (with erratum) Preprint at https://arxiv.org/abs/2007.01723 (2021).
61. Zhou, J.-J., Hellman, O. & Bernardi, M. Electron-phonon scattering in the presence of soft modes and electron mobility in $SrTiO_3$ perovskite from first principles. *Phys. Rev. Lett.* **121**, 226603 (2018).
62. Kresse, G. & Hafner, J. Ab initio molecular dynamics for liquid metals. *Phys. Rev. B* **47**, 558–561 (1993).
63. Kresse, G. & Furthmüller, J. Efficient iterative schemes for ab initio total-energy calculations using a plane-wave basis set. *Phys. Rev. B* **54**, 11169–11186 (1996).
64. Kresse, G. & Furthmüller, J. Efficiency of ab-initio total energy calculations for metals and semiconductors using a plane-wave basis set. *Comp. Mater. Sci.* **6**, 15–50 (1996).
65. Kresse, G. & Hafner, J. Norm-conserving and ultrasoft pseudopotentials for first-row and transition elements. *J. Phys. Condens. Matter* **6**, 8245–8257 (1994).
66. Kresse, G. & Joubert, D. From ultrasoft pseudopotentials to the projector augmented-wave method. *Phys. Rev. B* **59**, 1758–1775 (1999).
67. Togo, A. & Tanaka, I. First principles phonon calculations in materials science. *Scr. Mater.* **108**, 1–5 (2015).
68. Mostofi, A. A. et al. An updated version of wannier90: a tool for obtaining maximally-localised wannier functions. *Comput. Phys. Commun.* **185**, 2309–2310 (2014).
69. Kresse, G. & Joubert, D. From ultrasoft pseudopotentials to the projector augmented-wave method. *Phys. Rev. B* **59**, 1758–1775 (1999).

ACKNOWLEDGEMENTS

We are grateful to E. Baldini, I. Mazin and Yann Gallais for enlightening discussions throughout the course of this work. We would like to thank M. Ye, G. Blumberg, K. Kim, B.J. Kim, M.J. Kim and S. Kaiser for sharing the experimental data of their Raman measurements and valuable discussions. This work is supported by the European Research Council (ERC-2015-AdG-694097), Grupos Consolidados (IT1249-19) and the Flatiron Institute, a division of the Simons Foundation. We acknowledge funding by the Deutsche Forschungsgemeinschaft (DFG) under Germany's Excellence Strategy - Cluster of Excellence Advanced Imaging of Matter (AIM) EXC 2056 - 390715994 and by the Deutsche Forschungsgemeinschaft (DFG, German Research Foundation) - SFB-925 - project 170620586. Support by the Max Planck Institute - New York City Center for Non-Equilibrium Quantum Phenomena is acknowledged. S.L. acknowledges support from the Alexander von Humboldt foundation. G.M. acknowledges support of the Swiss National Science Foundation FNS/SNF through an Ambizione grant.

AUTHOR CONTRIBUTIONS

A.R. and S.L. designed the project. L.W. performed the computations under the supervision of S.L. All authors discussed the computational results and contributed to the writing and revision of the manuscript.

FUNDING

Open Access funding enabled and organized by Projekt DEAL.

COMPETING INTERESTS

The authors declare no competing interests.

ADDITIONAL INFORMATION

Supplementary information The online version contains supplementary material available at https://doi.org/10.1038/s41524-021-00675-6.

Correspondence and requests for materials should be addressed to Lukas Windgätter, Simone Latini or Angel Rubio.

Reprints and permission information is available at http://www.nature.com/reprints

Publisher's note Springer Nature remains neutral with regard to jurisdictional claims in published maps and institutional affiliations.

4.6 Publication V: The spontaneous symmetry breaking in Ta_2NiSe_5 is structural in nature

State of the Art

While the electronic groundstate properties across the phase transition [20, 30, 31, 98, 106] in TNSe has been investigated already the role of the structural degrees of freedom was still not well understood. The goal of this joint theoretical and experimental work is to understand the bandgap dynamics using time resolved ARPES measurements upon prior excitation via a pump pulse. With this setup we would like to understand the gap response to such external perturbations.

Main Findings

Using this experimental pump probe setup we are able to show that upon prior excitation the electronic bandgap responds on an ionic timescale (ps-regime) rather than an electronic timescale (fs-regime). The bandgap at Gamma is modulated by four phononic modes. Using DFT + GW calculations we are able to show that two of these modes couple strongly to the electronic states at the bandedge and renormalize the bandgap strongly. Remarkably one of these modes is the soft mode partner that drives the structural phase transition. Furthermore, we are able to show that upon increasing the electronic temperature the conjectured excitonic condensate cannot be melted, i.e. no bandgap closing is being observed. This leads us to the same conclusion as in our purely theoretical work in publication IV that the phase transition in TNSe is predominantly structural in nature.

Status and Publication Details

This paper has been published as preprint on the arXiv server [90] and is currently being reviewed for publication in Physical Review X. This publication has a Supplementary Information that is being published at `https://arxiv.org/pdf/2007.02909.pdf` and not contained in this thesis.

Contribution

I performed all ab-initio calculations (Density Functional Theory and GW) and created the corresponding figures. All authors have contributed to the analysis of the data and the writing of the manuscript. A detailed list of all authors contributions is included in the publication.

The spontaneous symmetry breaking in Ta_2NiSe_5 is structural in nature

Edoardo Baldini,[1] Alfred Zong,[1] Dongsung Choi,[2] Changmin Lee,[1] Marios H. Michael,[3] Lukas Windgaetter,[4] Igor I. Mazin,[5] Simone Latini,[4] Doron Azoury,[1] Baiqing Lv,[1] Anshul Kogar,[1] Yao Wang,[3] Yangfan Lu,[6] Tomohiro Takayama,[6,7] Hidenori Takagi,[6,7] Andrew J. Millis,[8,9] Angel Rubio,[4,9,10] Eugene Demler,[3] and Nuh Gedik[1]

[1]*Department of Physics, Massachusetts Institute of Technology, 02139 Cambridge, Massachusetts, USA*
[2]*Department of Electrical Engineering & Computer Science, Massachusetts Institute of Technology, 02139 Cambridge, Massachusetts, USA*
[3]*Department of Physics, Harvard University, 02138 Cambridge, Massachusetts, USA*
[4]*Max Planck Institute for the Structure and Dynamics of Matter, Hamburg, Germany*
[5]*Department of Physics and Astronomy and Center for Quantum Materials, George Mason University, 22030 Fairfax, Virginia, USA*
[6]*Department of Physics, University of Tokyo, Bunkyo-ku, Tokyo 113-0033, Japan*
[7]*Max Planck Institute for Solid State Research, 70569 Stuttgart, Germany*
[8]*Department of Physics, Columbia University, New York, NY 10027, USA*
[9]*Center for Computational Quantum Physics, The Flatiron Institute, 162 Fifth Avenue, New York, NY 10010, USA*
[10]*Nano-Bio Spectroscopy Group, Departamento de Física de Materiales, Universidad del País Vasco, 20018 San Sebastían, Spain*

(Dated: July 8, 2020)

The excitonic insulator is an electronically-driven phase of matter that emerges upon the spontaneous formation and Bose condensation of excitons. Detecting this exotic order in candidate materials is a subject of paramount importance, as the size of the excitonic gap in the band structure establishes the potential of this collective state for superfluid energy transport. However, the identification of this phase in real solids is hindered by the coexistence of a structural order parameter with the same symmetry as the excitonic order. Only a few materials are currently believed to host a dominant excitonic phase, Ta_2NiSe_5 being the most promising. Here, we test this scenario by using an ultrashort laser pulse to quench the broken-symmetry phase of this transition metal chalcogenide. Tracking the dynamics of the materials electronic and crystal structure after light excitation reveals surprising spectroscopic fingerprints that are only compatible with a primary order parameter of phononic nature. We rationalize our findings through state-of-the-art calculations, confirming that the structural order accounts for most of the electronic gap opening. Not only do our results uncover the long-sought mechanism driving the phase transition of Ta_2NiSe_5, but they also conclusively rule out any substantial excitonic character in this instability.

The excitonic insulator (EI) is an elusive state of matter proposed theoretically in 1965 [1–3] and expected to exhibit many unusual properties, such as superfluid energy transport [4], electronic ferroelectricity [5], and superradiant emission [6]. In several ways the EI is analogous to a conventional superconductor, but pairing in an electron-hole rather than electron-electron channel. Similar to a superconductor, the EI is a many-body effect beyond the scope of non-interacting electron theory. Unlike conventional superconductivity, the EI develops entirely within the electronic subsystem, driven by electron-electron interactions based on Coulomb repulsion rather than phonon exchange. However, the EI instability has the same symmetry as a structural phase transition, so the EI and structural order parameters are in general linearly coupled and occur together [7]. Because there is no symmetry distinction, the question whether the transition is excitonic or structural in nature is necessarily quantitative rather than qualitative, involving comparison of energy scales. A phase can be classified as predominantly excitonic on the basis of two theoretically-defined criteria: (i) the instability occurs in the electronic subsystem alone, at fixed ionic positions [1, 2], and (ii) the symmetry breaking leads to the emergence of a pseudo-Goldstone collective mode (phason) with a much smaller energy than the Higgs-like mode (see Supplementary Note 1) [8].

There are only a few EI candidates, of which Ta_2NiSe_5 is one of the most extensively studied. Above a critical temperature $T_C = 328$ K, this material crystallizes in a layered orthorhombic unit cell that consists of parallel Ta and Ni chains (Fig. 1a). At T_C, a second-order phase transition lowers the crystalline symmetry to monoclinic and the material simultaneously undergoes a semimetal-to-semiconductor transition [9, 10]. Of note is the breaking of mirror symmetry [8, 11] and the development of spontaneous strain below T_C [11, 12]. In the semiconducting phase, a gap opens in the electronic structure [9, 13] and the valence band (VB) top acquires an M-like flat shape around the Γ point of the Brillouin zone [10, 14]. Since this band flattening is expected from the Bogoliubov transformation for an electron-hole pair, it has been quoted as evidence of an electronic origin for

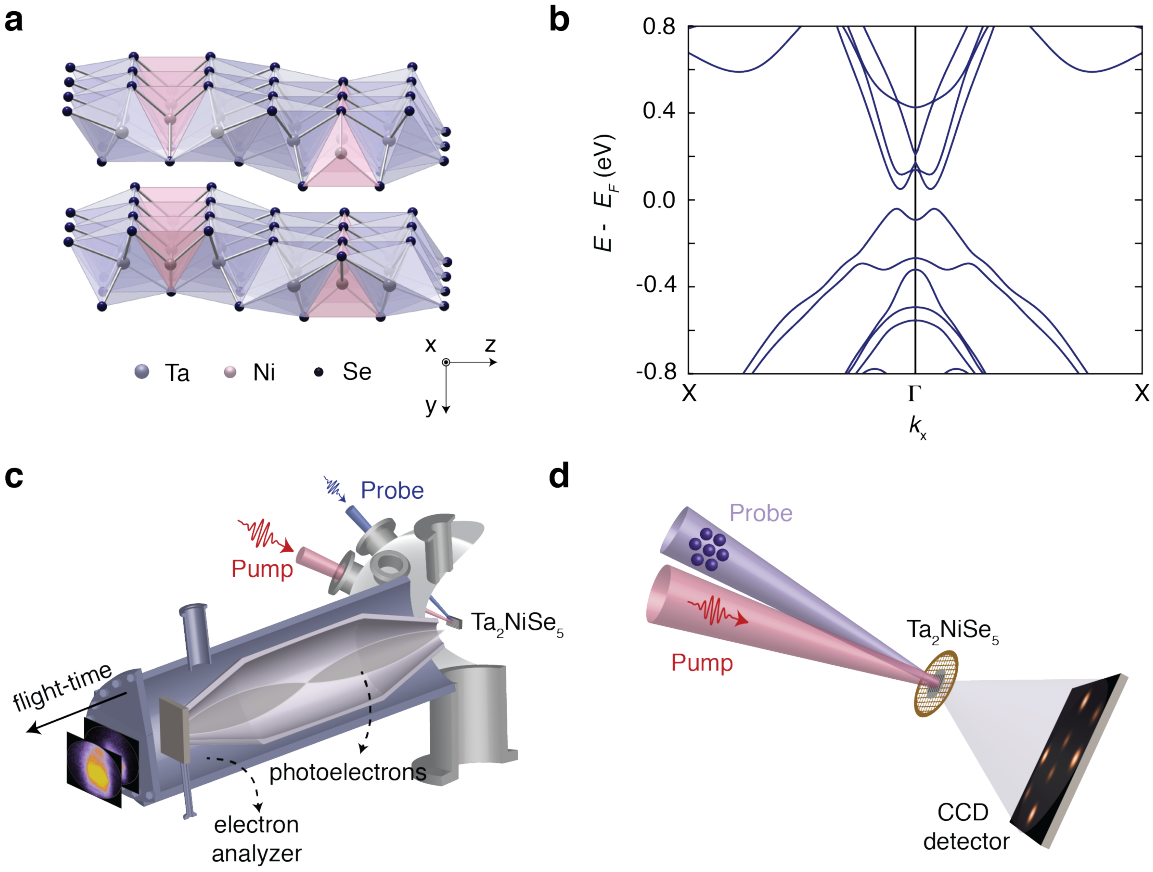

FIG. 1. **Ta_2NiSe_5 and experimental methods. a**, High-temperature orthorhombic crystal structure of Ta_2NiSe_5 showing the layered nature of the system along the y axis and the quasi-one dimensional Ta- and Ni chains running along the x axis. The $TaSe_6$ octahedra and $NiSe_4$ tetrahedra are represented in light-blue and pink, respectively. **b**, Calculated electronic structure of Ta_2NiSe_5 in the low-temperature monoclinic unit cell along the X-Γ-X momentum direction (parallel to the Ta and Ni chains). The electronic structure is computed using *GW* calculations. A bandgap opens in the single-particle band structure and its lower value is close to the Γ point of the Brillouin zone (see Supplementary Note 7 for the details). The VB (CB) dispersions acquire an M-like (W-like) shape around Γ, consistent with the dispersion found in experiments. **c**, Schematic of the trARPES experiment. An ultrashort near-infrared pump pulse illuminates the sample and a delayed ultraviolet probe pulse photo-ejects electrons at different energies and momenta. The photoelectrons are finally detected in a time-of-flight analyzer. **d**, Schematic of the UED experiment performed in a transmission geometry. An ultrashort near-infrared pump pulse excites the sample and a delayed electron pulse is diffracted by the specimen and captured by a CCD detector. The specimen is in the form of an ultrathin flake deposited on a standard TEM Cu mesh.

the phase transition of Ta_2NiSe_5. In this scenario, the changes in the lattice degrees of freedom accompanying the electronic structure reconstruction are interpreted in terms of linear coupling of the lattice to the putative EI order parameter [8, 15]. Nevertheless, it is crucial to remark that the opening of the hybridization gap and the M-shaped dispersion could also follow from a fundamentally distinct effect, the lowering of the crystal symmetry alone [10, 16]. Under this circumstance, the primary order parameter would be structural in nature, with relevant consequences on the fate of the EI. Such an underlying complexity in Ta_2NiSe_5 so far has posed significant challenges to disentangling different contributions to the gap formation in experiments performed under equilibrium conditions. This calls for the development of advanced nonequilibrium schemes to separate the time dependence of the electronic and structural components of the instability [17–20], assessing their relative importance with the support of state-of-the-art computational methods.

Here, we present an experimental study of quench dynamics aimed at uncovering the nature of the phase transition in Ta_2NiSe_5. The ultrafast destabilization of the order parameter is imprinted on the material's nonequilibrium electronic structure, which we track via time- and angle-resolved photoemission spectroscopy (trARPES,

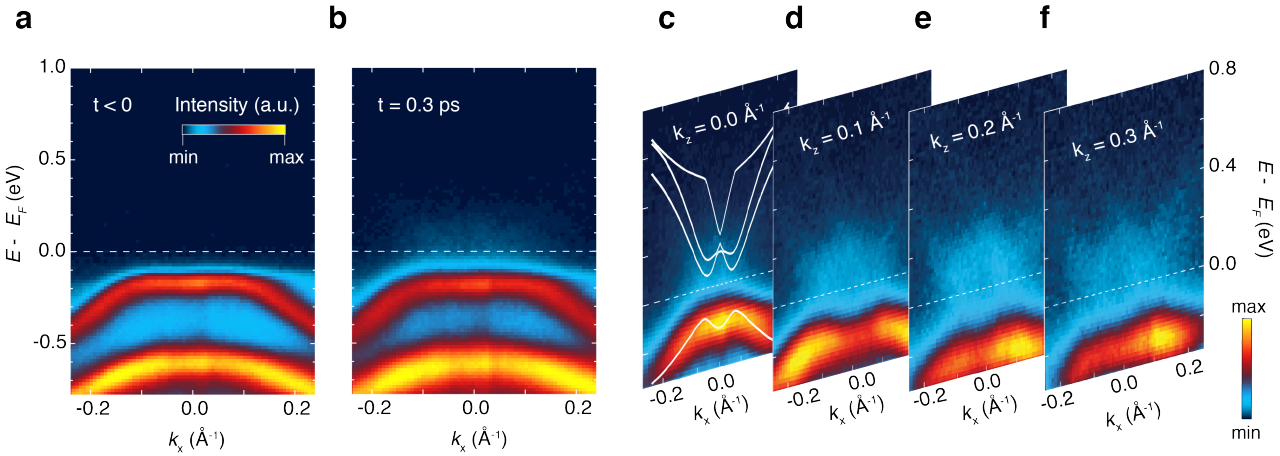

FIG. 2. **Light-induced modification of the electronic structure. a,b** Snapshots of the trARPES spectra along the k_x momentum direction and for $k_z = 0$ Å^{-1}. The data have been measured at 11 K with a probe photon energy of 10.75 eV and an absorbed pump fluence of 0.4 mJ/cm^2. (a) Snapshot before photoexcitation ($t < 0$). At the Γ point of the Brillouin zone ($k_x = 0$ Å^{-1}), the flat anti-bonding VB is located around -0.16 eV, whereas the bonding VB appears around -0.65 eV. (b) Snapshot measured at the maximum of the pump-probe response ($t = 0.3$ ps). Upon photoexcitation, the VB is depleted in intensity and broadens significantly. Spectral weight is transfered above E_F and accumulates close to Γ. **c-f**, Evolution of the photoexcited state (at $t = 0.3$ ps) along k_x at representative k_z momenta, as indicated in the labels. Note that the color scale is different from that of panels (a,b). The spectral weight above E_F assumes a W-like shape consistent with the dispersion of the CB. The VB and CB never crosses each other and thus the gap size remains finite in the whole k_x-k_z momentum space around Γ. The white lines denote the energy-momentum dispersion calculated at the *GW* level (Fig. 1b). A rigid shift of -84 meV has been applied to the VB to account for the underestimated gap resulting from the *GW* method. The calculated dispersions have an excellent match with the experimental findings.

Fig. 1c). We observe that the electronic gap never collapses upon intense photoexcitation even though the depletion of the electronic states near the VB maximum is strong; moreover, the dominant response proceeds over a phononic rather than electronic timescale. The central role of the crystal structure in the symmetry breaking is confirmed by direct visualization of the lattice dynamics, provided by ultrafast electron diffraction (UED, Fig. 1d). Advanced first-principles calculations performed in the realistic low-temperature unit cell clarify that the leading contribution to gap opening in Ta_2NiSe_5 is of structural origin, as encountered in phonon-driven displacive transitions.

As a first step, we map the light-induced modification of the electronic structure of Ta_2NiSe_5 via trARPES. We drive the material deep in the low-temperature phase ($T = 11$ K) with an intense near-infrared laser pulse that rapidly changes the electronic distribution, in effect increasing the electronic temperature (T_e) to values well above T_C while keeping the lattice cold. The theoretical estimates indicate that the carriers initially photoexcited by the pump rapidly relax, leading to a nonequilibrium distribution corresponding to a substantial depletion of the VB edge states (see Supplementary Note 2). The combination of a vacuum ultraviolet probe beam and a time-of-flight electron analyzer allows us to access a large portion of the Brillouin zone, elucidating how the electronic gap reacts to photoexcitation along both k_x, the direction parallel to the chains in the orthorhombic cell and k_z, the one perpendicular to it. This feature is crucial because the material's electronic structure is not purely one-dimensional, with the interchain coupling establishing a well-defined dispersion along k_z [10]. If the instability in Ta_2NiSe_5 was purely excitonic in nature, our experimental protocol would lead to the observation of a complete gap closure on an electronic timescale.

Figures 2a,b show snapshots of trARPES spectra along k_x for $k_z = 0$ Å^{-1}. At negative time delays (Fig. 2a), the flat anti-bonding VB is observed around an energy of -0.16 eV relative to the Fermi level (E_F) at the Γ point, whereas the bonding VB appears at -0.65 eV [14]. Photoexciting electron-hole pairs with T_e of several hundred kelvins above T_C induces a modification of the band structure that is the strongest around 0.3-0.4 ps (Fig. 2b). The flat VB is depleted in intensity and broadened substantially, but its peak energy remains nearly unchanged at all momenta (see Supplementary Figure 5). This is in stark contrast to the behavior observed in equilibrium upon increasing the lattice temperature, which involves a significant energy shift of the VB toward E_F [10, 14]. Another important feature in the pump-probe spectrum is found above E_F, where spectral weight accumulates around the Γ point. To investigate the nature of these states, we acquire data at 0.3 ps with improved sensitivity

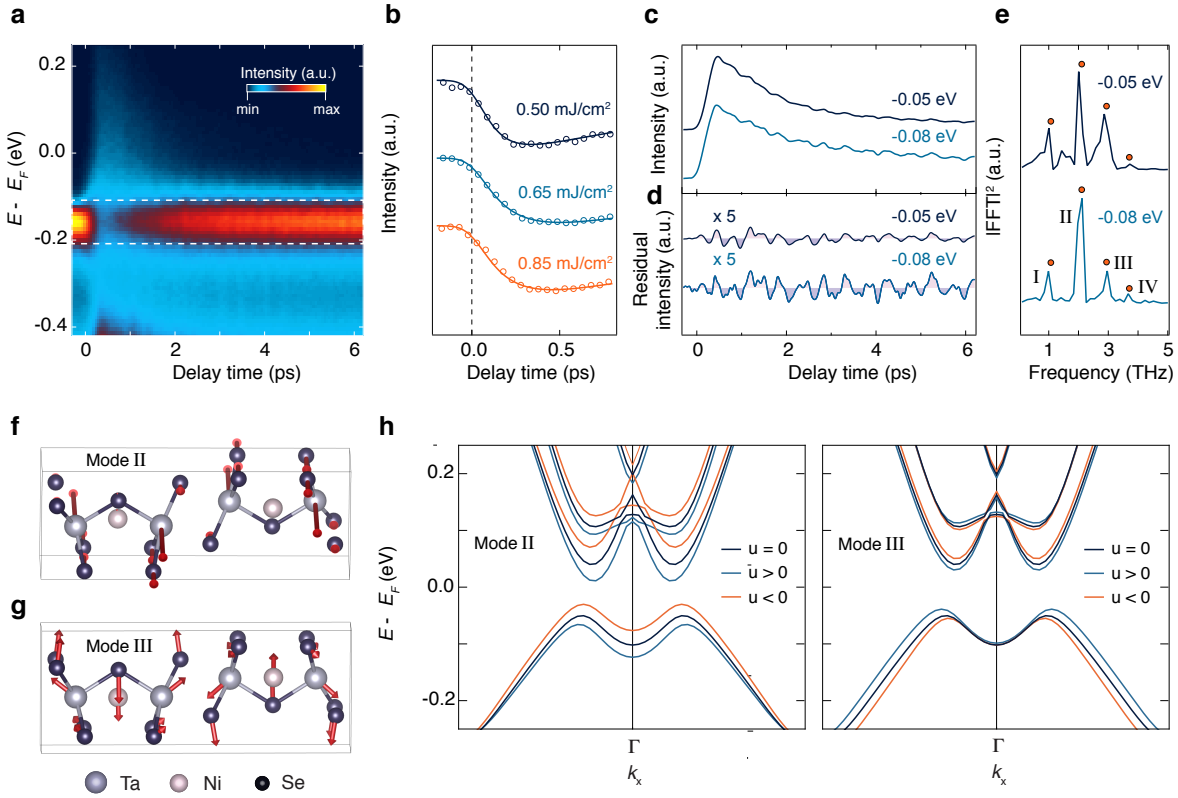

FIG. 3. **Role of the collective modes in the gap response.** **a**, Map of the photoelectron intensity at the Γ point as a function of energy and pump-probe delay. The data have been acquired at 14 K with a probe photon energy of 6.20 eV and an absorbed pump fluence of 0.85 mJ/cm^2. **b**, Excitation-density dependence rise of the photoelectron intensity response at Γ (dotted lines). Fits to the experimental traces are overlapped in solid lines. The traces are selected at an energy of -0.158 eV with respect to E_F and averaged over an energy window of ±0.05 eV, as indicated by the dashed rectangle in panel (a). **c**, Time dependence of the momentum-integrated photoelectron intensity in selected energy intervals referenced to E_F. Intensities are normalized to the average intensity I_0 in the delay interval [-300,-50] fs; curves are offset for clarity and smoothed. The energy interval over which the intensity is integrated is ±0.05 eV around the indicated energy. **d**, Oscillatory component singled out from the temporal traces of panel (c) by subtracting the nonoscillatory transient. For visualization purposes, the residuals have been multiplied by a factor of 5 and smoothed. **e**, Fourier transform analysis of the oscillatory signal in (d). Four frequency components (labelled as I-IV) appear in the spectrum and they are identified as Raman-active phonons of Ta_2NiSe_5. The corresponding frequencies detected in spontaneous Raman scattering [15] are indicated by orange dots. **f-g**, Calculated eigenvectors of the dynamical matrix of Ta_2NiSe_5 corresponding to modes II and III, respectively. Violet atoms refer to Ta, pink atoms to Ni, and blue atoms to Se. The phonon spectrum has been computed using DFT. To enhance the visibility of the atomic motion, the amplitude is scaled by a factor of 8. **h-i**, Calculated electronic structure of Ta_2NiSe_5 displaced along the eigenvectors of the modes showed in panels (f-g). The dark blue lines refer to the electronic structure of the initial (undisplaced, $u = 0$) low-temperature unit cell, whereas the light blue (organge) lines indicate the band structure for positive (negative) displacements. The electronic structures are computed on the *GW* level of theory.

around E_F and show them in Fig. 2c-f at representative k_z values. At $k_z = 0$ Å^{-1} and an energy of ∼50 meV (Fig. 2c), we observe an upward-dispersing band with a characteristic W shape, which we identify as the lowest conduction band (CB). While the exact estimate of the final gap size is hindered by the experimental resolution, the relevant aspect for our discussion is that the gap along k_x remains open. Direct inspection of the snapshots simultaneously taken at finite k_z (Fig. 2d-f) confirms that the VB and CB never cross each other throughout the two-dimensional momentum space around Γ. We remark that this behavior occurs in the presence of a clear separation between the electronic and lattice temperatures, differing from the response observed when the lattice is also transiently heated above T_C [21, 22].

To elucidate whether the electronic or ionic degrees of freedom control the dynamics, we measure the trARPES signal with a high time resolution setup. Figure 3a dis-

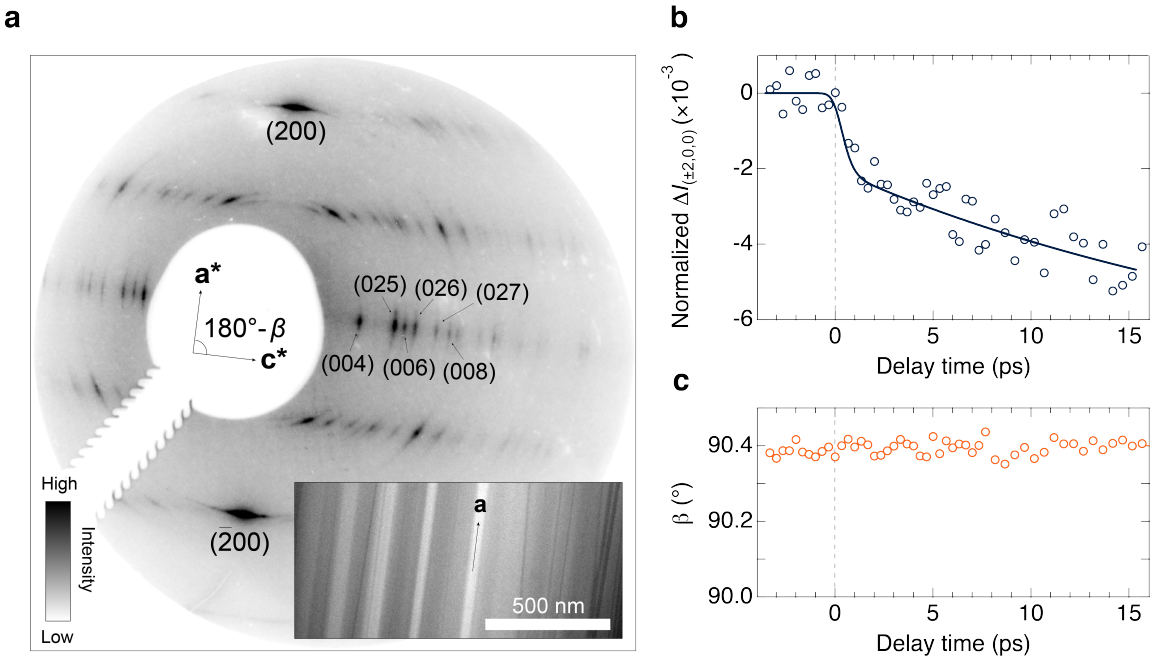

FIG. 4. **Direct visualization of the structural dynamics. a**, Static electron diffraction pattern of Ta_2NiSe_5 taken at room temperature and with electrons at an energy of 26 kV. Inset: electron micrograph of the UED sample taken at 120 kV, showing nanoscale needle-like morphology. Though all needles are aligned along the a-axis, their b- and c-axis differ, resulting in peaks observed out of the [010] zone axis; some of these peaks are labeled. **b**, Photoinduced change of the integrated diffraction intensity, normalized to its value before excitation. The absorbed fluence is 0.1 mJ/cm^2. Intensity values are taken as the average between (200) and ($\bar{2}$00) peaks. The fitted curve (solid line) shows a fast drop with $\tau_1 = 0.32 \pm 0.18$ ps and a slow decay of $\tau_2 = 26 \pm 1$ ps. **c**, Time evolution of the monoclinic distortion angle β, shown in panel (a), upon photoexcitation. While the sensitivity of the UED setup is not sufficient to resolve the pump-induced change, the angle never reaches the 90° value associated with the orthorhombic unit cell. Qualitatively similar data were measured at 77 K and 295 K.

plays the energy distribution of the photoemission intensity around Γ (integrated over ±0.05 Å^{-1} in the k_x-k_z plane) as a function of pump-probe delay. Tracking the evolution of the VB intensity at different pump fluences (Fig. 3b) allows us to observe a response that is complete within ∼0.3-0.4 ps, a timescale longer than our instrument response function. This behavior is incompatible with the very short timescale (i.e. few fs, see Supplementary Note 5) that characterizes the plasma-induced screening of the Coulomb interaction. The latter effect plays an important role in the bandgap renormalization of conventional semiconductors and, in the case of a model two-band EI, it is expected to modify the excitonic gap amplitude on timescales of 10-100 fs [23, 24]. Direct inspection of our raw data and a combined analysis of the VB amplitude, broadening, and peak position indicates that plasma screening in Ta_2NiSe_5 provides only a small contribution to the gap renormalization compared to the phenomenon evolving on the slower timescale. The same analysis suggests that the dominant process involves the emission of optical phonons, a behavior usually observed in materials with a gap of structural origin [17, 25, 26]. To assess the validity of this scenario, we search for an unambiguous signature of strongly-coupled phonon modes in Ta_2NiSe_5. Figure 3c displays the momentum-integrated photoemission response as a function of time at representative energies of -0.05 eV and -0.08 eV. Both curves refer to the upper edge of the VB and show the presence of oscillations in the photoemission intensity due to coherent phonons. Subtracting the multi-exponential background from the data of Fig. 3c allows us to isolate the signal of the collective response (Fig. 3d). The residuals reveal that the coherent phonon oscillations already emerge during the rise of the pump-probe signal, confirming that the maximum gap response is locked to a phononic timescale. Applying a Fourier filter to the signal of Fig. 3d yields the frequency spectrum of Fig. 3e. The peaks (labelled as I-IV) match the frequencies of four Raman-active phonons previously observed in other ultrafast studies [15, 22, 27–29]. The sharp lineshape of mode II deserves special attention, as this is a characteristic fingerprint of the monoclinic phase of Ta_2NiSe_5 (see Supplementary Note 6). It indicates that the crystal maintains the low-temperature structure even if the electronic distribution becomes strongly nonequilibrium, another feature incompatible with a symmetry breaking

of purely excitonic origin.

To verify the inhibition of the monoclinic-to-orthorhombic transition, we directly visualize the evolution of the crystal structure through UED (details are given in the Methods). Figure 4a shows a static electron diffraction pattern of Ta_2NiSe_5 in the monoclinic phase, featuring two peaks at (±2, 0, 0). In Fig. 4b, we track the change in the diffraction intensity upon photoexcitation. We observe a signal that drops promptly and is followed by a slow evolution that marks the rise of lattice heating after ∼1 ps. Upon accounting for the instrument response function, we find that the initial sub-ps decrease is resolution-limited and indicates the immediate emission of multiple phonons (some of which revealed by trARPES) which redistribute intensity from Bragg reflections to elsewhere in the Brillouin zone. We then monitor how the β angle associated with the monoclinic distortion reacts to the sudden increase of T_e. The results show that β remains rather constant in time (Fig. 4c), never reaching the value of 90° expected for the orthorhombic cell. Although the sensitivity offered by our UED apparatus is not sufficient to resolve the small pump-induced change of β (within a scale of 0.014°), we can firmly establish that the structural transition never occurs at all time delays.

The presented data show that in Ta_2NiSe_5 the electronic distribution changes substantially and suddenly, the electronic gap remains open at all time delays, and the crystal retains its monoclinic structure. These results indicate that the material's instability is driven mostly by phonons and not by a pure EI order of electronic origin.

In the following, we rationalize these findings by performing state-of-the-art calculations based on DFT and its Hartree-Fock-like generalizations. As a first step, we establish the crystal structure that is favored at low temperature by relaxing the material's unit cell. We find that this structure is monoclinic, in agreement with previous results [10, 12, 16]. We also study how the low-symmetry distortion reacts to an increase in T_e by introducing a finite Fermi smearing in the Brillouin zone integrations. We observe that the electron heating does not remove the monoclinic distortion even at $T_e \gg T_C$, consistent with our experimental findings of Fig. 3e and Fig. 4c. The amplitude of the distortion is gradually reduced, albeit never to zero. Already at this stage, we could conclude that the orthorhombic-to-monoclinic transition is primarily driven by ion dynamics, and not by excitonic effects.

We then examine the evolution of the electronic structure as the lattice is varied between the orthorhombic and monoclinic phases. To capture the electronic structure in the monoclinic phase, DFT alone is not sufficient, as the standard functionals routinely yield severely underestimated gaps and inaccurate band dispersions in semiconductors. Nevertheless, this fact is not related to any EI physics and stems from an incomplete description of the long-range exchange interaction in DFT [30]. One can circumvent this problem by including the lowest-order correction in the screened electron-electron interaction. This is the essence of the so-called *GW* method, which largely improves the description of semiconductors [31]. Importantly, this method does not account for any ladder-diagrammatic effects (such as the EI order) and thus can serve as a crucial test for the EI hypothesis in Ta_2NiSe_5. We compute the material's electronic structure at the *GW* level in the monoclinic unit cell and show the results in Fig. 1b (details are given in the Methods and in Supplementary Note 7). We observe that the monoclinic distortion alone profoundly affects the electronic structure, changing it from semimetallic to semiconducting. Specifically, a hybridization gap opens around the Γ point, its size being half of the experimental value [9]; the change in structure also leads to large systematic changes in band offsets, with CBs moving up in energy with respect to VBs. Further corrections in the description of the screening and the inclusion of the electron-phonon coupling would likely refine the gap size to larger values. More importantly, along k_x the topmost VB acquires an M-like flat shape and the lowest CB develops a W-like structure, both consistent with the experimental dispersions (as shown by the white lines overlapped to the experimental data of Fig. 2c). These shapes are expected when two intersecting electron and hole bands hybridize, with the degree of flattening set by the strength of the hybridization potential. Starting from this electronic structure, we establish how it evolves upon increasing T_e. There are two mechanisms through which electron heating can modify the *GW* gap: (i) Screening of the long-range exchange interaction, which proceeds on the electronic timescale set by the plasma frequency, and (ii) the dependence of the structural distortion (involving the monoclinic angle and the internal displacements) on T_e, an effect that evolves on phononic timescales. At our values of T_e, the former mechanism has a small impact on the electronic structure of Ta_2NiSe_5, consistent with our experimental findings (see Supplementary Note 7D). In contrast, a small decrease in the monoclinic distortion would cause a larger shrinkage of the *GW* gap [32]. In our trARPES data, the phononic timescale associated with the largest gap response reinforces the idea that the dynamics is governed by a small reduction of the structural distortion. During this time, the electron-phonon coupling plays a key role in equilibrating the electron and the ion subsystems. We can quantify this coupling for each of the coherent phonons emerging in trARPES by computing the *GW* band structure while statically displacing the ions along the mode coordinates [33]. Figures 3f-i show representative results for modes II and III. In agreement with the experiment, our calculations show that the VB undergoes a substantial modulation around Γ, confirming a strong deformation potential coupling between the low-energy electronic states and the atomic

displacements. Such deformation potential coupling involves, together with band offsets, strong changes in band hybridization.

In conclusion, our joint experimental-theoretical study excludes the scenario wherein the instability in Ta_2NiSe_5 has a dominant (or even substantial) EI nature. Rather, the electronic gap in the material can be best described as a one-electron hybridization gap driven by ion-ion interactions, with the possible addition of a small secondary EI order. In such conditions, the phason of the EI (if present) would be pinned at the high energy scale of the structural gap, hindering dissipationless transport and excitonic superfluidity even upon application of intense external stimuli [8]. While our calculations (as well as those in Ref. [16]) predict that a zone-center soft phonon leads to a quadrupolar order below T_C, only high-resolution structural probes will clarify the lattice dynamics responsible for the symmetry breaking. Indeed, anharmonic effects beyond the perturbative approach can also conspire to trigger the phase transition, making the experimental identification of the relevant phonon more challenging. Irrespective of the detailed mechanism at play, we believe that our study reconciles the controversial results obtained experimentally on Ta_2NiSe_5 since its discovery in 1985 [34]. We envision that the strategy presented here will serve as a general protocol to establish the role of the crystal structure in future candidate EIs.

METHODS

Sample growth and preparation

Single crystals of Ta_2NiSe_5 were synthesized by chemical vapour transport. Elemental powders of Ta, Ni, and Se were mixed with a stoichiometric ratio and sealed into an evacuated quartz tube ($\sim 1\times10^3$ Pa) with a small amount of I_2 as transport agent. The mixture was sintered under a temperature gradient of 950/850°C. After sintering for 1 week, needle-like single crystals grew at the cold end of the tube.

For the trARPES experiment, the single crystals were directly glued on a copper holder using silver epoxy, in order to ensure a good thermal contact in the cryostat. For the UED experiments, an ultramicrotome fitted with a diamond blade was used to cleave a single crystal of Ta_2NiSe_5 along the *ac* plane, producing thin flakes with an approximate dimension of $600\,\mu$m $\times$ 50 nm $\times$ $200\,\mu$m. Flakes were scooped from water onto standard transmission electron microscopy (TEM) copper grids (300 lines/inch). The TEM grids were clamped to a copper holder that ensures good thermal contact. Sample characterization was done by a commercial TEM (Tecnai G2 Spirit TWIN, FEI) with a 120-kV electron beam energy.

Time- and angle-resolved photoemission spectroscopy

The Ta_2NiSe_5 single crystals were cleaved at 10-14 K under ultra-high-vacuum conditions ($<1\times10^{-10}$ torr). Systematic trARPES data were reproduced on a total of ten samples using two different laser schemes. The first scheme used a setup based on an amplified Yb:KGW laser system operating at 100 kHz (PHAROS SP-10-600-PP, Light Conversion). Details are reported in Ref. [35]. In brief, the laser ouput (with pulses centered around 1.19 eV) was split into a pump and probe beams. The pump beam was directed into an optical parametric amplifier (ORPHEUS, Light Conversion) to produce a near-infrared pulse at 1.55 eV. The probe pulse was frequency tripled to 3.58 eV and directed into a hollow fiber filled with Xe gas (XUUS, KMLabs). Here, pulses centered around 10.75 eV were obtained through nonlinear conversion of the 3.58 eV beam. The resulting vacuum ultraviolet pulse was passed through a custom-built grating monochromator (McPherson OP-XCT) to minimize pulse width broadening and enhance throughput efficiency. Finally, the probe was focused onto the sample with an in-plane polarization state perpendicular to the Ta and Ni chains. The temporal resolution of the setup was 230 fs, while the energy resolution was 43 meV. The second laser scheme consisted of an amplified Ti:Sapphire system (Wyvern, KMLabs), emitting ultrashort pulses around 1.55 eV and at a repetition rate of 30 kHz. A portion of the output beam was used directly as the near-infrared pump pulse at 1.55 eV, whereas the ultraviolet probe was obtained by frequency-quadrupling the laser fundamental photon energy to 6.20 eV. The probe light polarization state was set to circular. The overall time resolution was $\sim$160 fs (see Supplementary Note 3), while the energy resolution was 31 meV.

A time-of-flight analyzer (Scienta ARTOF 10k) was used to acquire the transient band structure of Ta_2NiSe_5 in the two-dimensional k_x-k_z plane around the Γ point of the Brillouin zone without rotating the sample or the detector. The pump beam was incident on the sample at an angle of $\sim45^\circ$ and its polarization could be set precisely to either S or P with respect to the incident plane. The sample was oriented such that S polarization had a pure in-plane electric field component perpendicular to the chains ($E_{in} \parallel$ c), while P polarization had an in-plane component parallel to the chains ($E_{in} \parallel$ a) and an out-of-plane component perpendicular to the sample surface ($E_{out} \parallel$ b). The position of E_F was carefully calibrated for each sample by acquiring the steady-state ARPES spectrum of an auxiliary Bi_2Se_3 single crystal.

Ultrafast electron diffraction

The 1.19 eV output of an amplified Yb:KGW laser system (PHAROS SP-10-600-PP, Light Conversion) operating at 100 kHz was split into pump and probe branches. The pump beam was focused onto the sample, while the probe beam was frequency quadrupled to 4.78 eV and focused onto a gold-coated sapphire in high vacuum ($<4\times10^{-9}$ torr) to generate photoelectrons. These electrons were accelerated to 26 kV in a dc field and focused with a solenoid before diffracting from Ta_2NiSe_5 in a transmission geometry. Diffracted electrons were incident on an aluminum-coated phosphor screen (P-46), whose luminescence was recorded by an intensified charge-coupled device (iCCD PI-MAX II) operating in shutter mode. The temporal resolution was 0.8 ps (see Supplementary Note 3). We calculated the β angle by fitting the positions of the (200), (-200) and (004) Bragg peaks, which allows for the determination of the reciprocal unit vectors [100] and [001]. Small detector aberrations resulted in a β angle of $\sim$90.4°, slightly deviating from the 90.57° reported previously [12]. The experiments were performed at 77 K and 300 K.

First-principles calculations

All *ab initio* calculations were performed using the Vienna Atomistic Simulation Package (VASP) implementing the projected augmented wave (PAW) method [36]. The DFT structural relaxation using the vdw-opt88-PBE functional (know to correctly describe both van der Waals and regular interactions) resulted in the monoclinic structure characteristic of the low-temperature phase of Ta_2NiSe_5. The relaxation was performed on a 24×4×6 k-mesh with a 460 eV cutoff. We obtained the lattice parameters a = 3.517 Å, b = 12.981 Å, and c = 15.777 Å, and unit cell angles α = 90.005°, β = 90.644°, and γ = 89.948°. Note that this structure has a small triclinic distortion, but it is very close to the monoclinic one, as analyzed in the Supplementary Note 7. This structure agrees, within our numerical accuracy, to the monoclinic $C2/c$ cell measured in experiments [11, 34] and in agreement with the findings of Ref. [16].

DFT band structure calculations were performed on a 16×4×4 k-mesh using the standard Perdew-Burke-Ernzerhof (PBE) exchange-correlation functional [37]. Afterwards, the GW bands were calculated on top of DFT at the G_0W_0 level with a 12×4×2 k-mesh. We used a 100 eV cutoff for the calculation of the random-phase approximation (RPA) polarizability and we included 1086 conduction bands and 160 frequencies for the calculation of the screened interaction. For the analysis of the electronic temperature effect on the band structure, we performed G_0W_0 calculations with the parameters reported above on top of DFT calculation with the PBE functional. A Fermi smearing for different temperatures was set for the self-consistent cycle. This allowed us to have a depletion of the top valence bands and finite occupation of the bottom conduction bands, which in turns affected the G_0W_0 corrections as discussed in the text. The complete electronic structure analysis is given in Supplementary Note 7C,D.

The computation of the phonon dispersion and eigenmodes was performed on a 4×4×3 k-mesh with a 4×2×1 supercell. The analysis of the phonon modes was performed with the *Phonopy* package [38]. To analyze the effect of representative phonon modes on the electronic bands, we performed G_0W_0 calculations as described above, but with the atomic positions displaced along the phonon eigenmodes by an amount equal to $\pm\sqrt{\langle\mathbf{r}^2\rangle_{\mathrm{T=0K}}}$, with $\langle\mathbf{r}^2\rangle_{\mathrm{T=0K}}$ being the amplitude of the zero-point oscillation of this mode. Similar calculations were repeated at different temperatures. More details are provided in Supplementary Note 7E,F.

DATA AVAILABILITY

The data that support the findings of this study are available from the corresponding author upon reasonable request.

SUPPLEMENTARY INFORMATION

Supplementary Information is available for this paper.

ACKNOWLEDGEMENTS

We thank F. Boschini, S. Kaiser, D. Chowdhury, A. Georges, G. Mazza, and A. Subedi for insightful discussions. We are grateful to F. Mahmood, E.J. Sie, T. Rohwer, B. Freelon for early instrumentation work of the trARPES and UED setups at MIT. The work at MIT was supported by DARPA DSO under DRINQS program grant number D18AC00014 (trARPES data taking and analysis), Army Research Office Grant No. W911NF-15-1-0128 (instrumentation for the trARPES setup), and the US Department of Energy BES DMSE (UED measurements). The work at Harvard was supported by Harvard-MIT CUA, AFOSR-MURI: Photonic Quantum Matter (award FA95501610323), and DARPA DRINQS program (award D18AC00014). E.B acknowledges additional support from the Swiss National Science Foundation under fellowships P2ELP2-172290 and P400P2-183842. Y.W. acknowledges the Postdoctoral Fellowship in Quantum Science of the Harvard-MPQ Center for Quantum Optics. The theory work was supported by the European Research Council (ERC-2015-AdG694097), the Cluster of

Excellence “Advanced Imaging of Matter” (AIM), Grupos Consolidados (IT1249-19) and SFB925. The Flatiron Institute is a division of the Simons Foundation. Support by the Max Planck Institute - New York City Center for Non-Equilibrium Quantum Phenomena is acknowledged. S. L. acknowledges support from the Alexander von Humboldt foundation. I.I.M. acknowledges support from the Office of Naval Research (ONR) through the grant #N00014-20-1-2345. A.J.M. acknowledges e support from DOE BES Pro-QM EFRC (de-sc0019443). Part of the calculations used resources of the National Energy Research Scientific Computing Center (NERSC), a US Department of Energy Office of Science User Facility operated under Contract No. DE-AC02-05CH11231. A.Z. and A.K. thank Y. Zhang for assisting us at the MRSEC Shared Experimental Facilities at MIT, supported by the NSF under award number DMR-14-19807. A.Z. and A.K. also thank C. Marks for the assistance in preparing UED samples at Center for Nanoscale Systems, a member of the National Nanotechnology Coordinated Infrastructure Network (NNCI), which is supported by the National Science Foundation under NSF award no. 1541959. CNS is part of Harvard University.

AUTHOR CONTRIBUTIONS

E.B. conceived the project. E.B., D.C., D.A. and B.L performed the trARPES experiments with the 10.75 eV probe setup. E.B., C.L. and A.Z. performed the trARPES experiments with the 6.20 eV probe setup. A.Z. and A.K. performed the UED experiments. Y.L., T.T. and H.T. performed the crystal growth. E.B. and A.Z. analyzed the data. L.W., I.I.M, S.L. and A.R. performed the first-principles calculations. M.M., Y.W., I.I.M., A.J.M. and E.D. performed the analytical calculations. I.I.M., A.J.M., A.R., E.D. and E.B. interpreted the data. E.B., I.I.M., A.J.M., E.D. and N.G. wrote the manuscript. All the authors contributed to the final version of the paper. The entire project was supervised by N.G.

AUTHOR INFORMATION

The authors declare having no competing financial interests. Correspondence and requests for materials should be addressed to N.G. (email: gedik@mit.edu).

a frequency of ∼3.5 THz. We analyze the eigenmodes of the phonons emerging in our trARPES experiment using the *Phonopy* package [38]. The phonon eigenvectors are displayed in Fig. S14 and show agreement with those analyzed previously in the literature [15]. In particular, mode IV is the mode that originates from the soft phonon driving the orthorhombic-to-monoclinic transition. As such, its eigenvector involves the shear motion of the neighboring Ta chains around the Ni chain.

F. Electronic structure in a frozen-phonon unit cell

We also analyze the effect that phonon modes I-IV have on the electronic band structure of Ta_2NiSe_5. We perform G_0W_0 calculations while statically displacing the atoms in the unit cell along specific phonon eigenmodes. While this adiabatic method can provide information only on the electron-phonon coupling in the electronic ground state [76], it represents a first important step to elucidate how specific atomic motions affect the electronic properties of Ta_2NiSe_5. Our results are shown in Fig. S14, where we present the band structure along the Γ-X and Z-M momentum directions for modes I-IV. Note that, to enhance the visibility of the phonon-induced changes, the energy axis is not aligned around E_F, but it is referenced to the energy of infinitely separated atoms. We observe that the low-energy VB states around the Γ point are more sensitive toward the displacement of mode II, in agreement with our results of Fig. 3e. Mode IV leads to an asymmetric and nonlinear behavior of the band structure upon the application of positive and the negative displacements. This behavior occurs in the presence of a non-perturbative strong electron-phonon coupling, which breaks the linear and symmetric dependence expected from the traditional deformation potential theory. Finally, repeating similar calculations at different temperatures (100 K and 300 K) yields no substantial changes in our results.

[1] L. V. Keldysh and Y. V. Kopaev, Soviet Physics Solid State, USSR **6**, 2219 (1965).
[2] J. Des Cloizeaux, J. Phys. Chem. Sol. **26**, 259 (1965).
[3] B. I. Halperin and T. M. Rice, Rev. Mod. Phy. **40**, 755 (1968).
[4] D. Snoke, Science **298**, 1368 (2002).
[5] C. D. Batista, J. E. Gubernatis, J. Bonča, and H. Q. Lin, Phys. Rev. Lett. **92**, 187601 (2004).
[6] G. Mazza and A. Georges, Phys. Rev. Lett. **122**, 017401 (2019).
[7] D. Jérome, T. Rice, and W. Kohn, Phys. Rev. **158**, 462 (1967).
[8] G. Mazza, M. Rösner, L. Windgätter, S. Latini, H. Hübener, A. J. Millis, A. Rubio, and A. Georges, Phys. Rev. Lett. **124**, 197601 (2020).
[9] Y. F. Lu, H. Kono, T. I. Larkin, A. W. Rost, T. Takayama, A. V. Boris, B. Keimer, and H. Takagi, Nat. Commun. **8** (2017).
[10] M. D. Watson, I. Marković, E. A. Morales, P. Le Fèvre, M. Merz, A. A. Haghighirad, and P. D. C. King, Phys. Rev. Res. **2**, 013236 (2020).
[11] A. Nakano, T. Hasegawa, S. Tamura, N. Katayama, S. Tsutsui, and H. Sawa, Phys. Rev. B **98**, 045139 (2018).
[12] F. J. Di Salvo, C. H. Chen, R. M. Fleming, J. Waszczak, R. G. Dunn, S. A. Sunshine, and J. A. Ibers, J. Less Comm. Met. **116**, 51 (1986).
[13] J. Lee, C.-J. Kang, M. J. Eom, J. S. Kim, B. I. Min, and H. W. Yeom, Phys. Rev. B **99**, 075408 (2019).
[14] Y. Wakisaka, T. Sudayama, K. Takubo, T. Mizokawa, M. Arita, H. Namatame, M. Taniguchi, N. Katayama, M. Nohara, and H. Takagi, Phys. Rev. Lett. **103**, 026402 (2009).
[15] D. Werdehausen, T. Takayama, M. Höppner, G. Albrecht, A. W. Rost, Y. Lu, D. Manske, H. Takagi, and S. Kaiser, Sci. Adv. **4** (2018).
[16] A. Subedi, arXiv:2002.08352 (2019).
[17] S. Hellmann, T. Rohwer, M. Kalläne, K. Hanff, C. Sohrt, A. Stange, A. Carr, M. M. Murnane, H. C. Kapteyn, L. Kipp, *et al.*, Nat. Commun. **3**, 1069 (2012).
[18] M. Porer, U. Leierseder, J.-M. Ménard, H. Dachraoui, L. Mouchliadis, I. Perakis, U. Heinzmann, J. Demsar, K. Rossnagel, and R. Huber, Nat. Mater. **13** (2014).
[19] W. Zhang, C. Hwang, C. L. Smallwood, T. L. Miller, G. Affeldt, K. Kurashima, C. Jozwiak, H. Eisaki, T. Adachi, Y. Koike, *et al.*, Nat. Commun. **5**, 1 (2014).
[20] Y. Zhang, X. Shi, W. You, Z. Tao, Y. Zhong, F. C. Kabeer, P. Maldonado, P. M. Oppeneer, M. Bauer, K. Rossnagel, *et al.*, Proc. Natl. Acad. Sci. **117**, 8788 (2020).
[21] K. Okazaki, Y. Ogawa, T. Suzuki, T. Yamamoto, T. Someya, S. Michimae, M. Watanabe, Y. Lu, M. Nohara, H. Takagi, *et al.*, Nat. Commun. **9**, 4322 (2018).
[22] T. Suzuki, Y. Shinohara, Y. Lu, M. Watanabe, J. Xu, K. L. Ishikawa, H. Takagi, M. Nohara, N. Katayama, H. Sawa, *et al.*, arXiv:2002.10037 (2020).
[23] D. Golež, P. Werner, and M. Eckstein, Phys. Rev. B **94**, 035121 (2016).
[24] Y. Murakami, D. Golež, M. Eckstein, and P. Werner, Phys. Rev. Lett. **119**, 247601 (2017).
[25] F. Schmitt, P. S. Kirchmann, U. Bovensiepen, R. G. Moore, L. Rettig, M. Krenz, J.-H. Chu, N. Ru, L. Perfetti, D. H. Lu, *et al.*, Science **321**, 1649 (2008).
[26] J. C. Petersen, S. Kaiser, N. Dean, A. Simoncig, H. Y. Liu, A. L. Cavalieri, C. Cacho, I. C. E. Turcu, E. Springate, F. Frassetto, *et al.*, Phys. Rev. Lett. **107**, 177402 (2011).
[27] S. Mor, M. Herzog, J. Noack, N. Katayama, M. Nohara, H. Takagi, A. Trunschke, T. Mizokawa, C. Monney, and J. Stähler, Phys. Rev. B **97**, 115154 (2018).
[28] T. Tang, H. Wang, S. Duan, Y. Yang, C. Huang, Y. Guo, D. Qian, and W. Zhang, Phys. Rev. B **101**, 235148 (2020).
[29] P. Andrich, H. M. Bretscher, Y. Murakami, D. Golež, B. Remez, P. Telang, A. Singh, L. Harnagea, N. R. Cooper, A. J. Millis, *et al.*, arXiv:2003.10799 (2020).
[30] E. G. Maksimov, I. I. Mazin, S. Y. Savrasov, and Y. A. Uspenski, J. Phys. Condens. Matter **1**, 2493 (1989).
[31] L. Hedin, Phys. Rev. **139**, A796 (1965).
[32] S. V. Faleev, M. van Schilfgaarde, T. Kotani, F. Léonard,

and M. P. Desjarlais, Phys. Rev. B **74**, 033101 (2006).
[33] S. Gerber, S.-L. Yang, D. Zhu, H. Soifer, J. Sobota, S. Rebec, J. Lee, T. Jia, B. Moritz, C. Jia, *et al.*, Science **357**, 71 (2017).
[34] S. A. Sunshine and J. A. Ibers, Inorg. Chem. **24**, 3611 (1985).
[35] C. Lee, T. Rohwer, E. J. Sie, A. Zong, E. Baldini, J. Straquadine, P. Walmsley, D. Gardner, Y. S. Lee, I. R. Fisher, and N. Gedik, Rev. Sci. Instrum. **91**, 043102 (2020).
[36] G. Kresse and J. Hafner, Phys. Rev. B **47**, 558 (1993).
[37] J. P. Perdew, K. Burke, and M. Ernzerhof, Phys. Rev. Lett. (1996).
[38] A. Togo and I. Tanaka, Scr. Mater. **108**, 1 (2015).
[39] Y. Murakami, D. Golež, T. Kaneko, A. Koga, A. J. Millis, and P. Werner, Phys. Rev. B **101**, 195118 (2020).
[40] D. Pekker and C. M. Varma, Annu. Rev. Condens. Matter Phys. **6**, 269 (2015).
[41] B. Zenker, H. Fehske, and H. Beck, Phys. Rev. B **90**, 195118 (2014).
[42] S. Weinberg, *The Quantum Theory of Fields*, Vol. 1 (Cambridge University Press, 1995).
[43] Z. He and A. J. Millis, Phys. Rev. B **93**, 115126 (2016).
[44] M. Eckstein and P. Werner, Phys. Rev. B **84**, 035122 (2011).
[45] T. Larkin, A. Yaresko, D. Pröpper, K. Kikoin, Y. Lu, T. Takayama, Y.-L. Mathis, A. Rost, H. Takagi, B. Keimer, *et al.*, Phys. Rev. B **95**, 195144 (2017).
[46] T. I. Larkin, PhD Thesis (2016).
[47] S. Mor, M. Herzog, D. Golež, P. Werner, M. Eckstein, N. Katayama, M. Nohara, H. Takagi, T. Mizokawa, C. Monney, *et al.*, Phys. Rev. Lett. **119**, 086401 (2017).
[48] D. Werdehausen, T. Takayama, G. Albrecht, Y. Lu, H. Takagi, and S. Kaiser, J. Phys. Cond. Matt. (2018).
[49] S. P. Weathersby, G. Brown, M. Centurion, T. F. Chase, R. Coffee, J. Corbett, J. P. Eichner, J. C. Frisch, A. R. Fry, M. Gühr, N. Hartmann, C. Hast, R. Hettel, R. K. Jobe, E. N. Jongewaard, J. R. Lewandowski, R. K. Li, A. M. Lindenberg, I. Makasyuk, J. E. May, D. McCormick, M. N. Nguyen, A. H. Reid, X. Shen, K. Sokolowski-Tinten, T. Vecchione, S. L. Vetter, J. Wu, J. Yang, H. A. Dürr, and X. J. Wang, Rev. Sci. Instrum. **86**, 073702 (2015).
[50] Y. Wakisaka, T. Sudayama, K. Takubo, T. Mizokawa, N. L. Saini, M. Arita, H. Namatame, M. Taniguchi, N. Katayama, M. Nohara, *et al.*, J. Superc. Nov. Mag. **25**, 1231 (2012).
[51] G. Beni and T. M. Rice, Phys. Rev. B **18**, 768 (1978).
[52] S. G. Han, Z. V. Vardeny, K. S. Wong, O. G. Symko, and G. Koren, Phys. Rev. Lett. **65**, 2708 (1990).
[53] P. Kusar, V. V. Kabanov, J. Demsar, T. Mertelj, S. Sugai, and D. Mihailovic, Phys. Rev. Lett. **101**, 227001 (2008).
[54] L. Stojchevska, P. Kusar, T. Mertelj, V. V. Kabanov, Y. Toda, X. Yao, and D. Mihailovic, Phys. Rev. B **84**, 180507 (2011).
[55] S. Dal Conte, L. Vidmar, D. Golež, M. Mierzejewski, G. Soavi, S. Peli, F. Banfi, G. Ferrini, R. Comin, B. M. Ludbrook, *et al.*, Nat. Phys. **11**, 421 (2015).
[56] F. Boschini, E. H. da Silva Neto, E. Razzoli, M. Zonno, S. Peli, R. P. Day, M. Michiardi, M. Schneider, B. Zwartsenberg, P. Nigge, *et al.*, Nat. Mater. **17**, 416 (2018).
[57] T. Larkin, R. Dawson, M. Höppner, T. Takayama, M. Isobe, Y.-L. Mathis, H. Takagi, B. Keimer, and A. Boris, Phys. Rev. B **98**, 125113 (2018).
[58] P. Hein, A. Stange, K. Hanff, L. Yang, G. Rohde, K. Rossnagel, and M. Bauer, Phys. Rev. B **94**, 205406 (2016).
[59] F. Liu, M. E. Ziffer, K. R. Hansen, J. Wang, and X. Zhu, Phys. Rev. Lett. **122**, 246803 (2019).
[60] T. E. Stevens, J. Kuhl, and R. Merlin, Phys. Rev. B **65**, 144304 (2002).
[61] J. Yan, R. Xiao, X. Luo, H. Lv, R. Zhang, Y. Sun, P. Tong, W. Lu, W. Song, X. Zhu, *et al.*, Inorg. Chem. **58**, 9036 (2019).
[62] S. Kaiser, Private communication (2019).
[63] A. Jain, S. P. Ong, G. Hautier, W. Chen, W. D. Richards, S. Dacek, S. Cholia, D. Gunter, D. Skinner, G. Ceder, and K. a. Persson, APL Mat. **1**, 011002 (2013).
[64] S. P. Ong, S. Cholia, A. Jain, M. Brafman, D. Gunter, G. Ceder, and K. A. Persson, Comput. Mater. Sci. **97**, 209 (2015).
[65] J. Klimeš, D. R. Bowler, and A. Michaelides, J. Phys. Condens. Matter **22**, 022201 (2009).
[66] J. Klimeš, D. R. Bowler, and A. Michaelides, Phys. Rev. B **83**, 195131 (2011).
[67] A. Togo and I. Tanaka, arXiv:1808.01590 (2018).
[68] A. N. Kolmogorov, S. Shah, E. R. Margine, A. K. Kleppe, and A. P. Jephcoat, Phys. Rev. Lett. **109**, 075501 (2012).
[69] J. P. Perdew, K. Burke, and M. Ernzerhof, Phys. Rev. Lett. **77**, 3865 (1996).
[70] J. Sun, A. Ruzsinszky, and J. P. Perdew, Phys. Rev. Lett. **115**, 036402 (2015).
[71] T. Kaneko, T. Toriyama, T. Konishi, and Y. Ohta, Phys. Rev. B (2013).
[72] L. Windgaetter, S. Latini, and A. Rubio, Submitted (2020).
[73] C. D. Spataru, L. X. Benedict, and S. G. Louie, Phys. Rev. B **69**, 205204 (2004).
[74] M. van Schilfgaarde, T. Kotani, and S. Faleev, Phys. Rev. Lett. **96**, 226402 (2006).
[75] S. Baroni, P. Giannozzi, and A. Testa, Phys. Rev. Lett. **58**, 1861 (1987).
[76] E. Baldini, M. A. Sentef, S. Acharya, T. Brumme, E. Sheveleva, F. Lyzwa, E. Pomjakushina, C. Bernhard, M. Van Schilfgaarde, F. Carbone, *et al.*, Proc. Natl. Acad. Sci. **117**, 6409 (2020).

5 Discussion

In this thesis I presented two different systems that exhibit strong correlation phenomena between their excitonic and phononic quasiparticles. In both cases I have shown in joint theoretical and experimental collaborations that a deep understanding of both their electronic and ionic properties are necessary to be able to control and engineer the crystal and to understand the nature and microscopic origin of its competing phase transition. To achieve this I have employed state of the art ab-initio methods as well as model calculations.

In the first part of this thesis I have discussed how strong electron phonon-coupling can be utilized to dynamically control material properties and to characterize the nature of peculiar hybrid dimensional excitonic states.
In publication I I have shown in a combined theoretical and experimental study, how the quasi one-dimensionality in SiP_2 leads to the emergence of unconventional excitonic states with hybrid dimensionality, i.e. the electronic wavefunction being localized along the one dimensional Phosphorus chains of the crystal while the hole wavefunction is localized along the whole two dimensional layer. This feature is imprinted by its underlying crystal structure, which makes SiP_2 a prime example of a symmetry engineered material with the goal of controlling its electronic properties. I have shown that the excitonic state is very sensitive to phononic perturbations, that displace the one dimensional phosphorus chains, and that this results in a strong coupling of the exciton to such phonons. We could confirm this strong coupling both in theoretical and experimental Photoluminscence and Reflectivity measurements performed by our collaborators, where it leads to the emergence of phononic sidepeaks to the main excitonic peak. These sidepeaks stemming from low dimensional excitonic states coupling to phonons have so far only been measured in low dimensional materials such as graphene nanotubes or TMD monolayers [70–76], where, in contrast to SiP_2, the excitonic states have a clear one- or two-dimensional structure. Therefore, this presents the first bulk example which shows the emergence of exciton phonon sidepeaks of an exciton with hybrid dimensionality.
Due to its peculiar one-dimensional nature, SiP_2 could provide a perfect platform to control even more complex excitonic states through its symmetry engineering. It is conceivable that also trionic states with hybrid dimensionality could be realized in this system.

In publication II I have shown that a strong coupling between electronic and phononic degrees of freedom can also be employed to control the optical properties of a crystal. It has been shown by our experimental colleagues that the THz reflectivity of Ta_2NiSe_5

can be significantly increased by pumping the electronic subsystem with an initial laser pulse. To understand the underlying microscopic mechanism of the phenomenon I have used a combined ab-initio and model approach and identified the following mechanism: Upon exciting electronic states near the bandedge by a laser pulse the first conduction bands are populated. These electronic bands couple via a dipole interaction strongly to a specific 4.7 THz infrared active phonon mode and lead to coherent phonon fluctuations at twice the phonon frequency. This fluctuation effectively transforms the crystal into a Floquet medium, which leads to the strong amplification in THz reflectivity by up to 30%. Therefore, this non-linear coupling between the electronic and phononic states allows to selectively excite specific infrared phonon modes by pumping the corresponding electronic states to which these phonons are coupled strongly.

In the second part of this thesis I have investigated the conjectured EI state in Ta_2NiSe_5. First I have introduced the basic concept of an EI and shown that it describes the formation of an exotic groundstate which has a condensate of excitonic particles at its heart. Measuring such a state, however, is experimentally extremely challenging, because in TNSe as in many other EI candidate materials the conjectured EI state [21,26,27] is intrinsically coupled to another transition, i.e. a structural phase transition [20, 28, 29, 88]. In this work I have aimed at shining light on both competing transitions by disentangling their effects. This approach allowed to isolate the possible excitonic signature, which is crucial for the interpretation of the experimental data presented for this material. In the series of publications III-V I have first investigated, if TNSe could host such an excitonic instability and then if it is actually realized or if the transition is predominantly structurally driven.
In Publication III I have defined an excitonic instability as a charge density that breaks the lattice symmetries, which could trigger the structural phase transition in TNSe, and identified the corresponding excitonic order parameter. I have obtained a very narrow phase space region, that exhibits such an instability, which arises due to the hybridisation between the lowest lying valence and conduction bands and leads to a bandgap opening similar to the experimentally measured one. However, the phase space region is very small and using ab-initio calculations in publication IV, I showed that this instability is not realized: neither do I find a symmetry broken charge density nor can such a pure electronic instability account for the metal to insulator transition in our ab-initio calculations. Instead I have found a strongly coupled soft phononic state, which leads to a structural change that can explain the experimental evidence, such as band hybridisation and bandgap opening. These have so far been attributed to the conjectured EI phase in the interpretation of most of the available experiments [30, 106, 118] . Therefore, I could show that the dominant effect is the structural phase transition and that the EI plays a minor role. This result is reinforced by the combined theoretical and experimental work in publication V. Here I have shown, that the time resolved ARPES measurements from

our experimental collaborators agree very well with our theory calculations and exhibit a time dependent bandgap modulation which is only consistent on phononic timescales. This can be rationalized in term of a coupling to the soft mode driving the phase transition. Furthermore, our experimental collaborators have not been able to melt the excitonic condensate through the optical excitation of electrons, which is expected to be possible in a excitonic dominated phase transition.
However, the results of recent Raman spectroscopy studies still need to be understood [88, 96, 99–101]. These do not show softening of any phonon modes in the corresponding symmetry channels, but instead a strong asymmetric broadening of the relevant B_{2g} phonons. While the authors have interpreted this as a sign of the EI scenario, this experimental signature could also stem from phonon anharmonicities of the B_{2g} phonons coupling to surrounding phononic modes. It is conceivable that such an anharmonic coupling stabilizes the soft phonon modes and leads to the observed broadening in the experiment. To this end I have started a follow up project to analyze the phononic spectra at finite temperature using Molecular Dynamics (MD) calculations to understand the phononic and Raman spectra across the phase transition. These indeed show that the B_{2g} mode does not soften, but is constant in energy, which is consistent with the experimental measurements. Instead it broadens significantly approaching the critical temperature, which we can trace back to the coupling to other phonon modes rather than an EI state. I expect to publish these results soon. With this I believe to finally settle the controversial discussion surrounding TNSe as an EI candidate.

Summarizing, the projects in this thesis contribute to the current research how phononic degrees of freedom play a crucial role in excitonic and anisotropic systems. This is important to understand how crystals can be manipulated to engineer their properties either through the excitation of electronic modes that couple strongly to specific phononic modes or through engineering the underlying crystal symmetry. Furthermore I have shown how to disentangle the contributions of the different effects in competing ionic and electronic phase transitions such as the one in TNSe. Extensive theoretical simulations employing combined ab-initio and model calculations provide an optimal pathway to understand such phenomena, because only here one has total control on the interactions allowed to take part in the transition while being able to describe realistic systems. As such we were able to understand the nature of both the conjectured excitonic and structural phase transition in Ta_2NiSe_5 which will be important contribution to the controversial debate surrounding this material.

Outlook

In the previous section I have discussed the results presented in this dissertation, explained how they contribute to their line of research and which further investigations

need to be taken. In this section I would like to embed this discussion into the more general context of quantum materials and present what potential promising EI systems might be.

The goal of the field of quantum materials is to discover phenomena that involve quasiparticles, that behave in a possibly collective or strongly correlated way and that go beyond (semi-)classical physics. The most famous example for such a quantum material are superconductors which have a condensate of Cooper pairs as their groundstate. They emerge due to the renormalization of their electronic interaction mediated by phonons. Superconductivity has been an active field of research for over a century [119] with more and more materials being discovered that exhibit superconductivity at higher temperatures [2–4]. Other examples for quantum materials are charge density wave (CDW) materials, which show charge ordering due to the wave-like nature of electrons. This charge ordering ultimately leads to a modulation of the atomic lattice due to the coupling of electronic states to a phononic condensate [120, 121]. A third class of intensively investigated quantum materials are topological insulators [122, 123]. These quantum phenomena can appear separately or in some cases even at similar temperatures giving rise to competing phase transitions. An example for such a competing transition are CDW and superconducting states [124] which both arise due to their strong coupling to phonons.
Control of such quantum materials aims at understanding the underlying mechanisms of these phenomena and manipulating them in a controlled fashion. The ultimate goal is to be able to tune the properties of such quantum materials on demand. There are many ways with which this control can be exerted. It can for instance be done by crystal engineering, using heterostructures, introducing Moire potentials or applying external fields such as magnetic fields or laser pumps [125]. The latter can selectively excite specific quasiparticles within the system and drive phase transitions [125]. A famous example for this effect is light induced superconductivity, which is realized by pumping specific phonons via laser pulses [126]. Similarly superconducting states can also be tuned via symmetry engineering of the underlying lattice. One of the most exciting research fields exploiting this idea is twisttronics. It uses the ability to create monolayer graphene or TMD sheets and to stack them at arbitrary angles to induce a Moire potential in the system. Such a twisted system of graphene has been shown to exhibit a rich phase diagram which shows signs of superconductivity and correlated insulating states [12].
In the first part of the thesis we have seen two different examples for these quantum control mechanisms, one static via symmetry engineering and one dynamic via selective excitation, which both rely on the strong electron phonon coupling in their crystals. With this both fit very well into this line of research. The task of this field is now to learn and understand how these different techniques to manipulate materials can be combined. An example for this could be SiP_2. Due to its layered nature it can be used to create heterointerfaces with other materials or even host Moire physics introducing a twist. This might

allow to imprint its quasi one-dimensionality in the heterostructures and open pathways to induce symmetry constraints to the electronic system. A possible application could be symmetry engineered interlayer or Moire excitons in heterostructures. Similarly it could be used as a substrate for other materials such as superconductors to induce dimensionality effects which might give rise to new physical phenomena.
Closely related to the emergence of superconductivity is the EI phase, which is a controversally debated topic in quantum materials research. It is formally similar to the superconducting state, but has excitons rather than Cooper pairs at its heart. This leads to an insulating rather than an superconducting state. Identifying an EI insulating state is an immensely challenging task. In the case of Ta_2NiSe_5 it led to many experimental and theoretical efforts, that struggle to disentangle the competing phase transition, which all bulk candidate materials have in common. As a result, the interpretation of the experimental data has not been clear in many cases, because the unique signature of an EI state has not yet been identified. Therefore, it would be desirable to realize and understand such an EI state in a more controlled way to fully understand its properties. I believe that the right way to do this is to try to realize it in low dimensional systems. The reason for this is that these have, as already hinted in chapter 4, much higher excitonic binding energies due to their lack of screening. Thus, it should in principle be much easier to obtain excitonic binding energies, that exceed the electronic bandgap. It would be particularly interesting if we also had control of the electronic bandgap in those systems to be able to induce the phase transition through some external experimental parameter. A platform that fulfills all these properties are gated double layer systems [23, 82, 84]. Here it is possible to separate electrons and holes into the two different layers which, are commonly chosen to be graphene or TMDs. The interaction between these two particles can be tuned via the size of the separating hexagonal boron nitride (hBN) layer. The bandgap and chemical potential of such material can be controlled via gating, which should allow to switch between EI and conventional phase. Indeed, first experimental setups using these techniques have shown promising results, inducing a potentially EI groundstate which becomes exciton compressible, but charge incompressible upon closing the bandgap sufficiently [23]. In such double layer systems it is possible to contruct even more complex geometries using twisted Moire systems. These allow to confine single electrons and thus excitonic states to their Moire potential which acts as a potential well [84]. Another possible experimental setup to realize the EI state in a controlled way might be optical cavities. These could allow to control the EI phase transition through the fluctuations of the photonic field confined in the cavity [127]. Therefore, these systems might be very promising candidates to pinpoint a unique experimental signature of the EI state, which can be used to identify this elusive state also in more traditional candidate materials.

Bibliography

[1] J. Bardeen and W. H. Brattain. The transistor, a semi-conductor triode. *Phys. Rev.*, 74:230–231, Jul 1948.

[2] Z. Z. Sheng and A. M. Hermann. Bulk superconductivity at 120 K in the Tl–Ca/Ba–Cu–O system. *Nature*, 332(6160):138–139, Mar 1988.

[3] M. K. Wu, J. R. Ashburn, C. J. Torng, P. H. Hor, R. L. Meng, L. Gao, Z. J. Huang, Y. Q. Wang, and C. W. Chu. Superconductivity at 93 K in a new mixed-phase Y-Ba-Cu-O compound system at ambient pressure. *Phys. Rev. Lett.*, 58:908–910, Mar 1987.

[4] A. Schilling, M. Cantoni, J. D. Guo, and H. R. Ott. Superconductivity above 130 K in the Hg-Ba-Ca-Cu-O system. *Nature*, 363(6424):56–58, May 1993.

[5] Akihiro Kojima, Kenjiro Teshima, Yasuo Shirai, and Tsutomu Miyasaka. Organometal halide perovskites as visible-light sensitizers for photovoltaic cells. *Journal of the American Chemical Society*, 131(17):6050–6051, May 2009.

[6] Hanul Min, Do Yoon Lee, Junu Kim, Gwisu Kim, Kyoung Su Lee, Jongbeom Kim, Min Jae Paik, Young Ki Kim, Kwang S. Kim, Min Gyu Kim, Tae Joo Shin, and Sang Il Seok. Perovskite solar cells with atomically coherent interlayers on SnO_2 electrodes. *Nature*, 598(7881):444–450, Oct 2021.

[7] A. K. Geim and I. V. Grigorieva. Van der waals heterostructures. *Nature*, 499(7459):419–425, Jul 2013.

[8] Kin Fai Mak, Changgu Lee, James Hone, Jie Shan, and Tony F. Heinz. Atomically thin MoS_2: A new direct-gap semiconductor. *Phys. Rev. Lett.*, 105:136805, Sep 2010.

[9] B. Radisavljevic, A. Radenovic, J. Brivio, V. Giacometti, and A. Kis. Single-layer MoS_2 transistors. *Nature Nanotechnology*, 6(3):147–150, Mar 2011.

[10] Andrea Splendiani, Liang Sun, Yuanbo Zhang, Tianshu Li, Jonghwan Kim, Chi-Yung Chim, Giulia Galli, and Feng Wang. Emerging photoluminescence in monolayer MoS_2. *Nano Letters*, 10(4):1271–1275, Apr 2010.

[11] Qing Hua Wang, Kourosh Kalantar-Zadeh, Andras Kis, Jonathan N. Coleman, and Michael S. Strano. Electronics and optoelectronics of two-dimensional transition metal dichalcogenides. *Nature Nanotechnology*, 7(11):699–712, Nov 2012.

[12] Yuan Cao, Valla Fatemi, Shiang Fang, Kenji Watanabe, Takashi Taniguchi, Efthimios Kaxiras, and Pablo Jarillo-Herrero. Unconventional superconductivity in magic-angle graphene superlattices. *Nature*, 556(7699):43–50, Apr 2018.

[13] L. V. Keldysh and A. N. Kozlov. Collective properties of excitons in semiconductors. *Sov. Phys. JETP*, 27:978, 1968.

[14] N. F. Mott. The transition to the metallic state. *The Philosophical Magazine: A Journal of Theoretical Experimental and Applied Physics*, 6(62):287–309, 1961.

[15] AN Kozlov and LA Maksimov. The metal-dielectric divalent crystal phase transition. *Sov. Phys. JETP*, 21:790, 1965.

[16] AN Kozlov and LA Maksimov. Collective excitations in semimetals. *Sov. Phys. JETP*, 22:889, 1965.

[17] AN Kozlov and LA Maksimov. Possibility of "Superthermal Conductivity" in semiconductors. *Sov. Phys. JETP*, 23:88, 1966.

[18] D. Jérome, T. M. Rice, and W. Kohn. Excitonic insulator. *Phys. Rev.*, 158:462–475, Jun 1967.

[19] W. Kohn. Excitonic phases. *Phys. Rev. Lett.*, 19:439–442, Aug 1967.

[20] T Kaneko, T Toriyama, T Konishi, and Y Ohta. Electronic structure of Ta_2NiSe_5 as a candidate for excitonic insulators. *Journal of Physics: Conference Series*, 400(3):032035, dec 2012.

[21] B. Bucher, P. Steiner, and P. Wachter. Excitonic insulator phase in $TmSe_{0.45}Te_{0.55}$. *Phys. Rev. Lett.*, 67:2717–2720, Nov 1991.

[22] Sunny Gupta, Alex Kutana, and Boris I. Yakobson. Heterobilayers of 2d materials as a platform for excitonic superfluidity. *Nature Communications*, 11(1):2989, Jun 2020.

[23] Liguo Ma, Phuong X. Nguyen, Zefang Wang, Yongxin Zeng, Kenji Watanabe, Takashi Taniguchi, Allan H. MacDonald, Kin Fai Mak, and Jie Shan. Strongly correlated excitonic insulator in atomic double layers. *Nature*, 598(7882):585–589, Oct 2021.

[24] Daniele Varsano, Sandro Sorella, Davide Sangalli, Matteo Barborini, Stefano Corni, Elisa Molinari, and Massimo Rontani. Carbon nanotubes as excitonic insulators. *Nature Communications*, 8(1):1461, Nov 2017.

[25] Daniele Varsano, Maurizia Palummo, Elisa Molinari, and Massimo Rontani. A monolayer transition-metal dichalcogenide as a topological excitonic insulator. *Nature Nanotechnology*, 15(5):367–372, May 2020.

[26] H. Cercellier, C. Monney, F. Clerc, C. Battaglia, L. Despont, M. G. Garnier, H. Beck, P. Aebi, L. Patthey, H. Berger, and L. Forró. Evidence for an excitonic insulator phase in 1T-$TiSe_2$. *Phys. Rev. Lett.*, 99:146403, Oct 2007.

[27] Anshul Kogar, Melinda S. Rak, Sean Vig, Ali A. Husain, Felix Flicker, Young Il Joe, Luc Venema, Greg J. MacDougall, Tai C. Chiang, Eduardo Fradkin, Jasper van Wezel, and Peter Abbamonte. Signatures of exciton condensation in a transition metal dichalcogenide. *Science*, 358(6368):1314–1317, 2017.

[28] Steven A. Sunshine and James A. Ibers. Structure and physical properties of the new layered ternary chalcogenides tantalum nickel sulfide (Ta_2NiS_5) and tantalum nickel selenide (Ta_2NiSe_5). *Inorganic Chemistry*, 24(22):3611–3614, Oct 1985.

[29] F.J. Di Salvo, C.H. Chen, R.M. Fleming, J.V. Waszczak, R.G. Dunn, S.A. Sunshine, and James A. Ibers. Physical and structural properties of the new layered compounds Ta_2NiS_5 and Ta_2NiSe_5. *Journal of the Less Common Metals*, 116(1):51–61, 1986.

[30] K. Seki, Y. Wakisaka, T. Kaneko, T. Toriyama, T. Konishi, T. Sudayama, N. L. Saini, M. Arita, H. Namatame, M. Taniguchi, N. Katayama, M. Nohara, H. Takagi, T. Mizokawa, and Y. Ohta. Excitonic bose-einstein condensation in Ta_2NiSe_5 above room temperature. *Phys. Rev. B*, 90:155116, Oct 2014.

[31] T. Kaneko, T. Toriyama, T. Konishi, and Y. Ohta. Orthorhombic-to-monoclinic phase transition of Ta_2NiSe_5 induced by the bose-einstein condensation of excitons. *Phys. Rev. B*, 87:035121, Jan 2013.

[32] P. Hohenberg and W. Kohn. Inhomogeneous electron gas. *Phys. Rev.*, 136:B864–B871, Nov 1964.

[33] W. Kohn and L. J. Sham. Self-consistent equations including exchange and correlation effects. *Phys. Rev.*, 140:A1133–A1138, Nov 1965.

[34] John P. Perdew, Kieron Burke, and Matthias Ernzerhof. Generalized gradient approximation made simple. *Phys. Rev. Lett.*, 77:3865–3868, Oct 1996.

[35] John P. Perdew, J. A. Chevary, S. H. Vosko, Koblar A. Jackson, Mark R. Pederson, D. J. Singh, and Carlos Fiolhais. Atoms, molecules, solids, and surfaces: Applications of the generalized gradient approximation for exchange and correlation. *Phys. Rev. B*, 46:6671–6687, Sep 1992.

[36] Press release. nobelprize.org. nobel prize outreach ab 2022. mon. 5 sep 2022. `https://www.nobelprize.org/prizes/chemistry/1998/summary/`. Accessed: 2022-09-05.

[37] Andrew Zangwill. The education of walter kohn and the creation of density functional theory. *Archive for History of Exact Sciences*, 68(6):775–848, Nov 2014.

[38] Jacobs ladder of exchange correlation functionals. `https://www.sas.upenn.edu/~jianmint/Research/`. Accessed: 2022-08-25.

[39] D. M. Ceperley and B. J. Alder. Ground state of the electron gas by a stochastic method. *Phys. Rev. Lett.*, 45:566–569, Aug 1980.

[40] Fabien Tran and Peter Blaha. Accurate band gaps of semiconductors and insulators with a semilocal exchange-correlation potential. *Phys. Rev. Lett.*, 102:226401, Jun 2009.

[41] Axel D. Becke and Erin R. Johnson. A simple effective potential for exchange. *The Journal of Chemical Physics*, 124(22):221101, 2006.

[42] A. D. Becke and M. R. Roussel. Exchange holes in inhomogeneous systems: A coordinate-space model. *Phys. Rev. A*, 39:3761–3767, Apr 1989.

[43] V. Fock. Näherungsmethode zur Lösung des quantenmechanischen Mehrkörperproblems. *Zeitschrift für Physik*, 61(1):126–148, Jan 1930.

[44] John P. Perdew, Matthias Ernzerhof, and Kieron Burke. Rationale for mixing exact exchange with density functional approximations. *The Journal of Chemical Physics*, 105(22):9982–9985, 1996.

[45] Matthias Ernzerhof and Gustavo E. Scuseria. Assessment of the Perdew–Burke–Ernzerhof exchange-correlation functional. *The Journal of Chemical Physics*, 110(11):5029–5036, 1999.

[46] Mel Levy. Universal variational functionals of electron densities, first-order density matrices, and natural spin-orbitals and solution of the v-representability problem. *Proceedings of the National Academy of Sciences*, 76(12):6062–6065, 1979.

[47] Jochen Heyd, Gustavo E. Scuseria, and Matthias Ernzerhof. Hybrid functionals based on a screened coulomb potential. *The Journal of Chemical Physics*, 118(18):8207–8215, 2003.

[48] Aliaksandr V. Krukau, Oleg A. Vydrov, Artur F. Izmaylov, and Gustavo E. Scuseria. Influence of the exchange screening parameter on the performance of screened hybrid functionals. *The Journal of Chemical Physics*, 125(22):224106, 2006.

[49] M. van Schilfgaarde, Takao Kotani, and S. Faleev. Quasiparticle self-consistent *GW* theory. *Phys. Rev. Lett.*, 96:226402, Jun 2006.

[50] Giovanni Onida, Lucia Reining, and Angel Rubio. Electronic excitations: density-functional versus many-body green's-function approaches. *Rev. Mod. Phys.*, 74:601–659, Jun 2002.

[51] GL Stefanucci and R van Leeuwen. *Nonequilibrium Many-Body Theory of Quantum Systems*, volume 1. Cambridge University Press, 2013.

[52] LV Keldysh. Diagram technique for nonequilibrium process. *Sov. Phys. JETP*, 20:1018, 1964.

[53] VM Galitskii and Migdal AB. Application of Quantum Field Theory methods to the Many Body Problem. *Sov. Phys. JETP*, 34:96, 1957.

[54] Paul C. Martin and Julian Schwinger. Theory of many-particle systems I. *Phys. Rev.*, 115:1342–1373, Sep 1959.

[55] F. J. Dyson. The S matrix in quantum electrodynamics. *Phys. Rev.*, 75:1736–1755, Jun 1949.

[56] Lars Hedin. New method for calculating the one-particle green's function with application to the electron-gas problem. *Phys. Rev.*, 139:A796–A823, Aug 1965.

[57] E. E. Salpeter and H. A. Bethe. A relativistic equation for bound-state problems. *Phys. Rev.*, 84:1232–1242, Dec 1951.

[58] G. Strinati. Application of the green's functions method to the study of the optical properties of semiconductors. *La Rivista del Nuovo Cimento (1978-1999)*, 11(12):1–86, Dec 1988.

[59] Michael Rohlfing and Steven G. Louie. Electron-hole excitations and optical spectra from first principles. *Phys. Rev. B*, 62:4927–4944, Aug 2000.

[60] Andrea Marini and Rodolfo Del Sole. Dynamical excitonic effects in metals and semiconductors. *Phys. Rev. Lett.*, 91:176402, Oct 2003.

[61] J. Bardeen, L. N. Cooper, and J. R. Schrieffer. Microscopic theory of superconductivity. *Phys. Rev.*, 106:162–164, Apr 1957.

[62] J. Bardeen, L. N. Cooper, and J. R. Schrieffer. Theory of superconductivity. *Phys. Rev.*, 108:1175–1204, Dec 1957.

[63] Gerd Czycholl. *Theoretische Festkörperphysik*, volume 1. Springer Spektrum, 2017.

[64] Feliciano Giustino. Electron-phonon interactions from first principles. *Rev. Mod. Phys.*, 89:015003, Feb 2017.

[65] T Holstein. Studies of polaron motion: Part I. the molecular-crystal model. *Annals of Physics*, 8(3):325–342, 1959.

[66] T. Holstein. Studies of polaron motion: Part II. the "small" polaron. *Annals of Physics*, 8(3):343–389, 1959.

[67] Marios Michael, Sheikh Rubaiat Ul Haque, Lukas Windgaetter, Simone Latini, Yuan Zhang, Angel Rubio, Richard D. Averitt, and Eugene Demler. Fresnel-floquet theory of light-induced terahertz reflectivity amplification in Ta_2NiSe_5, 2022. Preprint published at `https://arxiv.org/abs/2207.08851`.

[68] Gabriel Antonius and Steven G. Louie. Theory of exciton-phonon coupling. *Phys. Rev. B*, 105:085111, Feb 2022.

[69] Ling Zhou, Junwei Huang, Lukas Windgaetter, Chin Shen Ong, Xiaoxu Zhao, Caorong Zhang, Ming Tang, Zeya Li, Caiyu Qiu, Simone Latini, Yangfan Lu, Di Wu, Huiyang Gou, Andrew T. S. Wee, Hideo Hosono, Steven G. Louie, Peizhe Tang, Angel Rubio, and Hongtao Yuan. Unconventional excitonic states with phonon sidebands in layered silicon diphosphide. *Nature Materials*, 21(7):773–778, Jul 2022.

[70] Dominik Christiansen, Malte Selig, Gunnar Berghäuser, Robert Schmidt, Iris Niehues, Robert Schneider, Ashish Arora, Steffen Michaelis de Vasconcellos, Rudolf Bratschitsch, Ermin Malic, and Andreas Knorr. Phonon sidebands in monolayer transition metal dichalcogenides. *Phys. Rev. Lett.*, 119:187402, Nov 2017.

[71] Kai-Qiang Lin, Chin Shen Ong, Sebastian Bange, Paulo E. Faria Junior, Bo Peng, Jonas D. Ziegler, Jonas Zipfel, Christian Bäuml, Nicola Paradiso, Kenji Watanabe, Takashi Taniguchi, Christoph Strunk, Bartomeu Monserrat, Jaroslav Fabian, Alexey Chernikov, Diana Y. Qiu, Steven G. Louie, and John M. Lupton. Narrow-band high-lying excitons with negative-mass electrons in monolayer WSe_2. *Nature Communications*, 12(1):5500, Sep 2021.

[72] Victor Funk, Koloman Wagner, Edith Wietek, Jonas D. Ziegler, Jonathan Förste, Jessica Lindlau, Michael Förg, Kenji Watanabe, Takashi Taniguchi, Alexey Chernikov, and Alexander Högele. Spectral asymmetry of phonon sideband luminescence in monolayer and bilayer WSe_2. *Phys. Rev. Research*, 3:L042019, Nov 2021.

[73] Vasili Perebeinos, J. Tersoff, and Phaedon Avouris. Effect of exciton-phonon coupling in the calculated optical absorption of carbon nanotubes. *Phys. Rev. Lett.*, 94:027402, Jan 2005.

[74] Hualing Zeng, Hongbo Zhao, Fu-Chun Zhang, and Xiaodong Cui. Observation of exciton-phonon sideband in individual metallic single-walled carbon nanotubes. *Phys. Rev. Lett.*, 102:136406, Apr 2009.

[75] Evgeny Bobkin, Andreas Knorr, and Ermin Malic. Exciton-phonon sidebands in metallic carbon nanotubes studied using semiconductor bloch equations. *Phys. Rev. B*, 85:033409, Jan 2012.

[76] Yuhei Miyauchi and Shigeo Maruyama. Identification of an excitonic phonon sideband by photoluminescence spectroscopy of single-walled carbon-13 nanotubes. *Phys. Rev. B*, 74:035415, Jul 2006.

[77] Mikhail F. Limonov, Mikhail V. Rybin, Alexander N. Poddubny, and Yuri S. Kivshar. Fano resonances in photonics. *Nature Photonics*, 11(9):543–554, Sep 2017.

[78] M. Budden, T. Gebert, M. Buzzi, G. Jotzu, E. Wang, T. Matsuyama, G. Meier, Y. Laplace, D. Pontiroli, M. Riccò, F. Schlawin, D. Jaksch, and A. Cavalleri. Evidence for metastable photo-induced superconductivity in K_3C_{60}. *Nature Physics*, 17(5):611–618, May 2021.

[79] Pavel E. Dolgirev, Alfred Zong, Marios H. Michael, Jonathan B. Curtis, Daniel Podolsky, Andrea Cavalleri, and Eugene Demler. Periodic dynamics in superconductors induced by an impulsive optical quench, 2021. Preprint published at `https://arxiv.org/abs/2104.07181`.

[80] Marios H. Michael, Michael Först, Daniele Nicoletti, Sheikh Rubaiat Ul Haque, Yuan Zhang, Andrea Cavalleri, Richard D. Averitt, Daniel Podolsky, and Eugene Demler. Generalized fresnel-floquet equations for driven quantum materials. *Phys. Rev. B*, 105:174301, May 2022.

[81] Daniel Werdehausen, Tomohiro Takayama, Gelon Albrecht, Yangfan Lu, Hidenori Takagi, and Stefan Kaiser. Photo-excited dynamics in the excitonic insulator Ta_2NiSe_5. *Journal of Physics: Condensed Matter*, 30(30):305602, Jul 2018.

[82] J. I. A. Li, T. Taniguchi, K. Watanabe, J. Hone, and C. R. Dean. Excitonic superfluid phase in double bilayer graphene. *Nature Physics*, 13(8):751–755, Aug 2017.

[83] Liang Li, Penglai Gong, Weike Wang, Bei Deng, Lejing Pi, Jing Yu, Xing Zhou, Xingqiang Shi, Huiqiao Li, and Tianyou Zhai. Strong in-plane anisotropies of optical and electrical response in layered dimetal chalcogenide. *ACS Nano*, 11(10):10264–10272, Oct 2017.

[84] Jie Gu, Liguo Ma, Song Liu, Kenji Watanabe, Takashi Taniguchi, James C. Hone, Jie Shan, and Kin Fai Mak. Dipolar excitonic insulator in a moiré lattice. *Nature Physics*, 18(4):395–400, Apr 2022.

[85] S. Samaneh Ataei, Daniele Varsano, Elisa Molinari, and Massimo Rontani. Evidence of ideal excitonic insulator in bulk MoS_2 under pressure. *Proceedings of the National Academy of Sciences*, 118(13):e2010110118, 2021.

[86] Th. Pillo, J. Hayoz, H. Berger, F. Lévy, L. Schlapbach, and P. Aebi. Photoemission of bands above the fermi level: The excitonic insulator phase transition in 1T-$TiSe_2$. *Phys. Rev. B*, 61:16213–16222, Jun 2000.

[87] K. Rossnagel, L. Kipp, and M. Skibowski. Charge-density-wave phase transition in 1T-$TiSe_2$: Excitonic insulator versus band-type jahn-teller mechanism. *Phys. Rev. B*, 65:235101, May 2002.

[88] Mai Ye, Pavel A. Volkov, Himanshu Lohani, Irena Feldman, Minsung Kim, Amit Kanigel, and Girsh Blumberg. Lattice dynamics of the excitonic insulator $Ta_2Ni(Se_{1-x}S_x)_5$. *Phys. Rev. B*, 104:045102, Jul 2021.

[89] Tianwei Tang, Hongyuan Wang, Shaofeng Duan, Yuanyuan Yang, Chaozhi Huang, Yanfeng Guo, Dong Qian, and Wentao Zhang. Non-coulomb strong electron-hole binding in Ta_2NiSe_5 revealed by time- and angle-resolved photoemission spectroscopy. *Phys. Rev. B*, 101:235148, Jun 2020.

[90] Edoardo Baldini, Alfred Zong, Dongsung Choi, Changmin Lee, Marios H. Michael, Lukas Windgaetter, Igor I. Mazin, Simone Latini, Doron Azoury, Baiqing Lv, Anshul Kogar, Yao Wang, Yangfan Lu, Tomohiro Takayama, Hidenori Takagi, Andrew J. Millis, Angel Rubio, Eugene Demler, and Nuh Gedik. The spontaneous symmetry breaking in Ta_2NiSe_5 is structural in nature, 2020. Preprint published at `https://arxiv.org/abs/2007.02909`.

[91] Matthew D. Watson, Igor Marković, Edgar Abarca Morales, Patrick Le Fèvre, Michael Merz, Amir A. Haghighirad, and Philip D. C. King. Band hybridization at the semimetal-semiconductor transition of Ta_2NiSe_5 enabled by mirror-symmetry breaking. *Phys. Rev. Research*, 2:013236, Mar 2020.

[92] Cheng Chen, Xiang Chen, Weichen Tang, Zhenglu Li, Siqi Wang, Shuhan Ding, Chris Jozwiak, Aaron Bostwick, Eli Rotenberg, Makoto Hashimoto, Donghui Lu, Jacob P. C. Ruff, Steven G. Louie, Robert Birgeneau, Yulin Chen, Yao Wang, and Yu He. Lattice fluctuation induced pseudogap in quasi-one-dimensional Ta_2NiSe_5, 2022. Preprint published at `https://arxiv.org/abs/2203.06817`.

[93] Harshvardhan Jog, Luminita Harnagea, Eugene J. Mele, and Ritesh Agarwal. Exchange coupling mediated broken symmetries in Ta_2NiSe_5 revealed from quadrupolar circular photogalvanic effect. *Science Advances*, 8(7):eabl9020, 2022.

[94] Giacomo Mazza, Malte Rösner, Lukas Windgätter, Simone Latini, Hannes Hübener, Andrew J. Millis, Angel Rubio, and Antoine Georges. Nature of symmetry breaking at the excitonic insulator transition: Ta_2NiSe_5. *Phys. Rev. Lett.*, 124:197601, May 2020.

[95] Lukas Windgätter, Malte Rösner, Giacomo Mazza, Hannes Hübener, Antoine Georges, Andrew J. Millis, Simone Latini, and Angel Rubio. Common microscopic origin of the phase transitions in Ta_2NiS_5 and the excitonic insulator candidate Ta_2NiSe_5. *npj Computational Materials*, 7(1):210, Dec 2021.

[96] Kwangrae Kim, Hoon Kim, Jonghwan Kim, Changil Kwon, Jun Sung Kim, and B. J. Kim. Direct observation of excitonic instability in Ta_2NiSe_5. *Nature Communications*, 12(1):1969, Mar 2021.

[97] T. I. Larkin, A. N. Yaresko, D. Pröpper, K. A. Kikoin, Y. F. Lu, T. Takayama, Y.-L. Mathis, A. W. Rost, H. Takagi, B. Keimer, and A. V. Boris. Giant exciton fano resonance in quasi-one-dimensional Ta_2NiSe_5. *Phys. Rev. B*, 95:195144, May 2017.

[98] Jinwon Lee, Chang-Jong Kang, Man Jin Eom, Jun Sung Kim, Byung Il Min, and Han Woong Yeom. Strong interband interaction in the excitonic insulator phase of Ta_2NiSe_5. *Phys. Rev. B*, 99:075408, Feb 2019.

[99] P. A. Volkov, Mai Ye, H. Lohani, I. Feldman, A. Kanigel, and G. Blumberg. Critical charge fluctuations and emergent coherence in a strongly correlated excitonic insulator. *npj Quantum Materials*, 6(1):52, May 2021.

[100] Pavel A. Volkov, Mai Ye, Himanshu Lohani, Irena Feldman, Amit Kanigel, and Girsh Blumberg. Failed excitonic quantum phase transition in $Ta_2Ni(Se_{1-x}S_x)_5$. *Phys. Rev. B*, 104:L241103, Dec 2021.

[101] Min-Jae Kim, Armin Schulz, Tomohiro Takayama, Masahiko Isobe, Hidenori Takagi, and Stefan Kaiser. Phononic soft mode behavior and a strong electronic background across the structural phase transition in the excitonic insulator Ta_2NiSe_5. *Phys. Rev. Research*, 2:042039, Dec 2020.

[102] Jacques Des Cloizeaux. Exciton instability and crystallographic anomalies in semiconductors. *Journal of Physics and Chemistry of Solids*, 26(2):259–266, 1965.

[103] GD Mahan. *Many-Particle Physics*. Springer Science+Business Media, New York, 3 edition, 2000.

[104] C. Monney, H. Cercellier, F. Clerc, C. Battaglia, E. F. Schwier, C. Didiot, M. G. Garnier, H. Beck, P. Aebi, H. Berger, L. Forró, and L. Patthey. Spontaneous exciton condensation in 1T-$TiSe_2$: BCS-like approach. *Phys. Rev. B*, 79:045116, Jan 2009.

[105] Franz X. Bronold and Holger Fehske. Possibility of an excitonic insulator at the semiconductor-semimetal transition. *Phys. Rev. B*, 74:165107, Oct 2006.

[106] Y. F. Lu, H. Kono, T. I. Larkin, A. W. Rost, T. Takayama, A. V. Boris, B. Keimer, and H. Takagi. Zero-gap semiconductor to excitonic insulator transition in Ta_2NiSe_5. *Nature Communications*, 8(1):14408, Feb 2017.

[107] Ashish Arora, Matthias Drüppel, Robert Schmidt, Thorsten Deilmann, Robert Schneider, Maciej R. Molas, Philipp Marauhn, Steffen Michaelis de Vasconcellos, Marek Potemski, Michael Rohlfing, and Rudolf Bratschitsch. Interlayer excitons in a bulk van der waals semiconductor. *Nature Communications*, 8(1):639, Sep 2017.

[108] Nihit Saigal, Vasam Sugunakar, and Sandip Ghosh. Exciton binding energy in bulk MoS_2: A reassessment. *Applied Physics Letters*, 108(13):132105, 2016.

[109] A.T. Hanbicki, M. Currie, G. Kioseoglou, A.L. Friedman, and B.T. Jonker. Measurement of high exciton binding energy in the monolayer transition-metal dichalcogenides WS_2 and WSe_2. *Solid State Communications*, 203:16–20, 2015.

[110] Bairen Zhu, Xi Chen, and Xiaodong Cui. Exciton binding energy of monolayer WS_2. *Scientific Reports*, 5(1):9218, Mar 2015.

[111] A. R. Klots, A. K. M. Newaz, Bin Wang, D. Prasai, H. Krzyzanowska, Junhao Lin, D. Caudel, N. J. Ghimire, J. Yan, B. L. Ivanov, K. A. Velizhanin, A. Burger, D. G. Mandrus, N. H. Tolk, S. T. Pantelides, and K. I. Bolotin. Probing excitonic states in suspended two-dimensional semiconductors by photocurrent spectroscopy. *Scientific Reports*, 4(1):6608, Oct 2014.

[112] Heather M. Hill, Albert F. Rigosi, Cyrielle Roquelet, Alexey Chernikov, Timothy C. Berkelbach, David R. Reichman, Mark S. Hybertsen, Louis E. Brus, and Tony F. Heinz. Observation of excitonic rydberg states in monolayer MoS_2 and WS_2 by photoluminescence excitation spectroscopy. *Nano Letters*, 15(5):2992–2997, May 2015.

[113] Chendong Zhang, Amber Johnson, Chang-Lung Hsu, Lain-Jong Li, and Chih-Kang Shih. Direct imaging of band profile in single layer MoS_2 on graphite: Quasiparticle energy gap, metallic edge states, and edge band bending. *Nano Letters*, 14(5):2443–2447, May 2014.

[114] Hailong Chen, Xiewen Wen, Jing Zhang, Tianmin Wu, Yongji Gong, Xiang Zhang, Jiangtan Yuan, Chongyue Yi, Jun Lou, Pulickel M. Ajayan, Wei Zhuang, Guangyu Zhang, and Junrong Zheng. Ultrafast formation of interlayer hot excitons in atomically thin MoS_2/WS_2 heterostructures. *Nature Communications*, 7(1):12512, Aug 2016.

[115] Pasqual Rivera, John R. Schaibley, Aaron M. Jones, Jason S. Ross, Sanfeng Wu, Grant Aivazian, Philip Klement, Kyle Seyler, Genevieve Clark, Nirmal J. Ghimire, Jiaqiang Yan, D. G. Mandrus, Wang Yao, and Xiaodong Xu. Observation of long-lived interlayer excitons in monolayer $MoSe_2$–WSe_2 heterostructures. *Nature Communications*, 6(1):6242, Feb 2015.

[116] Yanyu Jia, Pengjie Wang, Cheng-Li Chiu, Zhida Song, Guo Yu, Berthold Jäck, Shiming Lei, Sebastian Klemenz, F. Alexandre Cevallos, Michael Onyszczak, Nadezhda Fishchenko, Xiaomeng Liu, Gelareh Farahi, Fang Xie, Yuanfeng Xu, Kenji Watanabe, Takashi Taniguchi, B. Andrei Bernevig, Robert J. Cava, Leslie M. Schoop, Ali Yazdani, and Sanfeng Wu. Evidence for a monolayer excitonic insulator. *Nature Physics*, 18(1):87–93, Jan 2022.

[117] J. I. A. Li, T. Taniguchi, K. Watanabe, J. Hone, and C. R. Dean. Excitonic superfluid phase in double bilayer graphene. *Nature Physics*, 13(8):751–755, Aug 2017.

[118] Y. Wakisaka, T. Sudayama, K. Takubo, T. Mizokawa, M. Arita, H. Namatame, M. Taniguchi, N. Katayama, M. Nohara, and H. Takagi. Excitonic insulator state in Ta_2NiSe_5 probed by photoemission spectroscopy. *Phys. Rev. Lett.*, 103:026402, Jul 2009.

[119] J. Clay and H. Kamerlingh Onnes. n the change of the resistance of the metals at very low temperatures and the influence exerted on it by small amounts of admixtures.I. *KNAW, Proceedings*, 10:207–215, 1907.

[120] R. Peierls. Zur theorie der elektrischen und thermischen leitfähigkeit von metallen. *Annalen der Physik*, 396(2):121–148, 1930.

[121] G. Grüner. The dynamics of charge-density waves. *Rev. Mod. Phys.*, 60:1129–1181, Oct 1988.

[122] Xiao-Liang Qi and Shou-Cheng Zhang. Topological insulators and superconductors. *Rev. Mod. Phys.*, 83:1057–1110, Oct 2011.

[123] C. L. Kane and E. J. Mele. Z_2 topological order and the quantum spin hall effect. *Phys. Rev. Lett.*, 95:146802, Sep 2005.

[124] J. Chang, E. Blackburn, A. T. Holmes, N. B. Christensen, J. Larsen, J. Mesot, Ruixing Liang, D. A. Bonn, W. N. Hardy, A. Watenphul, M. v. Zimmermann, E. M. Forgan, and S. M. Hayden. Direct observation of competition between superconductivity and charge density wave order in yba2cu3o6.67. *Nature Physics*, 8(12):871–876, Dec 2012.

[125] D. N. Basov, R. D. Averitt, and D. Hsieh. Towards properties on demand in quantum materials. *Nature Materials*, 16(11):1077–1088, Nov 2017.

[126] M. Mitrano, A. Cantaluppi, D. Nicoletti, S. Kaiser, A. Perucchi, S. Lupi, P. Di Pietro, D. Pontiroli, M. Riccò, S. R. Clark, D. Jaksch, and A. Cavalleri. Possible light-induced superconductivity in k3c60 at high temperature. *Nature*, 530(7591):461–464, Feb 2016.

[127] Giacomo Mazza and Antoine Georges. Superradiant quantum materials. *Phys. Rev. Lett.*, 122:017401, Jan 2019.

Eidesstattliche Versicherung / Declaration of Oath

Hiermit versichere ich an Eides statt, die vorliegende Dissertationsschrift selbst verfasst und keine anderen als die angegebenen Hilfsmittel und Quellen benutzt zu haben.

Hamburg, den 14.9.2022

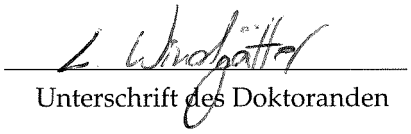

Unterschrift des Doktoranden